CRANFIELD UNIVERSITY

GAUTE LINDKVIST

INDIRECT BOUNDARY ELEMENT METHODS FOR MODELLING BUBBLES UNDER THREE DIMENSIONAL DEFORMATION

DEFENCE COLLEGE OF MANAGEMENT AND TECHNOLOGY

PhD THESIS

CRANFIELD UNIVERSITY

DEFENCE COLLEGE OF MANAGEMENT AND TECHNOLOGY

DEPARTMENT OF ENGINEERING SYSTEMS AND MANAGEMENT

PhD THESIS

Academic Year 2007-2008

Gaute Lindkvist

Indirect Boundary Element Methods for Modelling Bubbles under Three Dimensional Deformation

Supervisor: Dr S.A. Forth

May 2008

Abstract

The nonlinear behaviour of gas and vapour bubbles is a complex phenomenon which plays a significant role in many natural and man-made processes. For example, bubbles excited by an acoustic field play important roles in lithotripsy, drug delivery, ultrasonic imaging, surface cleaning and give rise to the phenomenon of sonoluminescence (light emission from a bubble excited by sound). In such contexts, the oscillation of even a single bubble is not yet fully understood, let alone the behaviour of multiple bubbles interacting with each other. An essential part of understanding such problems is understanding the complex and sometimes unpredictable coupling between the oscillation of the bubble volume and the bubble shape, a problem requiring experimental research, theoretical work and numerical studies.

In this Thesis we focus on numerical simulation of a single gas bubble oscillating in a free liquid. Previously, such numerical simulations have almost exclusively assumed axisymmetry and small amplitude oscillations. To avoid these assumptions we build upon and extend previous boundary element methods used for three dimensional simulations of other bubble problems. We use high order elements and parallel processing to yield an indirect boundary element method capable of capturing fine surface effects on three dimensional bubbles subjected to surface tension, over extended periods of time.

We validate the method against the classical Rayleigh-Plesset equation for spherical oscillation problems before validating the indirect boundary element method and the method used by Shaw (2006), against each other, on several small amplitude axisymmetric oscillation problems. We then proceed to study near-resonant non-axisymmetric shape oscillations of order 2 and 4 and the effect these oscillations have on higher order modes, with a level of

detail we believe has not been achieved in a non-axisymmetric study before. We also confirm some predictions made by Pozrikidis' on resonant interactions between the second order modes and the volume mode in addition. Finally we study the spherical instability of a bubble trapped in a uniform acoustic field, demonstrating, as expected, that instabilities show up in all resonant shape modes, including non-axisymmetric ones.

Acknowledgements

I would like to thank my former supervisor, Dr. Stephen J. Shaw for all his guidance throughout the first two years of my PhD and for providing data and a Rayleigh-Plesset code, used for comparison with my results. I would also like to thank my current supervisor, Dr. Shaun A. Forth for picking up where Dr. Shaw left off by providing solid supervision despite difficult circumstances. I would like to thank my Thesis committee for reading and commenting on previous iterations of my work, with special thanks to Dr. Tim A. Lowe for his panel method expertise.

I want to thank the ESD department at Shrivenham for having provided me with the funding I needed to develop the work contained within this thesis and thanks also go out to past and present staff and students of the department, including but not limited to the AMOR group. You have made my time at Shrivenham an enjoyable experience and I have had the pleasure of calling many of you my friends.

Thanks also to the Science & Technology Facilities Council for allowing me access to the SCARF super computer during my employment there.

I would like to thank my mother, Birgit, whose love and support has made it possible for me to reach this far. Last, but certainly not least, I would like to thank my wonderful wife, Carmel, whom I met as I was contemplating taking up the offer of studying for a PhD. Without you I would probably not even have started on this journey, and I would definitely never have been able to finish without your patience, love, encouragement and support.

Contents

List of Tables

List of Figures

Chapter 1

Introduction

1.1 Bottoms up

Soap bubbles, the fizz in carbonated drinks or the bubbles in a boiling pot of water are among the most visible and common association people have with bubbles. Bubbles occur in a very diverse spectrum of situations, in both natural and man-made processes, and, in the case of carbonated drinks the creation of bubbles is an intentional process meant to improve the taste and texture of the drink. In many other processes, bubbles are an unfortunate side-effect, and while they have been known at least since antiquity [1], the research impetus was born out of one of these damaging side-effects.

Nearly one hundred years ago, when the propellers of big ocean liners showed signs of heavy erosion after a short time in use, bubbles were identified as potential culprits ([2] cited in [3, 4]). This type of bubble was later found to occur in many other types of hydraulic machinery, including pumps and turbines. They can also be created naturally, in for instance, brooks where bubbles can cause audible "babbling". These bubbles can be created due to sudden drops in pressure, causing pockets of water to evaporate in a process often referred to as *cavitation*, something which can, for instance, happen in sharp bends in pipes. Due to these damaging effects, much theoretical,

experimental and numerical research has been focused on bubbles oscillating near solid boundaries [5, 6, 7, 8]. Since the complex behaviour of a single collapsing bubble is not completely understood yet, let alone the collapse of clusters of bubbles, much experimental research has focused on generating single bubbles close to solid boundaries and studying them using high-speed photography techniques [9, 10]. While the cavitation damage has been well documented (i.e. [4, 11]), recent research has shown the possibility of using bubbles to move liquid in very small hydraulic devices, effectively creating pumps small enough to fit on a microchip [1, 12].

Hydraulic machinery has not been the only area of bubble research and bubbles have been found to play important roles in medicine. Lasers are often used to create bubbles for experimental bubble research [9, 4] and armed with that knowledge it is perhaps not suprising that bubbles can also be created in bodily fluids during laser surgery. During the collapse of these bubbles, several phenomenon such as shock waves and liquid jet formation may combine to cause damage to nearby tissue, leading to a substantial amount of research trying to determine how to limit this damage [13].

Another impact of bubbles in medicine is as both an undesired side effect and an exploited benefit of ultrasound treatment [14]. Clouds of bubbles have been found to be a side effect in the medical procedure of "lithotripsy" in which ultrasound is used to generate shock waves that disintegrate kidney and gallstones [15]. Because it has been hard to measure how many shocks are necessary to break up these stones, the patient has sometimes received too few, leading to re-treatment or too many, increasing the risk of harmful side effects. This has, after many studies, led to a patented device for measuring the degree of stone fragmentation [15].

The interaction between bubbles and sound is at the core of much research. For instance, when a bubble is excited by an acoustic field, phenomenon such as translating motion or *bubble dancing* [16, 17] may occur.

The bubble may also undergo drastic changes of shape [18] in seemingly unpredictable ways. Perhaps most intriguing is the phenomenon of *sonoluminescence*, where bubbles under certain conditions may emit pulses of light when subjected to acoustic excitation [19, 20]. While studying sonoluminescence, researchers found that the wave length of the emitted light suggested very high temperatures inside the bubble. Some even estimated the temperatures to be so high as to allow for the process of nuclear fusion. Because of this, cavitation bubbles have been investigated as a possible solution to generating fusion in a controlled environment [21, 22], although this research is controversial and has received criticism [23] due to replication problems.

The bubble motion in an acoustic field is nonlinear, and the radius can not be expressed in terms of simple or familiar functions of time [24]. The motion is therefore highly complex, and in some situations chaotic, meaning that ininitesimal changes to the parameters may lead to drastically different behaviour [18, 25]. This has led to extensive experimental and theoretical research. Yet the behaviour of a single bubble oscillating in free liquid is still not yet fully understood and it is this particular field we wish to explore in this Thesis. Traditionally almost all theoretical studies were based on studies of volume oscillations of spherical bubbles [25] and, more recently, axisymmetric bubbles [26, 18, 27, 28]. The body of numerical research on shape oscillations using fully three dimensional methods [29, 30] is still limited, despite an extensive number of three dimensional studies on bubbles collapsing near solid boundaries (for instance [31, 32, 33, 34]).

1.2 Early Work on Bubble Oscillations

The first analysis of an oscillating bubble was made by Lord Rayleigh [35], who derived an equation governing the oscillation of a spherical gas bubble in an incompressible liquid. Plesset [36] later modified this equation to in-

clude the effects of surface tension and viscosity, leading to the well known Rayleigh-Plesset equation. Spherical bubble oscillations have been the focus of much research on bubbles and sound, since early studies, beginning with Minnaert [37], showed that the frequency of sound produced by bubbles forming at a nozzle was experimentally close to the frequency of the volume oscillation of a spherical bubble. Most of this early work on forced bubble dynamics was thoroughly reviewed by Plesset and Prosperetti in 1977 [38] and later works have been reviewed by Feng and Leal [25]; we will cover the most relevant parts here.

Some of the earliest studies on shape oscillations and surface deformations included those of Lamb [39] and Penney and Price [40]. When the amplitudes of the shape oscillations are small it is common practise to represent the bubble deformation in terms of an infinite sum of spherical harmonics modes $Y_l^m(\theta, \varphi)$ of order l and degree m, where θ and φ are the polar and azimuthal angles respectively [25, 28]. If $m = 0$, the mode's amplitude is dependent only on θ and the mode is thus axisymmetric. Lamb derived an equation for the natural frequency of these modes in an inviscid fluid and Penny and Price, motivated by trying to understand why explosion bubbles tend to lose their spherical shape, derived equations for the volume oscillations, translation and shape oscillations of a bubble undergoing small amplitude motion in an incompressible and inviscid liquid using linear terms only. Similarly to Penny and Price, Plesset [41] derived equations for the shape modes which included the effects of surface tension, omitting the effects of gravity.

An early study, not discussed by Plesset and Prosperetti [38], was the discovery of the phenomenon of "bubble dancing" [17] by Gaines [42]. Gaines noticed that a gas bubble submerged in a liquid and trapped in a strong acoustic standing wave, experienced erratic "dancing" movement away from its original position. Benjamin and Strasberg [16] later postulated that the erratic bubble motion was caused by the presence of shape oscillations excited

by acoustic forcing, something which was demonstrated experimentally in a related study by Strasberg and Benjamin [43]. Up until these studies it was generally assumed that surface deformations could only happen if the sound pressure field varied over the bubble surface and Strasberg and Benjamin changed this view by showing that shape oscillations could actually be excited even if the pressure field was uniform, provided the amplitude was large enough [28]. They also determined that for small amplitudes the spherical shape would be unstable if the frequency of the volume oscillations approached twice the frequency of the vibrations of a given shape mode, leading to the onset of shape oscillations, which were dampened by viscosity.

Although Benjamin and Strasberg concluded that surface deformation effects must be involved, they were unable to come up with theoretical thresholds for the onset of shape oscillations that adequately matched the experimental thresholds for dancing motion [17]. Later work by Eller and Crum [44] used a more accurate method and consequently arrived at good agreement between theoretical shape-oscillation thresholds and the observed dancing thresholds [17]. The close agreement prompted Eller and Crum to conclude that the dancing of trapped bubbles is a consequence of shape deformations and this has since been a universally accepted notion.

Shape oscillations have since been the subject of several studies. Prosperetti [45] showed that the inclusion of viscosity into Plesset's previously mentioned shape oscillation equations led to a complex integro-differential set of equations in small deformation terms, although if the viscous boundary layer thickness is small compared to the bubble radius, this can be simplified to a system of differential equations [28]. These equations have since been used in a number of studies [38, 25] related to the stability of the spherical oscillations of bubbles given infinitesimal shape distortions. The dominating factor has been found to be the parametric instability of the shape modes, rather than Rayleigh-Taylor instability, except in cases of large amplitude

volume oscillations [25]. Common for these studies was that they considered small shape deformations only.

Until the late 1980s most studies of heavily deformed bubbles were focused on the problem of the collapse of a bubble in a quiescent fluid near a solid wall (see for instance [5, 6, 7, 8, 46], or the review paper by Blake and Gibson [47]). These studies, which have included both experimental research and numerical simulations, showed that the deformation of the bubble shape when collapsing near a solid boundary fundamentally altered the dynamics of the bubble oscillation and revealed a new level of complexity involved in the production of noise and the damage associated with the bubble collapse. Most of the numerical simulations have been carried out by solving a boundary integral formulation, where the problem is recast over the bubble surface rather than the entire fluid domain. Some of the relevant numerical research will be discussed in Chapter 3.

While shape deformations have been considered important for the phenomenon of bubble dancing since the 1950s, they were, up until the late 1980s largely ignored in conjunction with sound production by bubbles oscillating in a free liquid [26, 25]. One of the reasons for this is that the spherical bubble problem is easier to solve and more easily allows for the inclusion of physical effects, such as compressibility, in the simulation [25]. Another reason is that volume oscillations were considered a much stronger source of sound than shape deformations [25].

Spherical bubble simulations has provided much new insight into the understanding of bubble collapse. The bubble oscillation has been found to be strongly non-linear and in many cases hard to predict [25]. One of the most important discoveries has been the realisation that bubble oscillations in a time-periodic pressure field may be chaotic even if no change of shape is seen [25]. Extensive study of chaotic bubble dynamics began in the 1980s and included amongst others the work of Lauterborn and Parlitz [48] who

used the Rayleigh-Plesset framework to demonstrate resonances and bifurcations leading to highly chaotic behaviour. Since then, research into bubble dynamics has contributed significantly to the general understanding of chaos physics [25], including experimental work by Lauterborn *et al* [49, 50] and later simulation work on chaotic bubble motion by Feng and Leal [18] who considered the chaotic coupling of shape and volume oscillations. Another important realisation has been that most of the important features of the chaotic motion are present in the dynamics of a vapour or ideal gas bubble in an unbounded, inviscid and incompressible fluid [25], something which may significantly simplify their study.

1.3 Coupling Between Oscillations of Shape and Volume

As mentioned in Section 1.2, the volume mode oscillations have traditionally been considered the dominant means of sound production from bubbles. This assumption had its roots in in linear theory where the motion and associated pressure field of the volume (or breathing) mode decays like r^{-1} (a monopole), where r is the distance from the bubble centroid. In contrast, the pressure field associated with the shape modes decay like r^{-2} or higher inverse powers of r [26]. As such, the pressure contributions from the shape modes were assumed to decay far too rapidly for them to have any noticeable effect away from the immediate vicinity of the bubble.

Shape oscillations for bubbles with a constant volume have been the focus of several studies, including Sevik and Park [51] and several papers by Kang and Leal [52, 53, 54]. There was, however, little work on understanding the interaction between oscillations of volume and shape [27]. This changed after Longuet-Higgins [26] extended the linear theory of sound production to

include nonlinear terms and found that at second order, the distortion modes contained monopole terms. In a follow up paper, the same author postulated that the sound emission would be amplified through resonant excitation when the frequency of the volume mode approaches twice the frequency of a shape mode [55].

The complex coupling between shape mode oscillations and volume mode oscillations has since been thought to be involved in both sound production and the phenomenon of bubble dancing. In terms of bubble dancing, Mei and Zhou [56], for instance, studied the resonant interaction between volume oscillation and one or two shape modes when the spherical mode is forced by a uniform pressure field. They derived amplitude equations governing the motion of these modes and found some numerical evidence of chaotic bubble motion, which, combined with earlier theory by Benjamin and Ellis [57], provided an explanation for bubble dancing. The work of Mei and Zhou, however, did not allow for direct coupling between the dancing motion of the bubble and the dynamics of the shape modes, leading to further studies by Feng and Leal [58] and Doinikov [17] to try to establish this coupling. Both studies involved an axisymmetric perturbation analysis up to quadratic terms, although where Feng and Leal assumed the interaction of only two adjacent shape modes whose natural frequencies were equal to half the driving frequency, Doinikov allowed for interaction between any shape mode, did not impose any limits on the frequencies, but included the first five shape modes only. Doinikov's results showed that translational instability may develop quickly even in the absence of resonance.

Shaw [28] later extended Doinikov's work to cubic terms and included the first 15 shape modes, showing that despite offering lower order excitation, cubic order effects provide a much wider and more complex set of interactions than quadratic order effects. Shaw's work took into account both even and odd mode oscillations and showed that for both quadratic and cubic orders,

odd mode oscillations may excite both other odd modes and even modes, while even mode oscillations will only excite other even modes. Since odd modes are associated with bubble translation, the results suggested that the disturbance of a single odd mode may result in translational motion, the same is not the case for even modes, which require interaction with an odd mode to contribute to bubble dancing [28].

Resonance conditions between shape and volume mode oscillations, and the subsequent energy exchange between the modes, have also been studied by several authors since Longuet-Higgins. Ffowcs-Williams and Guo [59] for instance applied a multiple time scale analysis with asymptotic expansion techniques [28] to derive amplitude equations for the shape and volume oscillations. They questioned the earlier conclusions by Longuet-Higgins and claimed that slow energy transfer between the shape oscillations and volume oscillations falsified the perturbation analysis and that the volume mode oscillations never grew sufficiently to produce sound of the magnitude suggested by Longuet-Higgins. Longuet-Higgins [60] later refuted these claims by showing that they were only valid if no damping was considered, and when damping in the form of viscosity and acoustic raditation was included, the pressure pulses found would be essentially identical to the earlier work of Longuet-Higgins. Also, Longuet-Higgins concluded that the initial energy of the shape oscillations was far greater than what was required to show the volume pulses seen in field data and the previous simulation work.

Other work also followed, including Yang *et al* [61] who confirmed the previous work by Longuet-Higgins and also considered resonant oscillations in an axisymmetric external flow which deformed the bubble to a "barrel like" mean shape and lead to more complex interaction between the modes.

In general, two cases of resonance were identified as particularly important. If the pressure forcing is uniform or *isotropic*, the bubble mean shape will remain spherical. In this case, small amplitude theory predicts that

the most significant interaction between the shape and volume modes are quadratic and thus occurring when the frequency of the volume oscillations are twice that of a shape mode [25]. This form of resonance is usually referred to as *2:1 resonance*.

If, however, the pressure forcing is *anisotropic*, not uniform, the bubble mean shape would not be spherical and the resonance conditions would occur when the frequency of the volume oscillations is the same as that of a shape mode. This is usually referred to as *1:1 resonance*.

The studies by Longuet-Higgins [26], Ffowcs-Williams and Gui [59] and Yang *et al* [61] suggested that at exact resonance, there was a one-directional exchange of energy from the shape modes to the volume mode, while if there was a slight offset from exact resonance, the energy transfer was instead bi-directional and the two modes exchanged energy in a periodic fashion. This suggested a very sharp difference in behaviour as the oscillations were detuned from exact resonance.

Feng and Leal [62] later built upon and generalised the work of Longuet-Higgins [26], Ffowcs-Williams [59] and Yang *et al* [61] using phase-space analysis and coordinate transforms. In this study, Feng and Leal discovered that for 2:1 resonance, this strong separation happened only for a very narrow case of initial conditions, such as the ones chosen by the previous authors, and in general, for 2:1 resonance, the energy transfer between the volume mode and resonant shape modes was bi-directional. They also found that in the case of 2:1 resonance, there was a critical level of detuning from resonance conditions, above which there was no energy exchange between the volume and shape oscillations. For 1:1 resonance, Feng and Leal found no such critical value, and instead there was a smooth increase in energy exchange as the level of detuning was decreased.

Experimental studies on the subject have also been performed, including Holt *et al* [63] who demonstrated a bubble forced into oscillation in the ax-

isymmetric modes $l = 3$ and $l = 4$ modes. Trinh *et al* [64] used high-speed photography to observe an initially spherical bubble, of radius between 0.2 and 0.8 cm, subjected to a non-uniform forcing, observing interaction between a non-axisymmetric $l = 2$ mode and an axisymmetric $l = 3$ mode. They also observed interaction between the axisymmetric $l = 3$ and $l = 6$ modes, showing strong resonant energy transfer from higher modes to lower modes, as well as less effective energy transfer in the opposite direction. Ohsaka and Trinh [65] later demonstrated resonant coupling of shape oscillations between the axisymmetric modes $l = 3$ to $l = 6$ for gas bubbles and $l = 4$ and $l = 5$ for vapour bubbles. They concluded that for an even order l, the 1:1 resonant coupling had more efficient energy transfer than the 2:1 resonant coupling. This relationship, however, was reversed when the order l was odd. The experimental studies have illustrated that an external factor has to be applied in order for a bubble to undergo shape oscillations. These external factors can occur in turbulent flow such as breaking waves or fast moving propellers [26, 28].

Common for the early numerical studies showing energy exchange between shape and volume oscillations is that they were performed using small perturbation techniques. For small amplitude oscillations, the period of energy exchange is very long, and so in many cases the resonant effects may be dampened out by viscous effects before having any impact on the real bubble dynamics [62, 27]. This prompted McDougald and Leal [27, 66] to study the shape and volume oscillations at resonant conditions using both a spectral method and an axisymmetric boundary integral method, allowing the simulation of bubbles undergoing much higher amplitude oscillations and consequently shorter periods of interaction. They observed the same continuous energy exchange as predicted by Feng and Leal [62] and also predicted the excitation of other shape modes which they claimed could not be accounted for by small deformation theory [27]. Some of these obervations

have later been examined in more detail by Shaw [28].

The studies discussed so far have been limited to studies of the interactions between the volume mode and the axisymmetric modes Y_l^0. To the best of our knowledge, the only fully three dimensional work on the interaction between shape and volume oscillations of bubbles have been the work by Pozrikidis [29, 30] following work by the same author on the related problem of droplet oscillation [67]. However, none of this work examined the interaction between different orders of shape modes and the studies were all limited to oscillations of the volume mode and the $l = 2$ modes, with the exception of [67] which also studies the $l = 3$ modes. Also, the numerical simulations were carried out using the generalised vortex method which, by the authors own admission [29], was less reliable for large surface deformations than the regular boundary integral methods, something which makes Pozrikidis' claim that the method was superior [30] only valid for a narrow range of problems.

As previously mentioned, other three dimensional bubble work has been mostly focused on the problem of a collapsing bubble near a solid boundary or underwater explosion bubbles. Some recent research in this area (i.e. [68, 69, 70]) has considered compressible effects by solving the compressible euler equations for two-phase flow. Such methods allow for the study of additional physical effects of the bubble collapse such as the interactions between emitted shock waves and the bubble interfaces. These methods are, however, computationally costly and so far they have been used to study spherical, axisymmetric and two-dimensional bubbles only.

Since we intend to study fine surface effects on a micron scale three-dimensional oscillating gas bubble in water, we instead build upon and expand on some of the previous incompressible methods developed, namely boundary element methods, given the physical assumption discussed in the next Chapter. Previous boundary element methods will be discussed in Chapter 3 along with the different issues and solutions to achieving our aim

of arriving at a fully three dimensional boundary element method, which is capable of simulating the volume and shape oscillations of a high resolution deformed bubble in an unbounded liquid for an extended period of time.

In order to allow for a surface mesh fine enough to pick out details in the interactions between different shape modes, we will utilise distributed memory parallelisation, so as to be able to deploy the code efficiently on modern cluster computers. In Chapter 4, we will demonstrate the method's parallel performance and accuracy on a set of test problems, giving an indication as to how well the numerical method will perform when used to simulate bubble problems. Finally we will, in Chapter 5, demonstrate the capabilities of the method on a selection of bubble simulation problems, including spherical bubble oscillations as well as axisymmetric and fully three dimensional bubble oscillations. Most of the non-spherical bubble oscillations will be focused on simulating bubbles given initial distortions to the volume mode and one or two shape modes, some of which will be near $2:1$ resonant with the volume oscillations. For these simulations the liquid surrounding the bubble is assumed to be at rest in the absence of bubble oscillation.

We will focus on a comparison with previous theoretical and numerical studies. The results for spherical bubble oscillations being compared to results using a traditional Rayleigh-Plesset based code. The results for small axisymmetric shape distortions will be compared with results using Shaw's perturbation approach [28] using data kindly provided by Dr. Shaw. Some comparisons with Pozrikidis' [29] will also be made, as well as some non-axisymmetric shape oscillations, which to the best of our knowledge, have not been presented before. These results will be summarised and discussed in Chapter 6 together with some general conclusions.

The objective of this Thesis is thus to develop a fully three dimensional boundary element method capable of modelling various bubble oscillation problems as well applying this method to study the interaction between shape

and volume oscillations of three dimensional gas bubbles in water.

Bibliography

[1] A. Prosperetti. Bubbles. *Physics of Fluids*, 16(6):1852–1865, 2004.

[2] D. Silberrad. Propeller erosion. *Engineering*, 100:33–35, 1912.

[3] S.J. Shaw, W.P. Schiffers, and D.C. Emmony. Experimental observations of the stress experienced by a solid surface when a laser-created bubble oscillates in its vincinity. *J.Acoust. Soc. Am.*, 110(4):1822–1827, 2001.

[4] A. Philipp and W. Lauterborn. Cavitation erosion by single laser-produced bubbles. *J.Fluid.Mech*, 361:75–116, 1998.

[5] C.F. Naude. *On the mechanism of cavitation damage by non-hemispherical cavities collapsing in contact with a solid boundary.* PhD thesis, California Institute of Technology, California, US, 1960.

[6] M.S. Plesset. Shock waves from cavity collapse. *Phil.Trans. A*, 260:241, 1966.

[7] T.B. Benjamin and A.T. Ellis. The collapse of cavitation bubbles and the pressures thereby produced against solid boundaries. *Phil.Trans. A*, 260:221–240, 1966.

[8] M.S. Plesset and R.B. Chapman. Collapse of an initially spherical vapour cavity in the neighbourhood of a solid boundary. *Journal of Fluid Mechanics*, 47(2):283–290, 1971.

[9] O. Lindau and W. Lauterborn. Cinematographic observation of the collapse and rebound of a laser-produced cavitation bubble near a wall. *J.Fluid.Mech*, 479:327–348, 2003.

[10] S.J. Shaw, W.P. Schiffers, T.P. Gentry, and D.C. Emmony. A study of the interaction of a laser-generated cavity with a nearby solid boundary. *J.Phys.D:Appl.Phys*, 32:1612–1617, 1999.

[11] A. Philipp and W. Lauterborn. Damage of solid surfaces by single laser-produced cavitation bubbles. *Acustica*, 83, 1997.

[12] Z. Yin and A. Prosperetti. Blinking bubble; micropump with micro-fabricated heaters. *Journal of Micromechanics and Microengineering*, 15(9):1683–1691, 2005.

[13] D. Palanker, A. Vankov, J. Miller, M. Friedman, and M. Strauss. Prevention of tissue damage by water jet during cavitation. *Journal of Applied Physics*, 94(4):2654–2661, 2003.

[14] E.A. Brujan. The role of cavitation microjets in the therapeutic applications of ultrasound. *Ultrasound in Med. & Biol.*, 30(3):381–387, 2004.

[15] T.G. Leighton. From sea to surgeries, from babbling brooks to baby scans: Bubble acoustics at ISVR. *Proceedings of the Institute of Acoustics*, 26:357–381, 2004.

[16] T.B. Benjamin and M. Strasberg. Excitation of oscillations in the shape of pulsating gas bubbles; theoretical work (abstract). *Journal of the Acoustic Society of America*, 30:697, 1958.

[17] A.A. Doinikov. Translational motion of a bubble undergoing shape oscillations. *Journal of Fluid Mechanics*, 501:1–24, 2004.

[18] Z.C. Feng and L.G. Leal. Bifurcation and chaos in shape and volume oscillations of a periodically driven bubble with two-to-one internal resonance. *Journal of Fluid Mechanics*, 266:209–242, 1994.

[19] S.J. Putterman and K.R. Weninger. Sonoluminescence: How bubbles turn sound into light. *Annual Review of Fluid Mechanics*, 32, 2000.

[20] M.P. Brenner, D. Lohse, and T. F. Dupont. Bubble shape oscillations and the onset of sonoluminescence. *Phys. Rev. Lett.*, 75(5):954–957, Jul 1995.

[21] R.I. Nigmatulin, R.P. Taleyarkhan, and R.T. Lahey. Evidence for nuclear emissions during acoustic cavitation revisited. *Proceedings of the Institute of Mechanical Engineers Part A-Journal of Power and Energy*, 218(A5):345–364, 2004.

[22] Y.B. Xu and A. Butt. Confirmatory experiments for nuclear emissions during acoustic cavitation. *Nuclear Engineering and Design*, 235:1317–1324, 2005.

[23] D. Shapira and M. Saltmarsh. Nuclear fusion in collapsing bubbles - is it there? An attempt to repeat the observation of nuclear emissions from sonoluminescence. *Physical Review Letters*, 89:104302, 2002.

[24] LP. Solomon and MS. Plesset. Nonlinear bubble oscillations. Office of Naval Research, Department of the Navy. Report No 85-38, 1967.

[25] Z.C. Feng and L.G. Leal. Nonlinear bubble dynamics. *Annual Review of Fluid Mechanics*, 29:201–243, 1997.

[26] M.S. Longuet-Higgins. Monopole emissions of sound by asymmetric bubble oscillations. Part 1. Normal modes. *Journal of Fluid Mechanics*, 201:525–541, 1989.

[27] N.K. McDougald and L.G. Leal. Numerical study of the oscillations of a non-spherical bubble in an inviscid, incompressible liquid. Part I: free oscillations from non-equilibrium initial conditions. *International Journal of Multiphase Flow*, 25:887–919, 1999.

[28] S.J. Shaw. Translation and oscillation of a bubble under axisymmetric deformation. *Physics of Fluids*, 18(7):072104, 2006.

[29] C. Pozrikidis. Numerical simulation of three-dimensional bubble oscillations by a generalized vortex method. *Theoretical and Computational Fluid Dynamics*, 16:151–169, 2002.

[30] C. Pozrikidis. Three-dimensional oscillations of rising bubbles. *Engineering Analysis with Boundary Elements*, 28:315–323, 2004.

[31] G.L. Chahine and T.O. Perdue. Simulation of the three-dimensional behaviour of an unsteady large bubble near a structure. In *3rd International Colloquim On Bubbles and Drops*, volume 197, pages 188–199, Silver Spring, Maryland, USA, Sept 1988. AIP Conference Proceedings.

[32] S.A. Wilkerson. *A boundary integral approach to three-dimensional underwater explosion bubble dynamics*. PhD thesis, Johns Hopkins University, Baltimore, MD, 1990.

[33] Y.L. Zhang, K.S. Yeo, B.C. Khoo, and C. Wang. 3d jet impact and toroidal bubbles. *Journal of Computational Physics*, 166:336–360, 2001.

[34] C. Wang and B.C Khoo. An indirect boundary element method for three-dimensional explosion bubbles. *Journal of Computational Physics*, 194:451–480, 2004.

[35] Lord Rayleigh. On the pressure developed in a liquid during the collapse of a spherical cavity. *Phil.Mag*, 34:94–98, 1917.

[36] M.S Plesset. The dynamics of cavitation bubbles. *J. Appl. Mech*, 16:277, 1949.

[37] M. Minnaert. On musical air-bubbles and the sounds of running water. *Phil. Mag.*, 16:235–248, 1933.

[38] M.S. Plesset and A. Prosperetti. Bubble dynamics and cavitation. *Annual Review of Fluid Mechanics*, 9:145–185, 1977.

[39] H. Lamb. *Hydrodynamics, Dover Edition 1945*. Cambridge University Press, US, 1932.

[40] Penney W.G. and A.T. Price. On the changing form of a nearly spherical submarine bubble. In G.K. Hartmann and E.G. Hill, editors, *Underwater Explosion Research*. Office of Naval Research, Washington D.C., 1942.

[41] M.S Plesset. On the stability of fluid flows with spherical symmetry. *J. Appl. Phys*, 25:96, 1954.

[42] N. Gaines. Magnetostriction oscillator producing intense audible sound and some effects obtained. *Physics*, 3:209–229, 1932.

[43] M. Strasberg and T.B. Benjamin. Excitation of oscillations in the shape of pulsating gas bubbles; experimental work (abstract). *Journal of the Acoustic Society of America*, 30:697, 1958.

[44] A.I. Eller and L.A. Crum. Instability of the motion of a pulsating bubble in a sound field. *Journal of the Acoustical Society of America*, 47:762–767, 1970.

[45] A. Prosperetti. Viscous effects on perturbed spherical flows. *Q. Appl. Mech*, 34:339, 1977.

[46] J.R. Blake, Taib B.B., and Doherty G. Transient cavities near boundaries. Part 1. Rigid boundary. *Journal of Fluid Mechanics*, 180:479–497, 1986.

[47] J.R. Blake and D.C. Gibson. Cavitation bubbles near boundaries. *Annual Review of Fluid Mechanics*, 19:99, 1987.

[48] W. Lauterborn and U. Parlitz. Methods of chaos physics and their application to acoustics. *Journal of the Acoustical Society of America*, 84:1975–1993, 1988.

[49] W. Lauterborn, E. Schmitz, and A. Judt. Experimental approach to a complex acoustic system. *International Journal of Bifurcation and Chaos*, 3(3), 1993.

[50] W. Lauterborn and J. Holzfuss. Acoustic chaos. *International Journal of Bifurcation and Chaos*, 1(1), 1991.

[51] M. Sevik and S.H. Park. The splitting of drops and bubbles by turbulent fluid flow. *Journal of Fluids Engineering - Transactions of the ASME*, 95:53–60, 1973.

[52] I.S. Kang and L.G. Leal. Numerical solution of axisymmetric, unsteady free-boundary problems at finite Reynolds number. I. Finite-difference scheme and its applications to the deformation of a bubble in uniaxial straining flow. *Physics of Fluids*, 30:1929–1940, 1987.

[53] I.S. Kang and L.G. Leal. Small-amplitude perturbations of shape for a nearly spherical bubble in an inviscid straining flow (steady shapes and oscillatory motion). *Journal of Fluid Mechanics*, 218:41–69, 1988.

[54] I.S. Kang and L.G. Leal. Numerical solution of axisymmetric, unsteady free-boundary problems at finite Reynolds number. II. Deformation of a bubble in a biaxial straining flow. *Physics of Fluids A*, 1:644–660, 1989.

[55] M.S. Longuet-Higgins. Monopole emissions of sound by asymmetric bubble oscillations. Part 2. An initial-value problem. *Journal of Fluid Mechanics*, 201:543–565, 1989.

[56] C.C. Mei and X. Zhou. Parametric resonance of a spherical bubble. *Journal of Fluid Mechanics*, 229:29–50, 1991.

[57] T.B. Benjamin and A.T. Ellis. Self-propulsion of asymmetrically vibrating bubbles. *Journal of Fluid Mechanics*, 212:65–80, 1990.

[58] Z.C. Feng and L.G. Leal. Translational instability of a bubble undergoing shape oscillations. *Physics of Fluids*, 7:1325–1336, 1995.

[59] J.E. Ffowcs-Williams and Y.P. Gui. On resonant nonlinear bubble oscillations. *Journal of Fluid Mechanics*, 224:507–529, 1991.

[60] M.S. Longuet-Higgins. Resonance in nonlinear bubble oscillations. *Journal of Fluid Mechanics*, 224:531–549, 1991.

[61] S.M. Yang, Z.C. Feng, and L.G. Leal. Nonlinear effects in the dynamics of shape and volume oscillations for a gas bubble in an external flow. *Journal of Fluid Mechanics*, 247:417–454, 1993.

[62] Z.C. Feng and L.G. Leal. On energy transfer in resonant bubble oscillations. *Physics of Fluids A.*, 5(4):826–836, 1993.

[63] R.G. Holt, J. Holzfuss, A. Judt, A. Philip, and S. Horsburgh. Forced nonlinear oscillations of single air bubbles in water: experimental results. In *Frontiers of Nonlinear Acoustics. 12th ISNA*, page 497, 1990.

[64] E.H. Trinh, D.B. Thiessen, and R.G. Holt. Driven and freely decaying nonlinear shape oscillations of drops and bubbles immersed in a liquid: experimental results. *Journal of Fluid Mechanics*, 364:253–272, 1998.

[65] K. Ohsaka and E.H. Trinh. Experimental coupling of oscillating gas or vapor bubbles in water: an experimental study. *Physics of Fluids*, 12(2):283–288, 2000.

[66] N.K. McDougald and L.G. Leal. Numerical study of the oscillations of a non-spherical bubble in an inviscid, incompressible liquid. Part II: the response to an impulsive decrease in pressure. *International Journal of Multiphase Flow*, 25:921–941, 1999.

[67] C. Pozrikidis. Three-dimensional oscillations of inviscid drops induced by surface tension. *Computers & Fluids*, 30:417–444, 2000.

[68] R.R. Nourgaliev, T.N. Dinh, and T.G. Theofanous. Adaptive characteristics-based matching for compressible multifluid dynamics. *Journal of Computational Physics*, 213:500–529, 2006.

[69] X.Y. Hu and B.C. Khoo. An interface interaction method for compressible multifluids. *Journal of Computational Physics*, 198:35–64, 2004.

[70] S.Y. Kadioglu and M. Sussman. Adaptive solution techniques for simulating underwater explosions and implosions. *Journal of Computational Physics*, 227:2083–2104, 2008.

Chapter 2

Mathematical Model

2.1 Introduction

We are interested in modelling the oscillation of a gas bubble in an unbounded fluid. This problem is approached from a macroscopic level, dealing with characteristics that can be observed and measured at a laboratory scale, thus putting us within the scope of *fluid mechanics*. While any fluid flow is an aggregation of the movement of individual particles, fluid mechanics treats fluids as continuous substances through the averaging of very large numbers of molecules [1].

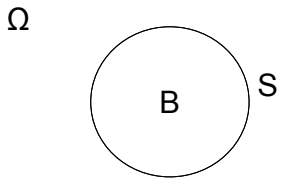

Figure 2.1: A Spherical body submerged in a fluid

Consider the bubble B in an unbounded fluid Ω shown in Figure 2.1 with the interface between B and Ω denoted by S. A Cartesian coordinate system (x, y, z) is used with the origin at the center of B. We seek equations to model the fluid flow in Ω, the boundary conditions applied at S, and the

conditions at the far-field (∞) and inside the bubble.

The basic laws of classical mechanics applicable to any fluid flow are [2]

- the conservation of momentum (linear and angular),
- the conservation of mass,
- the first law of thermodynamics, concerning the conservation of energy,
- the second law of thermodynamics, relating to entropy in a closed system.

Unfortunately, applying all these laws will result in a system of equations that is computationally expensive to solve. Thus, some simplifications are used to arrive at a timely solution with acceptable fidelity.

If the fluid can be considered inviscid, that is the viscosity of the fluid has a negligable effect on the fluid flow, conservation of momentum and mass are generally considered sufficient to accurately model the fluid flow [1]. This is also the case for viscous flow if the fluid can be considered incompressible, meaning the fluid flow is not noticeably affected by the compression of the fluid due to pressure changes. For many bubble problems, especially violent or rapid motions in water, the liquid may be considered to be inviscid because the time scale for viscous dissipation is much larger than the oscillation period of the bubbles [3, 4]. Also water and air are usually considered incompressible for bubble problems, although some phenomena, such as the propagation of shock waves emitted during bubble collapse, can not be captured using an incompressible fluid model [5].

With respect to understanding the bubble as a source of sound, it has been found that the assumption of incompressibility is only valid in the vincinity of the bubble. However, as long as the bubble radius is small and the velocity of the bubble interface is much smaller than the speed of sound in the liquid [6], the radiated pressure in the far field is indistinguishable from that using

a compressible model, with the exception of time being delayed so that t must be replaced by delayed time [7]

$$t_c = t - (r - R)/c \tag{2.1}$$

where r is the distance from the bubble centroid, R is the radius of the bubble and c is the speed of sound in the liquid. It can be seen that the pressure propagation time is reduced by the time it takes for sound to propagate in the liquid.

In this work, the liquid surrounding the bubble is assumed to be inviscid and incompressible while the fluid particles undergo irrotational motion only. Also the gas inside the bubble is considered ideal. Thus, shock wave emission and propagation will not be captured either through the liquid or the gas.

2.2 Derivation of Governing Equations

Given the assumptions of an inviscid and incompressible fluid, we will impose the conservation of mass and momentum only. The conservation of mass requires the mass in the system to stay constant regardless of any activity in the system and it is governed by the continuity equation [1],

$$\frac{\partial \rho}{\partial t} + \nabla \cdot (\rho \mathbf{v}) \;\; = \;\; 0, \tag{2.2}$$

where ρ is density, t is time and $\mathbf{v}$ is velocity. If the liquid is incompressible, ρ is contant, and thus the conservation of mass simplifies to

$$\nabla \cdot \mathbf{v} \;\; = \;\; 0. \tag{2.3}$$

The conservation of momentum is represented through the well-known Navier-Stokes equation for incompressible flow with constant viscosity μ

$$\frac{\partial \mathbf{v}}{\partial t} + (\mathbf{v} \cdot \nabla)\mathbf{v} \;\; = \;\; \mathbf{f} - \frac{\nabla p}{\rho} + \frac{\mu}{\rho}\nabla^2 \mathbf{v}, \tag{2.4}$$

where p is pressure and $\mathbf{f}$ is a body force. If the fluid is considered to be inviscid, this reduces to Euler's equation of motion [8],

$$\frac{\partial \mathbf{v}}{\partial t} + (\mathbf{v} \cdot \nabla)\mathbf{v} = \mathbf{f} - \frac{\nabla p}{\rho}. \tag{2.5}$$

By using the vector identity [1]

$$\mathbf{v} \cdot \nabla \mathbf{v} = \frac{1}{2}\nabla|\mathbf{v}|^2 - \mathbf{v} \times (\nabla \times \mathbf{v}), \tag{2.6}$$

where $\nabla \times \mathbf{v}$ denotes the "curl", or "rate of rotation", (2.5) can be rewritten as

$$\frac{\partial \mathbf{v}}{\partial t} + \frac{1}{2}\nabla|\mathbf{v}|^2 - \mathbf{v} \times (\nabla \times \mathbf{v}) = \mathbf{f} - \frac{\nabla p}{\rho}. \tag{2.7}$$

If the flow is assumed to be irrotational, meaning fluid particles do not change direction along their trajectory, the curl is zero, and (2.7) can be simplified to

$$\frac{\partial \mathbf{v}}{\partial t} + \frac{1}{2}\nabla|\mathbf{v}|^2 = \mathbf{f} - \frac{\nabla p}{\rho}. \tag{2.8}$$

This also allows us to define a scalar vector potential Φ so that

$$\mathbf{v} \equiv \nabla\Phi, \tag{2.9}$$

and thus (2.3) can be written as

$$\nabla \cdot \mathbf{v} = \nabla \cdot \nabla\Phi = \nabla^2\Phi = \frac{\partial^2\Phi}{\partial x^2} + \frac{\partial^2\Phi}{\partial y^2} + \frac{\partial^2\Phi}{\partial z^2} = 0. \tag{2.10}$$

The resulting fluid model is often referred to as the "ideal" fluid model, and (2.10) is usually referred to as *Laplace's equation*. Laplace's equation is the linear, elliptic partial differential equation solved by the boundary integral based methods (such as [9][10][11]) and the resulting methods have been found to give good results for many bubble problems.

2.3 Boundary Conditions

It should be clear that Laplace's equation is based only on the conservation of mass, and has no reference to time. Both the time dependence and the con-

servation of momentum are instead introduced through the surface boundary conditions. For velocity, the time dependence is introduced through the kinematic boundary condition. For ideal fluid flow velocities normal to the surface of the body must be continuous, giving

$$\frac{d\mathbf{x}}{dt} \cdot \hat{\mathbf{n}} = \nabla\Phi \cdot \hat{\mathbf{n}} = \mathbf{v} \cdot \hat{\mathbf{n}}, \tag{2.11}$$

where $\mathbf{x}$ is a point on the surface of the bubble and $\hat{\mathbf{n}}$ is the unit normal of the surface at $\mathbf{x}$.

For the potential we first assume that the force $\mathbf{f}$ in (2.8) is conservative with a potential E ($\mathbf{f} = \nabla E$), so that (2.8) can be integrated to yield [12]

$$C(t) = \frac{p}{\rho} + \frac{1}{2}|\mathbf{v}|^2 + \frac{\partial\Phi}{\partial t} - E, \tag{2.12}$$

where $C(t)$ varies with time only. Thus, by comparing $C(t)$ at two different points in the fluid ($\mathbf{x}$ and ∞), we get

$$\frac{p_\infty}{\rho} + \frac{1}{2}|\mathbf{v}_\infty|^2 + \frac{\partial\Phi_\infty}{\partial t} - E_\infty = \frac{p}{\rho} + \frac{1}{2}|\mathbf{v}|^2 + \frac{\partial\Phi}{\partial t} - E, \tag{2.13}$$

We assume that at the far-field the fluid flow is undisturbed by the oscillation of the bubble, thus

$$\frac{\partial\Phi_\infty}{\partial t} = 0 \ , \ \mathbf{v}_\infty = \mathbf{0}. \tag{2.14}$$

This allows equation (2.13) to be simplified to

$$\frac{\partial\Phi}{\partial t} = -\frac{p_\infty - p}{\rho} - \frac{1}{2}|\mathbf{v}|^2 + (E - E_\infty). \tag{2.15}$$

This is then substituted into the material derivative of Φ, which through repeated application of (2.9) becomes

$$\begin{aligned} \frac{d\Phi}{dt} &= \frac{\partial\Phi}{\partial t} + \mathbf{v} \cdot \nabla\Phi = \frac{\partial\Phi}{\partial t} + |\nabla\Phi|^2 = \frac{\partial\Phi}{\partial t} + |\mathbf{v}|^2 \\ &= \frac{1}{2}|\mathbf{v}|^2 - \frac{p_\infty - p}{\rho} + (E - E_\infty). \end{aligned} \tag{2.16}$$

Here we will assume that the body force $\mathbf{f} = \mathbf{g}$, the acceleration of gravity, so that $E_\infty = 0$ and we rewrite (2.16) using $E = \mathbf{g} \cdot \mathbf{x}$ to,

$$\frac{d\Phi}{dt} = \frac{1}{2}|\mathbf{v}|^2 - \frac{p_\infty - p}{\rho} + \mathbf{g} \cdot \mathbf{x}. \tag{2.17}$$

It should be noted that p in (2.17) is the pressure at the surface of the bubble. In order to specify the conditions inside the bubble, we instead introduce p_B, the pressure inside the bubble, using the Young-Laplace equation [13, 14],

$$p = p_B + 2\tau\,\kappa, \tag{2.18}$$

where τ is surface tension and κ is the curvature of the surface, which for a spherical bubble of radius R is $1/R$. Substituting this into (2.17) yields,

$$\frac{d\Phi}{dt} = \frac{1}{2}|\mathbf{v}|^2 - \frac{p_\infty - p_B - 2\tau\,\kappa}{\rho} + \mathbf{g}\cdot\mathbf{x}. \tag{2.19}$$

If the gas inside the bubble is modelled as an ideal gas, the pressure inside the bubble will change as

$$p_B = p_{B,0}\left(\frac{V_0}{V}\right)^\gamma, \tag{2.20}$$

where v is the volume of the bubble, the subscript 0 denotes the starting conditions and γ is the ratio of specific heats. Thus the final boundary conditions for the bubble surface are

$$\frac{d\Phi}{dt} = \frac{1}{2}|\mathbf{v}|^2 - \frac{1}{\rho}\left(p_\infty - p_{B,0}\left(\frac{V_0}{V}\right)^\gamma - 2\tau\,\kappa\right) + \mathbf{g}\cdot\mathbf{x}. \tag{2.21}$$

For small bubbles, $\frac{\tau\,\kappa}{\rho} >> \mathbf{g}\cdot\mathbf{x}$. In this Thesis we are interested in micron scale bubbles, where the ratio between the surface tension element and the gravity element will be of order 10^3 or larger. We will thus ignore the effects of gravity, simplifying (2.21) somewhat.

2.4 Solving Laplace's Equation

While the details of the boundary element method, used to solve Laplace's equation, will be discussed in Chapter 3, it is useful to introduce the concepts on which it is built. Consider the flow past a solid sphere B as described in Figure 2.1. We wish to solve Laplace's equation to find the fluid flow at an

arbitrary point $\mathbf{P}$ in Ω. First, both potential and velocity can be split into two components. For velocity this will be

$$\mathbf{v} = \mathbf{v}_\infty + \mathbf{v}_B, \tag{2.22}$$

where $\mathbf{v}_\infty$ is the undisturbed velocity and $\mathbf{v}_B$ is the disturbance to the velocity due to the presence of a body. The boundary element method implemented here solves Laplace's equation in terms of velocity potential,

$$\Phi = \Phi_\infty + \phi, \tag{2.23}$$

where Φ_∞ is the undisturbed potential and ϕ is the disturbance to the potential due the presence of the body, so that $\mathbf{v}_\infty = \nabla\Phi_\infty$ and $\mathbf{v}_B = \nabla\phi$.

$\mathbf{v}_\infty$ and Φ_∞ can be provided to the system in terms of initial conditions. We still need, however, a method of describing how the velocity and potential get distorted by the presence of B. Consider first the Green's function, which satisfies Laplace's equation [8]

$$G(\mathbf{P}, \mathbf{Q}) = \frac{1}{|\mathbf{r}(\mathbf{P}, \mathbf{Q})|}. \tag{2.24}$$

If multiplied by a strength $\sigma > 0$, this can be seen as a *fluid source* centered on $\mathbf{Q}$. This source adds fluid to the fluid domain, thus distorting the flow pattern in Ω. Likewise a *fluid sink* is a fluid source of negative strength $\sigma < 0$, removing fluid from the fluid domain. These constructs, are usually referred to as singularities since the Green's function approaches infinity as $\mathbf{P} \to \mathbf{Q}$. Other singularities such as dipoles and vortices exist, although they will not be used in this work.

Since Laplace's equation is linear, we can build more complex solutions through a linear combination of simple solutions

$$\phi(P) = \sum_i \sigma_i \, G(\mathbf{P}, \mathbf{Q}_i). \tag{2.25}$$

In this fashion a variety of potential flows can be constructed and this concept is utilised by the boundary element method discussed in Chapter 3, as well

as many analytical solutions to fluid flow problems, including the problem of ideal fluid flow past a solid sphere used as a test problem in Chapter 4.

For the general solution of flow past a solid object, one would normally use "Neumann" (velocity based) boundary conditions, where the assumption would be that there would be no flow normal to the surface of the object, $\mathbf{v} \cdot \hat{\mathbf{n}} = 0$. In the test problem of flow past a sphere, we will instead impose the analytical solution as Dirichlet boundary conditions. This is because our interest lies in ensuring that the boundary element method produces accurate surface velocities, given a set of surface potentials, which is exactly the problem the boundary element method will face for bubble simulation problems.

For most bubble simulation problems used in this Thesis, $\Phi_\infty = 0$ and $\mathbf{v}_\infty = \mathbf{0}$, meaning the fluid will assumed to be at rest in the absence of any bubble. The exceptions to this will be for the flow past a sphere test problem in Section 4.3, where there will be a uniform flow in the liquid and for Section 5.4 in which a uniform acoustic field is enforced in the liquid. The ordinary differential equation in (2.21) will be solved with a numerical time stepping scheme, which, for each step will provide "Dirichlet" (potential based) boundary conditions for the bubble surface. For example, using the notation $\Phi_i = \Phi(\mathbf{P}_i)$, an Euler scheme can be written as

$$\Phi_i(t + \delta t) = \Phi_i(t) + \frac{d\Phi_i}{dt} \tag{2.26}$$

where δt is the time step size and $\frac{d\Phi_i}{dt}$ is defined in (2.21). In practise more efficient and reliable solvers such as the Runge-Kutta schemes [15] are used. The velocities needed to advance the bubble boundary with (2.11) will be calculated with the boundary element method which will be described in detail in the next Chapter.

Combining the numerical solution of (2.21) with the boundary element method, we can summarise the procedure using the Euler scheme as

1. Set initial surface potential to 0 for all points on the surface, unless otherwise specified.

2. Apply boundary element method to calculate surface velocities. In the indirect boundary element method utilised here, this will involve an intermediate step solving for σ_i in (2.25).

3. Find new values for the surface potential by solving (2.21) for the next time step using (2.26).

4. Set $t \leftarrow t + \delta t$ and repeat from step 2 until a specified time has been reached.

In the Runge-Kutta schemes several intermediate steps are used before a full time step is taken and we refer to [15] for details. The fourth order optimal Runge-Kutta scheme (RK4) is used in this work.

Bibliography

[1] J.A. Fay. *Introduction to Fluid Mechanics*. MIT Press, Cambridge, MA, US, 1994.

[2] RW. Fox and AT. McDonald. *Introduction to Fluid Mechanics, 4th edition*. John Wiley & Sons, Inc, New York, US, 1994.

[3] A. Pearson, J.R. Blake, and S.R. Otto. Jets in bubbles. *Journal of Engineering Mathematics*, 48:391–412, 2004.

[4] A.M. Zhang, X.L. Yao, and X.B. Yu. The dynamics of three-dimensional underwater explosion bubble. *Journal of Sound and Vibration*, 311:1196–1212, 2008.

[5] K. Tsiglifis and N.A. Pelekasis. Numerical simulations of hte aspherical collapse of laser and acoustically generated bubbles. *Ultrasonics Sonochemistry*, 14:456–469, 2007.

[6] Z.C. Feng and L.G. Leal. Nonlinear bubble dynamics. *Annual Review of Fluid Mechanics*, 29:201–243, 1997.

[7] S.M. Yang, Z.C. Feng, and L.G. Leal. Nonlinear effects in the dynamics of shape and volume oscillations for a gas bubble in an external flow. *Journal of Fluid Mechanics*, 247:417–454, 1993.

[8] J. Katz and A. Plotkin. *Low-Speed Aerodynamics, 2nd Edition*. Cambridge University Press, Cambridge, UK, 2001.

[9] J.P. Best and A. Kucera. A numerical investigation of non-spherical rebounding bubbles. *Journal of Fluid Mechanics*, 245, 1992.

[10] S. Popinet and S. Zaleski. Bubble collapse near a solid boundary: a numerical study of the influence of viscosity. *Journal of Fluid Mechanics*, 464:137–163, 2002.

[11] L. Guerri, G. Lucca, and A. Prosperetti. A numerical method for the dynamics of non-spherical cavitation bubbles. In *Proceedings of 2nd International Colloquium on Drops and Bubbles*, pages 175–181. Jet Propulsion Laboratory, 1981.

[12] J.L. Hess and A.M.O Smith. Calculation of potential flow about arbitrary bodies. *Progress in Aeronautical Sciences*, 8, 1967.

[13] M.S. Longuet-Higgins. Monopole emissions of sound by asymmetric bubble oscillations. Part 1. Normal modes. *Journal of Fluid Mechanics*, 201:525–541, 1989.

[14] K. Tsiglifis and N.A. Pelekasis. Nonlinear oscillations and collapse of elongated bubbles subject to weak viscous effects. *Physics of Fluids*, 17(10):102101, 2005.

[15] J.R. Dormand. *Numerical Methods for Differential Equations*. CRC PRess, Boca Raton, 1996.

Chapter 3

The Boundary Element Method

3.1 Introduction

Boundary element formulations exist for both two dimensional and three dimensional problems, as well as axisymmetric problems. Axisymmetric methods benefit from being much faster than three dimensional methods, and have to date contributed greatly to the understanding of bubble oscillation and collapse starting with Guerri *et al* [1] and later used by numerous authors, including Baker *et al* [2], Blake *et al* [3] and Best & Kucera [4]. Typically these methods have been "direct" methods, where the material velocity is calculated directly. Some notable exceptions, such as the methods used by Blake and Gibson [5] and Boulton-Stone [6], were "indirect" methods, in which the strength of a singularity distribution on each element was solved for as an intermediate step. These singularities are mathematical constructs of varying complexity used to simulate real fluid flow. When assuming axisymmetry, as in both Blake and Gibson and Boulton-Stone, a singularity is rotated around an axis by integration to form a "ring singularity". These two methods differed in the distribution of these singularities, as Blake and Gibson used a finite number of ring singularities, while Boulton-Stone used a piecewise linear distribution.

There are, however, many cases which can not be modelled adequately with an axisymmetric model [7]. This, coupled with the increase in computing power over recent years, have made the three dimensional method an attractive option. Much of the recent research has therefore concentrated on developing three dimensional methods starting with work by Chahine and Perdue [7], Harris [8] and Wilkerson [9] (cited in [10]). Other work includes Blake *et al* [11, 12] and Zhang *et al* [13]. The focus of this thesis will be on fully three dimensional boundary element methods and, as a result of this, there are several implementation issues which will be addressed.

The first of these issues is the problem of surface discretisation. In a boundary element method, the surface of the body being modelled is represented by a set of nodal points, connected by surface elements. These surface elements are defined by the surrounding nodes and a set of interpolation functions, which are often called "shape functions". For three dimensional problems, the simplest surface elements used in three dimensional methods are flat (linear) triangles or quadrilaterals. Triangles are generally easier to use and allow for a more uniform representation of the body, and will thus be used in this work. Flat elements will invariably lead to a crude representation of a curved surface and many elements will be needed to provide an adequate fit to the surface being modelled. For this reason higher order elements may be preferable depending on the need for accuracy, though the added complexity of implementation and computation time can be substantial. A part of this increase in computational time, can be attributed to the evaluation of surface integrals over each element, a key part of the BEM. If linear elements are used this can be achieved cheaply analytically, but for higher order elements much more expensive numerical integration must be employed. For most bubble problems, the underlying problem is a Fredholm integral equation of the first kind, which is well known to be ill-conditioned [24], in particular for large numbers of elements [27]. Due to this, it may

be advantageous to increase the order of the elements rather than simply increase the number of linear panels.

Interpolation of the surface itself is, however, not the only form of interpolation needed in the BEM formulations. Another major issue is the required interpolation of velocity potential and material velocities as well as physical quantities. For 2D or axisymmetric problems this can be achieved to a high degree of accuracy through the use of either cubic or quintic splines, but accurate interpolation for a fully three dimensional problem is markedly more problematic. Many attempts have been made at adequately interpolating these physical quantities. Harris [8] used a weighted average of linear per element approximations of material velocity, which suffers from non-convergence during mesh refinement [14], while Chahine & Perdue [7] fitted quadratic polynomials to the surface locally, which fails for certain arrangements of the nodes [14]. Zhang *et al* [13] then used an interpolation scheme based on a nine-noded Lagrangian element, a method which can be cumbersome during mesh refinement or changes in bubble shape and so later work by Zhang *et al* reverted to weighted average approximations [14].

In the indirect boundary element method (IBEM) [15], the velocity influence and singularity strength are interpolated rather than the full material velocity. In any case, the interpolation functions are often referred to as "basis functions", to separate them from the interpolation functions used for the surface itself. A method which uses constant basis functions and linear elements is often referred to as the "Constant Panel Method", from its use in aerodynamics since Hess & Smith [16] in the 1960s. While the method is simple, the material velocity is calculated only for one control point per triangle, meaning interpolation is still required to find the velocities at the triangle vertices in order to advance the bubble surface.

A more accurate and elegant solution was used in the IBEM of Wang & Khoo [17] for simulating underwater explosion bubbles. Here the issue of

interpolation was made considerably simpler by using the same linear interpolation functions for both shape, velocity potential and material velocities. Thus material velocity was calculated directly at the triangle vertices removing the need for cumbersome fitting of interpolating polynomials to an existing surface mesh. As long as the shape functions and the basis functions used are the same, this elegance is maintained when increasing the order to quadratic, cubic or higher order elements. This comes at the cost of added computational time for a given number of surface elements, although it has been found that for a given required level of accuracy, quadratic basis functions can be computationally cheaper than linear or constant basis functions [18]. Care has to be taken when increasing the order beyond cubic, due to the well-known Runge effect, which can lead to highly oscillatory interpolants [20]. When using equally spaced interpolation points, which are common in traditional polynomial interpolation, this effect can cause high order interpolation schemes to yield considerably worse results than lower order schemes. While good interpolation sets have been found recently for triangular elements [19, 20, 21, 22] high order schemes are very sensitive to the positions of the nodal sets, making them hard to adopt to simulations with a dynamically changing mesh, which is the case with bubble simulation.

For bubble simulation, Pozrikidis [23, 24] used 6 point quadratic elements in a generalized vortex method derived from work by Baker *et al* [25]. This method differs from the a typical IBEM in that singularities used are "dipoles" rather than the more common, and simpler, sources. This increased the accuracy by an order of magnitude when the bubble was nearly spherical, although by the author's own admission, it was less reliable for large bubble deformations. For this reason we will use sources, as in the more traditional IBEMs [17].

Another major problem is evaluating the surface integral of an element when the evaluation point is on the element itself. One of the theoretical

advantages of the indirect methods is that interpolation of material velocity on the surface is unnecessary, and for this reason they can potentially be more accurate than direct methods [17]. This is, however, complicated by the strongly singular integrals that arise in velocity calculations in source based formulations and hyper-singular integrals in dipole based formulations. Boulton-Stone [26] tried to overcome this problem using quadratic fitting of the bubble boundary resulting in much smaller surface velocities [17]. Zhang *et al* [14] used the desingularisation technique, proposed by Cao *et al* [27] for general potential based problems, in which the singularity distribution was moved inside the bubble. This removes the problem of singular integrals and desingularisation was shown to work particularly well for indirect methods [27], but it also suffered from highly ill-conditioned solution matrices and it can give rise to problems regarding the uniqueness of the solution when bubble surfaces become close to each other.

The above mentioned approaches simply attempt to circumvent the problem of singular integrals rather than deal with them. It was shown by De Munck [28] for different BEM problems that it is possible to evaluate these integrals directly in terms of Cauchy principal values. Wang & Khoo [17] have used a similar approach for an indirect three dimensional method with linear panels to model large explosion bubbles. On higher order elements this approach is more problematic because the integration is performed numerically. Pozrikidis [24] reverted to linear panels in the neighbourhood of a given node and in doing so could use analytical integration formulae for the singular integrals. This increases discretisation error in the integrals that provide the largest impact on the solution and for this reason it is less than optimal. The direct BEM formulation used by Frijns *et al* [18] for biomedical engineering problems used quadratic basis functions and quadratic shape functions and thus provides a good reference for the method used in this work. The method used in their work for approximating the singular surface

integrals was, however, less convincing. Frijns *et al* recursively subdivided the elements into many smaller curved elements and discarded the contribution of the triangular subelement closest to the singularity. This gave integration errors of the order 10^{-4}, which was acceptable accuracy for their test problem, but the approach is computationally expensive and the order of errors it produces is not as clearly defined as with some of the other solutions that have been developed over the years. Some of these methods provide ways of approximating the Cauchy principal value of the surface integrals in ways which can be used in numerical integration methods.

One such solution is the Taylor expansion method developed by Aliabadi *et al* [29] in the 1980s. They used a Taylor expansion on the singular kernel to extract the singularity, which could then be treated separately with known analytical methods. The regular part of the kernel was integrated using standard repeated Gaussian integration formulae. Aliabadi *et al* only demonstrated this method on singular integrands ($\frac{1}{r}$), but the principles have since been used by other authors (i.e. [31, 36]) for higher order singularities. Importantly this method provided integration errors of around 10^{-6} for curved elements on a sphere using a mesh of 16×16 Gaussian integration points. The good accuracy and relative simplicity of this early method, makes it a good benchmark for comparison with newer methods. Aliabadi *et al* used a polar coordinate transform of the singular part of the integral, which was later found to be equivalent [30] (cited in [31]) to transforming the reference triangle to a square as used by Aliabadi & Hall [32]. In both approaches the Jacobian of the transform cancels out the singularity within the integral.

The method used in this work was developed for strongly singular integrals ($\frac{1}{r^2}$) and later hyper-singular integrals ($\frac{1}{r^3}$) by Guiggiani *et al* [33, 34, 35] and described in-depth in [36]. It is based on similar principles to the above-mentioned work, as it also uses polar-coordinate transforms and series ex-

pansion, but it is a uniform method for treating singularities of any order. When interpolating the surface potential, which has a singularity of order $1/r$ this method simply reduces to evaluating the integral in polar coordinates, while evaluation of the surface velocities require more work, which will be discussed in detail in Section 3.4.

This technique does require an order of magnitude more integration points for singular integrals than for non-singular integrals and some very recent work by Zhang *et al* [37] has exploited work by Cruse [38] and Liu [39] to eliminate the singularities in a quadratic direct BEM. The method only works for closed surfaces meaning open surfaces will have to be artificially closed using more surface elements. This work, published after our IBEM was completed, may result in a faster and more accurate method although it will be demonstrated that the techniques developed by Guiggiani will result in quite accurate surface integrals. Also the number of total surface integrals for a body with M elements is of order $O(M^2)$ while the number of singular integrals is only order $O(M)$, thus for fine surface meshes the added complexity of evaluating the singular integrals will not result in a significant increase in computational cost. Zhang *et al* utilised a maximum of 320 quadratic elements for the bubble surface and 1620 quadratic elements for the free surface, which is less than the maximum of 2880 quadratic elements used for the bubble surface in this Thesis.

It is the intention of this work to build upon the work done by Wang & Khoo to describe a general high order indirect boundary element method for solving bubble problems. The basis functions and elements can be of any order above and including linear, but for simplicity the basis functions and elements are assumed to be of the same order. Since higher order elements are assumed, numerical integration will have to be used, and the singularities will be dealt with using the method of Guiggiani. We shall show examples of linear, quadratic and cubic elements on a variety of problems including

spherical, axisymmetric and fully asymmetric bubble simulation problems. Through a high degree of parallelism the aim is to provide a level of mesh refinement not previously seen in boundary element simulation of bubbles.

3.2 General Solution

Recall that we are trying to solve Laplace's equation $\nabla^2\phi = 0$ in three spatial variables (x, y, z) over the domain described in Figure 2.1. We start by summarising the IBEM as described in [16, 17, 40]. As discussed in Chapter 2 a known solution to this problem is the Green's function in (2.24), $G(\mathbf{P}, \mathbf{Q}) = \frac{1}{|\mathbf{r}(\mathbf{P},\mathbf{Q})|}$, which clearly also satisfies the far-field condition of $\phi \to 0$ as $P \to \infty$. Since Laplace's equation is linear, we can build more complex solutions through a linear combination of this simple solution, as

$$\phi(P) = \sum_i \sigma_i \, G(\mathbf{P}, \mathbf{Q}_i), \tag{3.1}$$

where $\sigma_i \, G(\mathbf{P}, \mathbf{Q}_i)$ is a fluid source for $\sigma_i > 0$, or a fluid sink for $\sigma_i < i$. That is, it adds or removes $4\pi\sigma_i$ volume units of fluid per unit time. If a source of strength $\sigma(\mathbf{Q})$ is placed at every point $\mathbf{Q}$ on S, the total potential at $\mathbf{P}$ due to the presence of B can be thought of as a continuous distribution

$$\phi(\mathbf{P}) = -\iint_S \frac{\sigma(\mathbf{Q})}{|\mathbf{r}(\mathbf{P}, \mathbf{Q})|} \, dS \tag{3.2}$$

where $\int\int$ is a surface integration over S corresponding to an infinite sum of elementary solutions. From this, the velocity can be found as

$$\mathbf{v}(\mathbf{P}) = \nabla\phi = \iint_S \frac{\sigma(\mathbf{Q}) \, \mathbf{r}(\mathbf{P}, \mathbf{Q})}{|\mathbf{r}(\mathbf{P}, \mathbf{Q})|^3} \, dS, \tag{3.3}$$

The Indirect Boundary Element method works by providing the potential $\phi(P)$ at a set of points on the surface S and solving for the source distribution $\sigma(\mathbf{Q})$. This source distribution is then used to calculate the velocity $\mathbf{v}(\mathbf{P})$ needed to advance the bubble boundary. The intermediate step of calculating the source distribution strength separates the IBEM from the direct BEM.

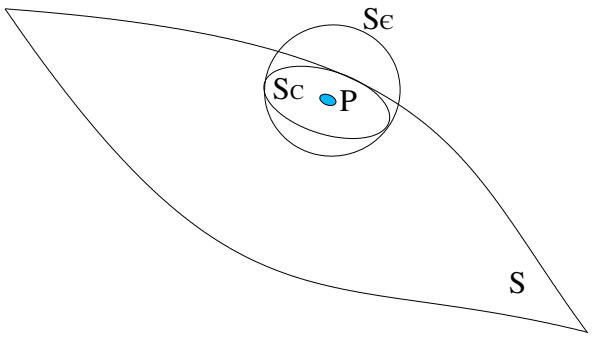

Figure 3.1: Sphere of radius $\epsilon > 0$ dividing surface S

Evaluating the integrals on S does, however, lead to a problem when $\mathbf{P} \to \mathbf{Q}$. In this case, ϕ and $\mathbf{v}$ approach infinity, making the integrands singular of order $1/r$ and $1/r^2$ respectively. This means that some care will have to be taken when evaluating these integrals. Following [17] we summarise how the equations can be represented in terms of Cauchy principal values of the integrals. Figure 3.1 shows a sphere of radius $\epsilon > 0$ which is placed so that its center coincides with the point $\mathbf{P}$ on the surface S. When ϵ is small, this sphere is cut into two portions, where the surface of the portion lying outside the body is called S_ϵ. The surface S of the body B is also divided into two parts, with the portion lying inside the sphere is denoted by S_c. The surfaces S_c and S_ϵ share the same boundary curve. Let $S' = S - S_c + S_\epsilon$ denote the surface of the body B merged with the sphere. As $\epsilon \to 0$, $S_\epsilon, S_c \to 0$ and ϵ will also approach $|\mathbf{r}(\mathbf{P}, \mathbf{Q})|$, thus equations 3.2 and 3.3 can be written as

$$\phi(\mathbf{P}) = -\iint_{S-S_c} \frac{\sigma(\mathbf{Q})}{|\mathbf{r}(\mathbf{P}, \mathbf{Q})|}\, dS - \iint_{S_\epsilon} \frac{\sigma(\mathbf{Q})}{\epsilon}\, dS \tag{3.4}$$

and

$$\mathbf{v} = \iint_{S-S_c} \frac{\sigma(\mathbf{Q})\, \mathbf{r}(\mathbf{P}, \mathbf{Q})}{|\mathbf{r}(\mathbf{P}, \mathbf{Q})|^3}\, dS + \iint_{S_\epsilon} \frac{\sigma(\mathbf{Q})\, \mathbf{r}(\mathbf{P}, \mathbf{Q})}{\epsilon^3}\, dS, \tag{3.5}$$

From Wang & Khoo [17], the limit of the velocity equation as $\epsilon \to 0$ can be evaluated using the solid angle extended under point $\mathbf{P}$ by surface S, which

is given as

$$\Theta = \lim_{\epsilon \to 0} \frac{1}{\epsilon^2} \iint_{S_\epsilon} dS \tag{3.6}$$

where Θ is a real number between 0 and 4π. If the surface is smooth at $\mathbf{P}$, $\Theta = 2\pi$. The centre of mass of the surface S_ϵ can be evaluated as

$$\mathbf{C} = \frac{\iint_{S_\epsilon} \mathbf{Q} dS}{\iint_{S_\epsilon} dS} \tag{3.7}$$

so that $\mathbf{C} \to \mathbf{P}$ as $\epsilon \to 0$. Knowing that $\mathbf{P} \to \mathbf{Q}$ we get

$$\lim_{\epsilon \to 0} \iint_{S_\epsilon} \frac{\sigma(\mathbf{Q})}{\epsilon} \, dS = \sigma(\mathbf{P}) \lim_{\epsilon \to 0} \frac{1}{\epsilon} \iint_{S_\epsilon} dS = \Theta \, \sigma(\mathbf{P}) \lim_{\epsilon \to 0} \epsilon = 0 \tag{3.8}$$

and

$$\begin{aligned} \lim_{\epsilon \to 0} \iint_{S_\epsilon} \frac{\sigma(\mathbf{Q}) \, \mathbf{r}(\mathbf{P}, \mathbf{Q})}{\epsilon^3} \, dS &= \sigma(\mathbf{P}) \lim_{\epsilon \to 0} \frac{1}{\epsilon^3} \iint_{S_\epsilon} (\mathbf{P} - \mathbf{Q}) dS \\ &= \Theta \sigma(\mathbf{P}) \lim_{\epsilon \to 0} \frac{\mathbf{P} - \mathbf{C}}{\epsilon}. \end{aligned} \tag{3.9}$$

By defining

$$\mathbf{n}_P = \lim_{\epsilon \to 0} \frac{\mathbf{C} - \mathbf{P}}{\epsilon} \tag{3.10}$$

(3.4) and (3.5) can be written as

$$\phi(\mathbf{P}) = - \fint\!\!\!\!\!\!\iint_S \frac{\sigma(\mathbf{Q})}{|\mathbf{r}(\mathbf{P}, \mathbf{Q})|} \, dS \tag{3.11}$$

and

$$\mathbf{v} = -\Theta \sigma(\mathbf{P}) \mathbf{n}_P + \fint\!\!\!\!\!\!\iint_S \frac{\sigma(\mathbf{Q}) \, \mathbf{r}(\mathbf{P}, \mathbf{Q})}{|\mathbf{r}(\mathbf{P}, \mathbf{Q})|^3} \, dS, \tag{3.12}$$

where $\fint\!\!\!\!\!\!\iint_S$ denotes the Cauchy principal value of the surface integral. This definition of $\mathbf{n}_P$ states that the direction of $\mathbf{n}_P$ is from the point $\mathbf{P}$ to the center of mass of S_ϵ, which is valid for non-smooth surfaces. Note that in [17] the calculation of the surface normal from the surrounding planar elements results in a surface normal of length Θ and so the solid angle is not present in 3.12 directly. In our work, however, we will calculate the solid angle explicitly from curved elements.

When discretised into M triangular elements, these integrals become

$$\phi(\mathbf{P}) = -\sum_{j=1}^{M} \iint_{\Delta_j} \frac{\sigma_j(\mathbf{Q})}{|\mathbf{r}(\mathbf{P},\mathbf{Q})|}\, dS_j \tag{3.13}$$

and

$$\mathbf{v} = \sigma(\mathbf{P})\, \mathbf{n}_P + \sum_{j=1}^{M} \iint_{\Delta_j} \frac{\sigma_j(\mathbf{Q})\, \mathbf{r}(\mathbf{P},\mathbf{Q})}{|\mathbf{r}(\mathbf{P},\mathbf{Q})|^3}\, dS_j, \tag{3.14}$$

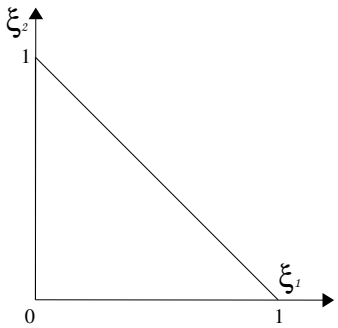

Figure 3.2: The reference triangle

The integrations are carried out in local triangle coordinate system shown in Figure 3.2 using a transform Jacobian [15]

$$J = \sqrt{\left(\frac{\partial y}{\partial \xi_1}\frac{\partial z}{\partial \xi_2} - \frac{\partial z}{\partial \xi_1}\frac{\partial y}{\partial \xi_2}\right)^2 + \left(\frac{\partial z}{\partial \xi_1}\frac{\partial x}{\partial \xi_2} - \frac{\partial x}{\partial \xi_1}\frac{\partial z}{\partial \xi_2}\right)^2 + \left(\frac{\partial x}{\partial \xi_1}\frac{\partial y}{\partial \xi_2} - \frac{\partial y}{\partial \xi_1}\frac{\partial x}{\partial \xi_2}\right)^2}. \tag{3.15}$$

The points $\mathbf{Q}$ are interpolated over each element j from the O element nodes $\mathbf{Q}_{j,k}$ using orthogonal shape functions S_k.

$$\mathbf{Q}(\xi_1, \xi_2) = \sum_{k=1}^{O} S_k(\xi_1, \xi_2)\, \mathbf{Q}_{j,k}. \tag{3.16}$$

Likewise we interpolate the source strengths on the surface with a set of orthogonal basis functions T_k.

$$\sigma(\mathbf{Q}(\xi_1, \xi_2)) = \sum_{k=1}^{O} T_k(\xi_1, \xi_2)\, \sigma(\mathbf{Q}_{j,k}). \tag{3.17}$$

By choosing $\lambda_k = T_k = S_k$ the boundary conditions are satisfied on every node on the discretised surface. Thus the potential can be rewritten as[1].

$$\phi(\mathbf{P}) = \sum_{j=1}^{M}\sum_{k=1}^{O} \sigma(\mathbf{Q}_{j,k}) \int_0^1 \int_0^{1-\xi_2} \frac{\lambda_{j,k}(\xi_1, \xi_2)}{|\mathbf{r}(\mathbf{P}_i, \mathbf{Q}(\xi_1, \xi_2))|}\, J\, d\xi_1 d\xi_2 \tag{3.18}$$

[1]Omitting the Cauchy principal value notation henceforth

In the summation the $\sigma(\mathbf{Q}_{j,k})$ are repeated for each element the node $\mathbf{Q}_{j,k}$ belongs to. By considering a mapping $j,k \rightarrow m$ where m is the global node number corresponding to local node numbers j,k we can rewrite the potential, using the Kronecker delta $\delta_{m,j}$ which is 1 if node m is on element j and 0 otherwise. This gives the potential as

$$\begin{aligned} \phi(\mathbf{P}_i) &= \sum_{m=1}^{N} \sigma(\mathbf{Q}_m)\, \mathbf{A}_i \qquad (3.19) \\ \mathbf{A}_i &= \sum_{j=1}^{M} \delta_{m,j} \sum_{k=1}^{O} \int_0^1 \int_0^{1-\xi_2} \frac{\lambda_{j,k}(\xi_1,\xi_2)}{|\mathbf{r}(\mathbf{P},\mathbf{Q}(\xi_1,\xi_2))|}\, J\, d\xi_1 d\xi_2, \end{aligned}$$

and velocity as

$$\begin{aligned} \mathbf{v}(\mathbf{P}_i) &= \sum_{m=1}^{N} \sigma(\mathbf{Q}_m)\, \mathbf{B}_i \qquad (3.20) \\ \mathbf{B}_i &= \sum_{j=1}^{M} \delta_{m,j} \sum_{k=1}^{O} \int_0^1 \int_0^{1-\xi_2} \frac{\lambda_{j,k}(\xi_1,\xi_2)\, \mathbf{r}(\mathbf{P},\mathbf{Q}(\xi_1,\xi_2))}{|\mathbf{r}(\mathbf{P},\mathbf{Q}(\xi_1,\xi_2))|^3}\, J\, d\xi_1 d\xi_2 \end{aligned}$$

Both potential and velocity can also be represented in matrix form as

$$\begin{aligned} \phi &= \overline{\mathbf{A}}\, \sigma, \qquad (3.21) \\ \mathbf{v} &= \overline{\mathbf{B}}\, \sigma \qquad (3.22) \end{aligned}$$

where the potential influence matrix $\overline{\mathbf{A}}$ and the velocity influence matrix $\overline{\mathbf{B}}$ are $N \times N$ matrices having rows $\mathbf{A}_i$ and $\mathbf{B}_i$ respectively and σ and ϕ are vectors containing the source strengths and potential at points $\mathbf{P}_i$, $i = 1, 2, \ldots, N$. Likewise, $\mathbf{v}$ contains N rows with the velocity at each point $\mathbf{P}_i$[2].

What is remaining to compute are the vertex normals $\mathbf{n}_P$ and the solid angle Θ. The surface normal at each node on an element can be calculated from the element's surface tangents $\mathbf{t}_{\xi_1} = \frac{\partial \mathbf{x}}{\partial \xi_1}$ and $\mathbf{t}_{\xi_2} = \frac{\partial \mathbf{x}}{\partial \xi_2}$ giving a surface normal

$$\hat{\mathbf{n}} = \frac{\mathbf{t}_{\xi_1} \times \mathbf{t}_{\xi_2}}{|\mathbf{t}_{\xi_1} \times \mathbf{t}_{\xi_2}|}. \qquad (3.23)$$

[2]The elements of $\mathbf{v}$ and $\overline{\mathbf{B}}$ are vectors containing the coordinates of the velocity and the velocity influence

Since the surface is only C_0 continuous, the normal will have a different direction for each element attached to the node, thus some averaging is necessary. Many ways of weighting the average using local information exists [41, 42, 43, 44] and Wang & Khoo [17] used the angles extended under the planar elements as weights, matching the approach previously used by Thurmer and Wuthrich [42] for computer graphics purposes

$$\Theta(\mathbf{P})\,\mathbf{n}_P = \frac{1}{2}\sum_{l=1}^{K}\alpha_l \mathbf{n}_l, \tag{3.24}$$

where K is the number of surrounding triangles, α_l is the angle at point $\mathbf{P}$ extended into triangle l and $\mathbf{n}_l$ is the unit normal vector on element l.

This approach can give too much weight to triangles with short edges extending from $\mathbf{P}$, leading to a small surface area despite a large angle α_l. Also the approach is less practical for curved elements, so instead we weight the normals using the element areas A_l [43, 44]

$$\mathbf{n}'_{\mathbf{P}} = \sum_{l=1}^{K}\frac{\mathbf{n}_l}{A_l} \tag{3.25}$$

which are normalised to unit length to yield $\mathbf{n_P}$. As will be seen in Chapter 4 this method provides good accuracy and convergence for linear and quadratic elements, although the results are sub-optimal for cubic elements and more investigation, possibly into using global information, may be necessary to find a method which yields good results for cubic elements.

For the solid angle we use the approach from Atkinson & Chien [45] to find the external solid angle

$$\Theta(\mathbf{P}) = 4\pi - \sum_{m=1}^{N}\sum_{k=1}^{O}\int_0^1\int_0^{1-\xi_2}\lambda_{m,j}(\xi_1,\xi_2)\frac{(\frac{\partial \mathbf{x}_m}{\partial \xi_1}\times\frac{\partial \mathbf{x}_m}{\partial \xi_2})\cdot(\mathbf{P}-\mathbf{x}_m)}{|\mathbf{P}-\mathbf{x}_m|^3}d\xi_1 d\xi_2, \tag{3.26}$$

where $\mathbf{x}_m = \mathbf{x}_m(\xi_1,\xi_2)$ is a point on the interpolated surface of element m.

3.3 Description of Elements

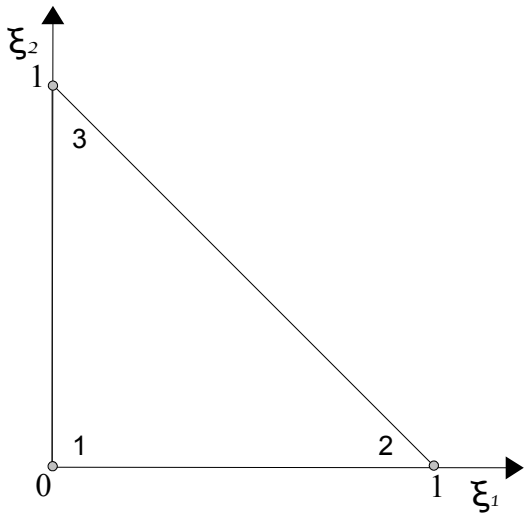

Figure 3.3: The linear triangle

The first elements used in this work are the 3-node linear elements used by Wang & Khoo [17] shown in Figure 3.3. This element has nodes at $[0,0]$, $[1,0]$ and $[0,1]$ in the reference triangle and interpolation functions [15]

$$\begin{aligned} \lambda_1^1 &= 1-\xi_1-\xi_2, \\ \lambda_2^1 &= \xi_1, \\ \lambda_3^1 &= \xi_2, \end{aligned} \tag{3.27}$$

where $\lambda_1^1(\xi_1,\xi_2)$ has been shortened for clarity. Using (3.16) we can derive the surface tangents

$$\begin{aligned} \frac{\partial \mathbf{x}}{\partial \xi_1} &= -\mathbf{x}_1+\mathbf{x}_2 \\ \frac{\partial \mathbf{x}}{\partial \xi_2} &= -\mathbf{x}_1+\mathbf{x}_3 \end{aligned} \tag{3.28}$$

Analytic integration over this element is possible as detailed in [17], although in this work numerical integration is used for simplicity.

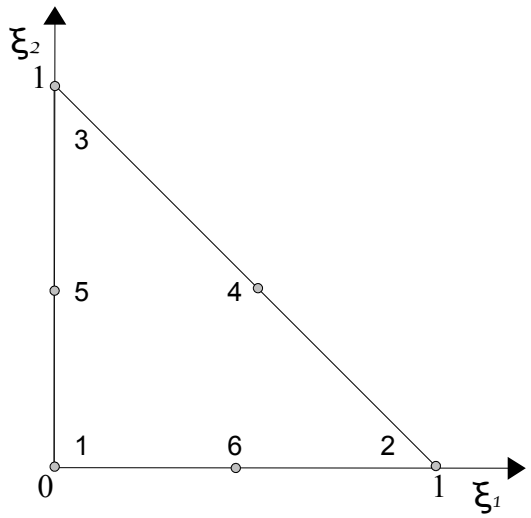

Figure 3.4: The quadratic triangle

The next element used in this work is the 6-node quadratic element shown in Figure 3.4. This element has three additional nodes at $[0.5, 0.5], [0.0, 0.5]$ and $[0.5, 0.0]$ and interpolation functions [15]

$$\begin{aligned}
\lambda_i^2 &= \lambda_i^1 \left(2\,\lambda_i^1 - 1\right), \; i = 1 \ldots 3 \\
\lambda_4^2 &= 4\,\lambda_2^1\,\lambda_3^1 \\
\lambda_5^2 &= 4\,\lambda_1^1\,\lambda_3^1 \\
\lambda_6^2 &= 4\,\lambda_1^1\,\lambda_2^1\,,
\end{aligned} \tag{3.29}$$

giving the surface tangents

$$\begin{aligned}
\frac{\partial \mathbf{x}}{\partial \xi_1} &= (-3 + 4\,\xi_1 + 4\,\xi_2)\,\mathbf{x}_1 + (4\,\xi_1 - 1)\,\mathbf{x}_2 \\
&\quad +4\,\xi_2 \mathbf{x}_4 - 4\,\xi_2 \mathbf{x}_5 + (-8\,\xi_1 + 4 - 4\,\xi_2)\,\mathbf{x}_6 \\
\frac{\partial \mathbf{x}}{\partial \xi_2} &= (-3 + 4\,\xi_1 + 4\,\xi_2)\,\mathbf{x}_1 + (4\,\xi_2 - 1)\,\mathbf{x}_3 \\
&\quad +4\,\xi_1 \mathbf{x}_4 + (-8\,\xi_2 + 4 - 4\,\xi_1)\,\mathbf{x}_5 - 4\,\xi_1 \mathbf{x}_6
\end{aligned} \tag{3.30}$$

In this case, analytical integration is no longer used due to the complexity of (3.16) and (3.17).

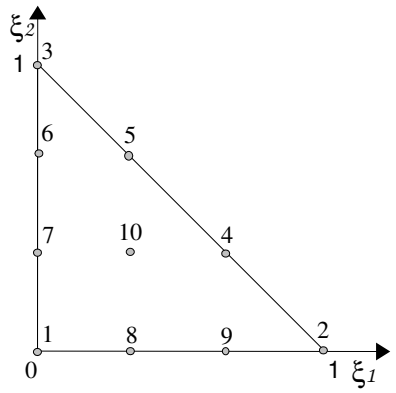

Figure 3.5: The cubic triangle

The third element used is the 10-node cubic element shown in Figure 3.5. The element is used in two forms differing in the spacing of the edge nodes. The first form is the equispaced triangle, with nodes as the linear element, plus edge nodes at $[2/3, 1/3], [1/3, 2/3], [0, 2/3],\ [0, 1/3], [1/3, 0]$ and $[2/3, 0]$ as well as a node at the triangle centroid. This gives interpolation functions

$$\begin{aligned}
\lambda_i^{3EQ} &= \lambda_i^1(3\lambda_i^1 - 1)(3\lambda_i^1 - 2)/2\,,\ i = 1 \ldots 3 \\
\lambda_4^{3EQ} &= 9\,\lambda_2^1\,\lambda_3^1(3\lambda_2^1 - 1)/2 \\
\lambda_5^{3EQ} &= 9\,\lambda_2^1\,\lambda_3^1(3\lambda_3^1 - 1)/2 \\
\lambda_6^{3EQ} &= 9\,\lambda_1^1\,\lambda_3^1(3\lambda_3^1 - 1)/2 \\
\lambda_7^{3EQ} &= 9\,\lambda_1^1\,\lambda_3^1(3\lambda_1^1 - 1)/2 \\
\lambda_8^{3EQ} &= 9\,\lambda_1^1\,\lambda_2^1(3\lambda_1^1 - 1)/2 \\
\lambda_9^{3EQ} &= 9\,\lambda_1^1\,\lambda_2^1(3\lambda_2^1 - 1)/2 \\
\lambda_{10}^{3EQ} &= 27\,\lambda_1^1\lambda_2^1\lambda_3^1\,.
\end{aligned} \tag{3.31}$$

and surface tangents

$$\begin{aligned}
\frac{\partial \mathbf{x}}{\partial \xi_1} &= \left(-\frac{11}{2} + 18(\xi_1 + \xi_2) - \frac{27}{2}(\xi_1^2 + 2\xi_1\xi_2 + \xi_2^2)\right)\mathbf{x}_1 \\
&+ \left(1 - 9\xi_1 + \frac{27}{2}\xi_1^2\right)\mathbf{x}_2 + \frac{9}{2}\left(6\xi_1\xi_2 - \xi_2\right)\mathbf{x}_4 \\
&+ \frac{9}{2}\left(3\xi_2^2 - 1\xi_2\right)(\mathbf{x}_5 - \mathbf{x}_6) + 27\left(\xi_1\xi_2 - \frac{5}{6}\xi_2 + \xi_2^2\right)\mathbf{x}_7 \\
&+ \frac{9}{2}\left(2 + 3(3\xi_1^2 + 2\xi_1\xi_2 + \xi_2^2) - 5(2\xi_1 + \xi_2)\right)\mathbf{x}_8 \\
&+ \frac{9}{2}(\xi_2 - 1 + \xi_1(8 - 6\xi_2 - 18\xi_1)\mathbf{x}_9 + 27\xi_2(1 - 2\xi_1 - \xi_2))\mathbf{x}_{10},
\end{aligned} \tag{3.32}$$

and

$$\begin{aligned}\frac{\partial \mathbf{x}}{\partial \xi_2} &= \left(-\frac{11}{2} + 18(\xi_1+\xi_2) - \frac{27}{2}(\xi_1^2 + 2\xi_1\xi_2 + \xi_2^2)\right)\mathbf{x}_1 \\ &+ \left(1 - 9\xi_2 + \frac{27}{2}\xi_2^2\right)\mathbf{x}_3 + \frac{9}{2}\left(3\xi_1^2 - 1\xi_1\right)(\mathbf{x}_4 + \mathbf{x}_9) \\ &+ \frac{9}{2}\left(6\xi_1\xi_2 - \xi_1\right)\mathbf{x}_5 + \frac{9}{2}(\xi_1 - 1 + \xi_2(8 - 6\xi_1 - 18\xi_2))\mathbf{x}_6 \\ &+ \frac{9}{2}\left(2 + 3(3\xi_2^2 + 2\xi_1\xi_2 + \xi_1^2) - 5(2\xi_2 + \xi_1)\right)\mathbf{x}_7 \\ &+ 27\left(\xi_1\xi_2 - \frac{5}{6}\xi_1 + \xi_1^2\right)\mathbf{x}_8 + 27\xi_1(1 - 2\xi_2 - \xi_1)\mathbf{x}_{10}.\end{aligned} \tag{3.33}$$

The second form is referred to as the Gauss-Lobatto spaced cubic triangle, since its edge points are spaced as Gauss Lobatto points, while retaining nodes at the triangle corners and the triangle centroid. This means that node 8 and 9 are situated at $\mathbf{x}(\xi_1, \xi_2) = [1/2\,(1 - 1/5\sqrt{5}),\, 0]$ and $[1/2\,(1 + 1/5\sqrt{5}),\, 0]$ with the remaining edge nodes being simple permutations of these coordinates.

In order to form an orthogonal basis for the interpolation, we use Proriol-Koornwinder-Dubiner (PKD) polynomials [20, 21]

$$\psi_{ij}(\xi_1, \xi_2) = \sqrt{(2i+1)(i+j+1)/2}\, P_i^{0,0}\left(\frac{2\xi_1' + \xi_2' + 1}{1 - \xi_2'}\right)\left(\frac{1 - \xi_2}{2}\right)^i P_j^{2i+1,0}(\xi_2'), \tag{3.34}$$

where $P_i^{a,b}$ are Jacobi polynomials. The indices are $i, j > 0$, $i + j \leq N$ where N is the order of interpolation thus corresponding to the size of the nodal set $n = (N+1)(N+2)/2$. Thus the notation φ_k with $k = 1 \ldots n$ is used instead with an arbitrary mapping $k \leftarrow i, j$. We can then set up the Vandermonde matrix

$$\overline{\mathbf{M}} = \begin{bmatrix} \psi_1(\mathbf{x}_1) & \psi_1(\mathbf{x}_2) & \cdots & \psi_1(\mathbf{x}_n) \\ \psi_2(\mathbf{x}_1) & \psi_2(\mathbf{x}_2) & \cdots & \psi_2(\mathbf{x}_n) \\ \vdots & \vdots & \cdots & \vdots \\ \psi_n(\mathbf{x}_1) & \psi_n(\mathbf{x}_2) & \cdots & \psi_n(\mathbf{x}_n) \end{bmatrix}, \tag{3.35}$$

leading to the interpolation functions

$$\lambda_i^N = \sum_{k=1}^{n} (\overline{\mathbf{M}}^{-1})_{ik}^T \, \psi(\xi_1, \xi_2). \tag{3.36}$$

This can be solved symbolically for low order elements and by using the equispaced nodal set the exact same interpolation functions as listed earlier will be derived. If we instead use the Gauss-Lobatto spaced set, we end up with the following interpolation functions

$$\begin{aligned}
\lambda_1^{3GL} &= 1 - 6(\xi_1 + \xi_2) + 10(\xi_1^2 + \xi_2^2) - 5(\xi_1^3 + \xi_2^3) + 21\xi_1\xi_2 - 16(\xi_1^2\xi_2 + \xi_1\xi_2^2) \\
\lambda_2^{3GL} &= \xi_1 - 5\xi_1^2 + \xi_1\xi_2 - \xi_1\xi_2^2 - \xi_1^2\xi_2 + 5\xi_1^3 \\
\lambda_3^{3GL} &= \xi_2 - 5\xi_2^2 + \xi_1\xi_2 - \xi_1\xi_2^2 - \xi_1^2\xi_2 + 5\xi_2^3 \\
\lambda_4^{3GL} &= \frac{5}{2}\left(-2\xi_1\xi_2 + (3+\sqrt{5})\xi_1^2\xi_2 + (3-\sqrt{5})\xi_1\xi_2^2\right) \\
\lambda_5^{3GL} &= \frac{5}{2}\left(-2\xi_1\xi_2 + (3+\sqrt{5})\xi_1\xi_2^2 + (3-\sqrt{5})\xi_1^2\xi_2\right) \\
\lambda_6^{3GL} &= \frac{5}{2}\Big((1-\sqrt{5})(\xi_2 + 3\xi_1\xi_2^2) - (1-3\sqrt{5})\xi_2^2 \\
&- 2(2-\sqrt{5})\xi_1\xi_2 + (3-\sqrt{5})\xi_1^2\xi_2 - 2\sqrt{5}\xi_2^3\Big) \\
\lambda_7^{3GL} &= \frac{5}{2}\Big((1+\sqrt{5})(\xi_2 + 3\xi_1\xi_2^2) - (1+3\sqrt{5})\xi_2^2 \\
&- 2(2+\sqrt{5})\xi_1\xi_2 + (3+\sqrt{5})\xi_1^2\xi_2 + 2\sqrt{5}\xi_2^3\Big) \\
\lambda_8^{3GL} &= \frac{5}{2}\Big((1+\sqrt{5})(\xi_1 + 3\xi_1^2\xi_2) - (1+3\sqrt{5})\xi_1^2 \\
&- 2(2+\sqrt{5})\xi_1\xi_2 + (3+\sqrt{5})\xi_2^2\xi_2 + 2\sqrt{5}\xi_1^3\Big) \\
\lambda_9^{3GL} &= \frac{5}{2}\Big((1-\sqrt{5})(\xi_1 + 3\xi_1^2\xi_2) - (1-3\sqrt{5})\xi_1^2 \\
&- 2(2-\sqrt{5})\xi_1\xi_2 + (3-\sqrt{5})\xi_2^2\xi_2 - 2\sqrt{5}\xi_1^3\Big) \\
\lambda_{10}^{3GL} &= 27(\xi_1\xi_2 - \xi_1^2\xi_2 - \xi_1\xi_2^2)
\end{aligned} \tag{3.37}$$

and the following surface tangents

$$
\begin{aligned}
\frac{\partial \mathbf{x}}{\partial \xi_1} &= (-6 + 20\xi_1 - 15\xi_1^2 + 21\xi_2 - 32\xi_1\xi_2 - 16\xi_2^2)\mathbf{x}_1 \\
&+ (1 - 10\xi_1 + \xi_2 - \xi_2^2 - 2\xi_1\xi_2 + 15\xi_1^2)\mathbf{x}_2 + (\xi_2 - 2\xi_1\xi_2 - \xi_2^2)\mathbf{x}_3 \\
&+ \frac{5}{2}(-2\xi_2 + 2(3+\sqrt{5})\xi_1\xi_2 + (3-\sqrt{5})\xi_2^2)\mathbf{x}_4 \\
&+ \frac{5}{2}(-2\xi_2 + 2(3+\sqrt{5})\xi_2^2 + (3-\sqrt{5})\xi_1\xi_2)\mathbf{x}_5 \\
&+ \frac{5}{2}(3(1-\sqrt{5})\xi_2^2 - 2(2-\sqrt{5})\xi_2 + 2(3-\sqrt{5})\xi_1\xi_2)\mathbf{x}_6 \\
&+ \frac{5}{2}(3(1+\sqrt{5})\xi_2^2 - 2(2+\sqrt{5})\xi_2 + 2(3+\sqrt{5})\xi_1\xi_2)\mathbf{x}_7 \\
&+ \frac{5}{2}((1+\sqrt{5})(1+6\xi_1\xi_2) - 2(1+3\sqrt{5})\xi_1 - 2(2+\sqrt{5})\xi_2 + (3+\sqrt{5})\xi_2^2 + 6\sqrt{5}\xi_1^2)\mathbf{x}_8 \\
&+ \frac{5}{2}((1-\sqrt{5})(1+6\xi_1\xi_2) - 2(1-3\sqrt{5})\xi_1 - 2(2-\sqrt{5})\xi_2 + (3-\sqrt{5})\xi_2^2 - 6\sqrt{5}\xi_1^2)\mathbf{x}_9 \\
&+ 27(\xi_2 - 2\xi_1\xi_2 - \xi_2^2)\mathbf{x}_{10}
\end{aligned} \tag{3.38}
$$

$$
\begin{aligned}
\frac{\partial \mathbf{x}}{\partial \xi_2} &= (-6 + 20\xi_2 - 15\xi_2^2 + 21\xi_1 - 32\xi_1\xi_2 - 16\xi_1^2)\mathbf{x}_1 \\
&+ (\xi_1 - 2\xi_1\xi_2 - \xi_1^2)\mathbf{x}_2 + (1 - 10\xi_2 + \xi_1 - \xi_1^2 - 2\xi_1\xi_2 + 15\xi_2^2)\mathbf{x}_3 \\
&+ \frac{5}{2}(-2\xi_1 + 2(3+\sqrt{5})\xi_1^2 + (3-\sqrt{5})\xi_1\xi_2)\mathbf{x}_4 \\
&+ \frac{5}{2}(-2\xi_1 + 2(3+\sqrt{5})\xi_1\xi_2 + (3-\sqrt{5})\xi_1^2)\mathbf{x}_5 \\
&+ \frac{5}{2}((1-\sqrt{5})(1+6\xi_1\xi_2) - 2(1-3\sqrt{5})\xi_2 - 2(2-\sqrt{5})\xi_1 + (3-\sqrt{5})\xi_1^2 - 6\sqrt{5}\xi_2^2)\mathbf{x}_6 \\
&+ \frac{5}{2}((1+\sqrt{5})(1+6\xi_1\xi_2) - 2(1+3\sqrt{5})\xi_2 - 2(2+\sqrt{5})\xi_1 + (3+\sqrt{5})\xi_1^2 + 6\sqrt{5}\xi_2^2)\mathbf{x}_7 \\
&+ \frac{5}{2}(3(1+\sqrt{5})\xi_1^2 - 2(2+\sqrt{5})\xi_1 + 2(3+\sqrt{5})\xi_1\xi_2)\mathbf{x}_8 \\
&+ \frac{5}{2}(3(1-\sqrt{5})\xi_1^2 - 2(2-\sqrt{5})\xi_1 + 2(3-\sqrt{5})\xi_1\xi_2)\mathbf{x}_9 \\
&+ 27(\xi_1 - 2\xi_1\xi_2 - \xi_1^2)\mathbf{x}_{10}
\end{aligned} \tag{3.39}
$$

It is also possible to invert the matrix numerically thus generating a spectral collocation method of arbitrary order [20, 21, 22]. One disadvantage is that this is computationally costly. Although the Vandermonde matrix need only be inverted once for the entire simulation the evaluation of several PKD polynomials per integration point is costly. Even if the value of the PKD polynomials is stored between time steps, this will be more costly than hard coded interpolation functions due to a considerable amount of array lookups.

3.4 Numerical Integration and Regularisation of Singularities

The integration over each triangle can be handled by standard triangular Gaussian integration whenever **P** is not one of the nodes of the triangle. For these regular integrals simple quadrature schemes of order 6, 12, 25, 48 and 79 points [46] have been implemented. When **P** is on the triangle itself, however, the Cauchy principal value will have to be evaluated. Figure 3.6 depicts the area of $e_\epsilon : r < \epsilon$ around a vertex P and its distorted contour d_e in the local triangle coordinate system. As $\epsilon \to 0$, $1/r$ approaches infinity

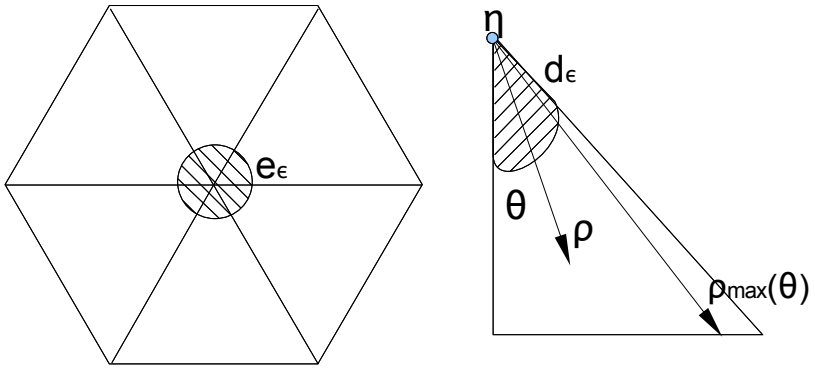

Figure 3.6: Vanishing neighbourhood

and the integration becomes singular. A local polar coordinate system is then introduced as follows

$$\begin{aligned} \xi_1 &= \eta_1 + \rho\cos\theta \\ \xi_2 &= \eta_2 + \rho\sin\theta, \end{aligned} \tag{3.40}$$

where (η_1, η_2) are the local coordinates of the singular node. The distorted neighbourhood d_ϵ can then be defined by a radius $\alpha(\theta)$. For the potential this transformation regularises the integral because the Jacobian of the transform ρ cancels the singularity [29, 36]. It also reduces the order of the velocity singularity to $\frac{1}{r}$, which can be dealt with in the following fashion.

First a Taylor expansion in the neighbourhood of the singular point is employed [29, 36] using $\mathbf{x}$ and $\mathbf{y}$ as the coordinates of $\mathbf{P}$ and $\mathbf{Q}$ respectively

$$\begin{aligned} x_k - y_k = & \ \tfrac{\partial x_k}{\partial \xi_1}|_{\xi=\eta}(\xi_1 - \eta_1) + \tfrac{\partial x_k}{\partial \xi_2}|_{\xi=\eta}(\xi_2 - \eta_2) + O(\rho^2) \\ = & \ \rho\left[\tfrac{\partial x_k}{\partial \xi_1}|_{\xi=\eta}\cos\theta + \tfrac{\partial x_k}{\partial \xi_2}|_{\xi=\eta}\sin\theta\right] + O(\rho^2), \qquad (3.41) \\ k = & \ 1, 2, 3. \end{aligned}$$

For brevity we define

$$A_k(\theta) = \left[\frac{\partial x_k}{\partial \xi_1}|_{\xi=\eta}\cos\theta + \frac{\partial x_k}{\partial \xi_2}|_{\xi=\eta}\sin\theta\right] \qquad (3.42)$$

and

$$A(\theta) = \sqrt{\sum_{i=1}^{3}[A_k(\theta)]^2}. \qquad (3.43)$$

Then expansions for the full kernel can be divided into

$$r^2(\rho,\theta) = \rho^2 A^2(\theta) + O(\rho^3) \qquad (3.44)$$

and

$$\frac{x_k - y_k}{r} = \frac{A_k(\theta)}{A(\theta)} + O(\rho) \qquad (3.45)$$

Thus at the singular point the kernel in (3.20) can be written as [36]

$$\begin{aligned} F_k(\rho,\theta) = \frac{\lambda(\rho,\theta)\,\mathbf{r}(\mathbf{P},\mathbf{Q}(\rho,\theta))\,\rho}{|\mathbf{r}(\mathbf{P},\mathbf{Q}(\rho,\theta))|^3}\,J &= \frac{A_k(\theta)}{\rho\,A^3(\theta)}\lambda(\eta)J(\eta) + O(1) \\ &= \frac{f_k(\theta)}{\rho} + O(1) \qquad (3.46) \end{aligned}$$

Thus

$$\lim_{\rho\to 0}\left\{F_k(\rho,\theta) - \frac{f_k(\theta)}{\rho}\right\} = O(1). \qquad (3.47)$$

This means that by subtracting $\frac{f_k(\theta)}{\rho}$ from the kernel, it becomes non singular. The singular remainder can then be integrated separately. In order to integrate the singular remainder correctly, the contour of the neighbourhood $(\alpha(\epsilon,\theta)))$ will have to be taken into account. The contour of the neighbourhood is given in the global coordinate system by [36]

$$\epsilon^2 = (x_k - y_k)(x_k - y_k),\ \mathbf{x},\mathbf{y} \in S. \qquad (3.48)$$

and in the ξ plane, from (3.42) and (3.43)

$$\epsilon^2 = \rho^2 A^2(\theta) + O(\rho^3). \tag{3.49}$$

Thus the contour of d_ϵ, the image of e_ϵ is given by

$$\alpha(\epsilon, \theta) = \rho = \frac{\epsilon}{A(\theta)} + O(\epsilon^2) = \epsilon\beta(\theta) + O(\epsilon^2). \tag{3.50}$$

The final formula for the velocity integration is then [36]

$$\begin{aligned} \mathbf{v}_{i,k} &= -\sigma(\mathbf{P})\,\mathbf{n}_P \\ &+ \sum_{m=1}^{N} \sigma_m \sum_{j=1}^{M} \delta_{m,j} \left\{ \int_{\theta_{1m,j}}^{\theta_{2m,j}} \int_0^{\rho_{max}^{m,j}(\theta)} \left[F_{i,k}^{m,j}(\rho,\theta) - \frac{f_{i,k}^{m,j}}{\rho} \right] d\rho d\theta \right. \\ &\left. + \int_{\theta_{1m,j}}^{\theta_{2m,j}} f_{i,k}^{m,j} \ln\left(\frac{\rho_{max}^{m,j}}{\beta^{m,j}(\theta)} \right) d\rho d\theta \right\}, \end{aligned} \tag{3.51}$$

where the integration of the remainder has been done with respect to ρ, taking into account the distorted shape of d_ϵ [36]. Both the potential and velocity integrals are then evaluated using repeated Gaussian quadrature in radial and angular direction. Unless integration is centered around node 1, the angular integration has to be split into at least two intervals as the value for $\rho_{\max}$ is discontinuous between edges of the triangle and for simplicity every angular integration is subdivided. The Gaussian quadrature has been implemented in orders of 6 and 10 following a notation of $(n_a \times a) \times (n_b \times b)$ where a is the order of the angular quadrature, b is the order of the radial quadrature and n_a and n_b are the number of times the intervals of the angular and radial integrations are to be subdivided. If only one interval is used in the radial direction, n_b is omitted, thus $(2 \times 6) \times 6$ is the lowest order of Gaussian integration used for singular integrals.

3.5 Mesh Generation

A common way of generating 3D bubble meshes is starting with a uniform polyhedron and utilising a subdivision and projection strategy to generate an approximation to a sphere with many facets [24, 47, 48]. The sphere-like shape is then distorted into other shapes by projecting the surface nodes onto the surface being modelled. An example subdivision mesh with 720 facets can be seen in figure 3.7 and architects would recognise this approach in "geodesic domes" [49], such as the ones found at the Eden Project in Cornwall, UK. Much of the mathematics behind geodesic domes are thus valid in generating this kind of mesh. Beyond the starting polyhedron, any such

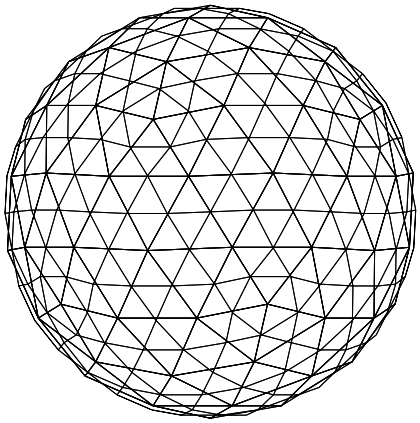

Figure 3.7: Icosahedron with each face subdivided into 36 new facets

approximation to a sphere using flat triangles can never become completely uniform [50], but choosing a good polyhedron as a starting point is important for achieving close to uniform tesselation. The most common starting point is the icosahedron, built up with twenty equilateral triangles. This is the uniform polyhedra with the most faces, and compared with other uniform polyhedra, less sub-division will have to be done to achieve a certain number of facets. An icosahedron [51] circumscribed in a sphere of radius R with the center at the origin will, with the chosen rotation, have two vertices at

$(0, 0, \pm R)$, and the other vertices corresponding to the vertices of two pentagons in the planes $z = \pm\frac{1}{5}\sqrt{5}R$. Both pentagons are inscribed in circles of radius $\ell = \frac{2}{5}\sqrt{5}R$. This gives the following first six vertices:

$$\eta_1 = (0, 0, R) \tag{3.52}$$

$$\eta_2 = (0, R_i, \frac{1}{5}\sqrt{5}R) \tag{3.53}$$

$$\eta_3 = (m_1, n_1, \frac{1}{5}\sqrt{5}R) \tag{3.54}$$

$$\eta_4 = (m_2, -n_2, \frac{1}{5}\sqrt{5}R) \tag{3.55}$$

$$\eta_5 = (-m_2, -n_2, \frac{1}{5}\sqrt{5}R) \tag{3.56}$$

$$\eta_6 = (-m_1, n_1, \frac{1}{5}\sqrt{5}R) \tag{3.57}$$

where

$$m_1 = \sin\left(\frac{2\pi}{5}\right)\ell \tag{3.58}$$

$$m_2 = \sin\left(\frac{4\pi}{5}\right)\ell \tag{3.59}$$

$$n_1 = \cos\left(\frac{2\pi}{5}\right)\ell \tag{3.60}$$

$$n_2 = \cos\left(\frac{\pi}{5}\right)\ell \tag{3.61}$$

The last six vertices are found by inverting the first six

$$\eta_{12} = -\eta_1 \tag{3.62}$$

$$\eta_i = -\eta_{i-5}\,,\ i = 7, \ldots, 11 \tag{3.63}$$

In order to make the shape approximation more accurate, each original triangle is divided up into f^2 new triangles, where f is called the frequency of subdivision and is the number of segments each edge of the triangle is divided into. The new nodal points are connected to each other by new lines, which will be parallel to one of the edges of the original triangle, something which can be seen in Figure 3.8. For $f > 2$ there will be one or more points of

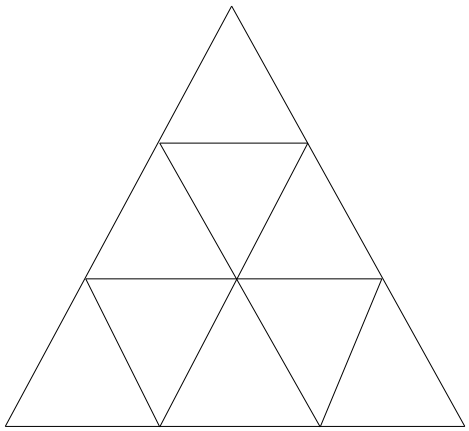

Figure 3.8: Subdivision of triangle, $f = 3$

intersection between these lines, each of the points of intersection forming a new vertex.

Simply subdividing the triangles would increase the complexity of the solution without improving the approximation to the sphere. Therefore, to improve the approximation each new vertex is projected onto the surface of the icosahedron's circumsphere. This is done by simply moving multiplying the unit position vector by the radius of the circumsphere R

$$\mathbf{P}_i \leftarrow R \, \frac{\mathbf{P}_i}{|\mathbf{P}_i|} \tag{3.64}$$

If the segments are chosen to be equal length as shown in Figure 3.8 and with the dashed lines in Figure 3.9, the resulting triangles will vary greatly in size once projected onto the circumsphere. In particular one can see that the middle triangles will be considerably larger than the others. A more uniform mesh can be created by chosing the segments to be of equal angle from origin, $\alpha_1 = \alpha_2 = \alpha_3$, as shown with solid lines in Figure 3.9.

The resulting triangles are still not of equal shape and size[3] but each

[3]If they were, the resulting shape would be a new uniform polyhedron

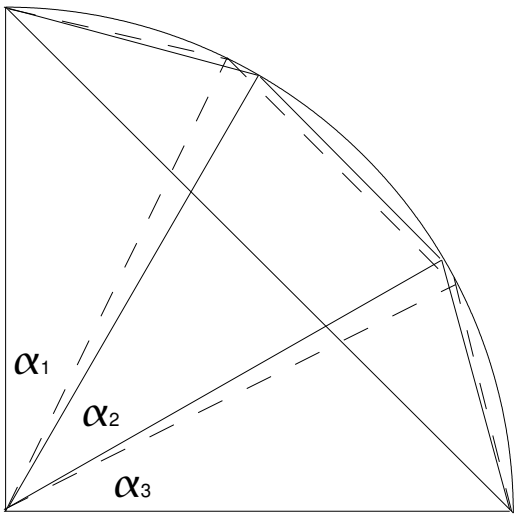

Figure 3.9: Subdivision of triangle, angles from origin, $f = 3$

group of panels originating from the original triangles will be of the same shape and size. It can be seen in Figure 3.7 that most nodes will have six neighbouring panels, but the 12 nodes coinciding with the vertices of the icosahedron will only have five neighbouring panels and by connecting the lines between each five neighbour node, it should be possible to discern each group of triangles originating from the same icosahedron face.

The value of f can be chosen to provide the level of mesh refinement desired, yielding the following number of faces M and nodes N

$$\begin{aligned} M &= 20f^2 \\ N &= 10f^2 + 2 \end{aligned} \tag{3.65}$$

For quadratic and cubic meshes, this subdivision is carried out one final time with $f = 2$ and $f = 3$ respectively to provide the additional mesh points required. For the Gauss-Lobatto spaced cubic element, this subdivision is not, however, done using equal angles, but each angle is weighted according to the coordinates in the reference triangle.

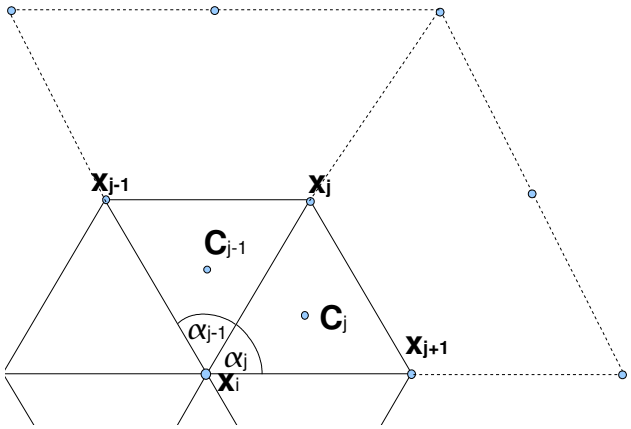

Figure 3.10: Neighbouring region for curvature calculation

3.6 Curvature Approximation

Finding appropriate curvature approximations for 3D BEM formulations is a complex enough problem to warrant a study of its own. This, however, is outside the scope of this Thesis, and we resort to recent literature from the area of computer graphics [52, 44, 53], which were found to give good results for at least some of the elements tested. For our curvature estimation we use local information seen in Figure 3.10 to calculate normal curvatures as [52]

$$\kappa_{i,j}^N = 2\frac{(\mathbf{x}_i - \mathbf{x_j}) \cdot \hat{\mathbf{n}}_i}{|\mathbf{x}_i - \mathbf{x}_j|^2}, \tag{3.66}$$

where $\mathbf{x}_j$ are the neighbouring nodes from $\mathbf{x}_i$ and $\hat{\mathbf{n}}_i$ is the unit normal at $\mathbf{x}_i$. For quadratic and higher order elements, the reduced neighbourhood, encapsulated by the closest nodes of the neighbouring triangles, is used, with the dotted lines in Figure 3.10 illustrating the full triangle. This procedure is analogous to fitting an osculating circle and calculating curvature as the inverse radius of this circle.The mean curvature is then found as a quadrature of the normal curvatures,

$$\kappa_H(\mathbf{x}_i) = \sum_j w_{ij}\kappa_{i,j}^N, \tag{3.67}$$

where the weights w_{ij} can be chosen in many different ways including cotangents of α_j as in Meyer *et al* [44] or the tangents of α_j as used by Langer *et al* [53] or as in this case, the centroid weights used by Chen & Wu [54]

$$w_{ij} = \frac{1}{|\mathbf{x}_i - \mathbf{c}_j|^2} \tag{3.68}$$

These weights were found to give slightly better convergence properties than the other weights.

An alternative method would be to calculate the mean curvature directly from the derivatives of the surface patches as [24]

$$\kappa_H = \frac{1}{2}\frac{EN - 2FM + LG}{EG - F^2}, \tag{3.69}$$

where

$$\begin{aligned} E &= \mathbf{t}_{\xi_1} \cdot \mathbf{t}_{\xi_1} \quad F = \mathbf{t}_{\xi_1} \cdot \mathbf{t}_{\xi_2} \quad G = \mathbf{t}_{\xi_2} \cdot \mathbf{t}_{\xi_2} \\ L &= \mathbf{t}_{\xi_1} \cdot \mathbf{n}_{\xi_1} \quad M = \mathbf{t}_{\xi_1} \cdot \mathbf{n}_{\xi_2} \quad N = \mathbf{t}_{\xi_2} \cdot \mathbf{n}_{\xi_2} \end{aligned} \tag{3.70}$$

and $\mathbf{n}_{\xi_1}$ and $\mathbf{n}_{\xi_2}$ denotes the derivatives of the surface normal with respect to ξ_1 and ξ_2 respectively. Both normal derivatives can be calculated from the interpolation of averaged vertex normals using (3.16) and (3.25) to raise the order of interpolation [24]. The curvature at a node is calculated as a weighted average using the same weights as (3.68).

3.7 Parallelisation and Implementation Issues

It should be clear that every element of the solution matrix and the corresponding velocity matrix can be calculated independently of each other. This means that assembling the solution matrix in the IBEM is a so-called "embarrassingly parallel" problem, meaning no particular effort is required to segment the problem into a very large number of parallel tasks. When using C processors, each processor can calculate a segment consisting of $\frac{N}{C}$

rows or columns of the matrix each and the matrix can then be solved using a parallel linear system solver.

For generating the solution matrix the *LAM* implementation of the distributed memory messaging system *MPI* [55, 56] is used. Also since calculating the potential influence based solution matrix shares many operations with calculating the velocity influences used for the surface velocity calculation, these operations are performed together and a velocity influence matrix is assembled as well. The final surface velocities are then calculated through the BLACS [57] based matrix-vector product routine "pdgemm".

As for solving the linear system, the most obvious choice is a direct solver such as LU-decomposition. Building the solution matrix scales quadratically with the number of surface nodes, while LU-decomposition scales cubically. Thus for a large number of surface nodes, the LU-decomposition will start to dominate the solution time. In that case it would be sensible to look for alternatives such as iterative solvers.

For our problem sizes, however, the considerable cost of calculating each element of the solution matrix means that assembling the matrix will still dominate and LU-decomposition will be used, since it is readily available through the ScaLaPACK routine "dgesvx" [57]. ScaLaPACK gives considerably better performance if the solution matrix is distributed by both row and column and banded in smaller segments. Therefore each processor will in practise evaluate a given set of segments, each of size 64×64, apart from the last segment in each row and column, all of which will be expanded to contain any remainder in the labour division.

The performance, accuracy and scalability of the IBEM will be discussed in the next Chapter.

Bibliography

[1] L. Guerri, G. Lucca, and A. Prosperetti. A numerical method for the dynamics of non-spherical cavitation bubbles. In *Proceedings of 2nd International Colloquium on Drops and Bubbles*, pages 175–181. Jet Propulsion Laboratory, 1981.

[2] G.R. Baker, Meiron D.I., and Orszag S.A. Boundary integral methods for axisymmetric and three-dimensional Rayleigh-Taylor instability problems. *Physica*, pages 19–31, 1984.

[3] J.R. Blake, Taib B.B., and Doherty G. Transient cavities near boundaries. Part 1. Rigid boundary. *Journal of Fluid Mechanics*, 180:479–497, 1986.

[4] J.P. Best and A. Kucera. A numerical investigation of non-spherical rebounding bubbles. *Journal of Fluid Mechanics*, 245, 1992.

[5] J.R. Blake and D.C. Gibson. Growth and collapse of a vapour cavity near a free surface. *Journal of Fluid Mechanics*, 111:123–140, 1981.

[6] J.M. Boulton-Stone. Applications of boundary integral methods to two-dimensional and axisymmetric bubbles. In *MSc Thesis*, Birmingham, UK, October 1991. University of Birmingham.

[7] G.L. Chahine and T.O. Perdue. Simulation of the three-dimensional behaviour of an unsteady large bubble near a structure. In *3rd Inter-*

national Colloquim On Bubbles and Drops, volume 197, pages 188–199, Silver Spring, Maryland, USA, Sept 1988. AIP Conference Proceedings.

[8] P.J. Harris. A numerical model for determining the motion of a bubble close to a fixed rigid structure in a fluid. *Int. J. Numer.Methods Eng.*, 33:1813, 1992.

[9] S.A. Wilkerson. *A boundary integral approach to three-dimensional underwater explosion bubble dynamics*. PhD thesis, Johns Hopkins University, Baltimore, MD, 1990.

[10] Q.X. Wang. Numerical simulation of violent bubble motion. *Physics of Fluids*, 16(5), May 2004.

[11] J.R. Blake and Tong R.P. Jet impact in collapsing bubbles. *12th Australian Fluid Mechanics Conference*, 2:819, 1995.

[12] J.R. Blake, J.M. Boulton-Stone, and Tong R.P. Boundary integral methods for rising, bursting and collapsing bubbles in BE. *Applications in Fluid mechanics*, 4:31, 1995.

[13] Y.L. Zhang, K.S. Yeo, B.C. Khoo, and W.K. Chong. Three-dimensional computation of bubbles near a free surface. *Journal of Computational Physics*, 146:105–123, 1999.

[14] Y.L. Zhang, K.S Yeo, B.C. Khoo, and W.K. Chong. Simulation of three-dimensional bubbles using desingularized boundary integral method. *International Journal for Numerical Methods in Fluids*, 31:1311–1320, 1999.

[15] C.A. Brebbia and J. Dominguez. *Boundary Elements An Introductory Course, 2nd Edition*. Computational Mechanics Publications and McGraw-Hill, Southampton, UK, 1992.

[16] J.L. Hess and A.M.O Smith. Calculation of potential flow about arbitrary bodies. *Progress in Aeronautical Sciences*, 8, 1967.

[17] C. Wang and B.C Khoo. An indirect boundary element method for three-dimensional explosion bubbles. *Journal of Computational Physics*, 194:451–480, 2004.

[18] J.H.M. Frijns, S.L. de Snoo, and R. Schoonhoven. Improving the accuracy of the boundary element method by the use of second-order interpolation functions. *IEEE Trans. on Biomed. Eng.*, 47(10):1336–1346, October 2000.

[19] J.S. Hesthaven. From electrostatics to almost optimal nodal sets for polynomial interpolation in a simplex. *SIAM Journal of Numerical Analysis*, 35(2):655–676, 1998.

[20] F.X. Giraldo and T. Warburton. A nodal triangle-based spectral element method for the shallow water equations on the sphere. *Journal of Computational Physics*, 207:129–150, 2005.

[21] R. Pasquetti and F. Rapetti. Spectral element methods on triangles and quadrilaterals: comparisons and applications. *Journal of Computational Physics*, 198:349–362, 2004.

[22] C. Pozrikidis. A spectral collocation method with triangular boundary elements. *Engineering Analysis with Boundary Elements*, 30:315–324, 2006.

[23] C. Pozrikidis. Three-dimensional oscillations of inviscid drops induced by surface tension. *Computers & Fluids*, 30:417–444, 2000.

[24] C. Pozrikidis. Numerical simulation of three-dimensional bubble oscillations by a generalized vortex method. *Theoretical and Computational Fluid Dynamics*, 16:151–169, 2002.

[25] G.R. Baker, Meiron D.I., and Orszag S.A. Generalized vortex methods for free-surface flow problems. *Journal of Fluid Mechanics*, 123:477–501, 1982.

[26] J.M. Boulton-Stone. A comparison of boundary integral methods for studying the motion of a two-dimensional bubble in an infinite fluid. *Comput. Methods Appl. Mech. Eng.*, 102:213–234, 1993.

[27] Y. Cao, W.W. Schultz, and R.F. Beck. Three-dimensional desingularized boundary integral methods for potential problems. *International Journal for Numerical Methods in Fluids*, 12:785–803, 1991.

[28] J.C. de Munck. A linear discretization of the volume conductor boundary integral equation using analytically integrated elements. *IEEE Trans. on Biomed. Eng.*, 39:986–990, 1992.

[29] M.H. Aliabadi, W.S. Hall, and T.G. Phemister. Taylor expansions for singular kernels in the boundary element method. *International Journal for Numerical Methods in Engineering*, 21, 1985.

[30] T.T. Hibbs. *C(1) Continuous Representations and Advanced Singular Kernel Integrations in the Three Dimensional Boundary Integral Method*. PhD thesis, C.N.A.A., London, UK, 1989.

[31] W.S. Hall and T.T Hibbs. Subtraction, expansion and regularising transformation methods for singular kernel integrations in elastostatics. *Mathl, Comput. Modelling*, 15(3-5):313–323, 1991.

[32] M.H. Aliabadi and W.S. Hall. The regularising transformation integration method for boundary element kernels - comparison with series expansion and weighted gaussian integration method. *Engineering Analysis with Boundary Elements*, 6(2):66–71, 1989.

[33] M. Guiggiani and A. Gigante. A general algorithm for multidimensional Cauchy principal value integrals in the boundary element method. *Transaction of the ASME*, 57:906–915, 1990.

[34] M. Guiggiani, G. Krishnasamy, T.J. Rudolphi, and F.J. Rizzo. A general algorithm for the numerical solution of hypersingular boundary integral equations. *Transaction of the ASME*, 59:604–614, 1992.

[35] A. Frangi and M. Guiggiani. Free terms and compatibility conditions for 3d hypersingular boundary integral equations. *ZAMM Z. Angew. Math. Mech.*, 81(10):651–664, 2001.

[36] M. Guiggiani. Singular integrals in B.E. methods: Formulation and numerical treatment of boundary integral equations with hypersingular kernels. In V. Sladek and J. Sladek, editors, *Singular Integrals in B.E. Methods*. Computational Mechanics Publications, 1998.

[37] A.M. Zhang, X.L. Yao, and X.B. Yu. The dynamics of three-dimensional underwater explosion bubble. *Journal of Sound and Vibration*, 311:1196–1212, 2008.

[38] T.A. Cruse. An improved boundary-integral equation method for three dimensional elastic stress analysis. *Computational Structures*, 4:741–754, 1974.

[39] Y.J. Liu. On the simple solution method and non-singular nature of the BIE/BEM-review and some new results. *Engineering Analysis with Boundary Elements*, 24:789–795, 2000.

[40] J. Katz and A. Plotkin. *Low-Speed Aerodynamics, 2nd Edition*. Cambridge University Press, Cambridge, UK, 2001.

[41] D.F. Rogers. *Procedural Elements for Computer Graphics, second edition*. McGraw-Hill, New York, 1998.

[42] G. Thurmer and C. Wurthrich. Computing vertex normals from polygonal facets. *Journal of Graphics Tools*, 3(1):43–46, 1998.

[43] N. Max. Weights for computing vertex normals from facet normals. *Journal of Graphics Tools*, 4(2):1–6, 1999.

[44] M. Meyer, M. Desbrun, P. Schroder, and A.H. Barr. Discrete differential-geometry operators for triangulated 2-manifolds. In *Visualization and Mathematics*, volume 3, 2003.

[45] K. Atkinson and D. Chien. Piecewise polynomial collocation for boundary integral equations. *SIAM journal on Scientific Computing*, 16(3):651–681, May 1995.

[46] D. Dunavant. High degree efficient symmetrical gaussian quadrature rules for the triangle. *International Journal for Numerical Methods in Engineering*, 21:1129–1148, 1985.

[47] A.Z. Zinchenko, A. Rother, and R.H Davis. A novel boundary-integral algorithm for viscous flows. *Physics in Fluids*, 9(6):1493–1511, 1998.

[48] Y.L. Zhang, K.S. Yeo, B.C. Khoo, and C. Wang. 3d jet impact and toroidal bubbles. *Journal of Computational Physics*, 166:336–360, 2001.

[49] E.W. Weisstein. Geodesic dome. MathWorld–A Wolfram web resource. http://mathworld.wolfram.com/GeodesicDome.html.

[50] Q. Du, M.D. Gunzburger, and L. Ju. Voronoi-based finite volume methods, optimal Voronoi meshes, and PDEs on the sphere. *Computer methods in applied mechanics and engineering*, 192:3933–3957, 2003.

[51] E.W. Weisstein. Icosahedron. MathWorld–A Wolfram web resource. http://mathworld.wolfram.com/Icosahedron.html.

[52] G. Taubin. Estimating the tensor of curvature of a surface from a polyhedral approximation. In *ICCV Proceedings of the Fifth International Conference on Computer Vision*, pages 902–907. IEEE Computer Society, 1995.

[53] T. Langer, A. Belyaev, and H.P. Seidel. Exact and approximate quadratures for curvature tensor estimation. In M. Desbrun and H. Pottmann, editors, *Third Eurographics Symposium on Geometry Processing (Poster Proceedings)*, pages 14–15, Vienna, Austria, July 2005. Eurographics.

[54] S.G. Chen and J.Y. Wu. Estimating normal vectors and curvatures by centroid weight. *Computer Aided Geometric Design*, 21(5):447–458, 2004.

[55] Greg Burns, Raja Daoud, and James Vaigl. LAM: An Open Cluster Environment for MPI. In *Proceedings of Supercomputing Symposium*, pages 379–386, 1994.

[56] Jeffrey M. Squyres and Andrew Lumsdaine. A Component Architecture for LAM/MPI. In *Proceedings, 10th European PVM/MPI Users' Group Meeting*, number 2840 in Lecture Notes in Computer Science, pages 379–387, Venice, Italy, September / October 2003. Springer-Verlag.

[57] L. S. Blackford, J. Choi, A. Cleary, E. D'Azevedo, J. Demmel, I. Dhillon, J. Dongarra, S. Hammarling, G. Henry, A. Petitet, K. Stanley, D. Walker, and R. C. Whaley. *ScaLAPACK Users' Guide*. Society for Industrial and Applied Mathematics, Philadelphia, PA, 1997.

Chapter 4

Geometry and Initial Tests

4.1 Surface and Curvature Approximation

The Boundary Element Method used for our bubble simulation is node-centric, meaning the solution matrix is assembled from each node's influence on every other node in the mesh. Since we are comparing the results using linear, quadratic and cubic elements, we construct meshes resulting in the same size solution matrix for all elements. This allows comparisons between the different elements with similar, although not identical, computational cost. Recall from (3.65) that for a given order of elements L, the number of elements are $M_L = 20 \times f_L^2$ and the number of nodes are $N_L = (20 \times (f_L \times L)^2)/2 + 2$, where f_L is the frequency of subdivision. Thus, in order to achieve the same number of nodes, we use the relation $f_1 = 2f_2 = 3f_3$, leading to the choice of meshes seen in Table 4.1.

#	Nodes	Linear elements	Quadratic elements	Cubic elements
1	362	720	180	80
2	1442	2880	720	320
3	3242	6480	1620	720
4	5762	11520	2880	1280

Table 4.1: Number of elements used for different element orders

Having decided upon the mesh sizes used, it is important to discover the quality of approximation of geometric variables on the mesh, as the accuracy of the simulation may be significantly lowered by poor approximation of the vertex normals or curvature of the bubble surface. Tables 4.2 and 4.3 show the volume error ϵV, the root mean square (RMS) error of the surface normals ϵN_{rms} and maximum $\max|\epsilon N|$ errors of the surface normals. The RMS $\epsilon\kappa_{\text{rms}}$ and maximum $\max|\epsilon\kappa|$ curvature errors on a sphere are calculated using (3.67), while curvature errors for curvature calculated using (3.69) are marked with an asterix. As expected the piecewise quadratic mesh provides considerable improvements over the linear mesh.

The results for equispaced cubic elements and Gauss-Lobatto spaced cubic elements are shown in Tables 4.4 and 4.5. The cubic results show regression for vertex normals and curvature for both types of meshes and the Gauss-Lobatto spaced elements does not yield the expected improvements.

#	ϵV	ϵN_{rms}	$\max\|\epsilon N\|$	$\epsilon\kappa_{\text{rms}}$	$\max\|\epsilon\kappa\|$
1	6.388e-2	4.618e-3	7.071e-3	4.681e-3	7.861e-3
2	1.610e-2	1.397e-3	2.123e-3	1.568e-3	3.134e-3
3	7.168e-3	6.657e-4	9.569e-4	7.420e-4	1.551e-3
4	4.034e-3	3.380e-4	5.388e-4	4.259e-4	9.110e-4

Table 4.2: Error in geometric variables on a sphere, linear elements

#	ϵV	ϵN_{rms}	$\max\|\epsilon N\|$	$\epsilon\kappa_{\text{rms}}$	$\max\|\epsilon\kappa\|$	$\epsilon\kappa^*_{\text{rms}}$	$\max\|\epsilon\kappa^*\|$
1	1.899e-3	3.331e-4	7.832e-4	1.613e-4	3.767e-4	2.503e-4	4.437e-4
2	1.221e-4	3.121e-5	5.525e-5	1.464e-5	3.597e-5	6.175e-5	1.636e-4
3	2.424e-5	6.886e-6	1.162e-5	3.478e-6	8.798e-6	2.225e-5	8.083e-5
4	7.684e-6	2.302e-6	3.702e-6	1.323e-6	4.955e-6	1.052e-5	4.571e-5

Table 4.3: Error in geometric variables on a sphere, quadratic elements

#	ϵV	ϵN_{rms}	$\max\lvert\epsilon N\rvert$	$\epsilon\kappa_{\text{rms}}$	$\max\lvert\epsilon\kappa\rvert$	$\epsilon\kappa^*_{\text{rms}}$	$\max\lvert\epsilon\kappa^*\rvert$
1	3.187e-4	7.434e-4	1.061e-3	6.317e-4	9.436e-4	5.888e-3	1.420e-2
2	2.381e-5	8.486e-5	1.254e-4	1.569e-4	2.401e-4	1.441e-3	3.985e-3
3	4.867e-6	2.401e-5	3.584e-5	6.782e-5	9.592e-5	6.484e-4	1.986e-3
4	1.558e-6	9.843e-6	1.427e-5	3.760e-5	5.313e-5	3.678e-4	1.111e-3

Table 4.4: Error in geometric variables on a sphere, equispaced cubic elements

#	ϵV	ϵN_{rms}	$\max\lvert\epsilon N\rvert$	$\epsilon\kappa_{\text{rms}}$	$\max\lvert\epsilon\kappa\rvert$	$\epsilon\kappa^*_{\text{rms}}$	$\max\lvert\epsilon\kappa^*\rvert$
1	1.715e-4	8.140e-4	1.142e-3	4.700e-4	6.392e-4	5.994e-3	1.422e-2
2	1.396e-5	9.627e-5	1.405e-4	1.177e-4	1.724e-4	1.509e-3	3.984e-3
3	2.883e-6	2.778e-5	3.994e-5	5.321e-5	7.881e-5	6.824e-4	1.982e-3
4	9.211e-7	1.152e-5	1.673e-5	3.068e-5	4.565e-5	3.875e-4	1.111e-3

Table 4.5: Error in geometric variables on a sphere, Gauss-Lobatto spaced cubic elements

A possible reason for the poor performance of the cubic methods may be strong sensitivity to nodal placement when using polynomial surface patches. Consider the division of the edge of a cubic triangle, as shown in Figure 4.1, where the angles from the body centroid to the edge nodes are all initially α, leading to edge lengths m and l. If the middle angle is perturbed by $2h$, the change in the interpolation quality can be quite substantial as can be seen in Table 4.6. It may well be that the optimum position is achieved when $-0.00005 < h < 0.0001$, although even if a small perturbation was applied to improve the interpolation, it would be hard to keep the nodal points in a cubic mesh at the optimum locations when simulating a deforming body. It may be possible that the elastic mesh technique developed by Wang *et al* [1], may be extended, using suitable weights, for this purpose.

In order to better evaluate the results we try to evaluate the convergence of the different meshes. For a given order of discretisation k, we expect the

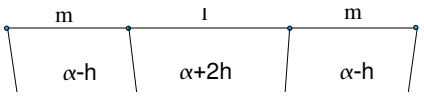

Figure 4.1: Division of triangle edge

h	ϵV	ϵN_{rms}	$\max \lvert\epsilon N\rvert$	$\epsilon\kappa_{\text{rms}}$	$\max \lvert\epsilon\kappa\rvert$	$\epsilon\kappa^*_{\text{rms}}$	$\max \lvert\epsilon\kappa^*\rvert$
1.0e-4	1.257e-5	5.478e-5	7.534e-5	2.389e-4	3.282e-4	1.660e-3	4.676e-3
0	4.867e-6	2.401e-5	3.584e-5	6.782e-5	9.592e-5	6.484e-4	1.986e-3
-5.0e-5	1.014e-6	1.196e-5	2.486e-5	2.751e-5	4.882e-5	2.098e-4	6.429e-4
-6.0e-5	2.433e-7	1.117e-5	2.443e-5	1.730e-5	4.066e-5	1.759e-4	5.669e-4
-7.5e-5	9.128e-7	1.173e-5	2.503e-5	1.968e-5	7.254e-5	2.248e-4	9.482e-4
-1.0e-4	2.840e-6	1.634e-5	2.900e-5	5.100e-5	1.257e-4	4.331e-4	1.633e-3

Table 4.6: 3242 nodes, equispaced cubic elements, sensitivity to h

interpolation error to be related to the mesh spacing δs by [2]

$$\epsilon_k \propto (\delta s)^{k+1}. \tag{4.1}$$

The plots in Figures 4.2 and 4.3 show the convergence rates of the meshes with the expected convergence given by the slope of the solid lines. The linear mesh converges as expected, with the slope of the curves for all geometric variables becoming parallel to the $(\delta s)^2$ line for small δs. The quadratic mesh converges approximately as expected and the cubic meshes shows expected convergence for volume, but sub-optimal convergence for vertex normals, leading to poor convergence for both types of curvature approximation.

Overall the curvature approximation from (3.67) is quick and gives reasonable accuracy for linear and quadratic meshes and will thus be used for the bubble simulations. For cubic meshes, the results are less convincing, so a different approach may yield better curvature approximations, although it seems likely that the dominating factor is the sensitivity to mesh spacing. Since no measurements will be taken to keep the nodes at optimum positions,

the cubic method may thus perform worse than the quadratic method for our simulations.

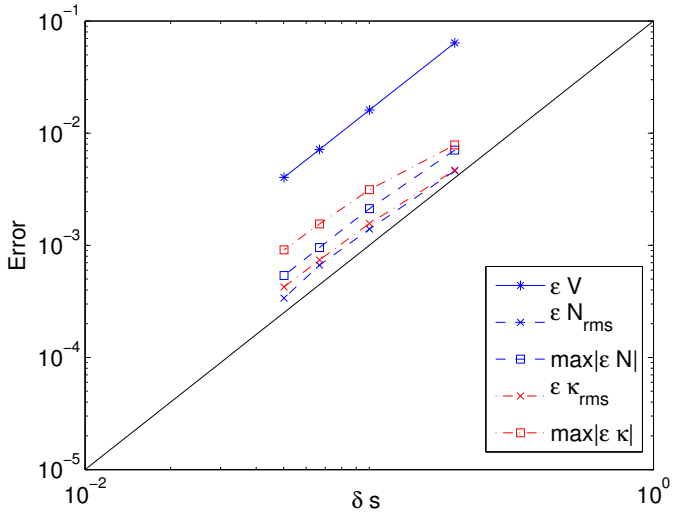

(a) Linear Elements

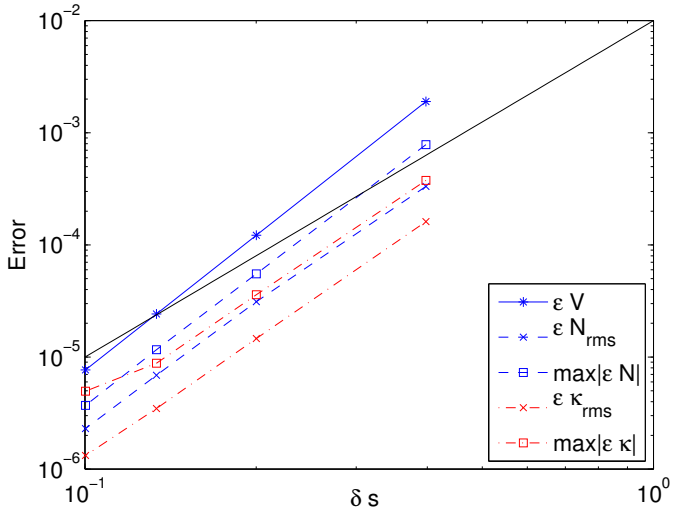

(b) Quadratic Elements

Figure 4.2: Comparison of Geometric Variables on a Sphere

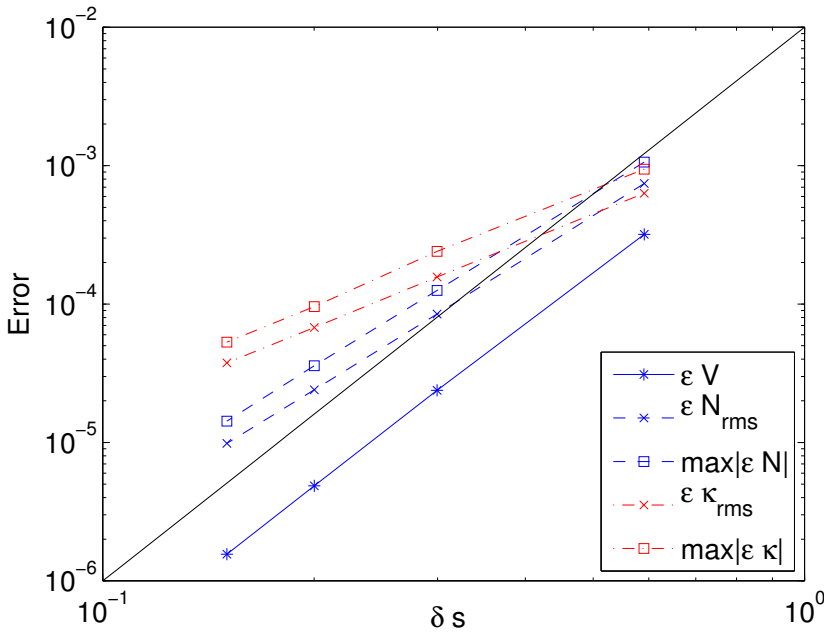

(a) Equispaced Cubic Elements

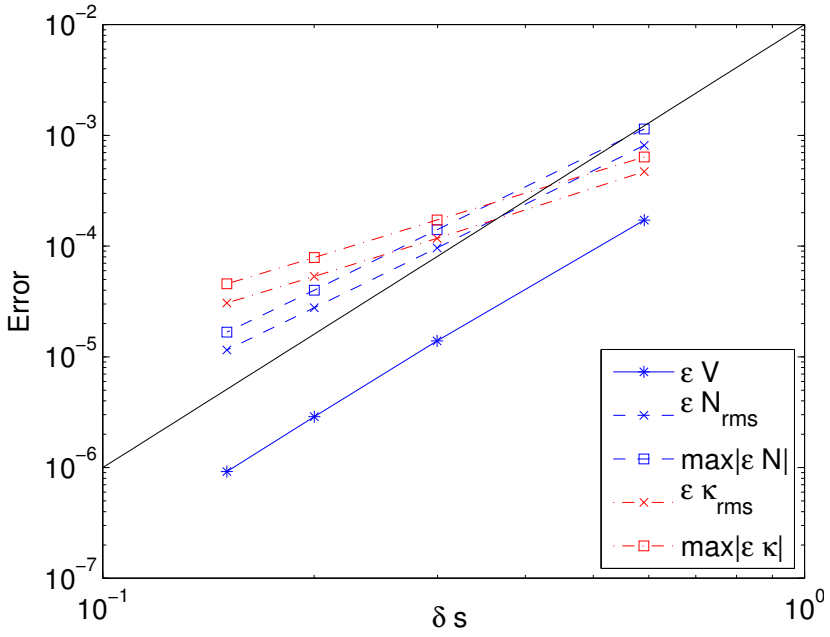

(b) Gauss-Lobatto-spaced Cubic Elements

Figure 4.3: Comparison of Geometric Variables on a Sphere

4.2 Integration Tests

As discussed in Section 3.4 the accurate resolution of surface integrals is of utmost importance to the stability and accuracy of the IBEM solution. First, we distinguish between three types of integrals; the singular integrals, the nearly singular integrals and the non-singular integrals. The singular integrals are those for which the evaluation point is on the triangle over which the integral is performed, while the nearly singular integrals are integrals over neighbouring triangles. The latter integrals, while not singular themselves, may still be ill-behaved due to the proximity of a singularity, yet no special treatment is performed for them. Thus, as will be shown, they may require a higher order of integration than the non-singular integrals. It should be noted that for N nodes, the number of singular and near-singular integrals are on the order $O(N)$, while the total number of integrals is of order $O(N^2)$. Thus, the integration order of singular and nearly singular integrals have a much smaller impact on the overall performance of the simulation than the remaining integrals for meshes with a large number of surface nodes.

In order to determine which integration orders to use for bubble simulation problems we first test the effect of integration orders on simple time-independent problems. The first test used is a simple integration test for Cauchy principal value integrals used by Guiggiani [3]. In Guiggiani's test a surface integral is performed over a square ($-1 \leq x \leq 1, -1 \leq y \leq 1$). The square is divided into four planar quadrilaterals joining at node $\mathbf{P} = (0.6, 0.)$, where the integral is singular. In this work, we focus on triangular elements, and set up the integration region as shown on Figure 4.4(a) for all types of elements. In addition we test the impact of integration order when the singular node coincides with an edge node with the configurations shown in Figures 4.4(b) and 4.4(c) for quadratic and cubic elements respectively.

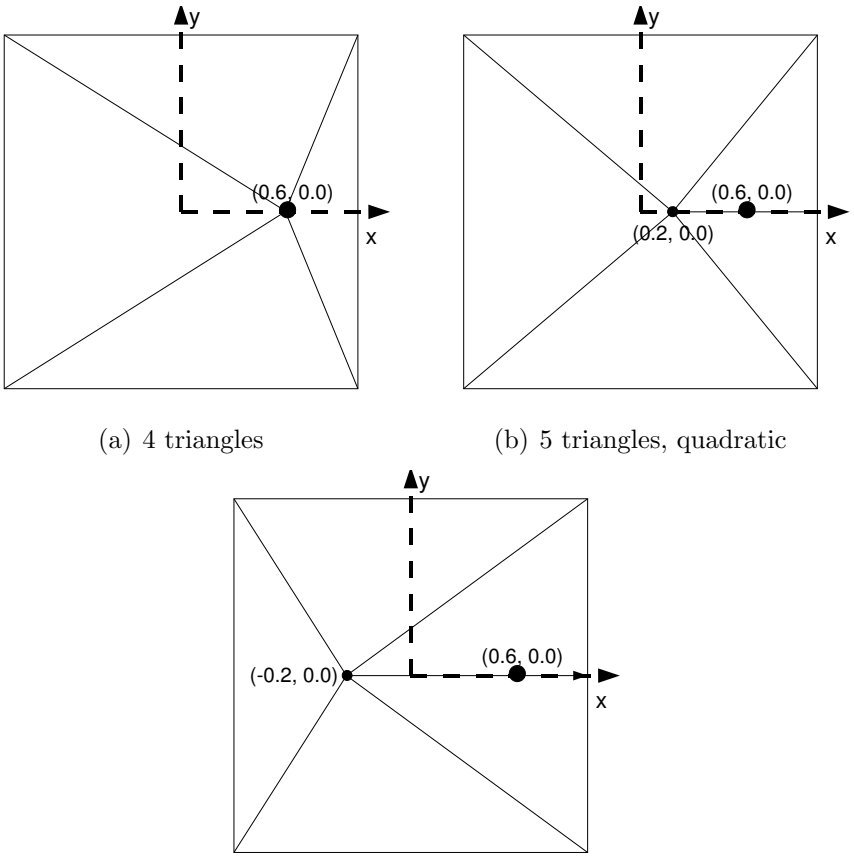

(a) 4 triangles

(b) 5 triangles, quadratic

(c) 5 triangles, cubic

Figure 4.4: Simple integration test: domain configuration

The strongly singular integral

$$I = \int_{-1}^{1}\int_{-1}^{1} \frac{x - 0.6}{\sqrt{(x-0.6)^2 + y^2}}\, dxdy \tag{4.2}$$

is evaluated as a sum of the per-triangle integrals and compared with the analytical solution of $I_a = -2.114175$ [3]. As can be seen in Table 4.7, the results with an integration order of $(4\times10)\times6$ matches the analytical solution to the seven digit accuracy provided.

Similarly the integration results for quadratic and cubic elements are shown in Tables 4.8 and 4.9. Since the integration region consists of the same flat square for all types of elements, the results are as expected very close for all types of elements with all integrations converging on ≈ -2.114174921.

Gaussian integration order	Solution
$(2 \times 6) \times 6$	-2.11352856660604
$(2 \times 10) \times 6$	-2.11417634784550
$(2 \times 10) \times 10$	-2.11417634784553
$(4 \times 10) \times 6$	-2.11417492119853
$(4 \times 10) \times 10$	-2.11417492119856
$(6 \times 10) \times (2 \times 10)$	-2.11417492117833

Table 4.7: Simple integration test: linear triangles

Gaussian integration order	Solution	
	4 elements	5 elements
$(2 \times 6) \times 6$	-2.11352856660602	-2.11079782671073
$(2 \times 10) \times 6$	-2.11417634784547	-2.11416463566382
$(2 \times 10) \times 10$	-2.11417634784552	-2.11416060188496
$(4 \times 10) \times 6$	-2.11417492119851	-2.11417895059133
$(4 \times 10) \times 10$	-2.11417492119854	-2.11417491637987
$(4 \times 10) \times (2 \times 10)$	-2.11417492119853	-2.11417491806418
$(6 \times 10) \times (2 \times 10)$	-2.11417492117821	-2.11417492116371
$(6 \times 10) \times (4 \times 10)$	-2.11417492117817	-2.11417492116305

Table 4.8: Simple integration test, quadratic triangles

It can be seen that the 5 element configurations for quadratic and cubic elements require a slightly higher integration order, something which is likely to be due to the singularity coinciding with a mid-edge node.

Gaussian integration order	Solution	
	4 elements	5 elements
$(2 \times 6) \times 6$	-2.11352856660599	-2.11626716444152
$(2 \times 10) \times 6$	-2.11417634784546	-2.11415785576971
$(2 \times 10) \times 10$	-2.11417634784556	-2.11416020550547
$(4 \times 10) \times 6$	-2.11417492119850	-2.11417257156823
$(4 \times 10) \times 10$	-2.11417492119859	-2.11417491620116
$(4 \times 10) \times (2 \times 10)$	-2.11417492119809	-2.11417491706396
$(6 \times 10) \times (2 \times 10)$	-2.11417492117782	-2.11417492104648
$(6 \times 10) \times (4 \times 10)$	-2.11417492117793	-2.11417492104666

Table 4.9: Simple integration test, cubic triangles

4.3 Flow Past a Solid Sphere

Obviously, integration on a flat square is insufficient to determine the required order of accuracy for integration over curved panels, therefore we test the effects of the integration order on a simulation of flow past a solid sphere, a problem with a known analytical solution. An oncoming flow of $\mathbf{U} = [0, 0, -1]$ is disturbed by the presence of a sphere of unit radius centered at the origin. The analytic velocity potential at any point $\mathbf{P}$ in spherical coordinates (ρ, θ, ϕ) is then [4]

$$\Phi(\mathbf{P}(\rho, \theta, \phi)) = -\cos\theta \left(\rho + \frac{R^3}{2\rho^2}\right). \tag{4.3}$$

The distance from origin ρ can be expressed as

$$\rho = \sqrt{x^2 + y^2 + z^2} \tag{4.4}$$

and

$$\cos\theta = \frac{z}{\rho}. \tag{4.5}$$

Thus, assuming $R = 1$, we can rewrite (4.3) in cartesian coordinates as

$$\Phi(\mathbf{P}(x,y,z)) = -z\left(1 + \frac{1}{2}\left\{\frac{1}{\sqrt{x^2+y^2+z^2}}\right\}^3\right) \tag{4.6}$$

giving velocity components

$$\begin{aligned} v_x &= \frac{\partial\Phi}{\partial x} = \frac{3zx}{2(x^2+y^2+z^2)^{5/2}} \\ v_y &= \frac{\partial\Phi}{\partial y} = \frac{3zy}{2(x^2+y^2+z^2)^{5/2}} \\ v_z &= \frac{\partial\Phi}{\partial y} = \frac{3z^2}{2(x^2+y^2+z^2)^{5/2}} - \frac{1}{2(x^2+y^2+z^2)^{3/2}} - 1 \end{aligned} \tag{4.7}$$

We impose the analytical velocity potential as surface boundary conditions to the IBEM and compare the surface velocities calculated with the IBEM to those from (4.7). This allows us to assess how well the method approximates the surface velocity from a set of known surface potentials, which is exactly what the IBEM will do in the case of bubble simulations. For several reasons we can not expect the surface errors to show smooth convergence towards particular numbers as the integration orders are increased. The conditioning of the solution matrix for BEMs is typically poor (see Section 4.4) and a small change in the matrix elements can lead to large changes in the solution. Also the integration is reliant on interpolation and some orders of integration may use sample points which are interpolated better than others with the base functions of the elements. Ideally the integration should reuse the element nodes as integration points, something which would be interesting to explore in the future. Given these issues, we are satisfied when results can not be substantially improved upon by increasing the order of integration. The first tests uses the singular integration orders $(4 \times 10) \times 6$ suggested by the simple integration tests, while changing the order of near-singular and non-singular integrals. The results when using linear elements, as seen in Table 4.10 suggest that increasing the integration orders beyond 12 and 6 for near-singular and non-singular integrals respectively, provides little improvement

in surface errors despite considerably increasing the computational cost. The rows marked with an asterix increases the singular integration order to $(6 \times 10) \times (4 \times 10)$, without providing much additional accuracy.

For quadratic elements we assume that the required integration order is at least as large as for linear elements, and Table 4.11 suggest that while increasing the integration orders beyond 25 and 12 for near-singular and non-singular integrals respectively may reduce the minimum velocity error, little improvement is had in the RMS and maximum errors. The rows marked with an asterix, as previously, employs integration orders of $(6 \times 10) \times (4 \times 10)$ for singular integrals without providing any substantial increase in accuracy.

3242 nodes					
Near-sing.	Non-sing.	RMS	Max.	Min.	t (s)
6	6	5.40770e-2	8.95477e-2	1.28987e-5	5.4
12	6	5.40808e-2	8.95538e-2	1.21307e-5	5.5
12	12	5.40808e-2	8.95538e-2	1.21273e-5	9.4
25	6	5.40808e-2	8.95537e-2	1.21852e-5	5.5
25	12	5.40808e-2	8.95537e-2	1.21819e-5	9.6
* 12	6	5.40808e-2	8.95538e-2	1.21307e-5	5.5
5276 nodes					
Near-sing.	Non-sing.	RMS	Max.	Min.	t(s)
6	6	4.39816e-2	7.28832e-2	5.64651e-5	13.5
12	6	4.39844e-2	7.28878e-2	5.10149e-5	13.6
12	12	4.39844e-2	7.28878e-2	5.09855e-5	24.1
12	6	4.39844e-2	7.28878e-2	5.13999e-5	13.7
25	12	4.39844e-2	7.28878e-2	5.13698e-5	24.2
*12	6	4.39844e-2	7.28878e-2	5.10149e-5	13.7

Table 4.10: Flow past a sphere: linear elements, absolute errors

3242 nodes					
Near-sing.	Non-sing.	RMS	Max.	Min.	t (s)
12	6	1.41737e-4	4.07648e-4	5.28750e-6	5.17
12	12	1.43127e-4	3.97444e-4	7.88717e-6	8.55
25	6	1.49525e-4	2.67626e-4	1.01007e-6	5.18
25	12	1.33980e-4	2.68766e-4	4.96243e-7	8.87
* 25	12	1.33980e-4	2.68766e-4	4.96249e-7	13.66
25	25	1.34580e-4	2.68716e-4	5.36365e-7	16.70
(2×10)×10	25	1.34533e-4	2.68467e-4	4.63780e-8	17.74
(2×10)×10	(2×10)×10	1.34475e-4	2.68379e-4	2.87143e-8	243.64
*(6×10)×(4×10)	(2×10)×10	1.34460e-4	2.68470e-4	1.24938e-8	263.05
5276 nodes					
Near-sing.	Non-sing.	RMS	Max.	Min.	t(s)
12	6	7.98908e-5	4.16678e-4	2.06474e-6	11.94
12	12	9.08843e-5	4.40876e-4	5.41630e-6	21.54
25	6	8.42566e-5	1.98931e-4	9.48154e-7	11.95
25	12	6.32137e-5	1.27245e-4	1.42742e-7	21.54
* 25	12	6.32136e-5	1.27245e-4	1.42769e-7	28.61
25	25	6.38276e-5	1.27245e-4	2.23440e-8	43.41
$(2 \times 10) \times 10$	25	6.37719e-5	1.27346e-4	5.50809e-9	44.58
$(2 \times 10) \times 10$	$(2 \times 10) \times 10$	6.37135e-5	1.27319e-4	8.86765e-9	631.80
*(6×10)×(4×10)	(2×10)×10	6.36959e-5	1.27313e-4	1.16373e-8	675.76

Table 4.11: Flow past a sphere: quadratic elements. Effect of integration orders, absolute errors

For the cubic integration tests we assume that the integration orders required will be at least as high as with the quadratic method and the results in Tables 4.12 and 4.13 show, as expected, that higher integration orders are required for cubic elements. As previously the rows marked with an asterix uses an integration order of $(6 \times 10) \times (4 \times 10)$ for singular integrals. The results suggest that repeated Gaussian quadrature does not make sense

Near-sing.	Non-sing.	RMS	Max.	Min.	t(s)
25	12	9.15674e-5	6.58048e-4	1.68981e-6	10.60
25	25	9.06708e-5	6.60126e-4	1.49081e-6	20.21
48	12	4.51633e-5	1.87034e-4	2.83203e-7	11.78
48	25	4.41411e-5	1.80653e-4	1.04804e-8	21.57
48	48	4.41470e-5	1.80685e-4	6.77983e-9	38.18
79	25	4.45885e-5	1.80085e-4	2.67252e-8	21.72
*79	25	4.45863e-5	1.80107e-4	1.69549e-8	31.25
*79	48	4.45920e-5	1.80139e-4	2.00760e-8	47.89
$(2 \times 10) \times 10$	25	4.38937e-5	1.76791e-4	4.48917e-7	22.95
$(2 \times 10) \times 10$	48	4.38914e-5	1.76779e-4	5.66000e-7	40.48
$(2 \times 10) \times 10$	$(2 \times 10) \times 10$	4.55378e-5	1.95121e-4	3.26643e-7	299.31
*$(2 \times 10) \times 10$	25	4.38918e-5	1.76814e-4	5.75950e-7	33.37
*$(2 \times 10) \times 10$	$(2 \times 10) \times 10$	4.55346e-5	1.95144e-4	3.41582e-7	303.27
$(6\times10)\times(4\times10)$	25	4.46157e-5	1.80132e-4	3.30288e-8	58.17
$(6\times10)\times(4\times10)$	$(4\times10)\times(2\times10)$	4.46216e-5	1.80245e-4	3.22973e-8	1187.26

Table 4.12: Flow past a sphere: cubic equispaced elements. Effect of integration orders, absolute errors, 3242 nodes.

for non-singular integrals and that integration orders of 48 for near-singular integrals and 25 for non-singular integrals is sufficient Although a decrease in minimum error can be achieved by increasing the singular integration order, there is very little improvement in RMS and maximum error. The results

from the Gauss-Lobatto based cubic elements are similar, yet more erratic as can be seen in Tables 4.14 and 4.15, although the integration orders of 48 and 25 seems like a good choice.

Near-sing.	Non-sing.	RMS	Max.	Min.	t(s)
25	12	8.49280e-5	6.66172e-4	1.38548e-6	26.37
25	25	8.42579e-5	6.63733e-4	1.22491e-6	50.60
48	12	2.17826e-5	9.42725e-5	2.06353e-7	27.38
48	25	2.06886e-5	8.80825e-5	2.00248e-8	51.94
48	48	2.06944e-5	8.81204e-5	1.76234e-8	97.48
79	25	2.08631e-5	8.74790e-5	1.03737e-8	52.97
*79	25	2.08607e-5	8.75056e-5	2.16507e-9	66.65
*79	48	2.08661e-5	8.75435e-5	3.46167e-9	110.24
$(2 \times 10) \times 10$	25	2.03026e-5	8.36489e-5	2.50459e-7	55.22
$(2 \times 10) \times 10$	48	2.03006e-5	8.36358e-5	2.50832e-7	99.54
$(2 \times 10) \times 10$	$(2 \times 10) \times 10$	2.27091e-5	1.02424e-4	2.18558e-7	756.79
*$(2 \times 10) \times 10$	25	2.03008e-5	8.36787e-5	2.61354e-7	68.95
*$(2 \times 10) \times 10$	$(2 \times 10) \times 10$	2.27066e-5	1.02452e-4	2.09936e-7	772.15
$(6\times10)\times(4\times10)$	25	2.08886e-5	8.75302e-5	1.40541e-8	103.60
$(6\times10)\times(4\times10)$	$(4\times10)\times(2\times10)$	2.08967e-5	8.76656e-4	6.48163e-9	3024.82

Table 4.13: Flow past a sphere: cubic equispaced elements. Effect of integration orders, absolute errors, 5762 nodes.

Near-sing.	Non-sing.	RMS	Max.	Min.	t(s)
25	12	1.85652e-4	1.01265e-3	4.26352e-7	12.71
25	25	1.85821e-4	1.01578e-3	1.61773e-7	23.80
48	12	5.02129e-5	1.69498e-4	4.22140e-8	12.72
48	25	4.93091e-5	1.63389e-4	4.99148e-8	23.82
48	48	4.93124e-5	1.63430e-4	5.01275e-8	43.51
79	25	5.01378e-5	1.66658e-4	3.69214e-8	24.27
*79	25	6.12772e-5	1.66940e-4	1.46383e-8	34.83
*79	48	6.12805e-5	1.66981e-4	1.63548e-8	54.87
$(2 \times 10) \times 10$	25	4.90295e-5	1.53115e-4	1.78784e-6	26.65
$(2 \times 10) \times 10$	48	4.90327e-5	1.53157e-4	1.79146e-6	46.21
$(2 \times 10) \times 10$	$(2 \times 10) \times 10$	5.71652e-5	2.14535e-5	6.33256e-7	309.17
$*(2 \times 10) \times 10$	25	6.05027e-5	1.53403e-4	2.36232e-6	36.85
$(6\times10)\times(4\times10)$	25	5.01583e-5	1.66800e-5	4.10024e-8	61.72
$(6\times10)\times(4\times10)$	$(4\times10)\times(2\times10)$	5.02338e-5	1.67375e-4	4.86733e-8	1347.93

Table 4.14: Flow past a sphere: cubic Gauss-Lobatto spaced elements. Effect of integration orders, absolute errors, 3242 nodes.

Near-sing.	Non-sing.	RMS	Max.	Min.	t(s)
25	12	1.71693e-4	1.00701e-3	8.19972e-7	30.07
25	25	1.68668e-4	1.00657e-3	5.75201e-8	58.34
48	12	2.54539e-5	8.21775e-5	2.45817e-7	29.79
48	25	2.48153e-5	8.16475e-5	2.90826e-8	58.24
48	48	2.47618e-5	8.11576e-5	3.47182e-8	108.04
79	25	2.44109e-5	8.06691e-5	4.25769e-8	58.50
*79	25	4.39144e-5	1.04034e-4	2.69461e-8	74.26
*79	48	4.34309e-5	1.02711e-4	3.21988e-9	127.53
$(2 \times 10) \times 10$	12	2.28132e-5	8.00721e-5	5.08812e-7	32.51
$(2 \times 10) \times 10$	25	2.24346e-5	7.70328e-5	1.63318e-7	61.51
$(2 \times 10) \times 10$	48	2.23670e-5	7.71760e-5	1.58381e-7	110.21
$(2 \times 10) \times 10$	$(2 \times 10) \times 10$	3.67860e-5	1.33821e-4	1.92949e-7	880.85
$*(2 \times 10) \times 10$	25	4.25690e-5	1.05925e-4	2.15503e-7	77.19
$(6\times10)\times(4\times10)$	25	2.44258e-5	8.08131e-5	4.50892e-8	85.97
$(6\times10)\times(4\times10)$	$(4\times10)\times(2\times10)$	2.44073e-5	8.16952e-5	9.78522e-9	3458.25

Table 4.15: Flow past a sphere: cubic Gauss-Lobatto spaced elements. Effect of integration orders, absolute errors, 5762 nodes.

4.4 Constant ϕ and Performance

Finally we consider a problem very similar to that of spherical bubble simulation, namely providing a uniform potential value of $\phi = 1.0$ across the surface of a spherical body centered on the origin. The potential is then expected to change only with the distance from the origin, making the velocity directly normal to the surface of the body, in this case $-1.0\,\mathbf{n}$, and we list surface velocity errors for a set of combinations of integration orders in Table 4.16 with the integration orders suggested by the flow past a sphere results marked with †. The results are similar to the results from the flow past a sphere problem and suggest that the chosen integration orders are suitable for bubble simulation problems. Using these integration orders we plot the convergence of the RMS error with respect to the number of surface nodes used in Figure 4.5, with "Cubic" referring to the equispaced cubic mesh and "Cubic GL" referring to the Gauss-Lobatto spaced cubic mehs. Expected convergence can be seen for linear and quadratic elements, while the cubic methods show quadratic convergence only. While curvature estimation is not involved in this test, vertex normal vector calculation is, and it is possible that the disappointing convergence for cubic elements is due to the sub-optimal convergence of surface normals previously seen.

Since the bubble simulation will consist of many iterations of a parallel boundary element solver run serially, this problem should give a good indication of the performance of the numerical method for bubble simulation problems. Figure 4.6 shows the performance of the quadratic IBEM[1], on a cluster of 2.2 GHz AMD Opterons, with up to $N_{\text{cpu}} = 32$ processors. The scaling beyond 4 processors is poor for 362 surface nodes, as the problem size is too small to see any added benefit of more processing nodes. For larger

[1]While only performance for the quadratic IBEM is presented, the basic scaling characteristics of the methods are the same

Singular	Near	Non	RMS	Max.	Min.
Quadratic					
$(2 \times 6) \times 6$	12	6	1.73193e-4	2.78373e-4	2.10137e-5
$\dagger(4 \times 10) \times 6$	25	12	1.54813e-4	2.11196e-4	4.02090e-5
$(6\times10)\times(4\times10)$	79	79	1.55240e-4	2.11174e-4	4.53259e-5
Cubic equispaced					
$(2 \times 6) \times 6$	25	12	5.83862e-4	1.36691e-3	2.14289e-4
$(4 \times 10) \times 6$	25	25	1.59777e-4	5.42470e-4	3.14305e-5
$(4 \times 10) \times 6$	48	25	5.06753e-5	1.48138e-4	5.47404e-6
$\dagger(4 \times 10) \times 6$	79	25	5.15230e-5	1.47684e-4	7.66402e-6
$(6\times10)\times(4\times10)$	79	79	5.15020e-5	1.47968e-4	7.51909e-6
$(6\times10)\times(4\times10)$	$(6\times10)\times(4\times10)$	79	5.14780e-5	1.48084e-4	7.39910e-5
Cubic Gauss-Lobatto spaced					
$(2 \times 6) \times 6$	25	12	1.04266e-3	2.35409e-3	3.55089e-4
$(4 \times 10) \times 6$	25	25	2.30146e-4	7.00110e-4	5.87058e-5
$(4 \times 10) \times 6$	48	25	6.03276e-5	1.34586e-4	5.40348e-7
$\dagger(4 \times 10) \times 6$	79	25	5.79785e-5	1.36794e-4	1.53374e-6
$(6\times10)\times(4\times10)$	79	79	7.08480e-5	1.37138e-4	1.82693e-5
$(6\times10)\times(4\times10)$	$(6\times10)\times(4\times10)$	79	7.08252e-5	1.36864e-4	1.75932e-5

Table 4.16: Surface error with a constant $\phi = 1.0$ on the surface, 3242 nodes

meshes, however, the method seems to scale almost linearly.

As can be seen in Figures 4.7 and 4.8 the two major parts of the cost is assembling and solving the solution matrix, while the "other" contributions consists of updating of nodes and vertex normals, curvature calculation and calculation of the spherical harmonics coefficients used in the next Chapter.

For N surface nodes, the assembly of the potential and velocity matrix has a total processing time of $4AN^2$ flops with a large constant multiplier A which reflects the operations involved in the surface integration. As noted in Section

3.7, the matrix assembly is embarrassingly parallel . This is not the case for the LU decomposition used through ScaLaPACK [5]. Solving the matrix with LU decomposition requires approximately $\frac{2}{3}N^3$ flops, and this operation does not scale linearly. With a small number of surface nodes, the matrix assembly is almost completely dominant and as we increase the number of surface nodes, the cubic scaling of the matrix solver starts becoming more important. However, at the surface resolutions and the number of CPUs used here, the matrix assembly is still over twice as costly as the matrix solver.

Finding the total computational time for bubble simulations, which are presented next, is a matter of multiplying the computational time for one time step by the number of time steps. This leads to a total of ≈ 2.5 hours for a 2000 step simulation using 362 nodes on one processor or approximately 4 days for a 10000 step simulation using 5762 nodes on 32 CPUs.

We present the condition numbers for the solution matrix for this problem as the inverse of the reciprocal condition number estimated by the LU-decomposition routine "pdgesvx" [5]. For a matrix A, the condition number is then defined as

$$c(A) = \frac{1}{c_{\text{pdgesvx}}(A)} = \frac{|\lambda_{\max}(A)|}{|\lambda_{\min}(A)|}, \tag{4.8}$$

where $\lambda_{\max}$ and $\lambda_{\min}$ are the largest and smallest eigenvalues of A respectively. As can be seen in Figure 4.9, the condition number for all elements seems to follow $O(\sqrt{N})$ for N surface nodes, or $O(\delta s^{-1})$, where δs is the mesh spacing, reaching 487.2 for $N = 5762$ on a piecewise quadratic mesh. Condition numbers are not typically presented in numerical bubble studies, although a study by Zhang *et al* [6] used a desingularised boundary element method from Cao *et al* [7], who reported condition numbers on the linear solver with $N = 231$ for a different test problem to be from $O(10^2)$ for little desingularisation, and up to $O(10^7)$ for the optimum amount of desingularisation and our condition numbers are, as expected, more comparible to the

former. Cao *et al* [7] found that the poor conditioning they observed, for optimum desingularisation, didn't necessarily lead to poor accuracy and the poor conditioning was more likely to simply increase the number of iterations needed for their iterative solver. The conditioning of the solution matrix for the IBEM presented here is not nearly as bad as that observed by Cao *et al*, and the accuracy of the linear solver should be further helped by the fact that "pdgesvx" performs iterative refinement.

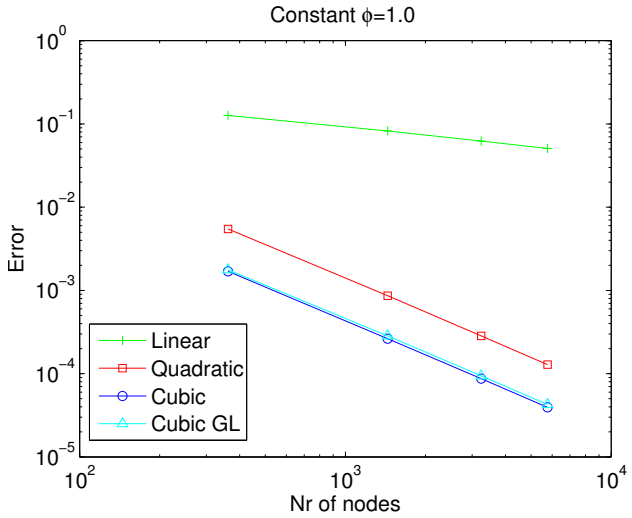

Figure 4.5: Absolute RMS errors, constant $\phi = 1.0$ over sphere of radius 1.0

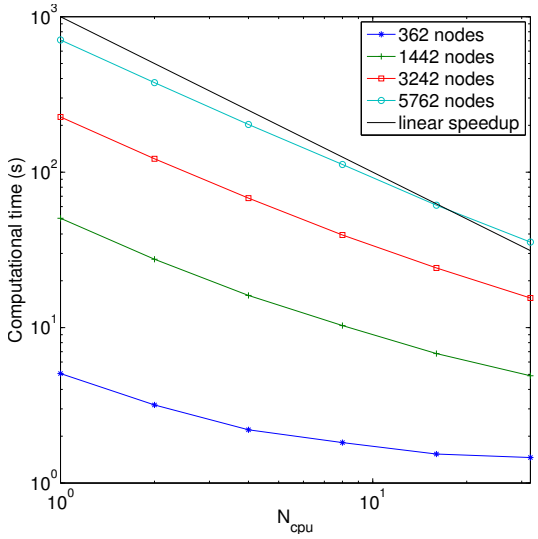

Figure 4.6: Parallel performance, constant $\phi = 1.0$ over sphere of radius 1.0

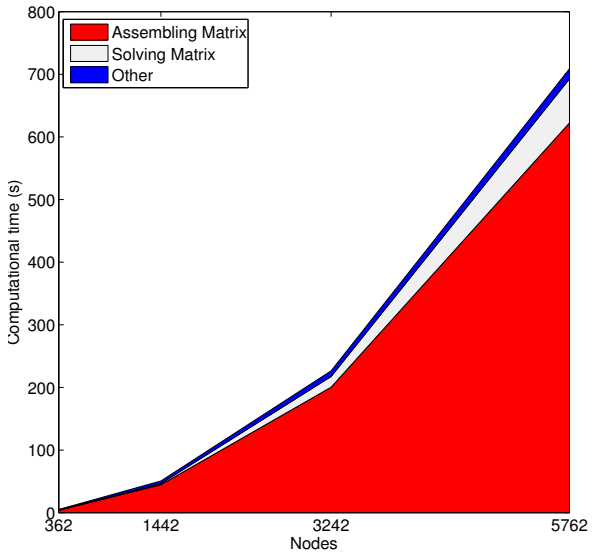

Figure 4.7: Breakdown of computational effort, 1 CPU

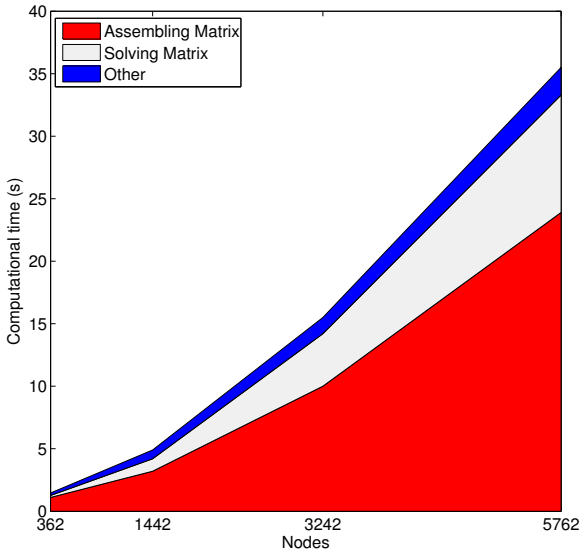

Figure 4.8: Breakdown of computational effort, 32 CPUs

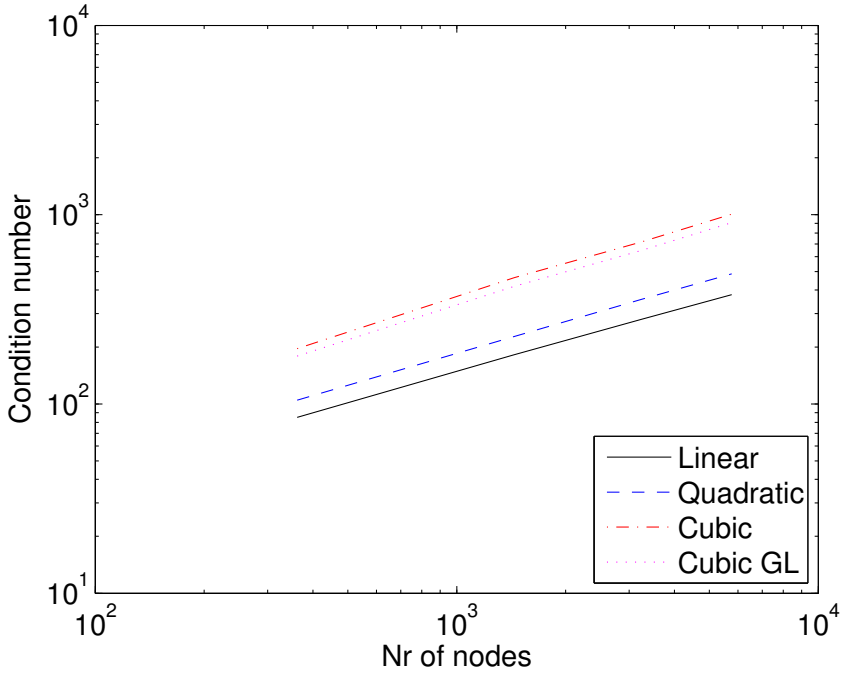

Figure 4.9: Condition numbers for solution matrix.

Bibliography

[1] C. Wang, B.C. Khoo, and K.S. Yeo. Elastic mesh technique for 3d bim simulation with an application to underwater explosion bubble dynamics. *Computers & Fluids*, 32:1195–1212, 2003.

[2] H. Kardestuncer and D.H Norrie. *Finite Element Handbook*. McGraw-Hill, US, 1987.

[3] M. Guiggiani. Singular integrals in B.E. methods: Formulation and numerical treatment of boundary integral equations with hypersingular kernels. In V. Sladek and J. Sladek, editors, *Singular Integrals in B.E. Methods*. Computational Mechanics Publications, 1998.

[4] J. Katz and A. Plotkin. *Low-Speed Aerodynamics, 2nd Edition*. Cambridge University Press, Cambridge, UK, 2001.

[5] L. S. Blackford, J. Choi, A. Cleary, E. D'Azevedo, J. Demmel, I. Dhillon, J. Dongarra, S. Hammarling, G. Henry, A. Petitet, K. Stanley, D. Walker, and R. C. Whaley. *ScaLAPACK Users' Guide*. Society for Industrial and Applied Mathematics, Philadelphia, PA, 1997.

[6] Y.L. Zhang, K.S Yeo, B.C. Khoo, and W.K. Chong. Simulation of three-dimensional bubbles using desingularized boundary integral method. *International Journal for Numerical Methods in Fluids*, 31:1311–1320, 1999.

[7] Y. Cao, W.W. Schultz, and R.F. Beck. Three-dimensional desingularized boundary integral methods for potential problems. *International Journal for Numerical Methods in Fluids*, 12:785–803, 1991.

Chapter 5

Bubble Simulation

5.1 Spherical Bubble Oscillation

Spherical bubble oscillation has been the subject of many studies throughout the last 50 years and provides a good way of validating the IBEM code against the well known Rayleigh-Plesset equation. The Rayleigh-Plesset equation, referred to as the "Rayleigh radius" in this text, is solved numerically with a fourth order Runge-Kutta scheme. We simulate an ideal gas bubble in an unbounded fluid with the following parameters, ignoring the effects of gravity

$$R_0^* = 40\mu\,\mathrm{m},\ \tau^* = 0.0725\,\mathrm{N\ m^{-1}},\ \rho^* = 998\,\mathrm{kg\ m^{-3}},$$
$$\lambda = 1.4,\ \ p_\infty^* = 1\times 10^5\,\mathrm{N\,m^{-2}}, \tag{5.1}$$

where R_0^* is the initial bubble radius, τ^* is the surface tension, ρ^* is the density of the liquid, λ is the ratio of specific heats and p_∞^* is the undisturbed pressure of the liquid. The asterix denotes dimensional variables, while the simulation is carried out in non-dimensional form through the following substitutions

$$R = \tfrac{R^*}{R_0^*}, \qquad p = \frac{p^*}{p_0^*}, \qquad \tau = \frac{\tau^*}{R_0^* p_\infty^*},$$
$$\mathbf{x} = \tfrac{\mathbf{x}^*}{R_0^*}, \quad \Phi = \left(\frac{\rho^*}{p_\infty^*(R_0^*)^2}\right)^{1/2}\Phi^*, \tag{5.2}$$
$$t = \left(\frac{p_\infty^*}{\rho^*(R_0^*)^2}\right)^{1/2} t^*, \quad \mathbf{v} = \left(\tfrac{\rho^*}{p_\infty^*}\right)^{1/2}\mathbf{v}^*,$$

where the subscript 0 denotes an initial value. This leads us to the non-dimensional form of the boundary conditions in (2.21)

$$\frac{d\Phi(\mathbf{P}_i)}{dt} = \frac{1}{2}|\mathbf{v}(\mathbf{P}_i)|^2 - \left(p_\infty - p_{B,0} \left\{ \frac{V^{(0)}}{V} \right\}^{3\gamma} \right) + 2\,\tau\,\kappa(\mathbf{P}_i). \tag{5.3}$$

The bubble pressure is set to equilibrum as

$$P_{B,0} = P_\infty + \frac{2\,\tau}{R_0} \tag{5.4}$$

and the bubble is then perturbed out of equilibrum by changing the initial radius by a value ϵR. This causes the bubble to oscillate spherically in a simple sinusoidal fashion between a maximum and minimum volume. As the mathematical model does not contain any energy dissipation the sum of potential and kinetic energy should, in the absence of numerical dissipation, remain constant during the oscillation, with potential energy defined as [1]

$$E_P = \tau A_B - V \left(\frac{P_{B,0}}{1-\gamma} \left[\frac{V_0}{V} \right]^\gamma - P_0 \right), \tag{5.5}$$

where A_B is the total surface area. Kinetic energy is then defined as [1]

$$E_K = -\frac{\rho}{2} \int_S \Phi \nabla\Phi \cdot \hat{\mathbf{n}}\, dS \tag{5.6}$$

the sum $E = E_P + E_K$ should remain constant during the oscillation and the oscillation should proceed for an infinite amount of time as long as no numerical error is introduced in the simulation. Since we present results using numerical simulation, however, some change in total energy will be found and the simulation will eventually break down due to the growth of numerical error.

Our first test is a radial perturbation $\epsilon R = 1\mu m$, leading to simple volume oscillation seen in Figures 5.1(a), 5.2(a), 5.3(a) and 5.4(a) for linear, quadratic and cubic elements respectively. All methods show good agreement with the Rayleigh radius, with only the coarsest method showing visible deviation towards the end of the simulation. It can be seen in Figures

5.1(b), 5.2(b), 5.3(b) and 5.4(b) that all meshes show slight oscillation of $\Delta E = \frac{E(t)-E(0)}{E(0)}$ although on the finer meshes with quadratic and cubic elements, these oscillations are bounded with amplitudes of order 10^{-7} or less.

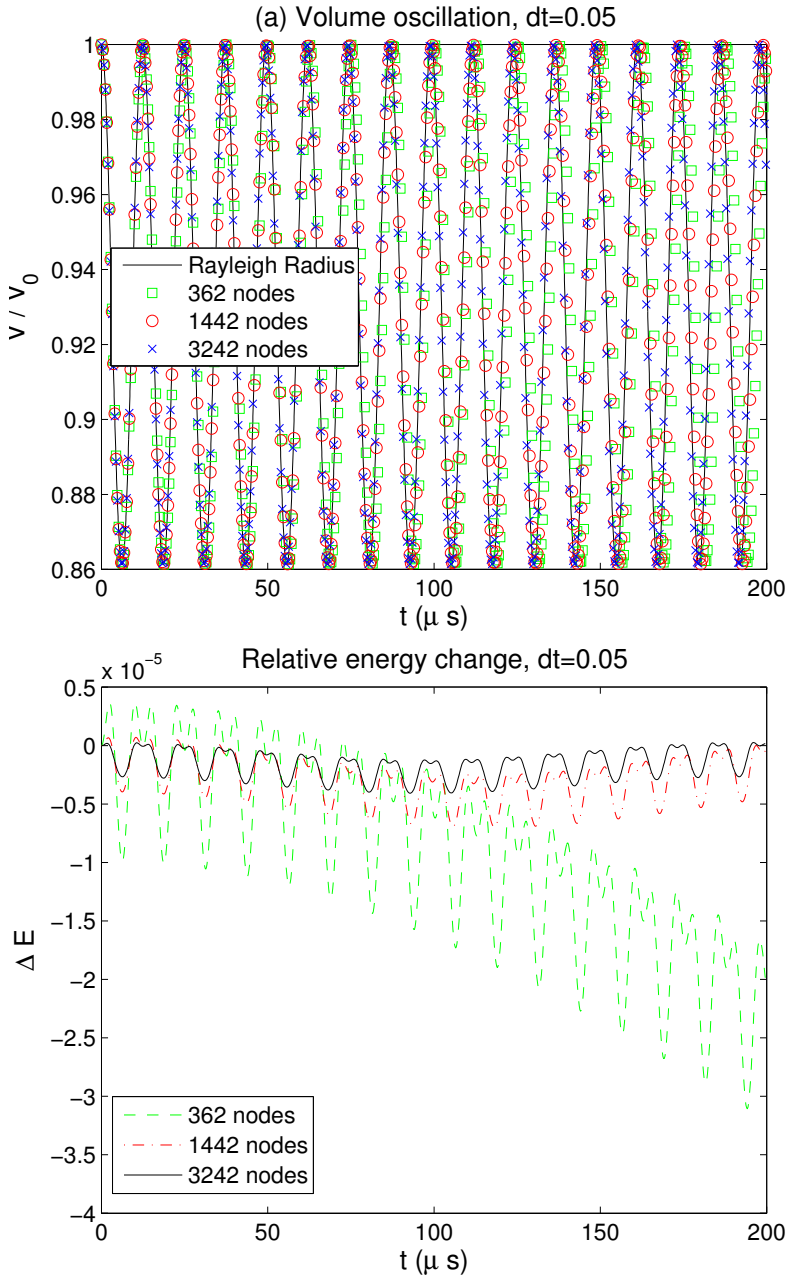

Figure 5.1: Volume oscillation, $\epsilon R = 1\mu m$, linear elements

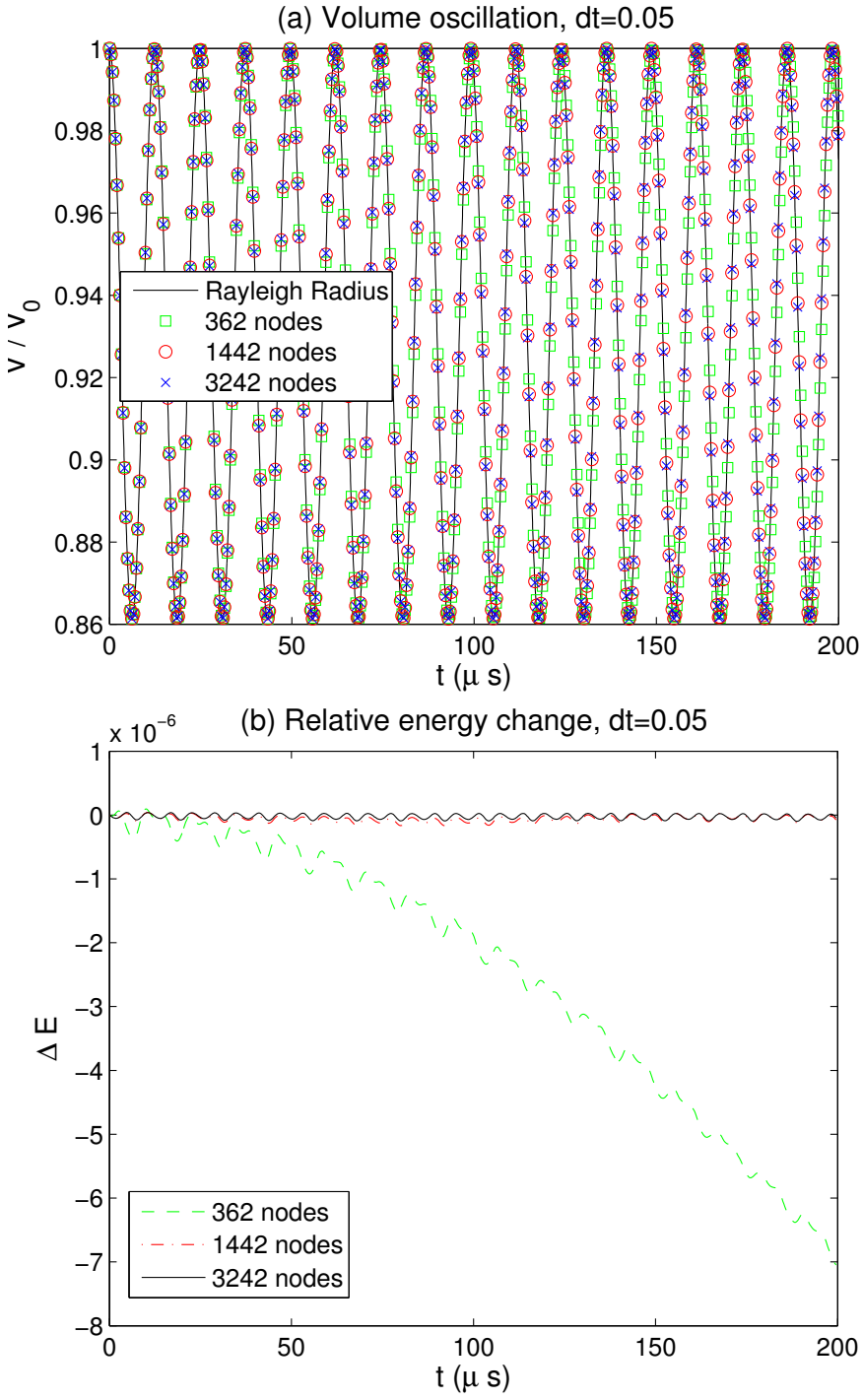

Figure 5.2: Volume oscillation, $\epsilon R = 1\mu m$, quadratic elements

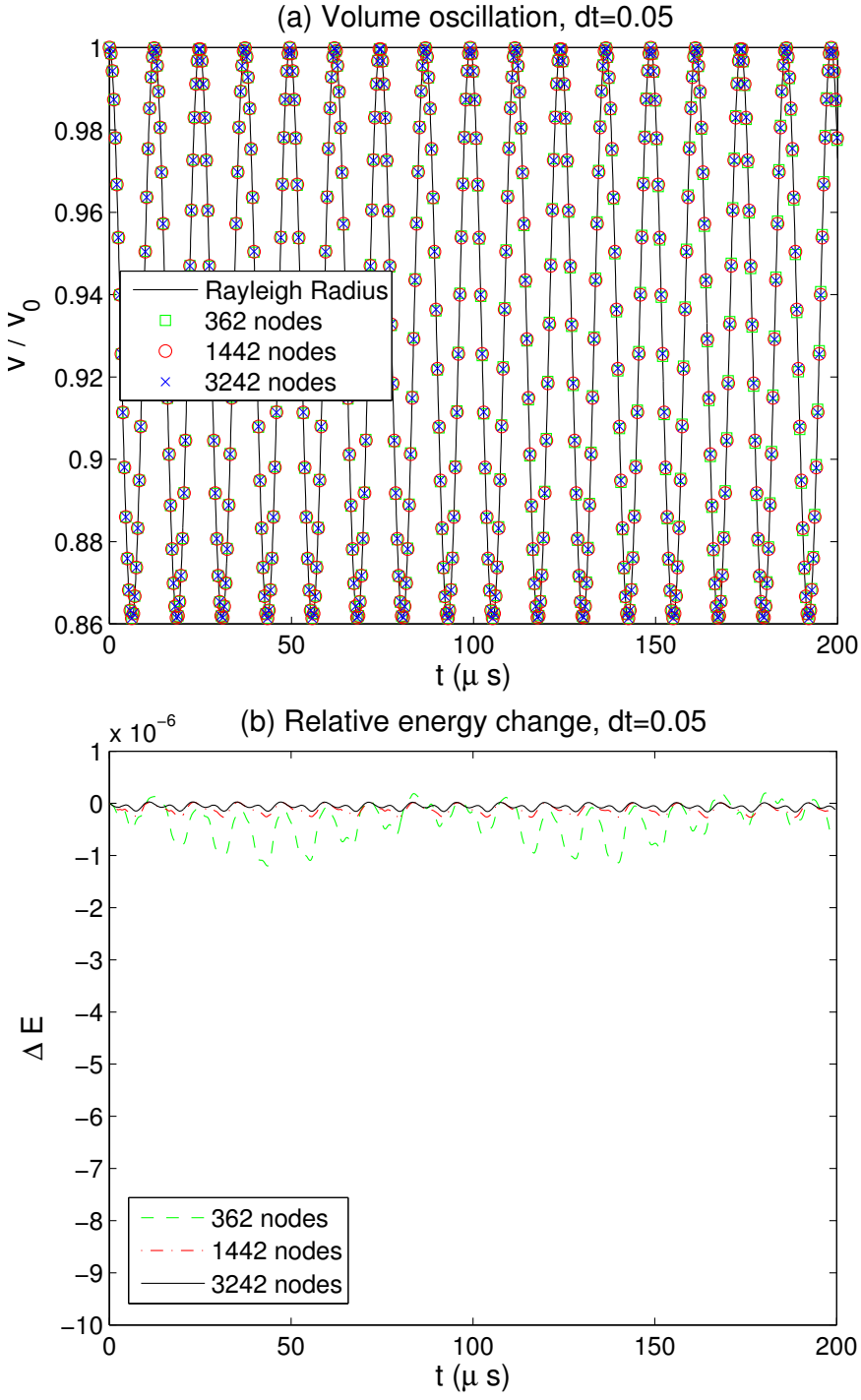

Figure 5.3: Volume oscillation, $\epsilon R = 1\mu m$, equispaced cubic elements

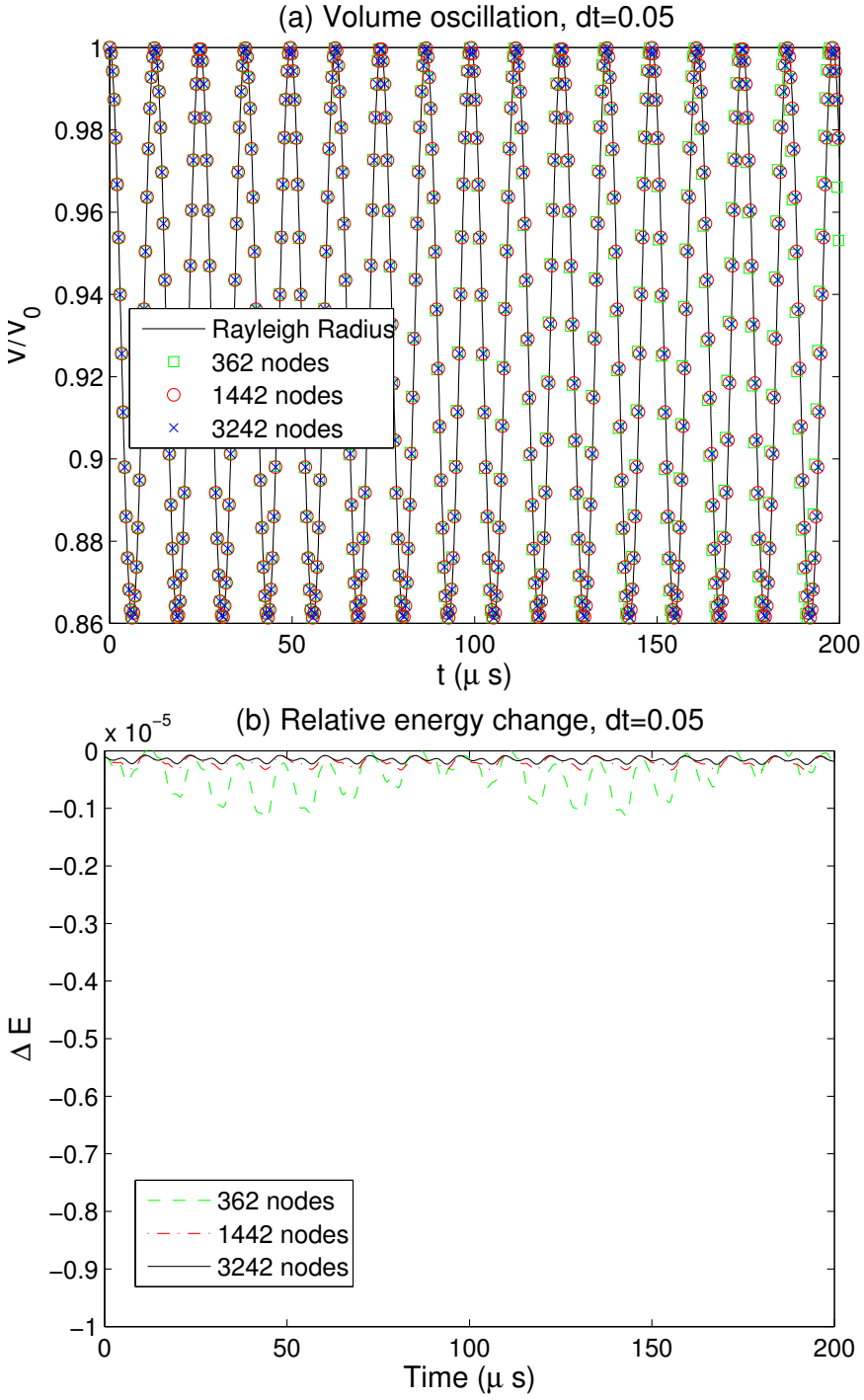

Figure 5.4: Volume oscillation, $\epsilon R = 1\mu m$, Gauss-Lobatto-spaced cubic elements

Figure 5.5 shows the level of distortion from the spherical shape through the simulation using 1442 and 3242 surface nodes. Since none of the meshes produce a perfect sphere, some level of shape oscillations are expected through the simulation. However, the simulations appear stable in the sense that the distortions are bounded, with the exception of the 1442 node cubic meshes for which unbounded growth can be seen towards the end of the simulation. Also the level of distortions produced by the linear mesh may be so high as to dominate physical shape mode oscillations.

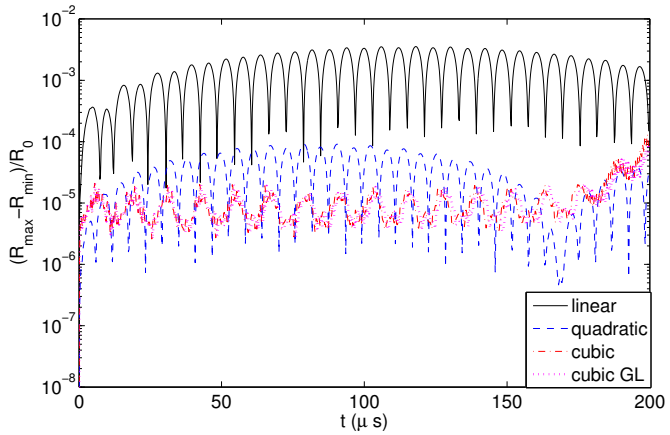

(a) 1442 nodes

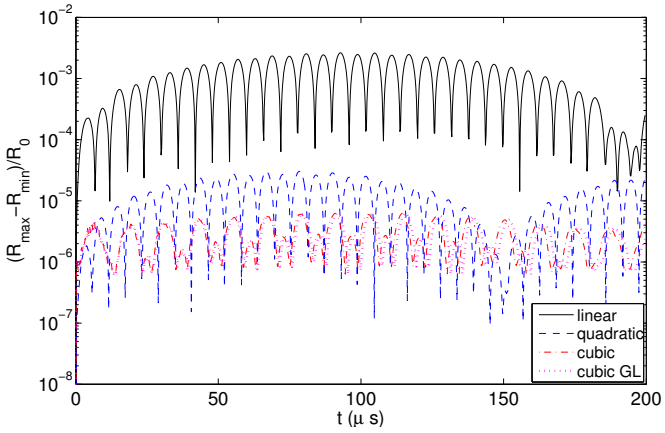

(b) 3242 nodes

Figure 5.5: Volume oscillation: distortion from spherical shape

Order	Linear elements	Quadratic elements	Cubic elements
low	$(2 \times 6) \times 6, 6, 6$	$(2 \times 10) \times 6, 12, 6$	$(2 \times 10) \times 6, 25, 12$
standard	$(4 \times 10) \times 6, 12, 6$	$(4 \times 10) \times 6, 25, 12$	$(4 \times 10) \times 6, 48, 25$
high	$(6 \times 10) \times 10, 25, 12$	$(6 \times 10) \times 10, 48, 25$	$(6 \times 10) \times (2 \times 10), 79, 48$

Table 5.1: Integration orders for various element orders

The simulations depicted in Figures 5.1 to 5.4 are all performed with the *standard* integration orders suggested in Section 4.3. Introducing the notation of $\{$*singular*, *near-singular*, *non-singular*$\}$, the suggested integration orders were $\{(4 \times 10) \times 6, 12, 6\}$, $\{(4 \times 10) \times 6, 25, 12\}$ and $\{(4 \times 10) \times 6, 48, 25\}$ for linear, quadratic and cubic elements respectively. To illustrate the importance of chosing acceptable integration orders we perform a Rayleigh radius simulation with 1442 surface nodes for $\epsilon R = 4.0\mu$m using three different sets of integration orders listed in Table 5.1 compared with a numerical solution of the Rayleigh radius equation.

The results when using the low integration orders are shown in Figure 5.6. The simulations break down early, showing considerable energy fluctuation, suggesting high numerical error. Increasing the integration orders to the standard level reduces the energy fluctuation and allows the simulation to proceed further for quadratic and cubic elements, while the linear mesh shows little change. This suggests that other factors reduce the stability using the linear mesh. As seen in Figure 5.8(b), increasing the integration orders to the highest listed in Table 5.1, has little or no effect on accuracy or energy change suggesting that standard integration order is sufficient.

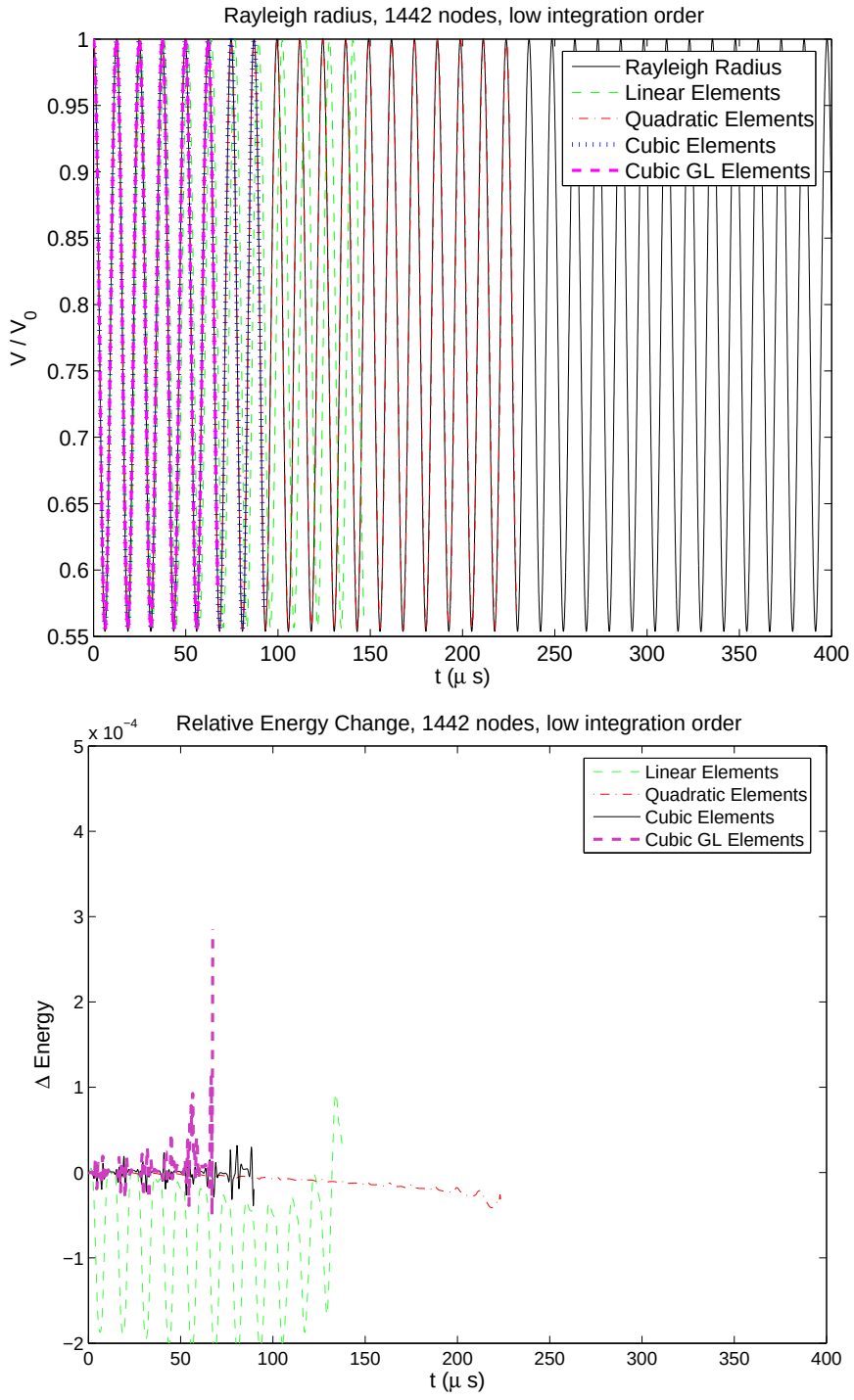

Figure 5.6: Volume oscillation: Integration test, low order, $\epsilon R = 4\mu m$

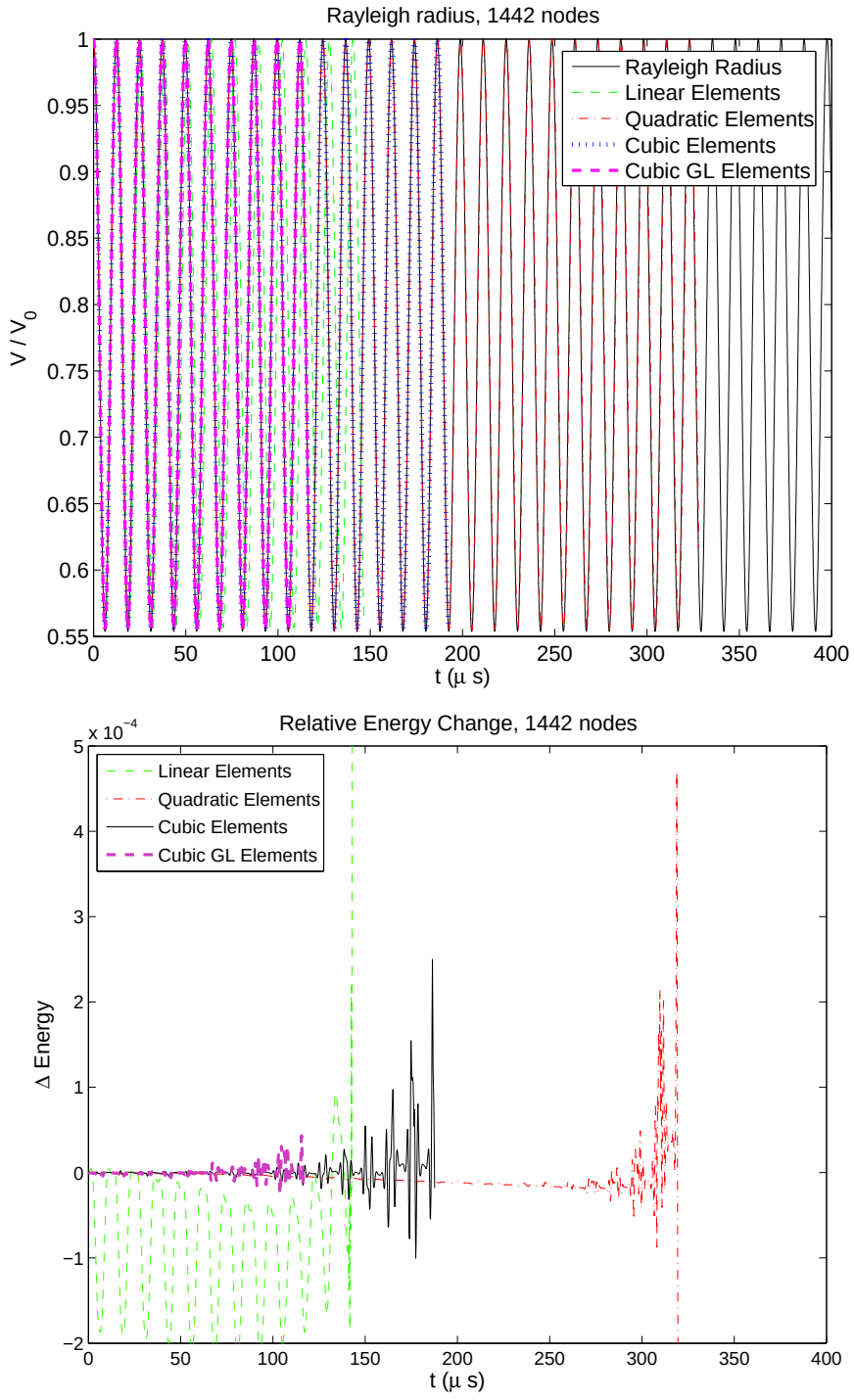

Figure 5.7: Volume oscillation: Integration test, standard order, $\epsilon R = 4\mu m$

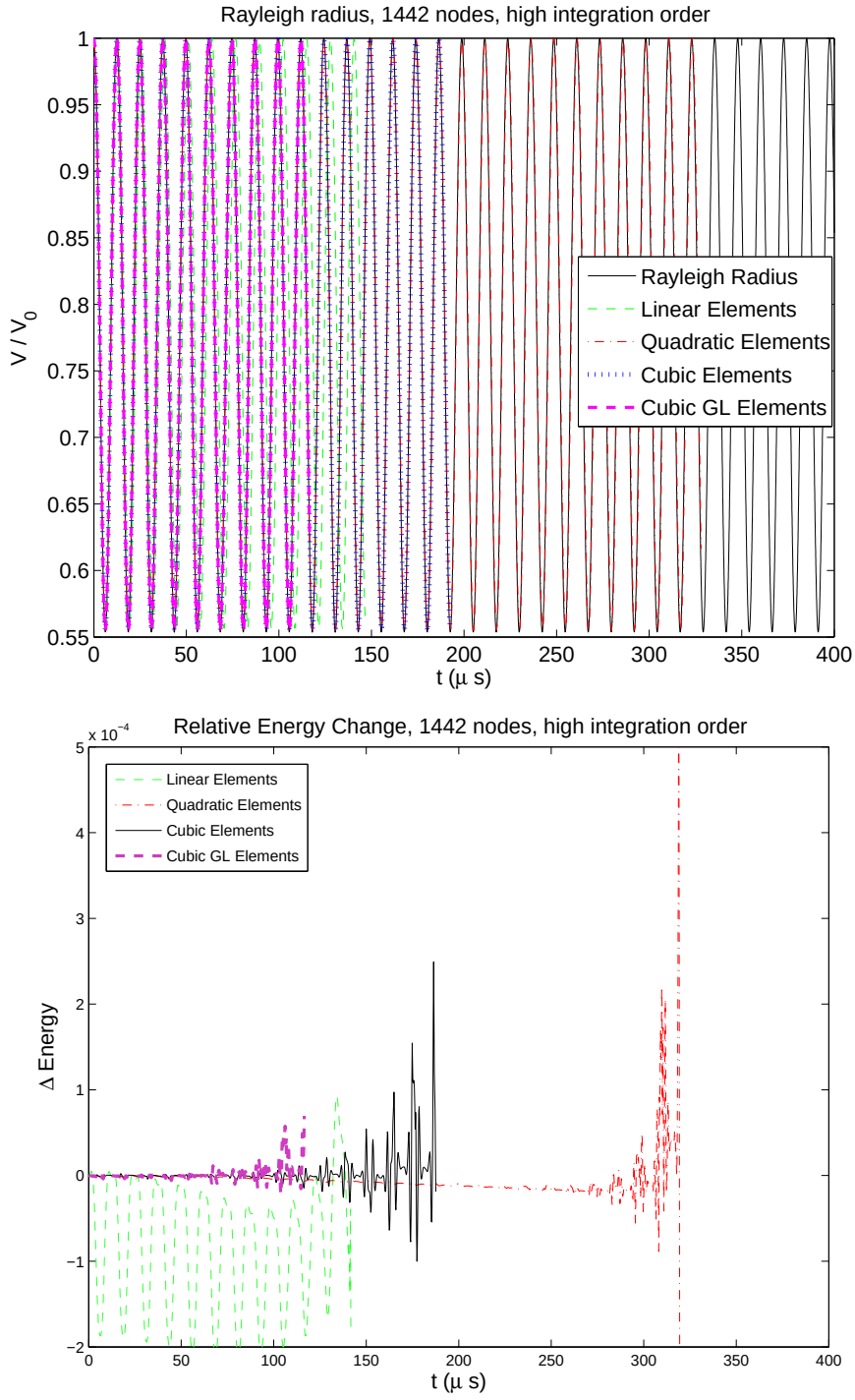

Figure 5.8: Volume oscillation: Integration test, high order, $\epsilon R = 4\mu m$

5.2 Shape Oscillations Through Initial Distortion of Shape

Having seen how the IBEM copes with spherical oscillations, we move on to simulate oscillations of shape. Any star-shaped body can be expressed as an infinite sum of spherical harmonics, which are orthogonal solutions to Laplace's equation [2, 3]

$$S(\theta, \varphi, t) = \sum_{l=0}^{\infty} \sum_{m=-l}^{l} \hat{a}_l^m(t) Y_l^m(\theta, \varphi), \tag{5.7}$$

where the spherical harmonics Y_l^m are defined as

$$Y_l^m(\theta, \varphi) = \sqrt{\frac{2l+1}{4\pi} \frac{(l-m)!}{(l+m)!}} P_l^m(\cos\theta) e^{im\varphi}, \tag{5.8}$$

and P_l^m are associated Legendre polynomials [4]. The coefficients a_l^m can be found by surface integration

$$\hat{a}_l^m(t) = \int_0^{2\pi} \int_0^{\pi} r(\theta, \varphi) Y_l^m(\theta, \varphi) \sin\theta \, d\varphi \, d\theta, \tag{5.9}$$

and by exploiting the relation with the complex conjugate $\overline{Y}$, the number of surface integrations needed can be almost halved

$$Y_l^{-m}(\theta, \varphi) = (-1)^m \overline{Y}_l^m(\theta, \varphi). \tag{5.10}$$

In practise, the infinite sum in (5.7) is replaced with a finite sum up to $l_{\max}$. The integrations are carried out with 25 point triangular Gaussian integration over all M triangles in the surface mesh leading to a total number of surface integrations of order $O(l_{\max}^2 \times M)$.

The mode Y_0^0 is spherical and is usually referred to as the *volume mode* or the *breathing mode*, while mode Y_1^0 is a displacement along the z-axis. When $l > 0$ and $m = 0$, the spherical harmonics do not have an imaginary component, and depend only on the polar coordinate θ, making them axisymmetric.

The axisymmetric spherical harmonics up to $l = 6$ are listed in (5.11) below. As l is increased, the harmonics modes take on increasingly complex shapes with sharper variations, meaning a finer surface mesh is required to differentiate between them.

$$\begin{aligned} Y_0^0(\theta,\varphi) &= \frac{1}{2}\frac{1}{\sqrt{\pi}} \\ Y_1^0(\theta,\varphi) &= \frac{1}{2}\sqrt{\frac{3}{\pi}}\cos\theta \\ Y_2^0(\theta,\varphi) &= \frac{1}{4}\sqrt{\frac{5}{\pi}}(3\cos^2\theta - 1) \\ Y_3^0(\theta,\varphi) &= \frac{1}{4}\sqrt{\frac{7}{\pi}}(5\cos^3\theta - 3\cos\theta) \\ Y_4^0(\theta,\varphi) &= \frac{3}{16\sqrt{\pi}}(35\cos^4\theta - 30\cos^2\theta + 3) \end{aligned} \tag{5.11}$$

When $m \neq 0$ the harmonics have a dependency on both θ and φ making the shape non-axisymmetric. The first few non-axisymmetric harmonics are

$$\begin{aligned} Y_2^1(\theta,\varphi) &= \frac{1}{24}\sqrt{\frac{30}{\pi}}(3\cos^2\theta - 1)e^{i\varphi} \\ Y_2^2(\theta,\varphi) &= \frac{1}{48}\sqrt{\frac{30}{\pi}}(3\cos^2\theta - 1)e^{2i\varphi} \\ Y_3^1(\theta,\varphi) &= \frac{1}{24}\sqrt{\frac{21}{\pi}}\cos\theta(5\cos^2\theta - 3)e^{i\varphi} \\ Y_3^2(\theta,\varphi) &= \frac{1}{240}\sqrt{\frac{210}{\pi}}\cos\theta(5\cos^2\theta - 3)e^{2i\varphi} \\ Y_3^3(\theta,\varphi) &= \frac{1}{240}\sqrt{\frac{35}{\pi}}\cos\theta(5\cos^2\theta - 3)e^{3i\varphi}. \end{aligned} \tag{5.12}$$

As can be seen, the non-axisymmetric harmonics are now complex. However, due to Euler's formula $e^{i\varphi} = \cos(\varphi) + i\sin(\varphi)$, the real and imaginary components can be calculated seperately. We will focus on distortions to the real component of the coefficients. However it will be demonstrated that distortions to a mode $Y_l^{m\neq 0}$ may lead to oscillations of the other modes with the same l. Due to (5.10), which links the real component of modes $m > 0$ to the imaginary components of modes $m < 0$ and vice versa, it may not

be too surprising that it seems possible for distortions to real components to lead to oscillations of the imaginary components.

Since all harmonics with even values of l contains positive powers of $\cos\theta$ only, there exists a plane for which the mode is reflection symmetric around, and the bubble centroid should thus remain stationary during oscillations of these modes. This is not the case for odd values of l, where asymmetry may lead to translation of the bubble. Consider for example an oscillation between $\epsilon a_3 = \pm s$, which would have different bubble centroids for the two extremas $+s$ and $-s$. For this reason we seperate between *even* and *odd* mode shape oscillations.

When the bubble is given an initial perturbation $\epsilon \hat{a}_l^m$, the perturbed mode is expected to oscillate in a simple cosine fashion with a frequency of F_l, which is independent of the azimuthal wave number m [5, 6],

$$F_0 = \frac{1}{2\pi}\sqrt{\frac{\tau}{R_0^3\rho}\left(3\kappa\left[\frac{P_\infty}{\tau/R_0}+2\right]-2\right)}, \tag{5.13}$$

$$F_l = \frac{1}{2\pi}\sqrt{\frac{\tau}{R_0^3\rho}(l+1)(l-1)(l+2)}, \quad l \neq 0. \tag{5.14}$$

For most of the previous work on shape oscillations, an axisymmetric model has been used [1, 5, 7], something which can be justified since oscillations of the axisymmetric modes Y_l^0 are not expected to excite the non-axisymmetric modes $Y_l^{m\neq 0}$. However, care has to be taken under resonance conditions for which frequencies match up to yield energy exchange between different modes, as under certain conditions it has been shown that even purely spherical oscillations may result in the onset of shape oscillations [5]. It is thus not automatically given that an axisymmetric model is well suited even if the initial conditions are axisymmetric.

5.2.1 Small Amplitude Axisymmetric Oscillation

We first test the three dimensional IBEM against the axisymmetric perturbation approach of Shaw [1]. Note that in Shaw's work the scaling factor in

(5.8) is omitted and for comparison we will use

$$a_l^0(t) = \left(\frac{2l+1}{4\pi}\right)^{-1/2} \hat{a}_l^0(t), \tag{5.15}$$

starting with an initial deformation of $\epsilon a_2^0 = 1\mu m$. With the parameters listed in (5.1) the natural frequency of mode a_2^0 is $F_2 \approx 18.57\,\text{kHz}$ giving an expected period of oscillation of $\approx 53.84\mu s$. The simulations are carried out with linear, quadratic, equispaced cubic and Gauss-Lobatto spaced cubic elements with 362, 1442 and 3242 surface nodes and a non-dimensional time step of 0.05 for the meshes with 362 and 1442 nodes and 0.01 for the finest meshes. For clarity we introduce the parameter $A(t) = a(t) - a(0)$.

The linear IBEM results (Figure 5.9) shows considerable deviation from Shaw's results for all modes, with only the finest mesh approaching the accuracy of the higher order methods. When using 3242 nodes, the simulation breaks down before one full oscillation cycle of a_2^0 has been completed. The quadratic IBEM (Figure 5.10) show good convergence towards Shaw's results, with mode 0, 2 and 4 being particularly well represented using 1442 and 3242 nodes. The finest mesh still causes the simulation to break down before completion, although not until almost four and a half oscillation cycles of a_2^0 has been completed. Figures 5.11 and 5.12 show that both cubic methods are less accurate and less stable than the quadratic method, something which may be related to the suboptimal accuracy of the vertex normals on the cubic elements already seen in Table 4.4.

Note that none of these methods show any improvement when decreasing the non-dimensional step size to 0.005 or 0.001, suggesting that smoothing may be required to improve the stability of the methods, something which will be explored further in Section 5.2.3 and onwards.

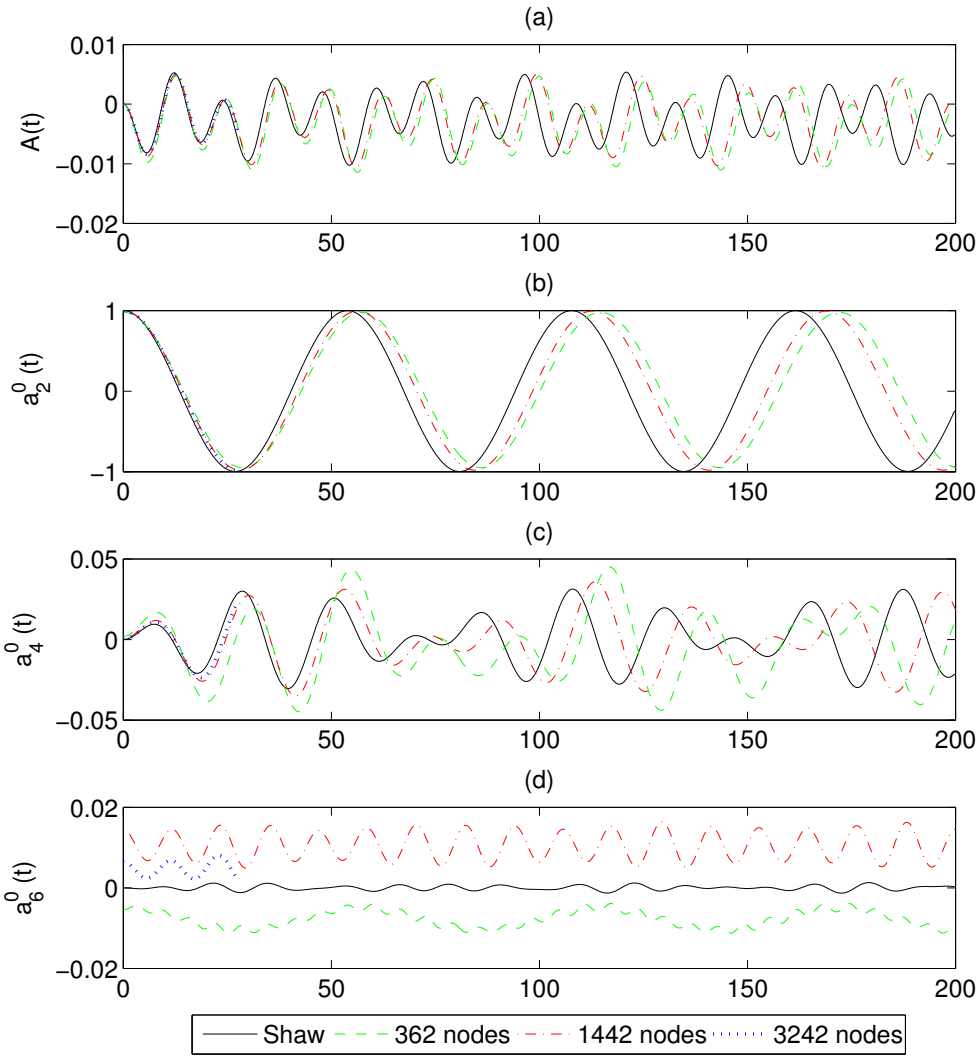

Figure 5.9: Harmonics oscillations, $\epsilon a_2^0 = 1\mu m$, linear elements, horizontal axes in μs, vertical axes in μm.

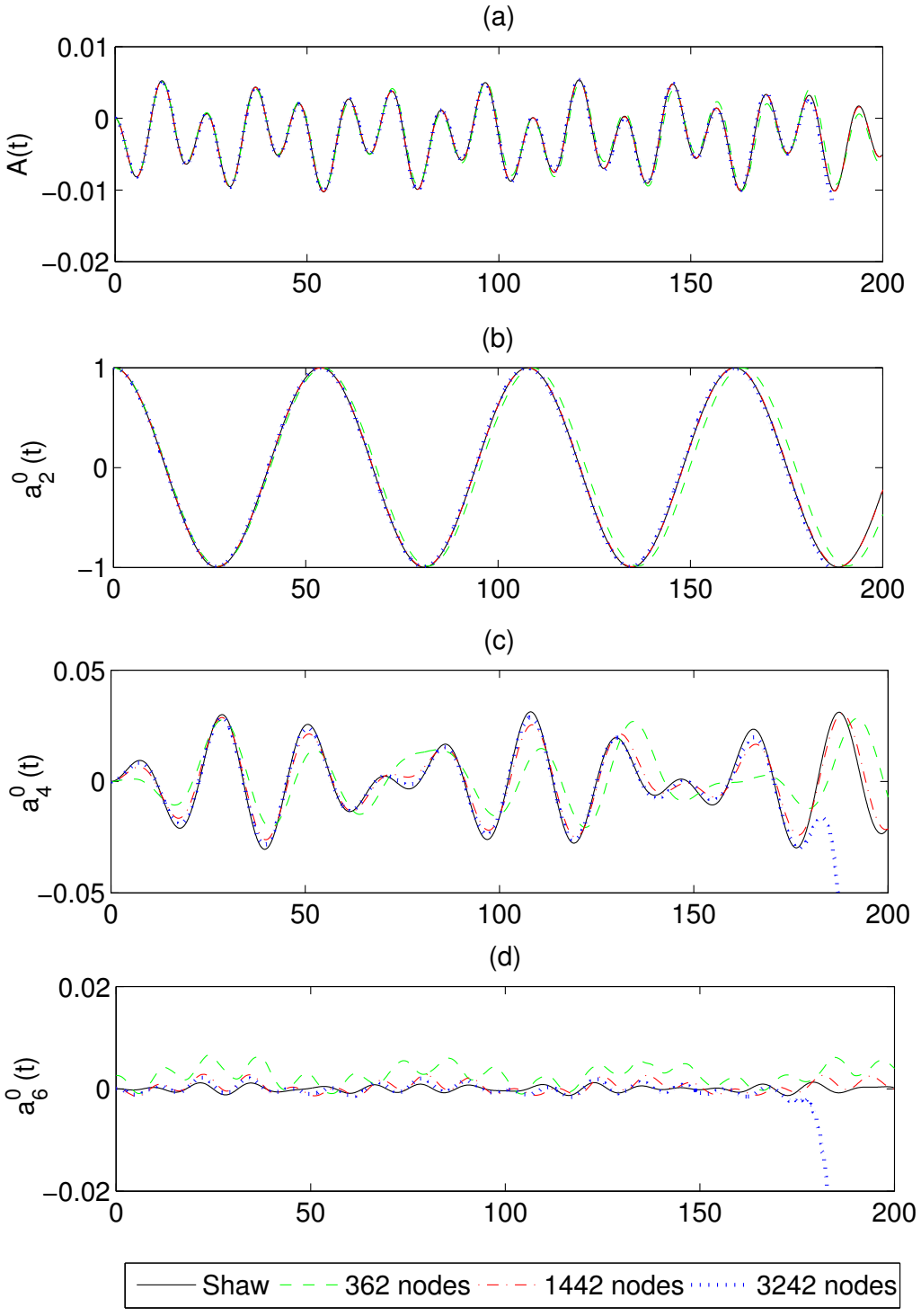

Figure 5.10: Harmonics oscillations, $\epsilon a_2^0 = 1\mu m$, quadratic elements, horizontal axes in μs, vertical axes in μm.

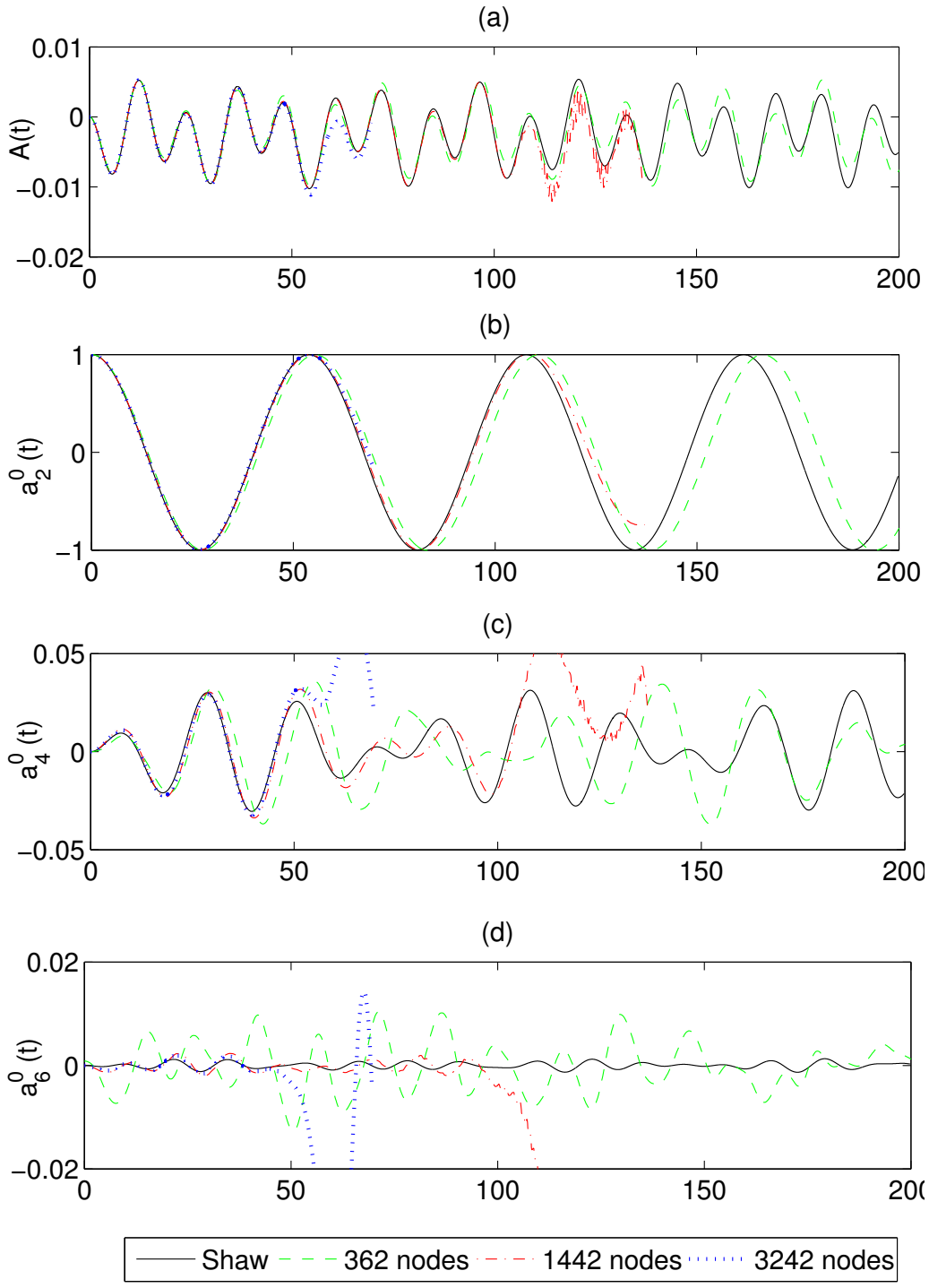

Figure 5.11: Harmonics oscillations, $\epsilon a_2^0 = 1\mu m$, cubic elements, horizontal axes in μs, vertical axes in μm.

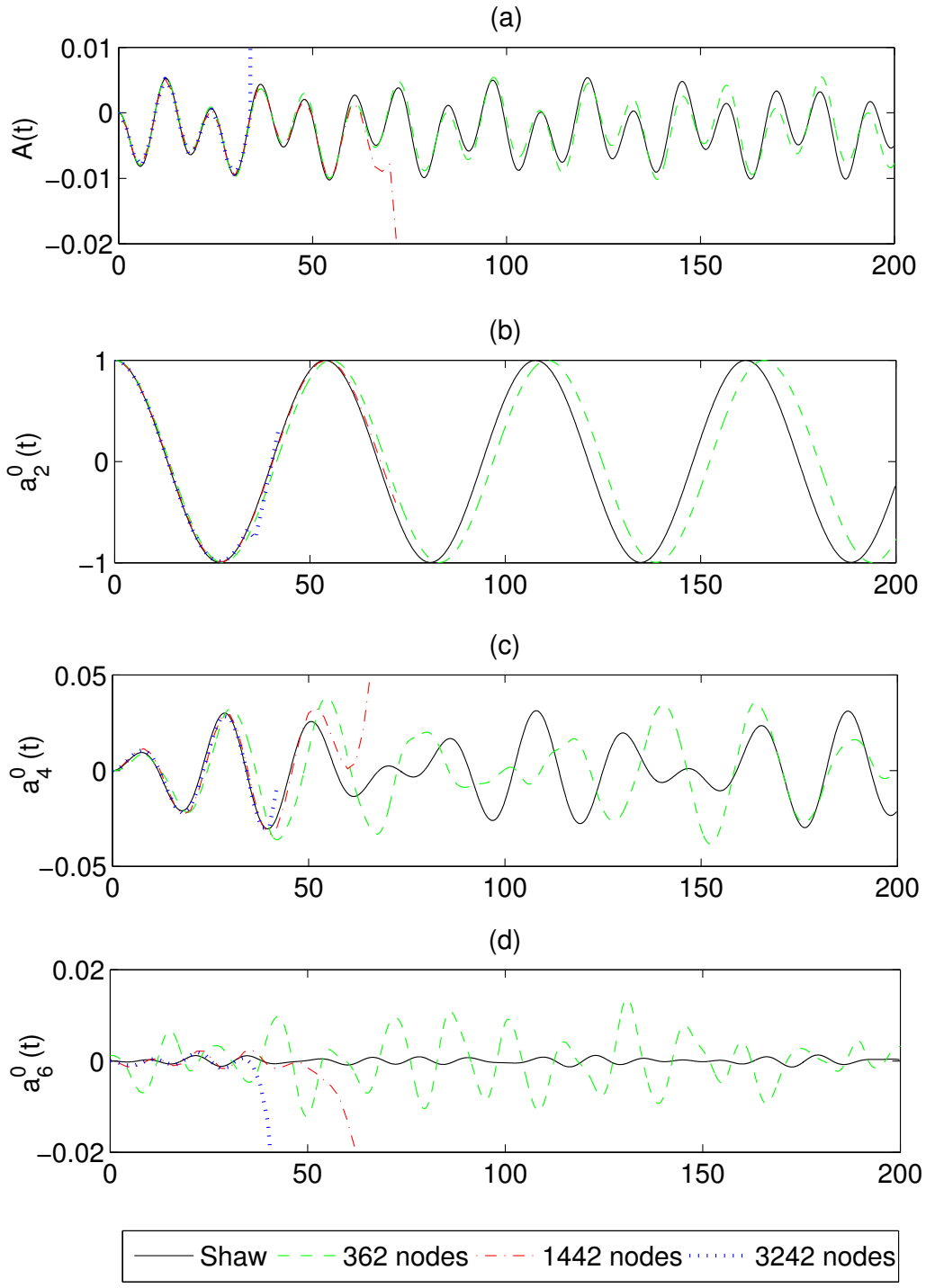

Figure 5.12: Harmonics oscillations, $\epsilon a_2^0 = 1\mu m$, Gauss-Lobatto cubic elements, horizontal axes in μs, vertical axes in μm.

Even mode shape oscillations are not expected to have any impact on odd shape modes in the absence of numerical error [1]. Figure 5.13 shows the first six odd mode oscillations for linear (green), quadratic (red) and equispaced cubic (blue) elements with 1442 (dashed) and 3242 (dash-dotted) surface nodes. The linear and quadratic meshes show oscillations with amplitudes less than 10^{-10}, while the cubic meshes show a sharp rise in the amplitudes prior to simulation break down, consistent with the increase in error seen with the even shape modes.

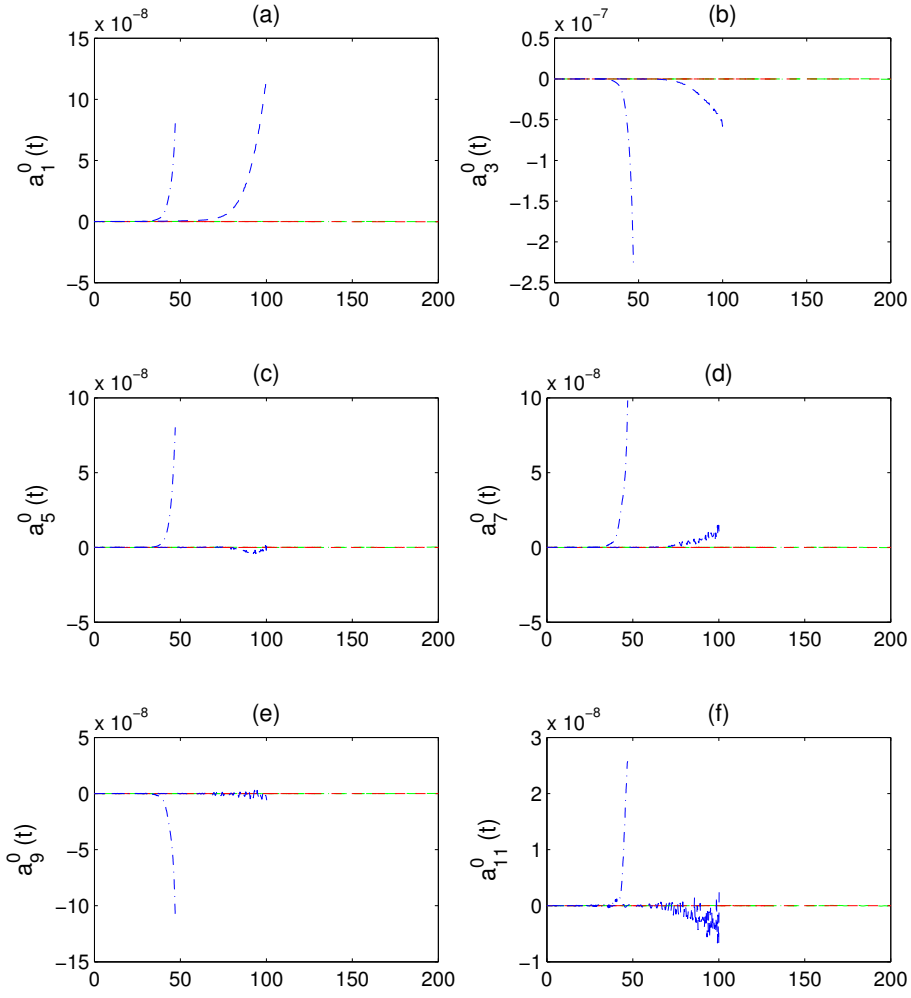

Figure 5.13: Odd shape mode oscillations, $\epsilon a_2^0 = 1\mu m$, horizontal axes in μs, vertical axes in μm.

To gain more insight into the behaviour of the different modes, we investigate the quadratic results further by using spectral decomposition of the shape oscillations using Matlab's discrete fourier transformation function "fft" [8], with results plotted in Figure 5.14. Each mode's natural frequency is marked with a vertical black line, while other important frequencies are labelled with the combination of natural frequencies that most closely matches them. It appears that the volume mode oscillation is a sum of two oscillations, the volume mode itself and an oscillation of twice the frequency of the second order mode, something which confirms the results in [1].

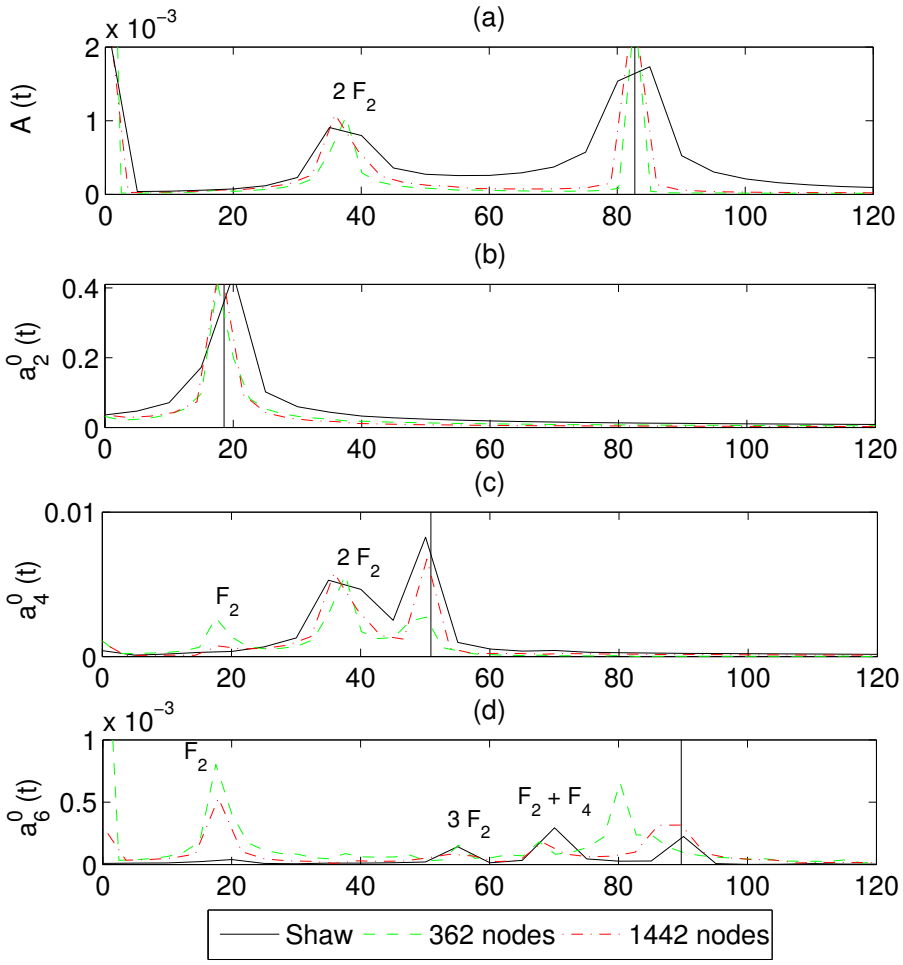

Figure 5.14: Spectral decomposition of harmonics oscillations, $\epsilon a_2^0 = 1\mu m$, quadratic elements, horizontal axes in kHz.

5.2.2 Small Amplitude Axisymmetric Odd Mode Oscillations

Odd shape modes are associated with bubble translation, and so the perturbation of for instance a_3^0 should cause the bubble center to move away from it's original position. While even shape mode distortions on their own will not cause bubble translation, it has been shown by others [1] that even mode oscillation may combine with odd mode oscillations to increase bubble movement. We perform a simulation with an initial distortion of $\epsilon a_2^0 = \epsilon a_3^0 = 1\mu m$ using quadratic and cubic elements only, due to the poor performance of the linear IBEM seen in Section 5.2.1.

Figure 5.15 shows the oscillation of the volume mode as well as the axisymmetric modes 1 to 5 using quadratic elements using 362, 1442, 3242 and 5762 nodes compared to results using Shaw's perturbation approach. The simulations are carried out with a non-dimensional time step of 0.05 for the coarsest mesh, 0.01 for 1442 and 3242 nodes, and 0.005 for the finest mesh.

With the exception of the fourth mode, the results seem to converge towards those of Shaw. From the spectral decomposition plots in Figure 5.16 it seems there is less impact of the fourth mode's own natural frequency in the IBEM simulation than with Shaw's approach.

Similar behaviour can be seen for cubic elements in Figure 5.17. The cubic IBEM does, however, break down early for fine surface meshes. As with previous second mode perturbation simulation, reducing the step size further to 0.005 (or 0.001 for the finest mesh) has no perceptible impact on the robustness or accuracy of the simulation.

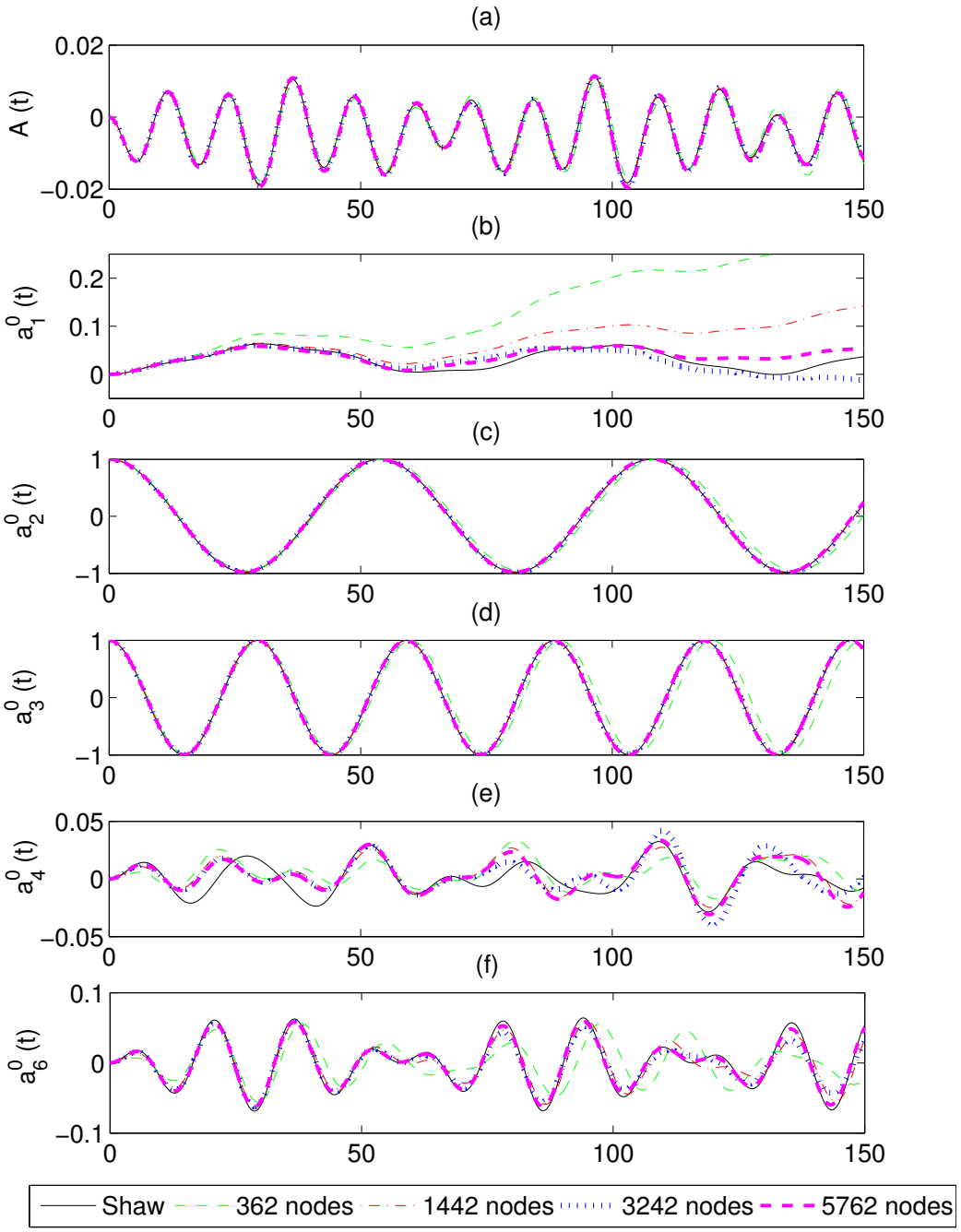

Figure 5.15: Harmonics oscillations, $\epsilon a_2^0 = \epsilon a_3^0 = 1\mu m$, quadratic elements, horizontal axes in μs, vertical axes in μm.

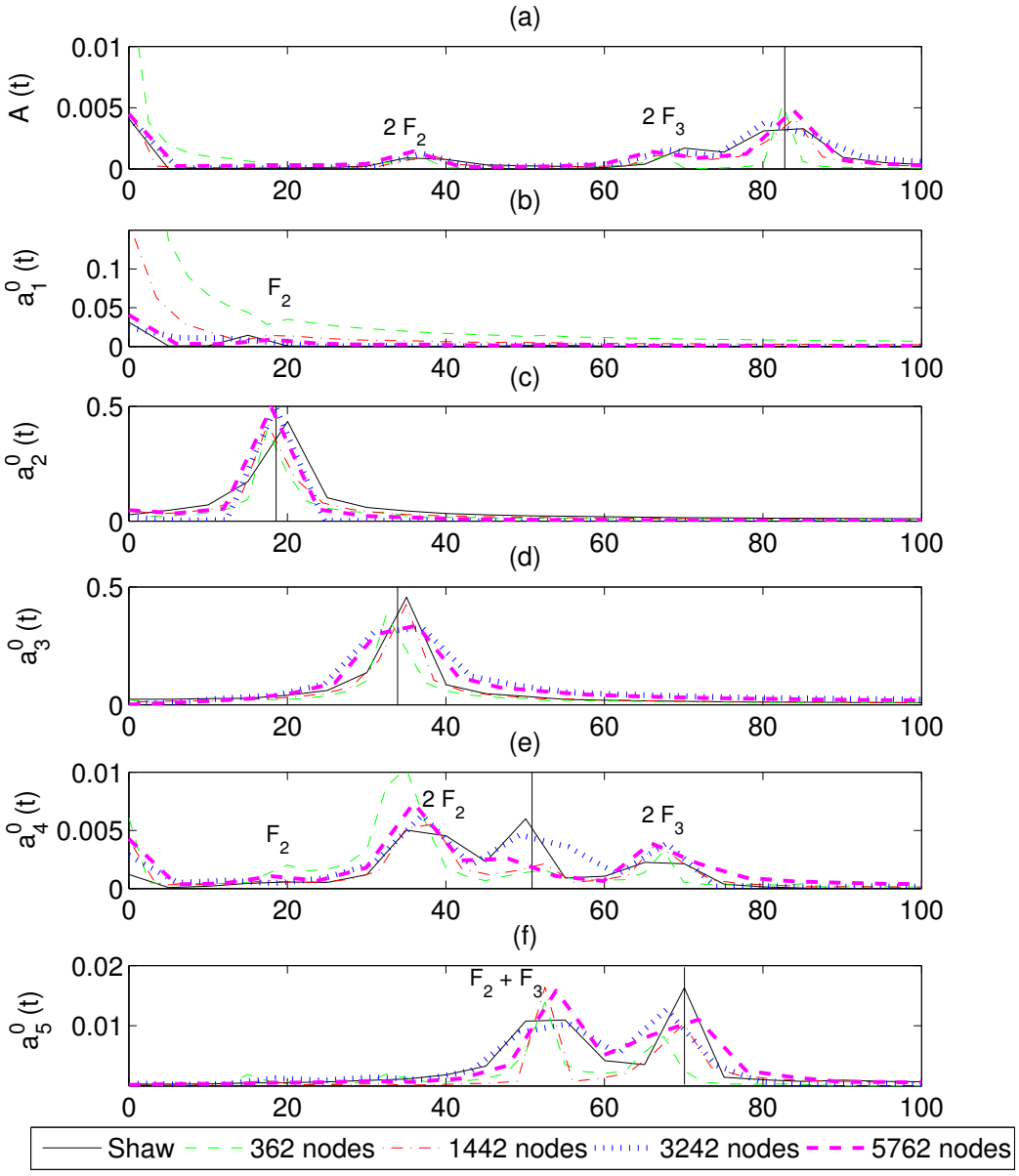

Figure 5.16: Spectral decomposition of harmonics oscillations, $\epsilon a_2^0 = \epsilon a_3^0 = 1\mu m$, quadratic elements, horizontal axes in kHz

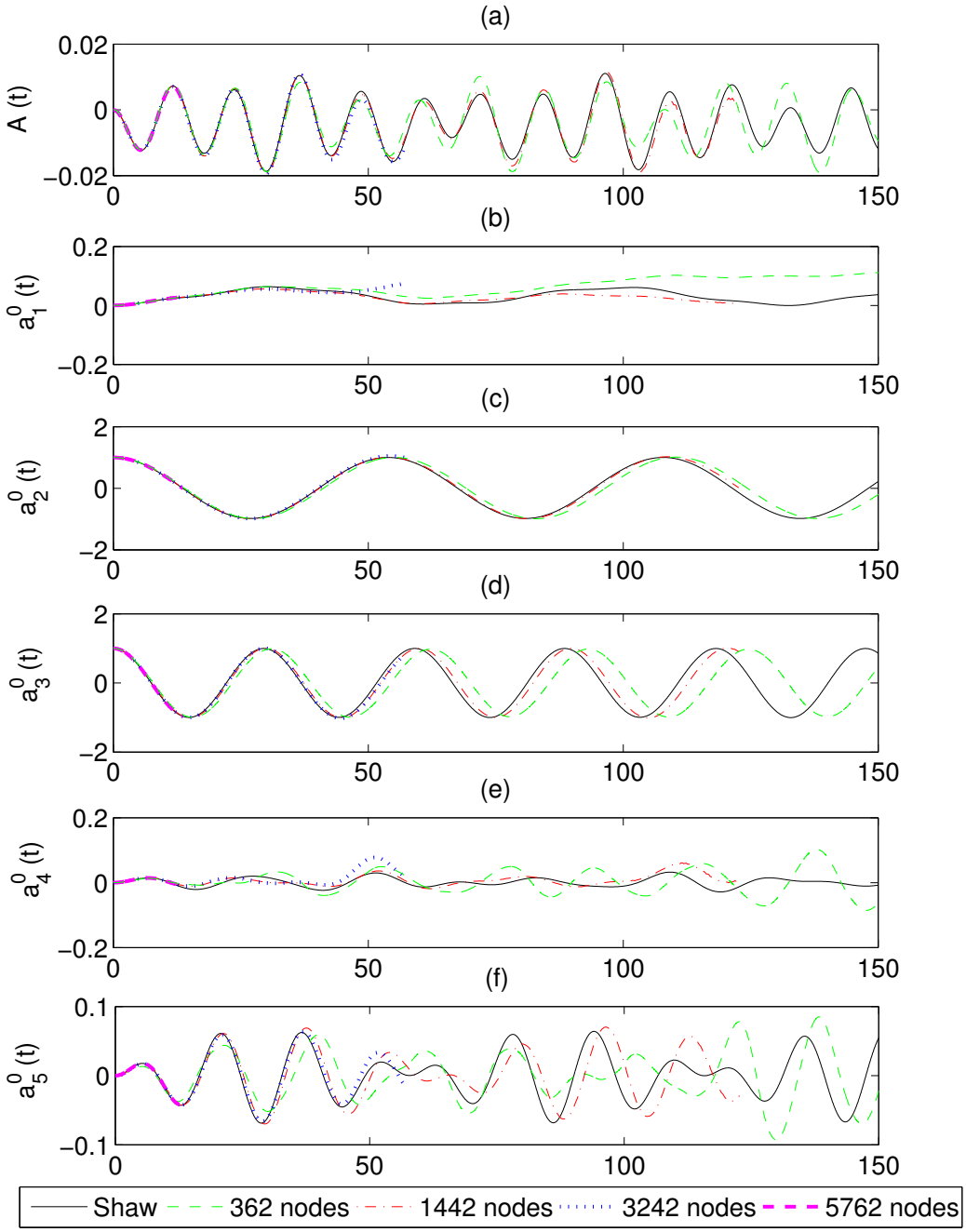

Figure 5.17: Harmonics oscillations, $\epsilon a_2^0 = \epsilon a_3^0 = 1\mu m$, cubic elements, horizontal axes in μs, vertical axes in μm.

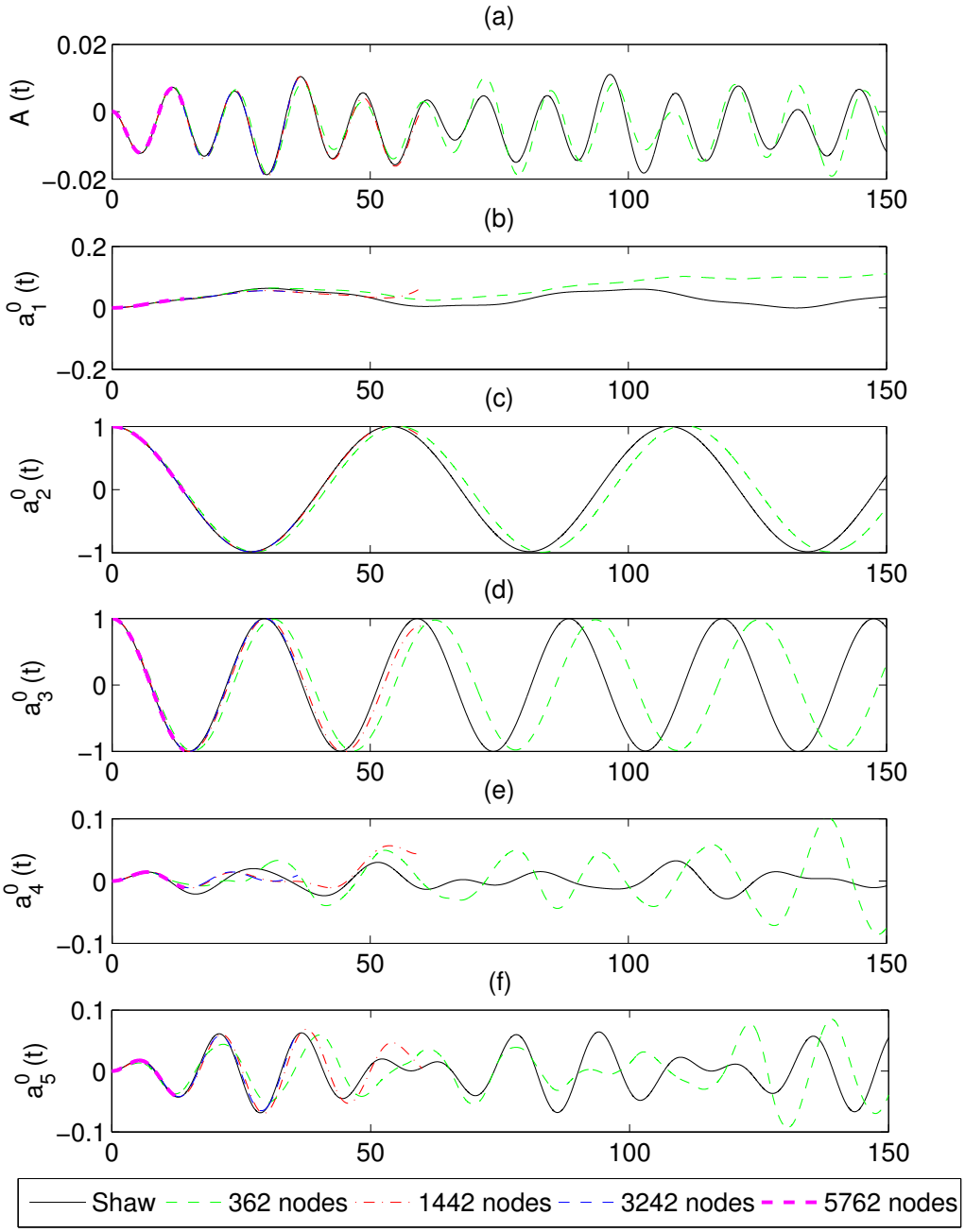

Figure 5.18: Harmonics oscillations, $\epsilon a_2^0 = \epsilon a_3^0 = 1\mu m$, Gauss-Lobatto cubic elements, horizontal axes in μs, vertical axes in μm.

Finally we plot the higher modes $l = 6, 7 \ldots 11$ for the quadratic IBEM in Figure 5.19. Excellent agreement can be seen for mode 6 for 5762 nodes and mode 8 shows good convergence towards Shaw's results. The IBEM deviates clearly from Shaw's results in the other modes, although, unlike in Figure 5.10, the numerical error is not many orders of magnitude larger than the shape oscillations, making it possible that the quadratic IBEM with 5762 nodes could accurately represent shape modes down to $l = 11$ given large enough shape oscillations.

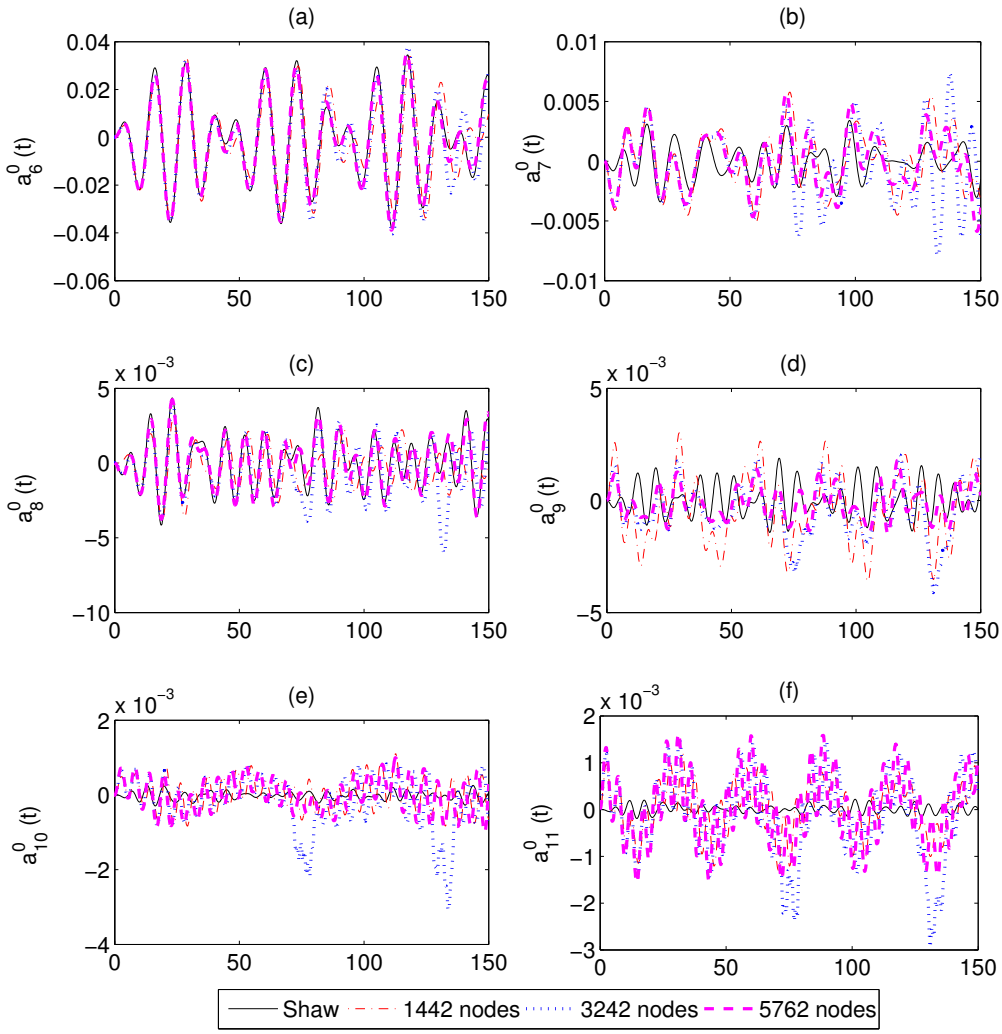

Figure 5.19: Harmonics oscillations, $\epsilon a_2^0 = \epsilon a_3^0 = 1\mu m$, quadratic elements, vertical axes in μm.

5.2.3 Larger Amplitude Axisymmetric Shape Oscillations

Having seen how the IBEM copes with small amplitude axisymmetric oscillations, we investigate the effect of larger axisymmetric shape deformations. Figure 5.20 shows a unit radius bubble distorted by $\epsilon a_l^0 = 0.125$ for $l = 2 \ldots 10$. As before, the distortions cause increasingly complex shapes as the order of the distorted mode increases.

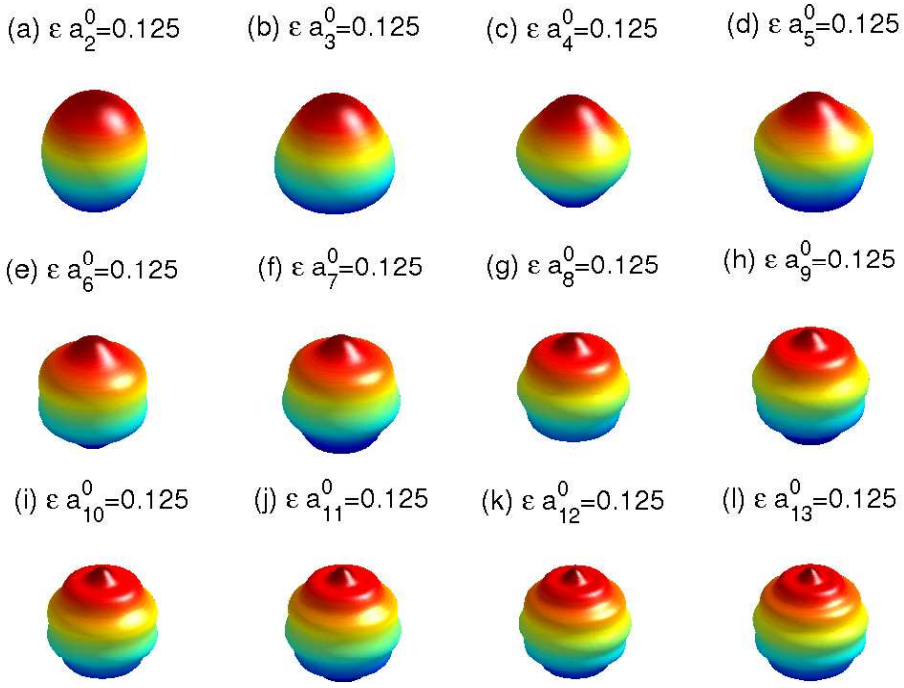

Figure 5.20: The axisymmetric spherical harmonics modes 2 to 10

Building on a previous simulation, we apply an initial perturbation of $\epsilon a_2^0 = \epsilon a_3^0 = 5\mu m$ with the non-dimensional step sizes $\delta t = 0.05$ for 362 nodes and $\delta t = 0.01$ for 1442 and 3242 nodes, leaving out the Gauss-Lobatto spaced elements for which we have seen little difference from the results using equispaced elements. In this case, the simulation breaks down early, both with quadratic elements (Figure 5.21) and cubic elements (Figure 5.22). The shape of the bubble body prior to break down for 1442 nodes can be seen in

Figures 5.23 and 5.24, revealing pitting towards the top of the bubble. Note that the top of the bubble sees the strongest change in curvature for these tests, which may explain why the pitting occurs at this point. Halving the step size to $\delta t = 0.025$ for 362 nodes and $\delta t = 0.005$ for 1442 and 3242 nodes, has no perceptible impact on the simulation, and smoothing may be required to advance the simulation.

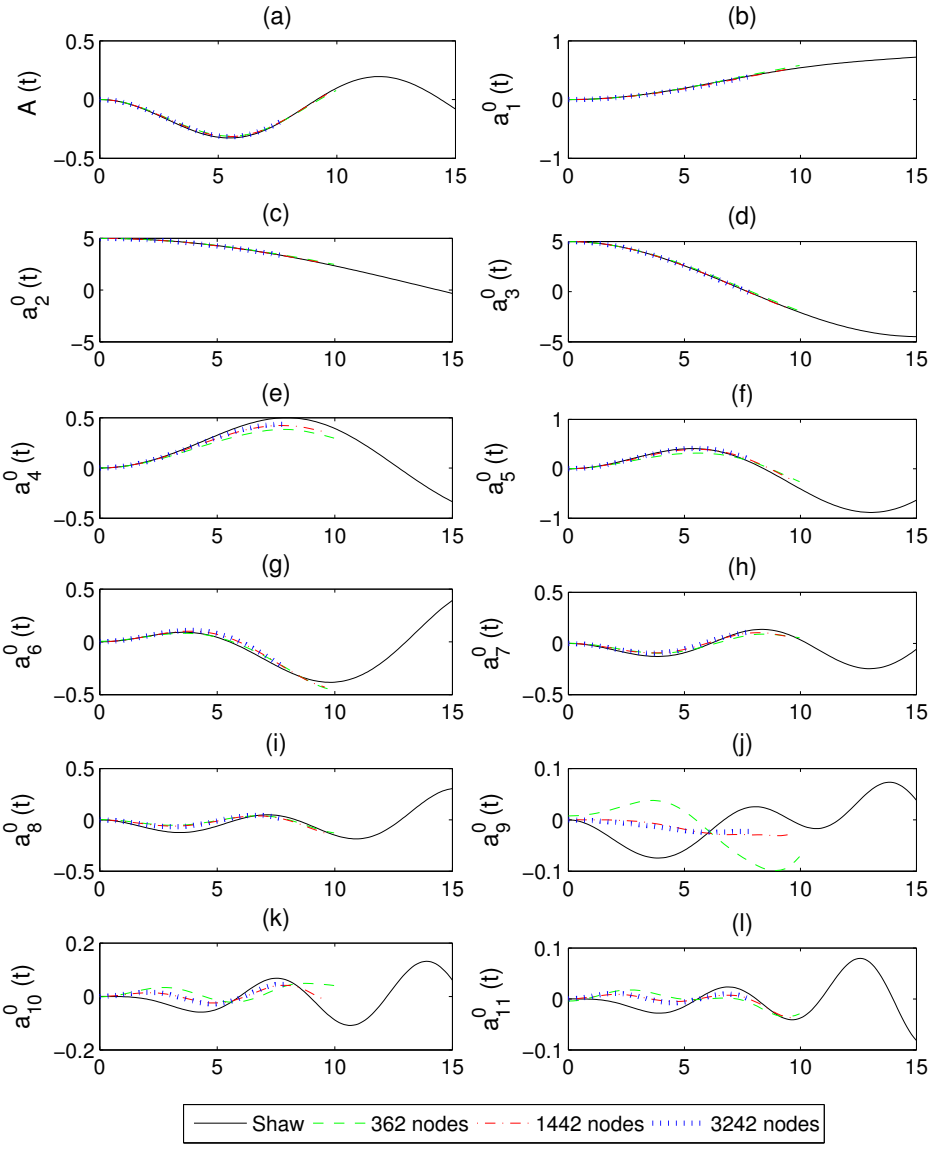

Figure 5.21: Harmonics oscillations, $\epsilon a_2^0 = \epsilon a_3^0 = 5\mu m$, quadratic elements, horizontal axes in μs, vertical axes in μm.

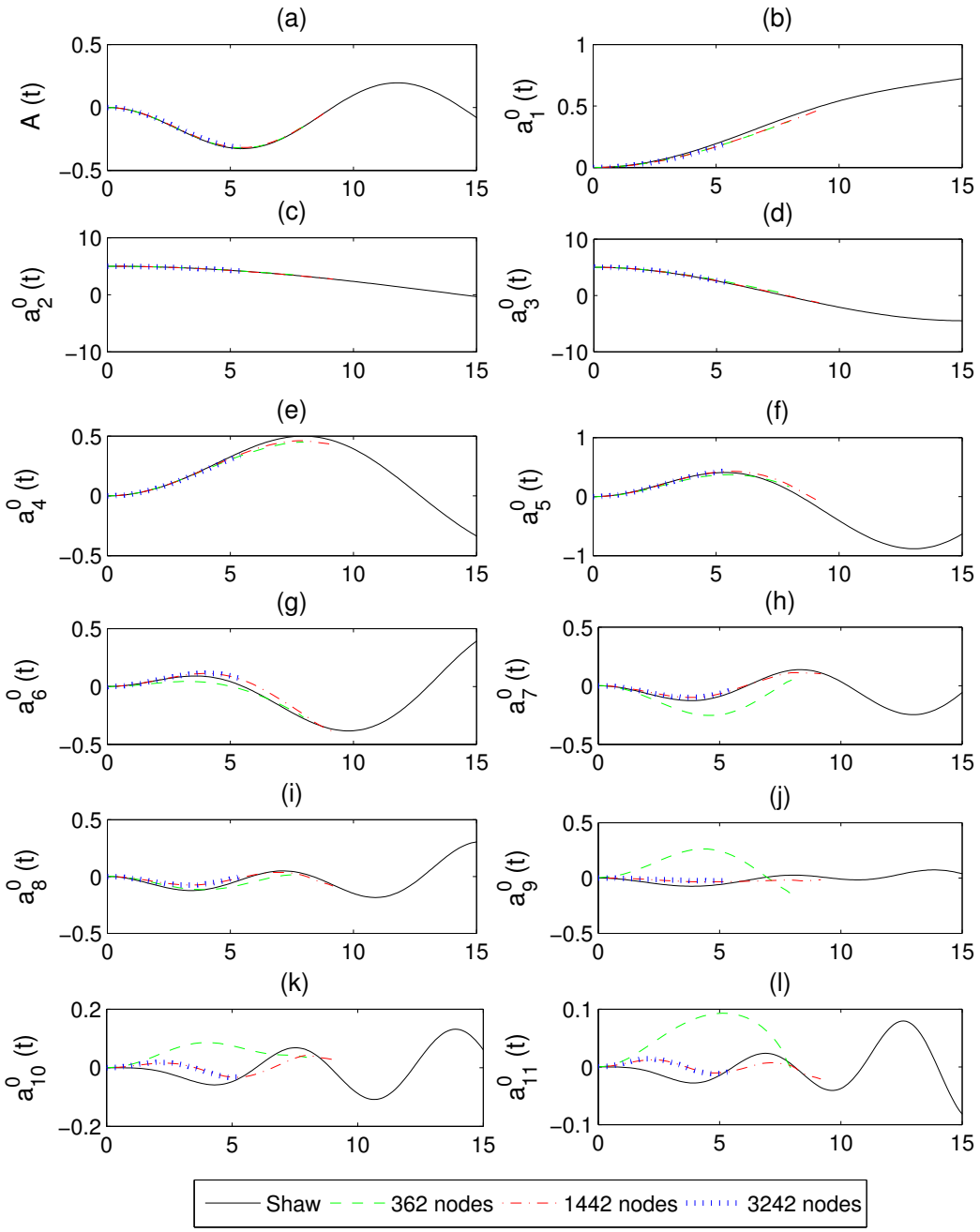

Figure 5.22: Harmonics oscillations, $\epsilon a_2^0 = \epsilon a_3^0 = 5\mu m$, cubic elements, horizontal axes in μs, vertical axes in μm.

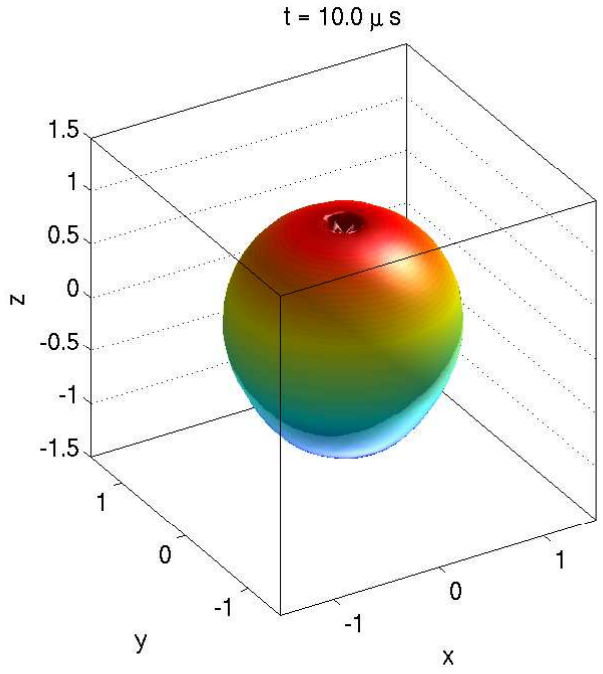

Figure 5.23: Bubble before breakdown, ϵa_2^0=ϵa_3^0=$5\mu m$, quadratic, 1442 nodes

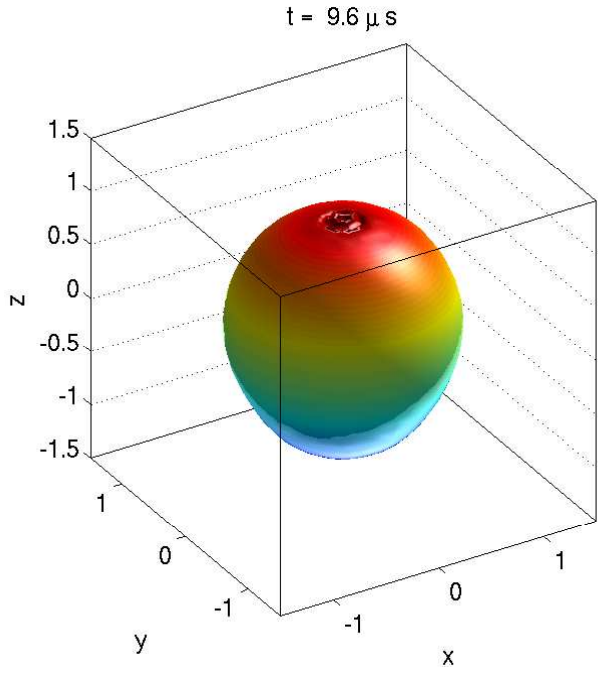

Figure 5.24: Bubble before breakdown, $\epsilon a_2^0 = \epsilon a_3^0 = 5\mu m$, cubic, 1442 nodes

In the beginning of this Section, we expressed the surface of the bubble in terms of a sum of spherical harmonics. Since this sum is finite and limited by $l_{\max}$, any surface features present in modes higher than $l_{\max}$ will be lost if the bubble is recreated from this harmonics representation. This will cause the bubble to become smoother as $l_{\max}$ is reduced, culminating in the bubble becoming spherical for $l_{\max} = 1$.

This feature is exploited in the smoothing scheme *spectrum truncation* [3] in which the velocity potential on the surface is represented by a finite sum of spherical harmonics. The potential in the boundary conditions is then replaced by the truncated potential and by smoothing the velocity potential one can avoid non-physical artifacts arising on the bubble surface through numerical error. It should be obvious that this procedure will also remove any physical features present in surface modes above $l_{\max}$, although as have been seen in the previous section, these modes will be dominated by numerical error anyway with the spatial resolution used in this Thesis.

We again apply an initial perturbation of $\epsilon a_2^0 = \epsilon a_3^0 = 5\mu m$ and simulate the bubble motion with the quadratic IBEM, using the non-dimensional step sizes 0.05 for 362 nodes and 0.01 for 1442 and 3242 nodes. This time, however, we truncate the potential with $l_{\max} = 12$ after every second time step with the results depicted in Figures 5.25 and 5.26.

It seems the 362 node mesh is so coarse that any changes to the potential on the surface impacts on too large of an area of the bubble, and the simulation suffers from considerable energy loss with the amplitudes of mode 2 and 3 diminishing every oscillation cycle. For the finer meshes, this energy loss is considerably smaller and the mesh with 1442 nodes completes the simulation in good agreement with the results using Shaw's method. Again, as in Figure 5.15, there is some deviation in mode 4, which should be accurately represented in the IBEM by the discretisation level used, given good representation of mode 5 and 6. The simulation using the finest mesh breaks down

halfway through the simulation, suggesting that the smoothing applied was not quite sufficient for fine meshes, although it can be seen that the results approach that of Shaw's for most modes.

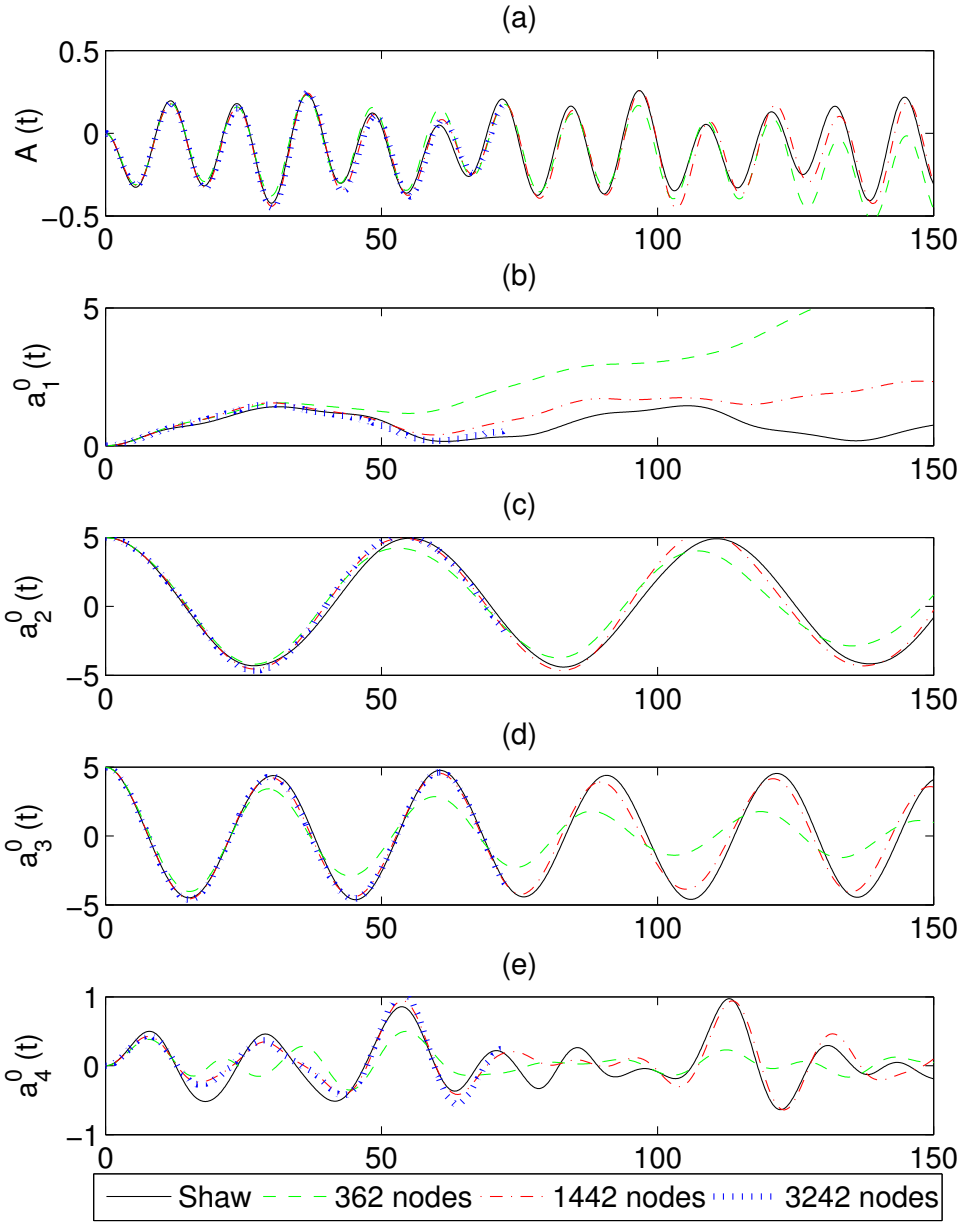

Figure 5.25: Harmonics oscillations, $\epsilon a_2^0 = \epsilon a_3^0 = 5\mu m$, quadratic, smoothing every second time step, horizontal axes in μs, vertical axes in μm.

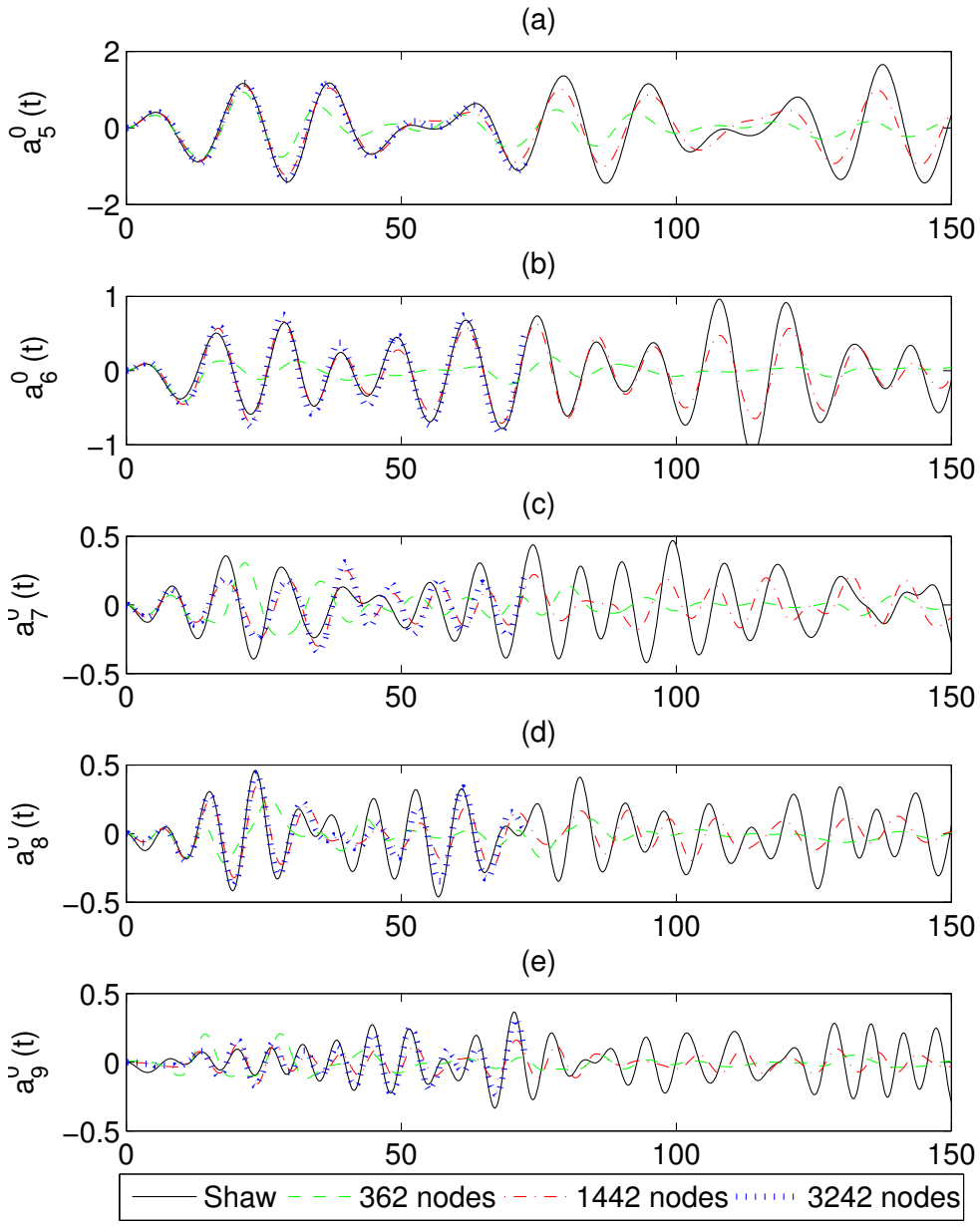

Figure 5.26: Harmonics oscillations, $\epsilon a_2^0 = \epsilon a_3^0 = 5\mu m$, quadratic, smoothing every second time step, horizontal axes in μs, vertical axes in μm.

Figure 5.27 shows the bubble shape at several times during the bubble oscillation. As the modes a_2^0 and a_3^0 have different oscillation periods, each mode will appear to dominate the bubble shape as the other approaches

zero. This can be seen most clearly at $t = 52.3\mu s$ and $t = 149.8\mu s$ where the bubble shape is almost completely dominated by mode a_2^0 and a_3^0 respectively. Around $t \approx 68\mu s$ both modes approach zero leading to an almost spherical bubble. It can also be seen that the bubble centroid moves away from the origin during simulation, since the bubble is not symmetric around the xy-plane.

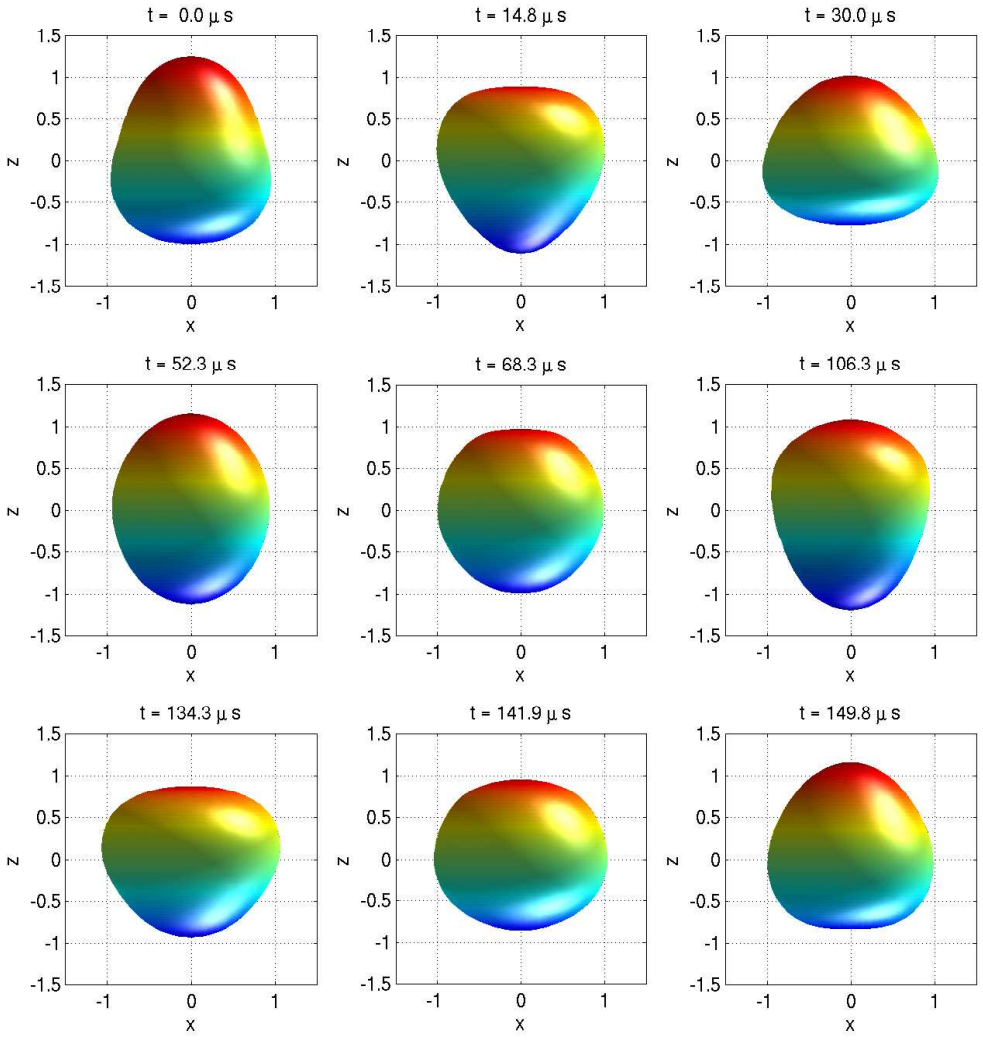

Figure 5.27: Non-dimensional bubble shapes at different times, $\epsilon a_2^0 = \epsilon a_3^0 = 5\mu m$, quadratic elements, smoothing every second time step, 1442 nodes.

The cubic results are again less robust and the simulation with the coarsest mesh and the finest mesh both breaking down before a quarter of the simulation has passed. The simulation using 1442 nodes progresses the furthest although shows no improvement over the quadratic method.

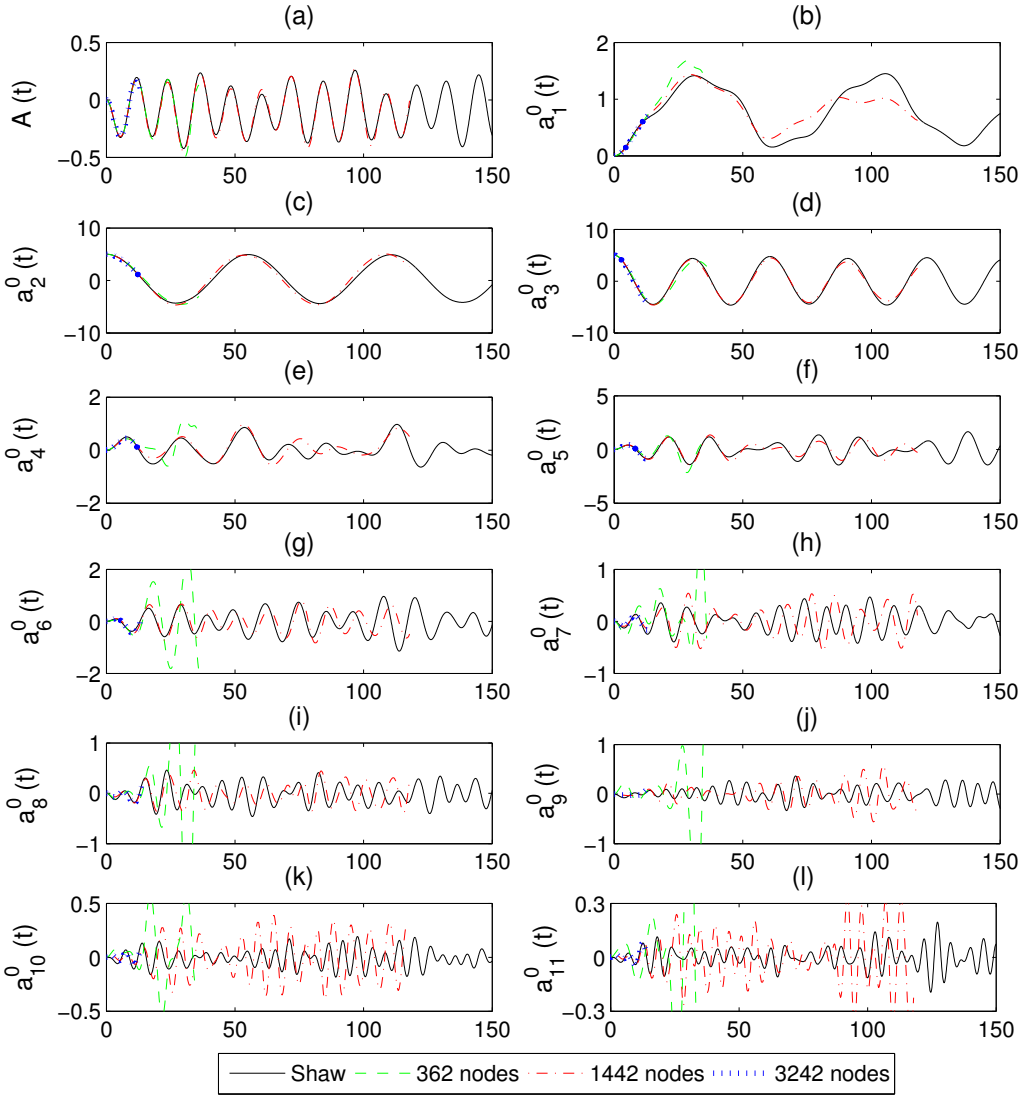

Figure 5.28: Harmoncs oscillations, $\epsilon a_2^0 = \epsilon a_3^0 = 5\mu m$, cubic elements, smoothing every second time step, horizontal axes in μs, vertical axes in μm.

Since the level of smoothing seemed insufficient for fine surface meshes, we investigate the effects of performing smoothing every time step. As can be seen in Figures 5.29 and 5.30 this improves the stability for the quadratic IBEM, allowing for stable operation with 5762 nodes. The additional smoothing does not result in any visible change in the energy loss, suggesting that smoothing every time step and varying the level of smoothing by changing $l_{\max}$, is the most sensible approach.

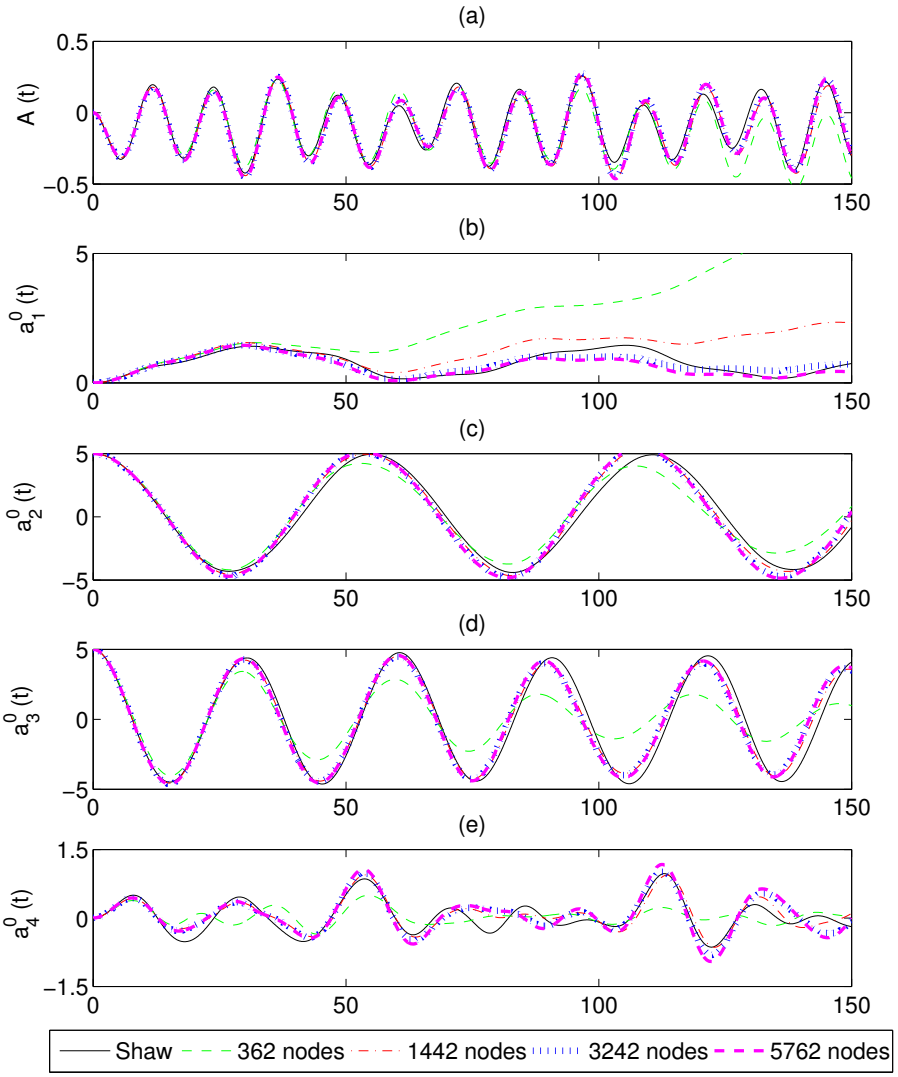

Figure 5.29: Harmonics oscillations, $\epsilon a_2^0 = \epsilon a_3^0 = 5\mu m$, quadratic elements, smoothing every time step, horizontal axes in μs, vertical axes in μm.

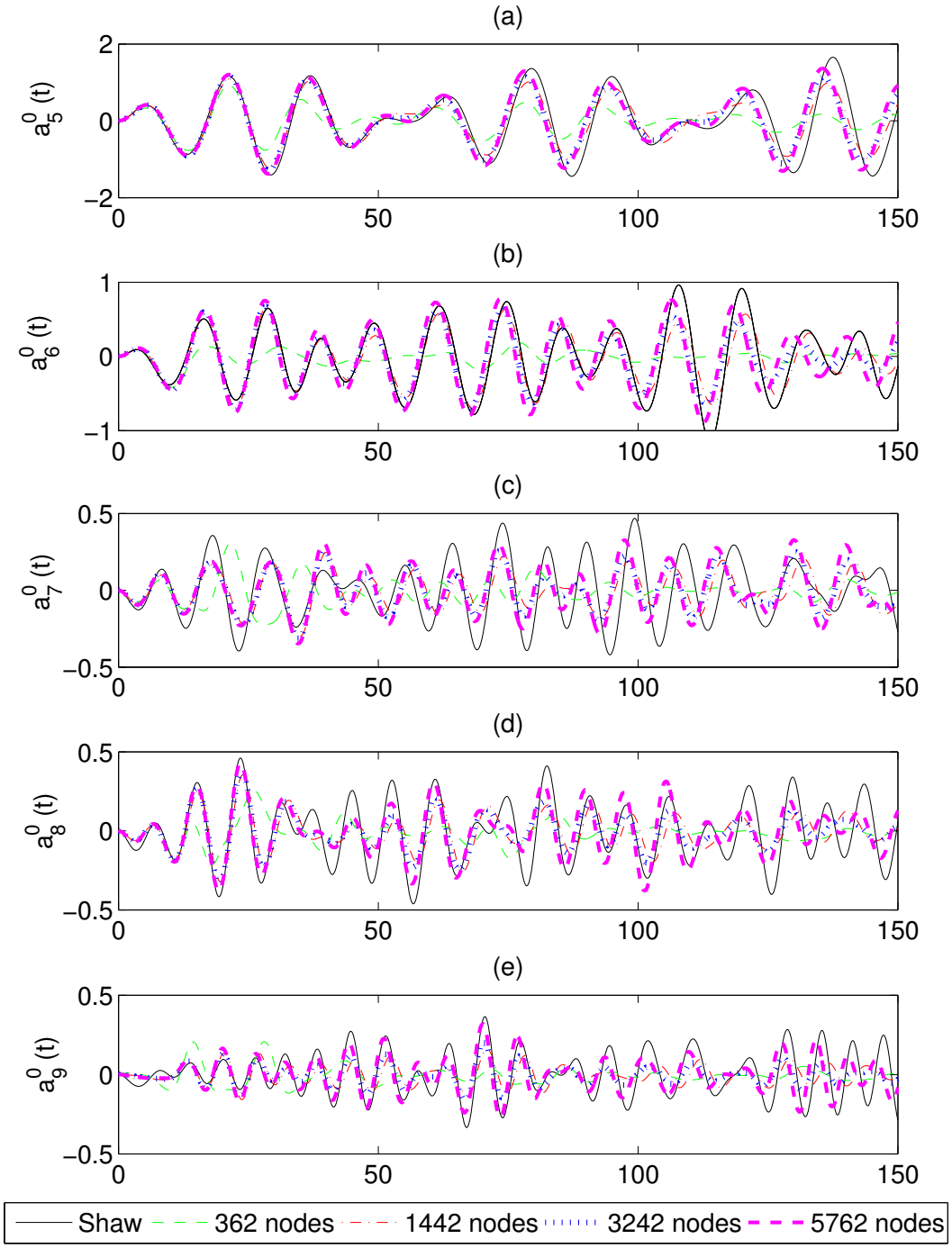

Figure 5.30: Harmonics oscillations, $\epsilon a_2^0 = \epsilon a_3^0 = 5\mu m$, quadratic elements, smoothing every time step, horizontal axes in μs, vertical axes in μm.

It can also be seen that the $a_4^0(t)$ oscillations simulated with the quadratic IBEM does not seem to converge to the results using Shaw's approach, something which may be examined in the spectral decomposition in Figure 5.31. Compared with Shaw's approach, the $a_4^0(t)$ coefficients in the IBEM has far stronger influence of the modes own natural frequency F_4 as well as $2F_2$, with both influences growing as the mesh is refined. For the coarser meshes there is also an influence of F_3 which diminishes as the mesh is refined. Due to the differences between the methods, it may be worth comparing both methods against a third approach. This is, however, outside the scope of this work.

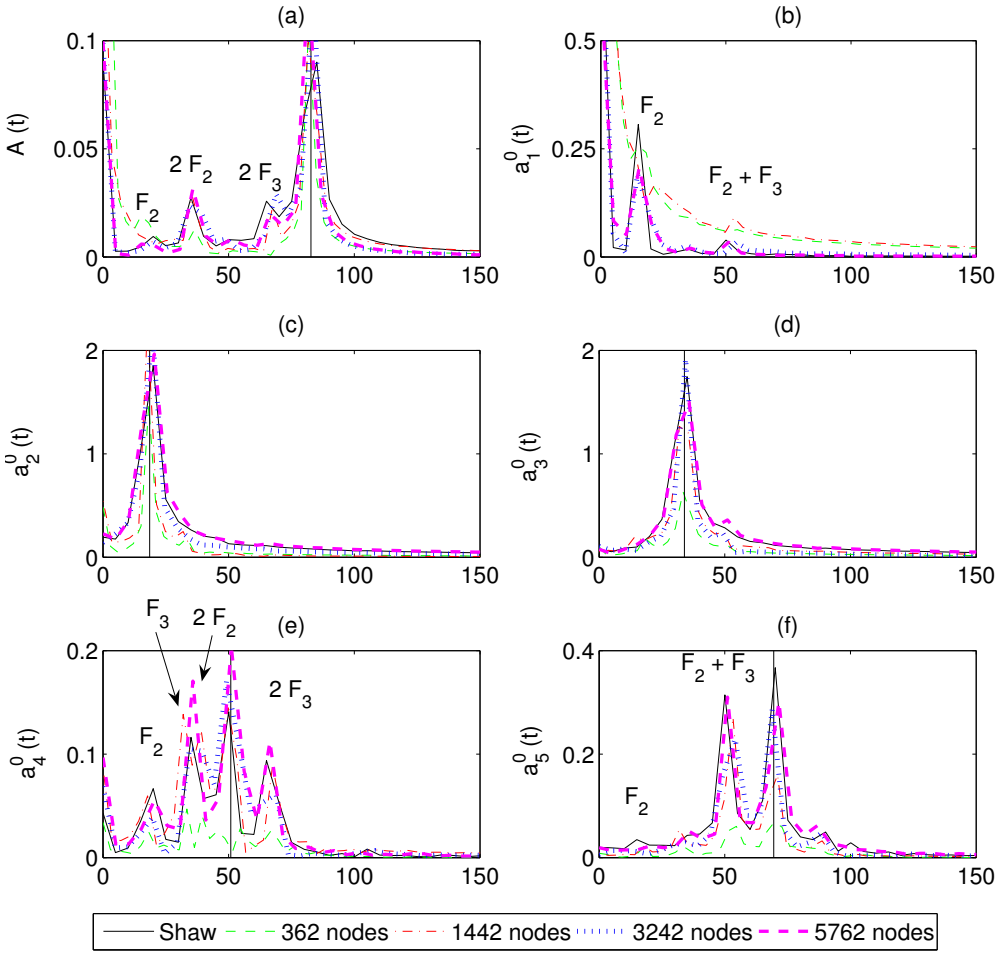

Figure 5.31: Spectral decomposition of harmonics oscillations, $\epsilon a_2^0 = \epsilon a_3^0 = 5\mu m$, quadratic elements, smoothing every time step, horizontal axes in kHz

Finally, Figure 5.32 shows the same oscillations using the cubic IBEM smoothed every time step. While the simulation using 3242 nodes advances over three times as far as before and a simulation using 5762 nodes nearly completes two oscillation cycles of the $a_2^0(t)$ coefficients, the cubic method is clearly less reliable for the same level of smoothing than the quadratic IBEM, though the same deviation in the $a_4^0(t)$ from Shaw's approach can be seen.

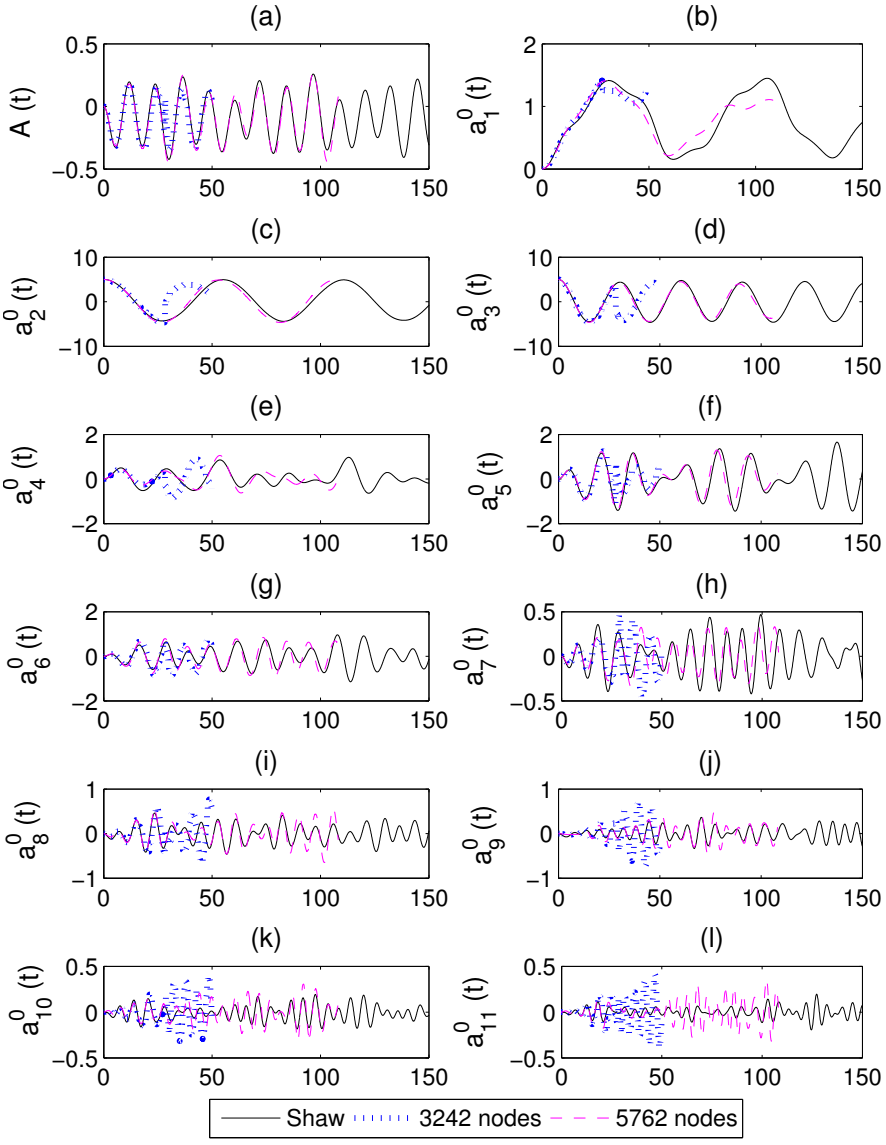

Figure 5.32: Harmonics oscillations, $\epsilon a_2^0 = \epsilon a_3^0 = 5\mu m$, cubic elements, smoothing every time step, horizontal axes in μs, vertical axes in μm.

We conclude this section with a perturbation of $\epsilon a_2^0 = 8\mu m$, using the quadratic IBEM with a step size of $\delta t = 0.01$ and smoothing every time step with $l_{\max} = 12$. In this case, the perturbation may be large enough to reach the limit of the small amplitude theory which Shaw's approach is based upon. Figure 5.33 shows similar amplitudes for the two methods, while clear deviation can be seen in the frequencies with the IBEM not converging upon the results from Shaw's method.

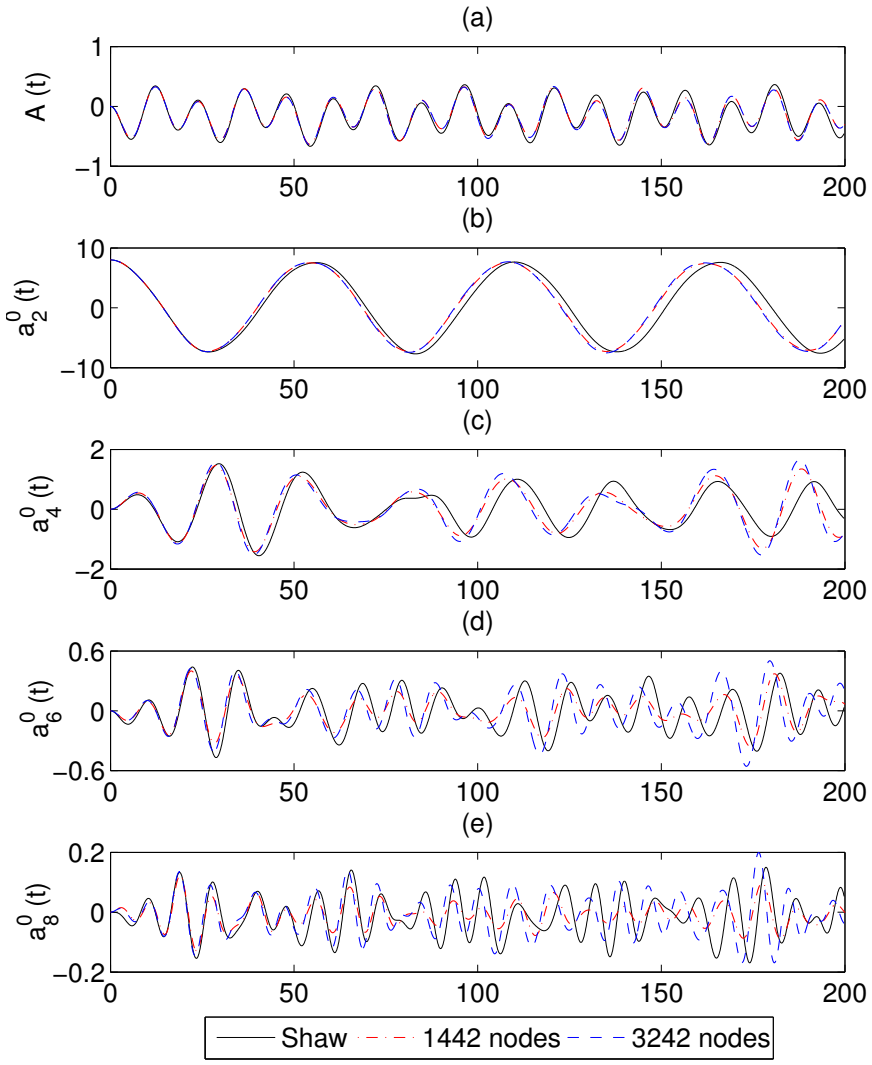

Figure 5.33: Harmonics oscillations, $\epsilon a_2^0 = 8\mu m$, quadratic elements, horizontal axes in μs, vertical axes in μm.

We can see from Figure 5.34 that the IBEM exhibits considerably less shifting away from the natural frequencies of the Y_2^0 mode. From (5.14) $2F_2 \approx 37.1$ kHz. In Figure 5.34 (a) and (c) the peaks for $2F_2$ appear around 35.0 Khz using Shaw's approach and around 37.8 kHz using the IBEM.

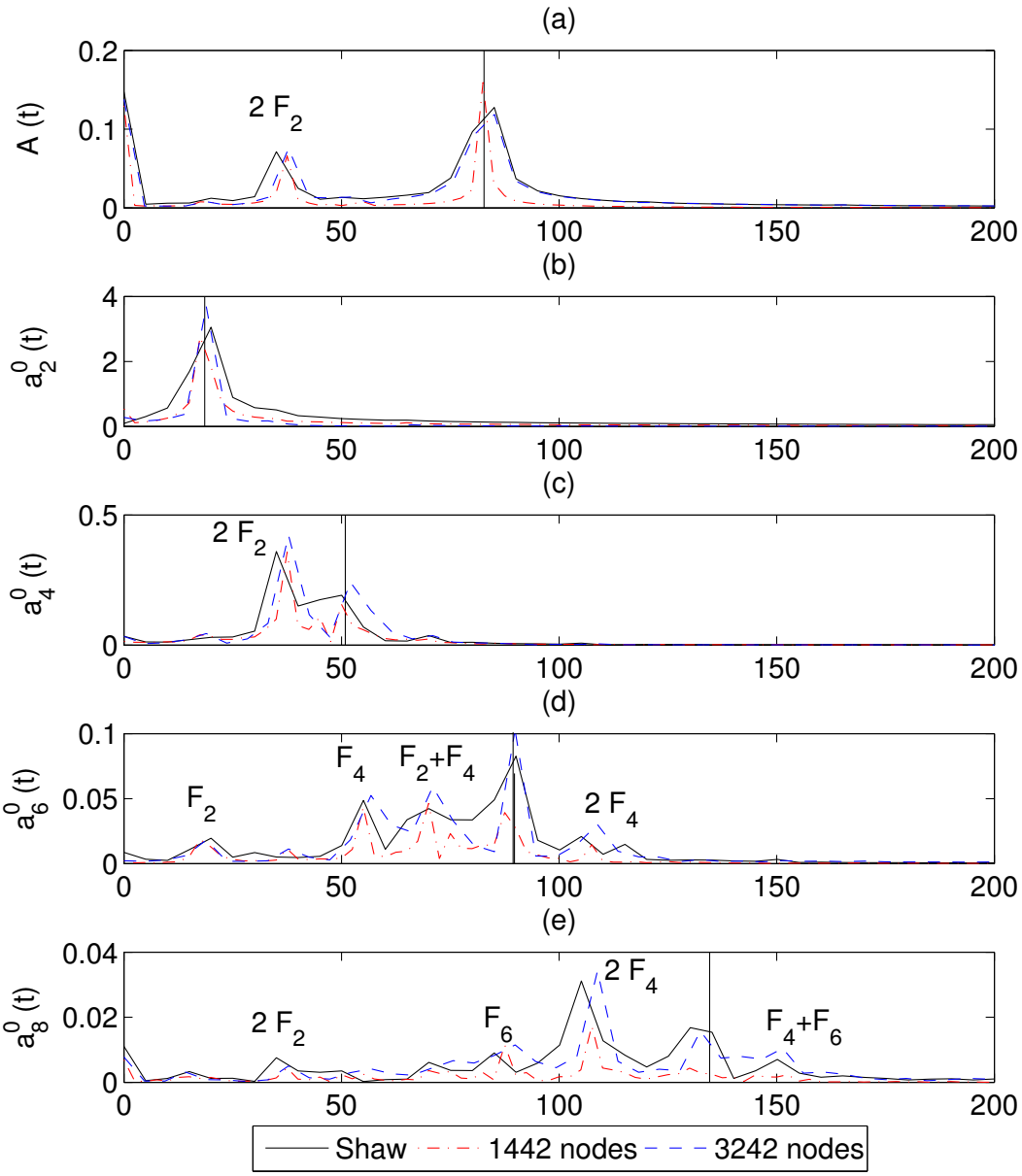

Figure 5.34: Spectral decomposition of harmonics oscillations, $\epsilon a_2^0 = 8\mu m$, quadratic elements, horizontal axes in kHz

Finally, Figure 5.35 shows the bubble at two local extrema of the second mode as well as $t \approx 39.6\mu s$ where the second mode coefficient is approximately zero. Due to the influence of the fourth mode, which is nearly at a local minima, the bubble is clearly not spherical at this point.

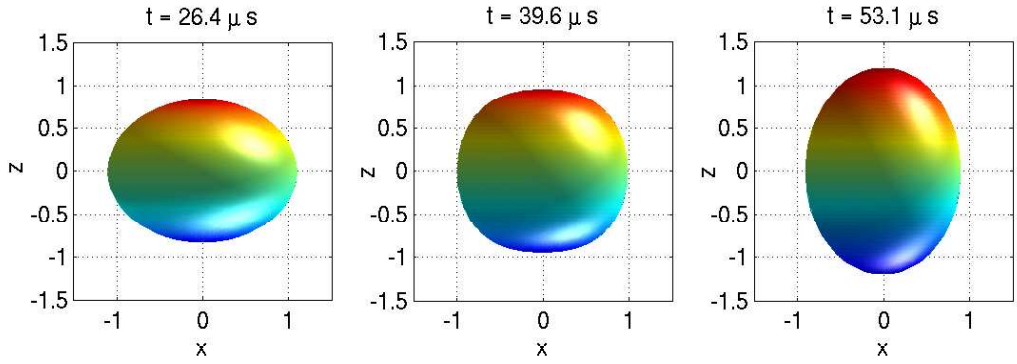

Figure 5.35: Non-dimensional bubble shapes at different times, $\epsilon a_2^0 = 8\mu m$, quadratic elements, smoothing every time step, 3242 nodes.

5.3 Near-Resonant Shape Oscillations

5.3.1 Initial Axisymmetric Distortions of Shape

From our previous shape mode simulations, including Figure 5.31, the volume mode oscillation could be seen as a sum of the sinusoidal oscillation of the volume mode's natural frequency and oscillations of twice the natural frequencies of the dominating shape modes. In the case of $R_0^* = 40.0\mu m$, used so far in our simulations, F_0 and $2F_l$ are far apart for any value of l, with $F_0 - 2F_3 \approx 14.9$ kHz being the closest. As can be seen in Figures 5.36 and 5.37, which shows the natural frequency of the volume mode against twice the natural frequencies of modes 2 to 20, there is a radius R_R^l for each mode $l > 1$ where $F_0 - 2F_l = 0$, thus corresponding to the $2:1$ resonance discussed by many researchers [5, 9, 7]. Table 5.2 lists the values of R_R^l for modes 2 to 11 found by combining (5.13) and (5.14) with the parameters listed in (5.1).

l	R_R^l	l	R_R^l
2	$7.180952e-6$	7	$2.971810e-4$
3	$2.651429e-5$	8	$4.338952e-4$
4	$6.103810e-5$	9	$6.065143e-4$
5	$1.114895e-4$	10	$8.191810e-4$
6	$1.922286e-4$	11	$1.076038e-3$

Table 5.2: Resonance radius in metres for modes 2 to 11

At R_R^l pure volume oscillation becomes *unstable* since small distortions of the shape get amplified through resonant excitation. Perturbation of both volume and the resonant shape mode should result in almost complete energy transfer between the two modes, periodically switching between almost pure volume oscillation and almost pure shape oscillation.

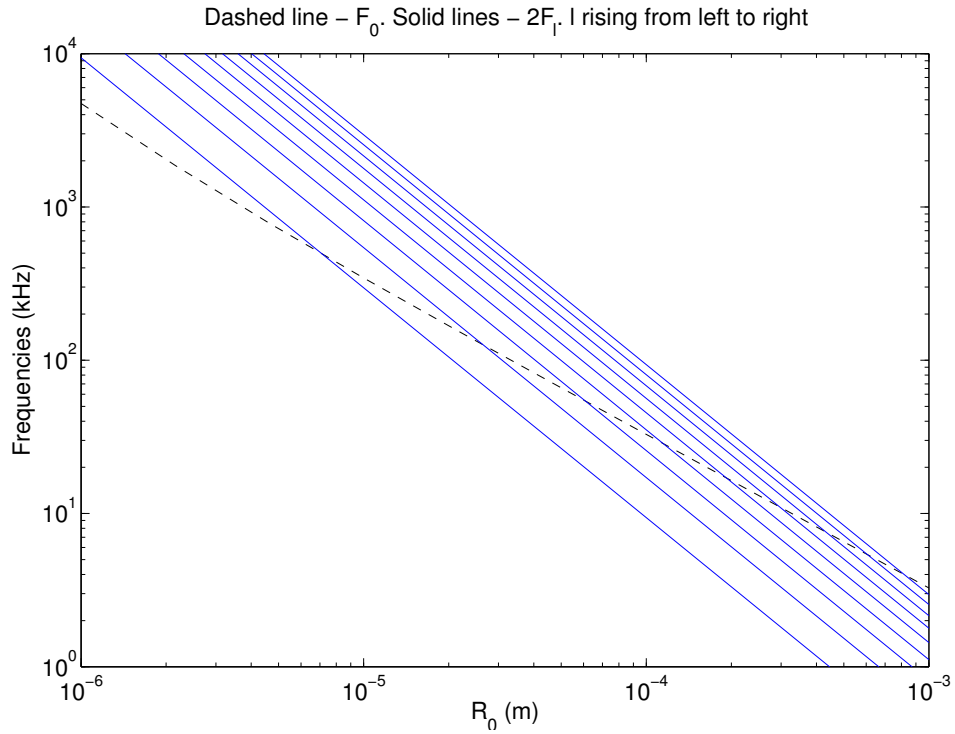

Figure 5.36: Natural frequencies, modes 2 to 10.

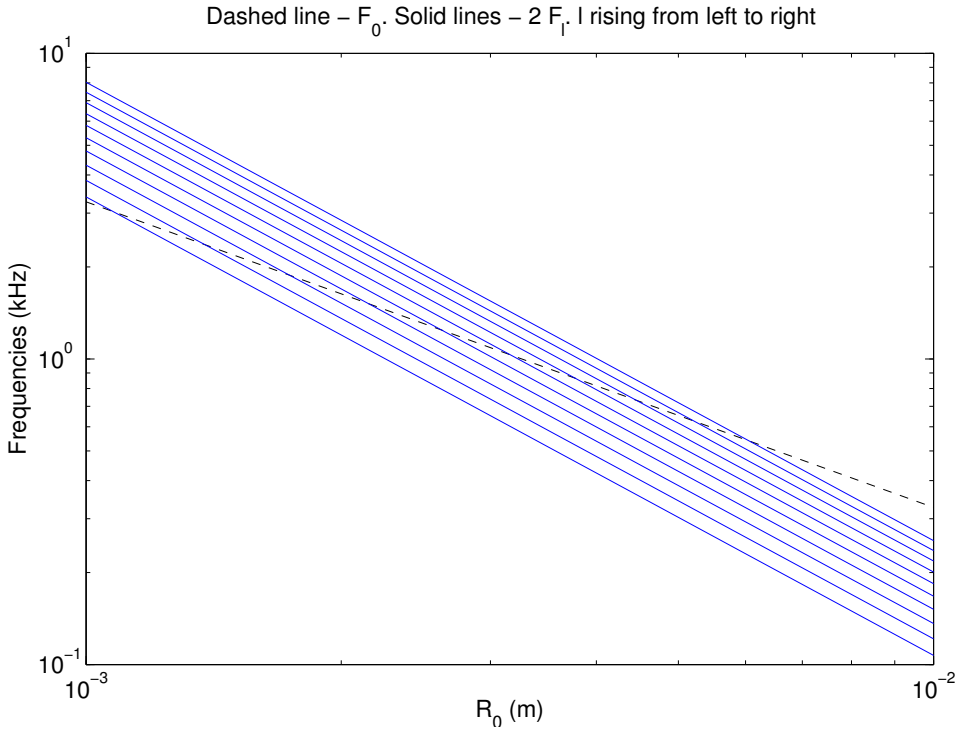

Figure 5.37: Natural frequencies, modes 11 to 20.

In all our simulations so far, the quadratic IBEM has performed far better in terms of speed, accuracy and reliability than the cubic IBEM in its current form. Therefore the remainder of this work will focus on the quadratic IBEM. Unless otherwise stated, all simulations will be carried out with 1442 nodes and spectral truncation applied every time step with $l_{\max} = 12$.

Starting with a perturbation of $\epsilon R = 1/16 R_0, \epsilon a_2^0 = 1/8 R_0$ we first show a simulation far from the resonance radius with $R_0^* = 40\mu m$ in Figure 5.38. There is little or no energy transfer between the volume and the second shape mode, although there appears to be some energy exchange between the second and fourth mode, leading to the amplitudes of the fourth mode approaching those of the second mode between $t = 100\mu s$ and $t = 200\mu s$. This can be seen in Figure 5.39 to have significant impact on the bubble shape and at $t = 149.8\mu s$, $t = 175.0\mu s$ and $t = 199.8\mu s$ we can see strong similarities with the fourth mode shown in Figure 5.20 (c) before the bubble reverts to shapes based on the second mode towards the end of the simulation.

The impact of the fourth mode is considerably larger than seen in the previous simulations, with amplitudes reaching half of the maximum amplitude of the second mode. The natural frequency of the fourth mode for a bubble of radius $40.0\mu m$ is 50.87 kHz leading to an oscillation period of $\approx 19.66\mu s$. The initial radial perturbation of $2.5\mu m$, however, causes the bubble radius to oscillate between $37.5\mu m$ and $42.5\mu m$, which seems to have varying impact on the oscillation periods of the shape modes. The oscillation period of the fourth mode appears to shift closer to $22\mu s$, giving a frequency of approximately 45 kHz and this can be seen clearly in the spectral decomposition of the oscillations in Figure 5.40. At the same time, the frequency of the second order mode increases to above 20 kHz, thus the frequency of the fourth mode approaches twice the frequency of the second mode. In all our simulations with an initial distortion to the second axisymmetric mode, we have seen the fourth mode influenced by $2F_2$ (for instance Figure 5.34), thus

the energy exchange seems to be resonant interaction between the two shape modes. The higher modes get increasingly complicated and differentiating between influences gets harder and thus the labels in Figure 5.40 above mode 4 must be seen as a "best effort". It does, however, appear that the natural frequencies of all modes $l > 2$ are shifted slightly downwards.

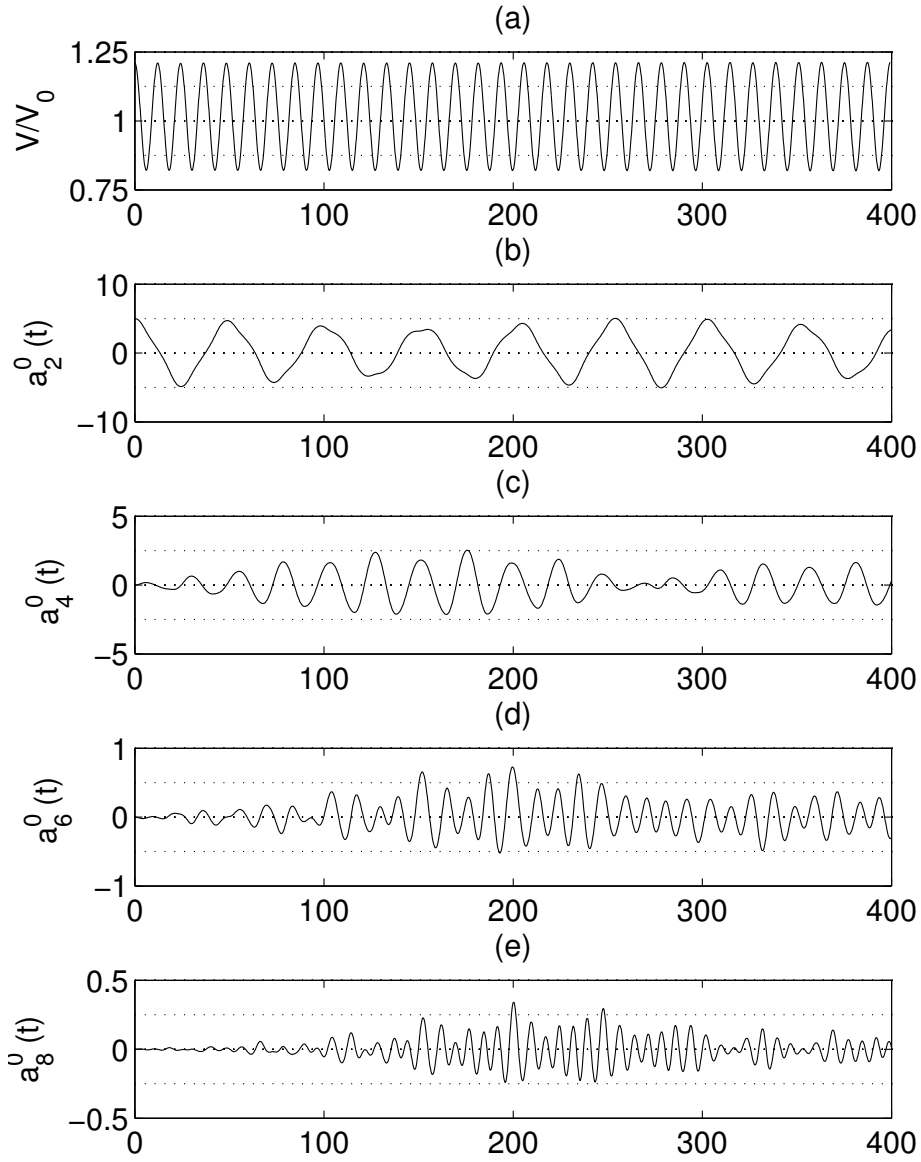

Figure 5.38: Harmonics oscillations, $\epsilon R = 1/16 R_0, \epsilon a_2^0 = 1/8 R_0$, quadratic, 1442 nodes, $R_0^* = 40 \mu m$, $\delta t = 0.05$, horizontal axes in μs, vertical axes in μm.

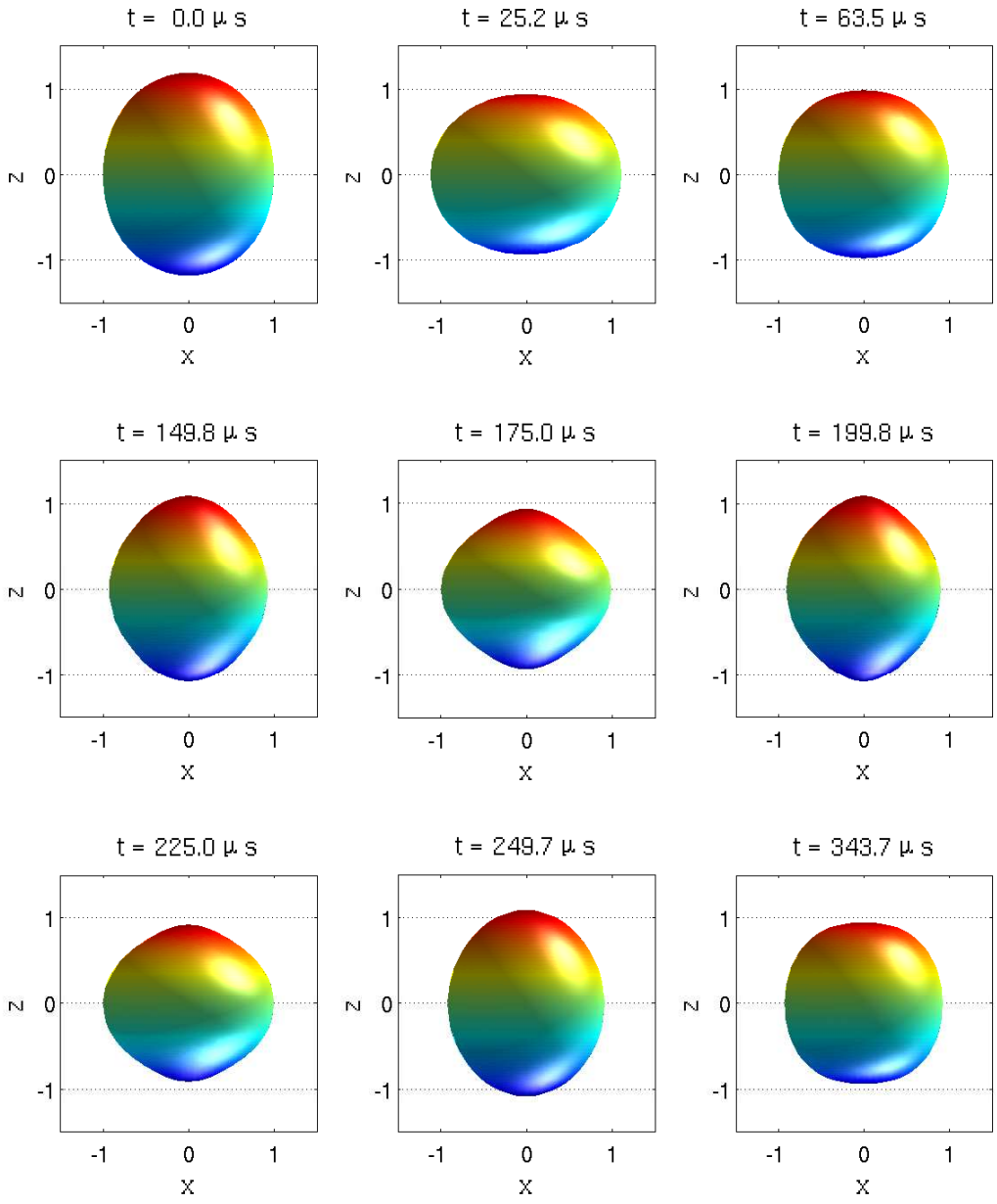

Figure 5.39: Non-dimensional bubble shapes at different times,$\epsilon R = 1/16 R_0, \epsilon a_2^0 = 1/8 R_0$, quadratic, 1442 nodes, $R_0^* = 40 \mu m$.

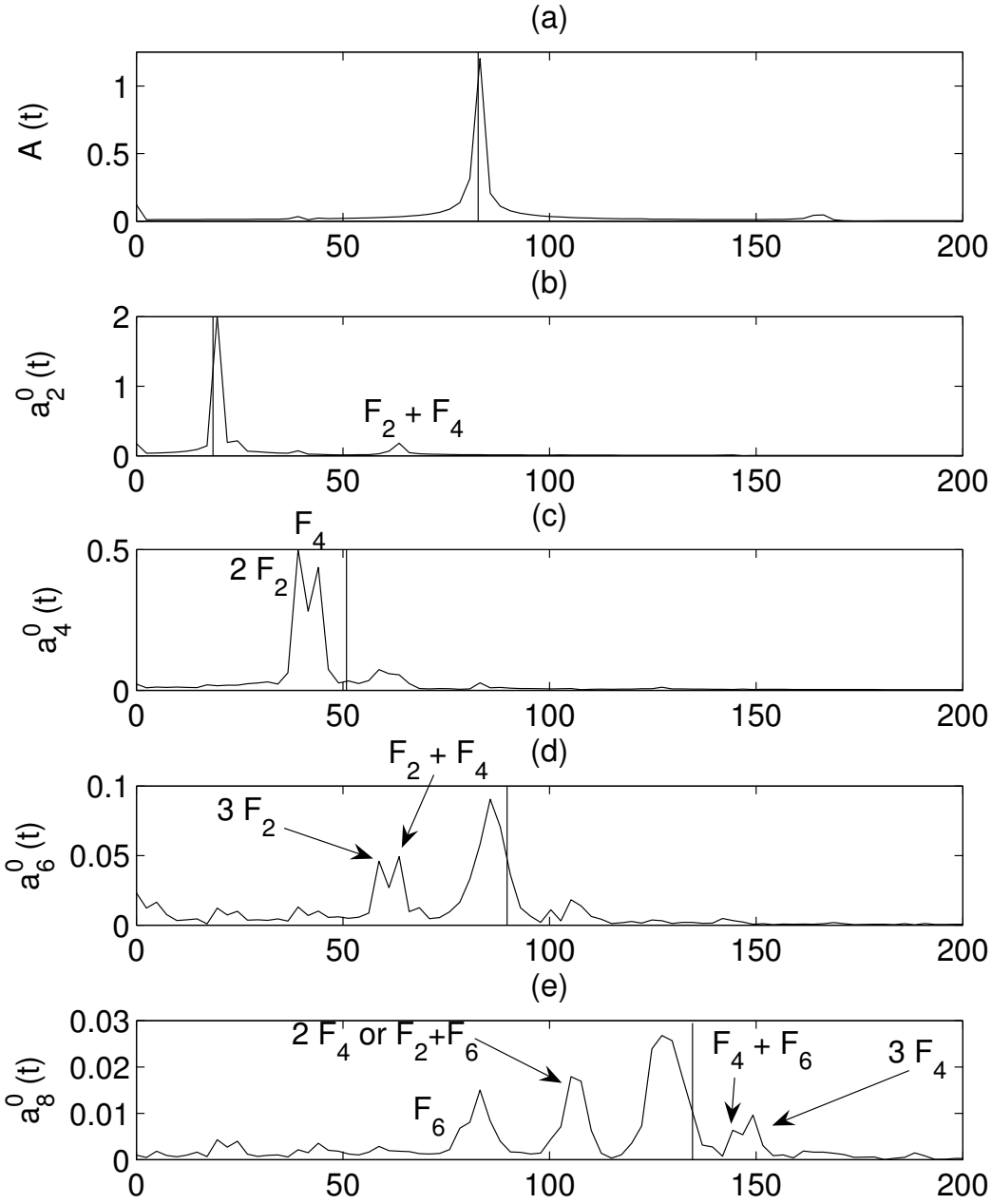

Figure 5.40: Spectral decomposition of harmonics oscillations, $\epsilon R = 1/16 R_0, \epsilon a_2^0 = 1/8 R_0$, quadratic, 1442 nodes, $R_0^* = 40 \mu m$, $\delta t = 0.05$, horizontal axes in kHz.

Despite the strong interaction between two shape modes at $R_0^* = 40\mu m$, the impact on the volume oscillation appeared to be minimal and the effect is thus unlikely to drastically change the sound output of the bubble. By changing R_0^* to $8\mu m$ we should start seeing resonant interaction between the volume mode and the second mode. As can be seen in Figure 5.41 this is

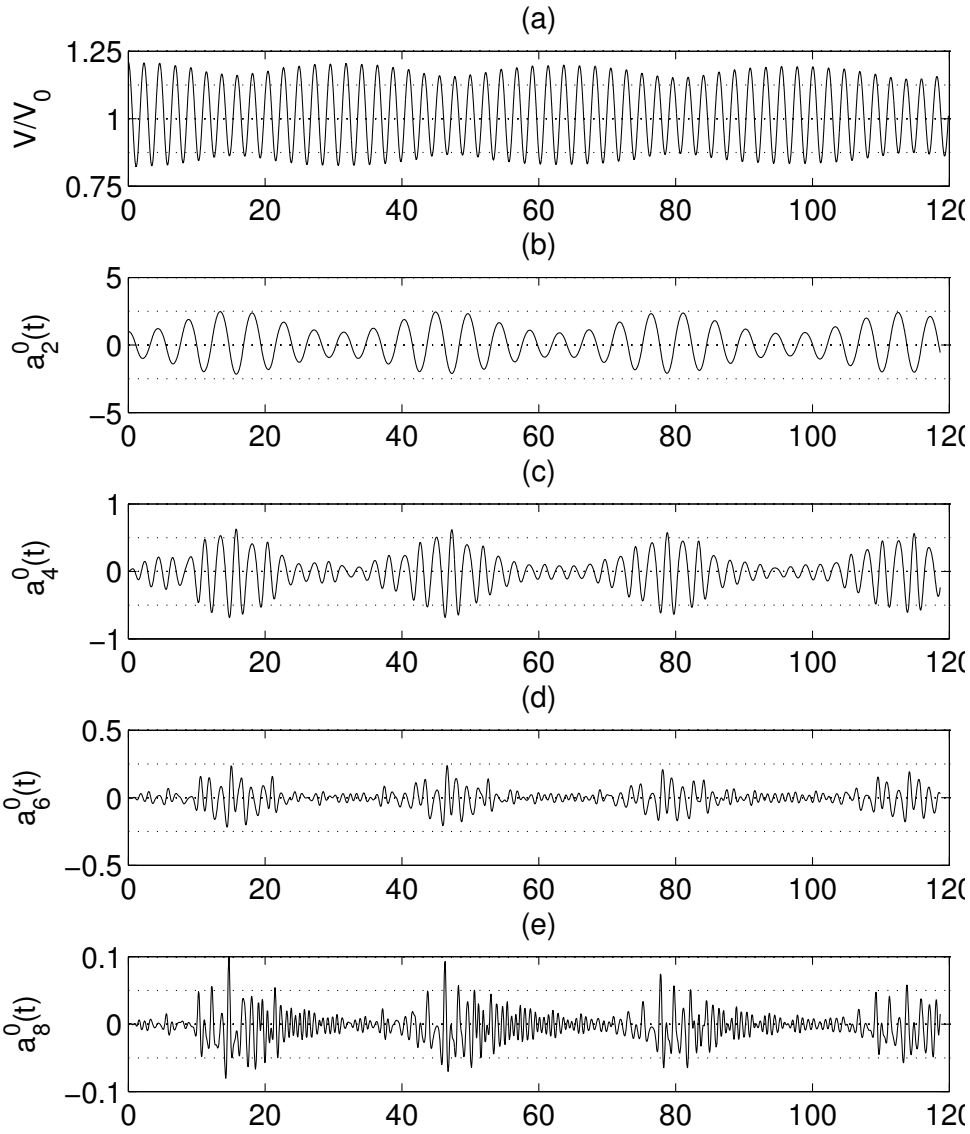

Figure 5.41: Harmonics oscillations, $\epsilon R = 1/16 R_0, \epsilon a_2^0 = 1/8 R_0$, 1442 nodes, quadratic, $\delta t = 0.01$, $R_0^* = 8\mu m$, horizontal axes in μs, vertical axes in μm.

clearly the case, with the volume amplitudes periodically being reduced from ≈ 0.2 to approximately 0.15 while the amplitude of the second mode increases from $1\mu m$ to approximately $2.5\mu m$. The impact on the higher modes is also substantial due to the influence of the second mode.

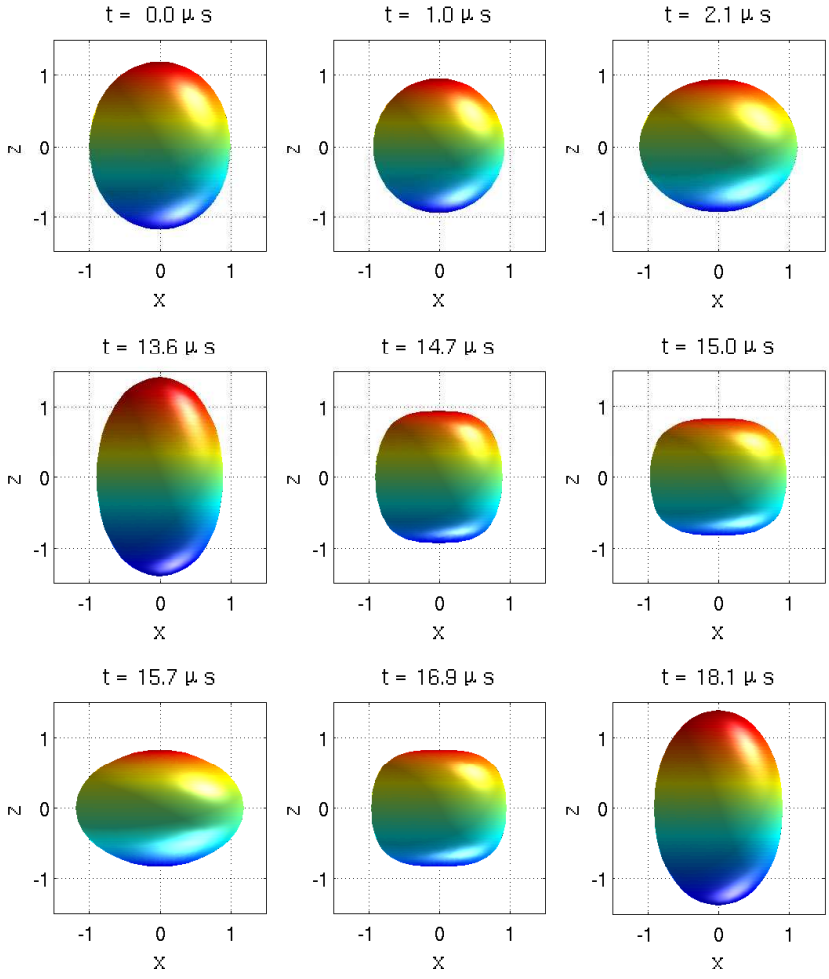

Figure 5.42: Non-dimensional bubble shapes at different times,$\epsilon R = 1/16R_0, \epsilon a_2^0 = 1/8R_0$, quadratic, 1442 nodes, $R_0^* = 8\mu m$.

Some snapshots of the bubble shape can be seen in Figure 5.42. For $t = 0\mu s$, $t = 1.0\mu s$ and $t = 2.1\mu s$ the bubble oscillates between the local extrema for $a_2^0(t)$ with the bubble being approximately spherical for $a_2^0(1.0\mu s) \approx 0$. As the bubble experiences energy transfer from the volume mode to the second

mode, the shapes at the local extrema for a_2^0 ($t \approx 13.6\mu s$, $t \approx 15.7\mu s$ and $t \approx 18.1\mu s$) show considerably stronger deformation, while the shape for $a_2^0(14.7\mu s) \approx 0$ no longer resembles a sphere.

Reducing R_0^* to $7.18\mu m$ increases the energy transfer further as can be seen in Figure 5.43. Since volume oscillations are associated with most of the sound output from bubble oscillation [9], this resonant interaction could result in a substantial reduction in sound output by the bubble oscillation.

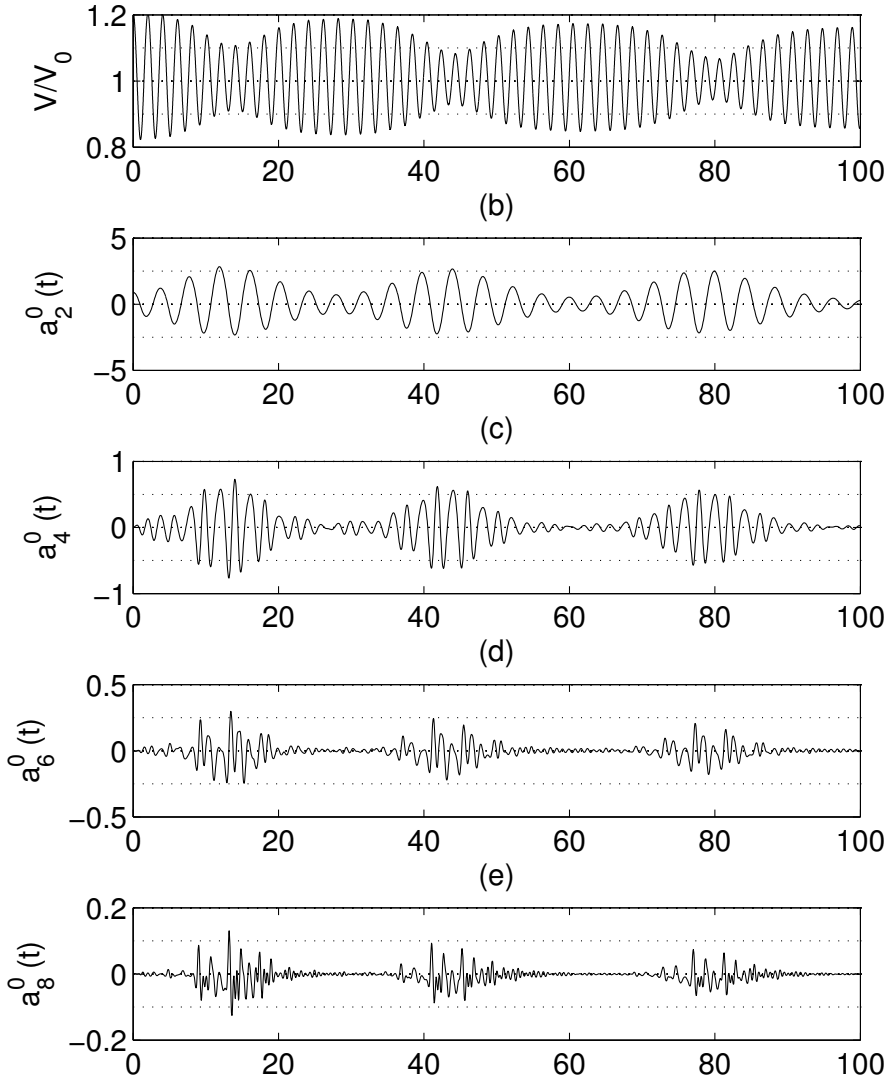

Figure 5.43: Harmonics oscillations, $\epsilon R = 1/16 R_0, \epsilon a_2^0 = 1/8 R_0$, 1442 nodes, quadratic, $\delta t = 0.01$, $R_0^* = 7.18\mu m$, horizontal axes in μs, vertical axes in μm.

The oscillation of the higher order modes are clearly very complex, as can be seen in the spectral decompositions in Figure 5.44 and we will make no attempt at differentiating between specific frequencies, other than to point out the closeness of F_0 and $2F_2$ in both oscillations, leading to the strong energy exchange, confirming the energy exchanges seen by McDougald & Leal [7] using an axisymmetric boundary element method. Also a frequency of ≈ 30 kHz can be seen for all modes, giving an oscillation period of $\approx 33\mu s$, matching the period of energy exchange.

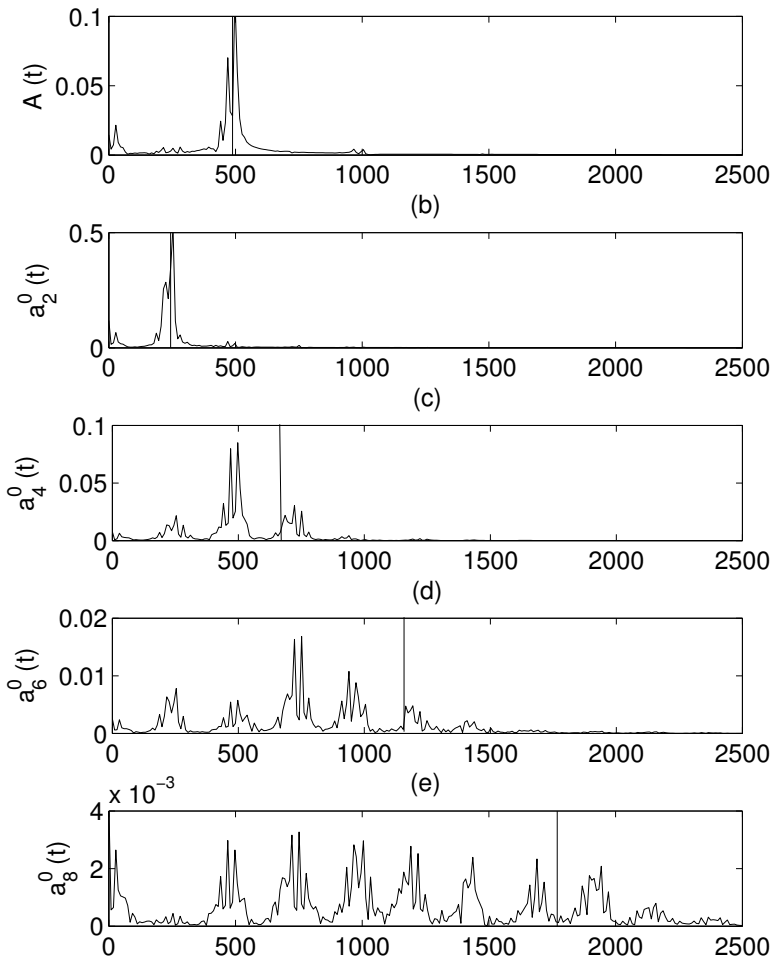

Figure 5.44: Spectral decomposition of harmonics oscillations, $\epsilon R = 1/16R_0, \epsilon a_2^0 = 1/8R_0$, quadratic, 1442 nodes, $R_0^* = 7.18\mu m$, $\delta t = 0.01$, horizontal axes in kHz.

Normally the non-axisymmetric modes $Y_2^{m\neq 0}$ are not expected to get excited through purely axisymmetric oscillations. However, since the natural frequencies are the same for all modes Y_2^m, it is possible, under resonant conditions, that infinitesimal perturbations to the coefficients $a_2^{m\neq 0}$ may grow and lead to finite non-axisymmetric changes of shape.

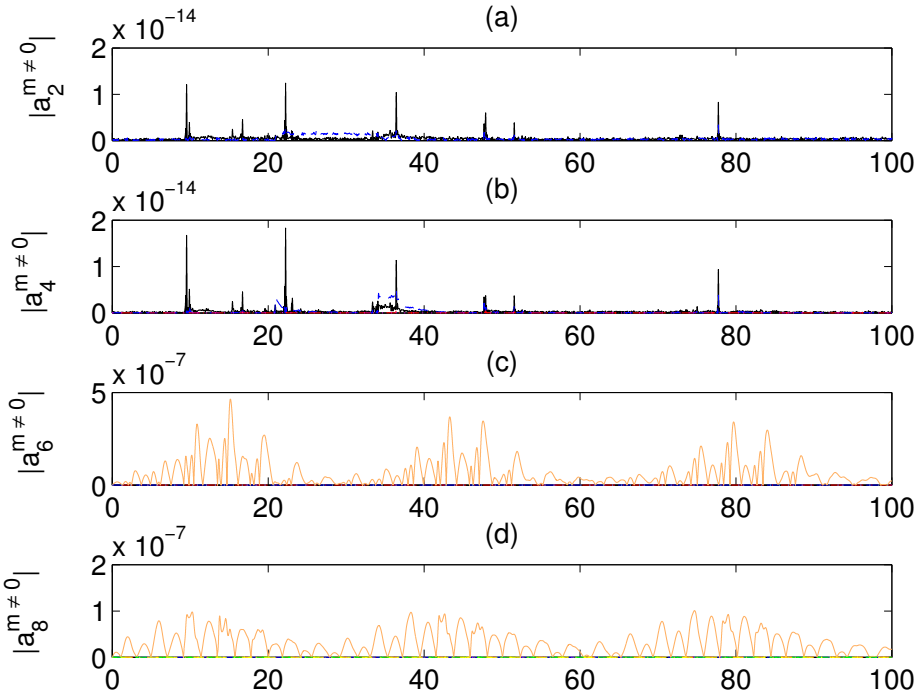

Figure 5.45: Amplitudes of non-axisymmetric modes, $\epsilon R = 1/16 R_0, \epsilon a_2^0 = 1/8 R_0$, 1442 nodes, quadratic, $\delta t = 0.01$, $R_0^* = 7.18 \mu m$, horizontal axes in μs, vertical axes in μm

As can be seen in Figure 5.45 there is considerable amplitude growth in certain of the axisymmetric modes for $l = 6$ and $l = 8$ and the relevant oscillations are shown in Figure 5.46. It is important to note that if these coefficients were scaled to the same level as the axisymmetric coefficients with the scaling factor $\left(\frac{(l-m)!}{(l+m)!}\right)^{-1/2}$ from (5.8), the amplitudes would both be of order 10^{-3} rather than 10^{-7}. While these non-axisymmetric amplitudes are still smaller than the axisymmetric amplitudes seen in Figure 5.43, they

are no longer irrelevant, and given other conditions one may see onset of non-axisymmetric oscillations on a similar scale to the axisymmetric ones.

In this case, the initial perturbation required to see this growth most likely comes from the inherit non-axisymmetric nature of the icosahedron based mesh, and this phenomenon may not appear if an octahedron based mesh is used. However, it still suggests that care is needed when applying axisymmetric models to problems involving resonant bubble interactions, as it is unlikely that any real bubble would avoid any non-axisymmetric distortion throughout its life.

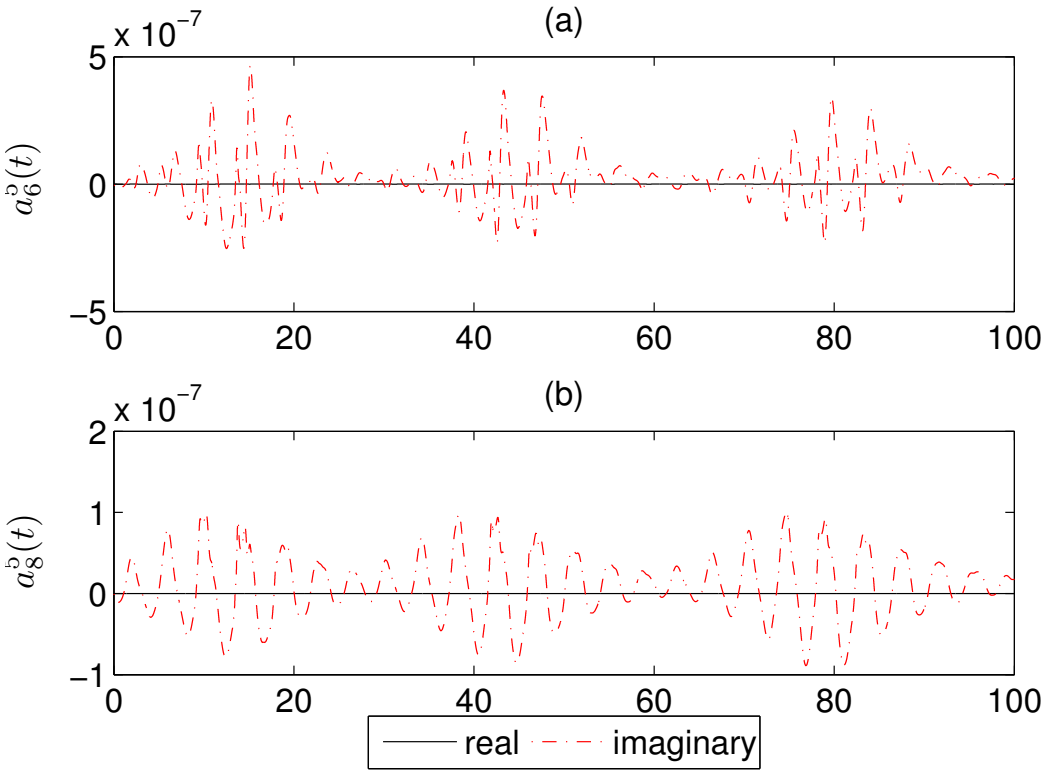

Figure 5.46: Selected non-axisymmetric modes, $\epsilon R = 1/16 R_0, \epsilon a_2^0 = 1/8 R_0$, 1442 nodes, quadratic, $\delta t = 0.01$, $R_0^* = 7.18 \mu m$, horizontal axes in μs, vertical axes in μm

5.3.2 Initial Non-Axisymmetric Distortions of Shape

So far we have dealt with spherical bubble oscillations and axisymmetric shape oscillation, neither of which requires the flexibility of the fully three dimensional IBEM used throughout this work. Figure 5.47 shows a unit radius bubble given an initial distortion of the unscaled parameter $a_l^m = 0.25$ for $l = 0 \ldots 4$, $m = 0 \leq l$. The amplitude of the distortion grows considerably when increasing m due to the factorials in (5.7) being ommitted in the unscaled parameters.

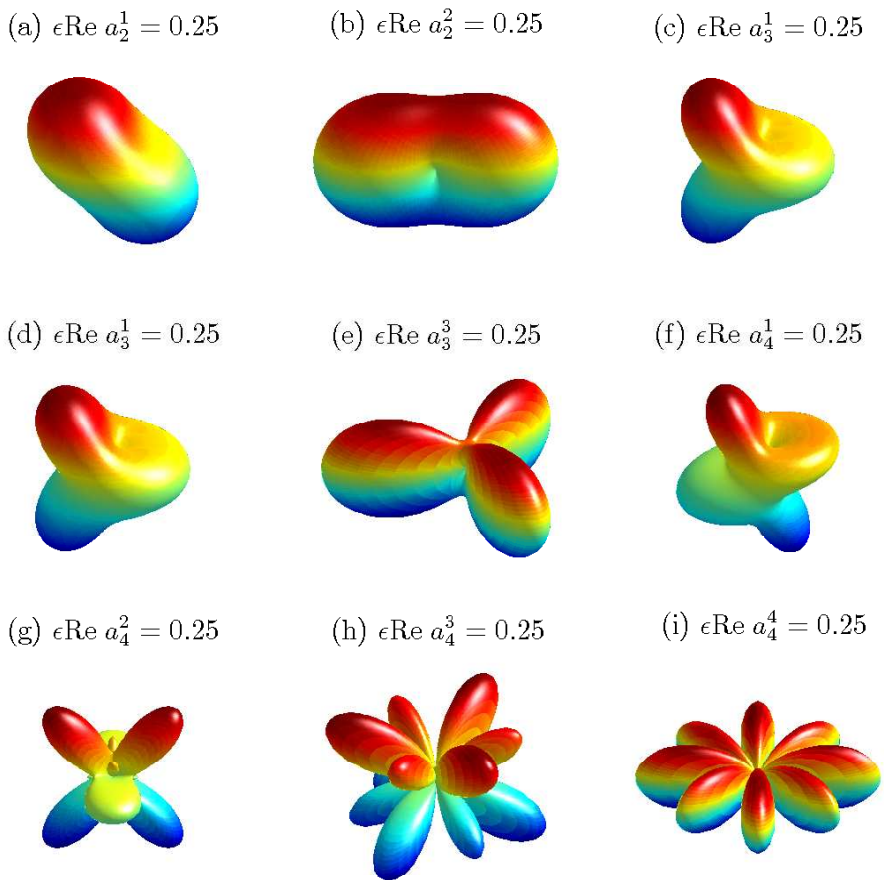

Figure 5.47: The non-axisymmetric modes 2 to 4, unscaled

To keep the harmonics oscillation comparable between modes, we instead use the scaled parameters $\hat{a}_l^m$ resulting in Figure 5.48. This time, all modes show a similar level of distortion from the original spherical shape.

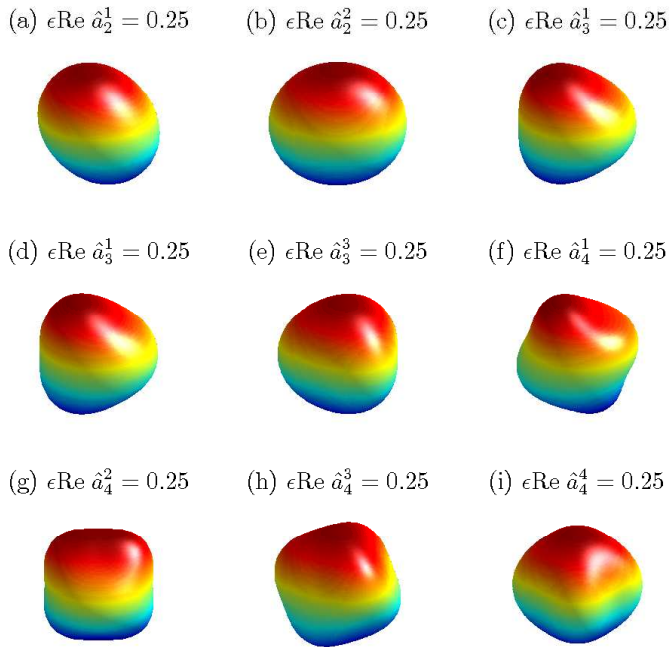

Figure 5.48: The non-axisymmetric modes 2 to 4, scaled

We will present the results from several simulations with an initial non-axisymmetric shape distortion, leading to oscillations of shape and volume, all of which are close to resonance conditions between the volume mode and the modes Y_2^m and Y_4^m. Since no imaginary initial distortions are applied, we will for simplicity let $\epsilon\hat{a}_l^m$ denote a distortion to the real part of $\hat{a}_l^m$ only.

Starting with a bubble of equilibrium radius of $R_0^* = 7.18\mu m$ we give the bubble a volume distortion of $\epsilon R = 0.1R_0$ and an initial shape distortion of $\epsilon a_2^1 = 0.1R_0$. Figures 5.49 to 5.51 shows similar energy exchanges between the volume and the perturbed shape mode as in the previous axisymmetric tests. However, unlike in the axisymmetric case, a distortion in mode $l = 2, m = 1$ causes oscillations in all even modes for any value of m. It can also be seen that a distortion of only the real component of a mode causes

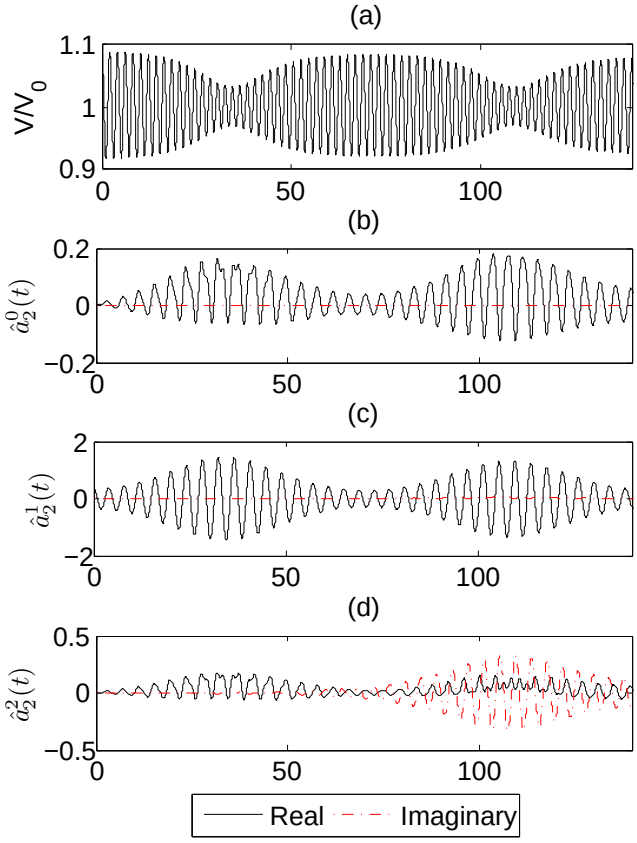

Figure 5.49: Harmonics oscillatios, $\epsilon R = 0.1R_0, \epsilon\hat{a}_2^1 = 0.1R_0$, 1442 nodes, quadratic elements, $\delta t = 0.025$, $R_0^* = 7.18\mu m$, horizontal axes in μs

oscillation of the imaginary component as well. Clearly the second order oscillations have a strong impact on the higher order oscillations as the oscillation envelopes follow the second order modes closely. The oscillations of $\hat{a}_2^0$ and $\hat{a}_2^2$ starts off quite similarly, but the oscillations start diverging as the oscillation amplitudes start growing for the second time. For the modes Y_2^2, Y_4^1 and Y_4^3 the imaginary parts of the Fourier-Legendre coefficients outgrow the real parts and the imaginary part of a_2^2 reaches the highest amplitudes of all coefficients apart from the perturbed one. It appears that the frequency

of the imaginary component oscillation shifts into phase with the oscillations of $\hat{a}_2^1$, whereupon considerable energy exchange takes place.

We also compare the results using 3242 surface nodes against 1442 surface nodes in Figures 5.55 and 5.56. While there is some clear visual difference, in particular for the oscillations with small amplitudes, the accuracy when using 1442 nodes seems good for the lower order modes.

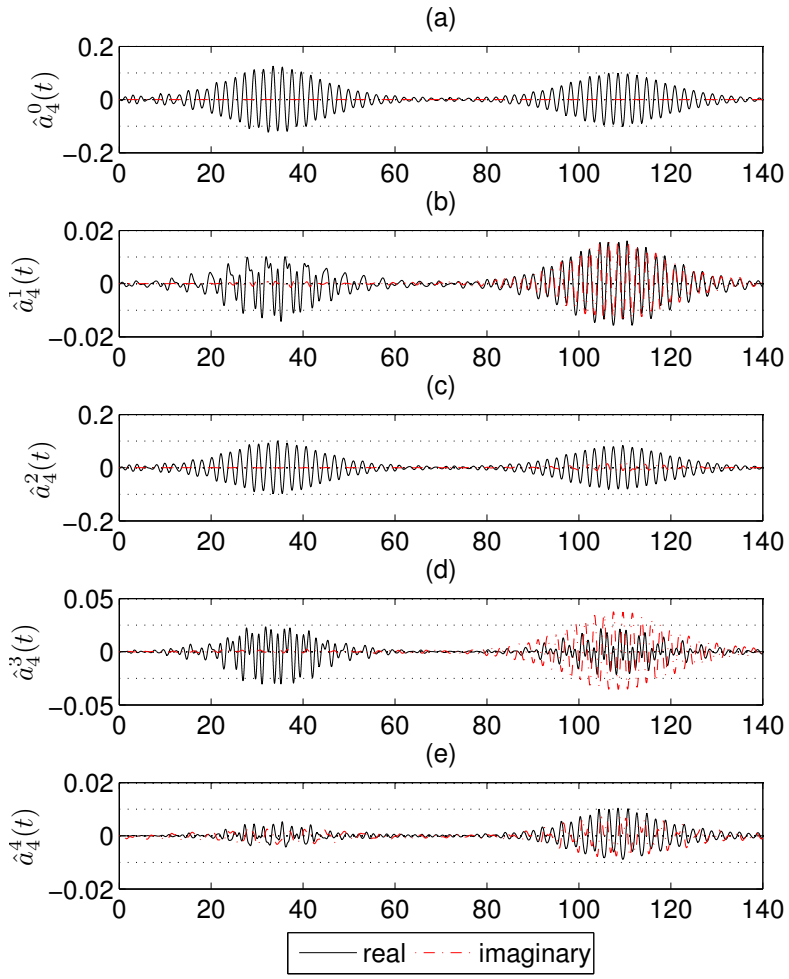

Figure 5.50: Harmonics oscillations, $\epsilon\hat{a}_0^0 = 0.1R_0, \epsilon\hat{a}_2^1 = 0.1R_0$, 1442 nodes, $\delta t = 0.025$, $R_0^* = 7.18\mu m$, horizontal axes in μs.

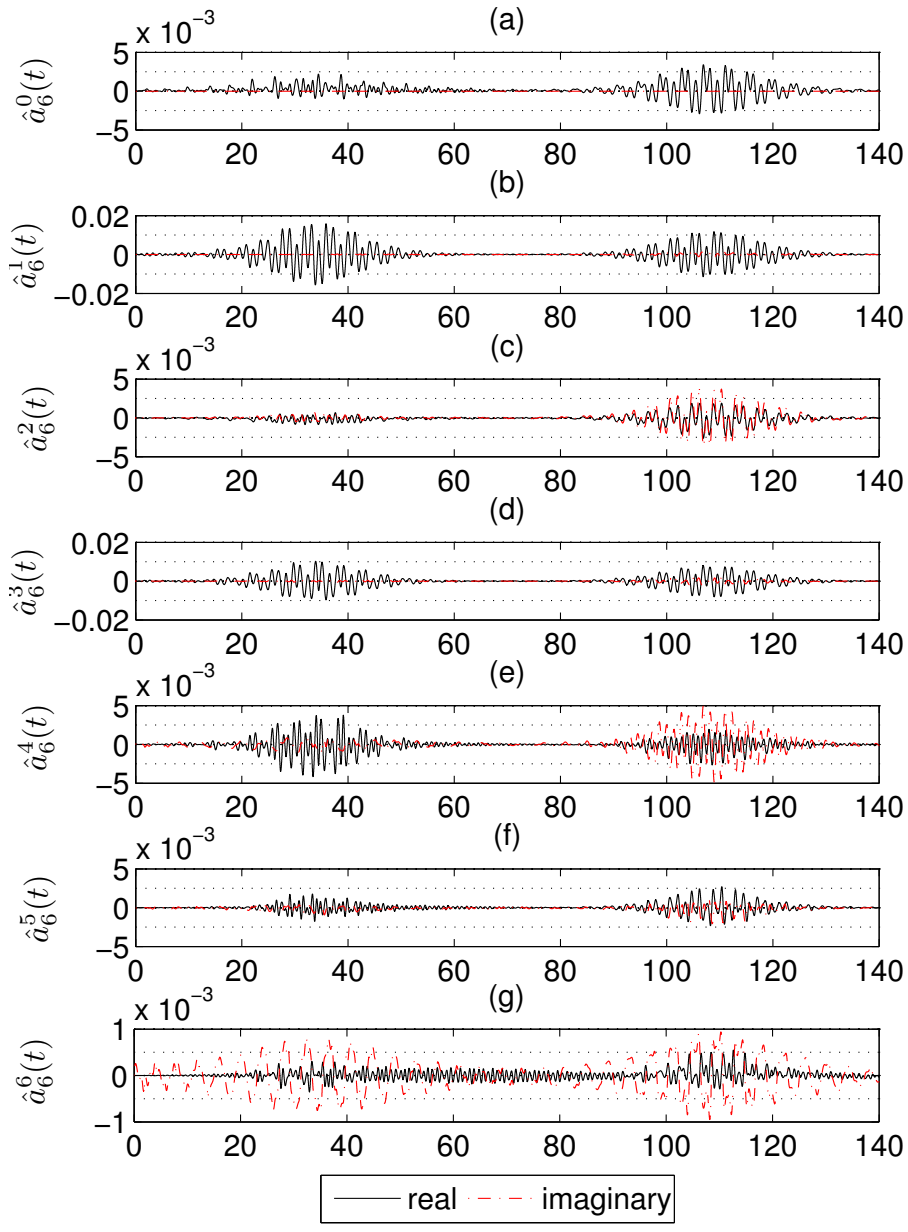

Figure 5.51: Harmonics oscillations, $\epsilon\hat{a}_0^0 = 0.1R_0, \epsilon\hat{a}_2^1 = 0.1R_0$, 1442 nodes, $\delta t = 0.025$, $R_0^* = 7.18\mu m$, horizontal axes in μs.

From the spectral decomposition in Figures 5.52 to 5.54 it appears the volume mode has very varying impact on the oscillations of the real and imaginary components of the coefficients. Since the oscillations need to be in phase, or nearly in phase for energy exchange to occur, a small frequency shift may considerably alter the oscillation amplitudes. Also the frequency of the energy exchange can be seen at around 15 kHz for the volume mode and the Y_2^m modes.

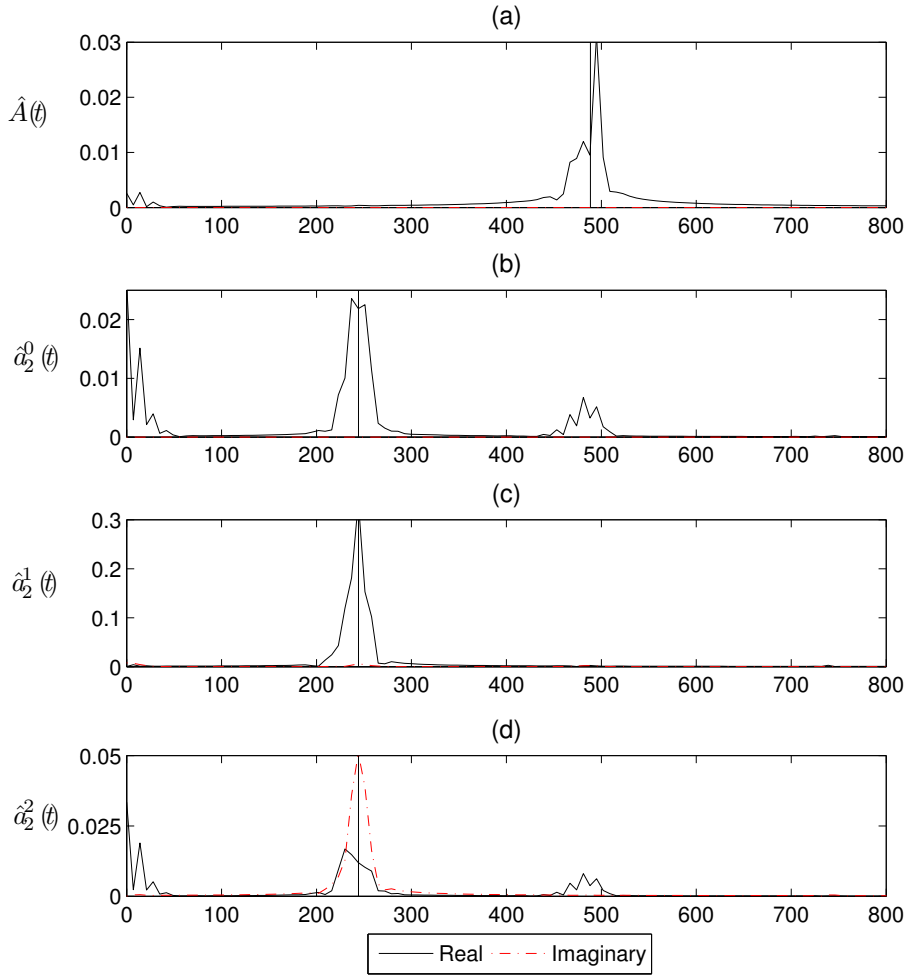

Figure 5.52: Spectral decomposition of Harmonics oscillations, $\epsilon\hat{a}_0^0 = 0.1R_0, \epsilon\hat{a}_2^1 = 0.1R_0$, 1442 nodes, $\delta t = 0.025$, $R_0^* = 7.18\mu m$, horizontal axes in kHz.

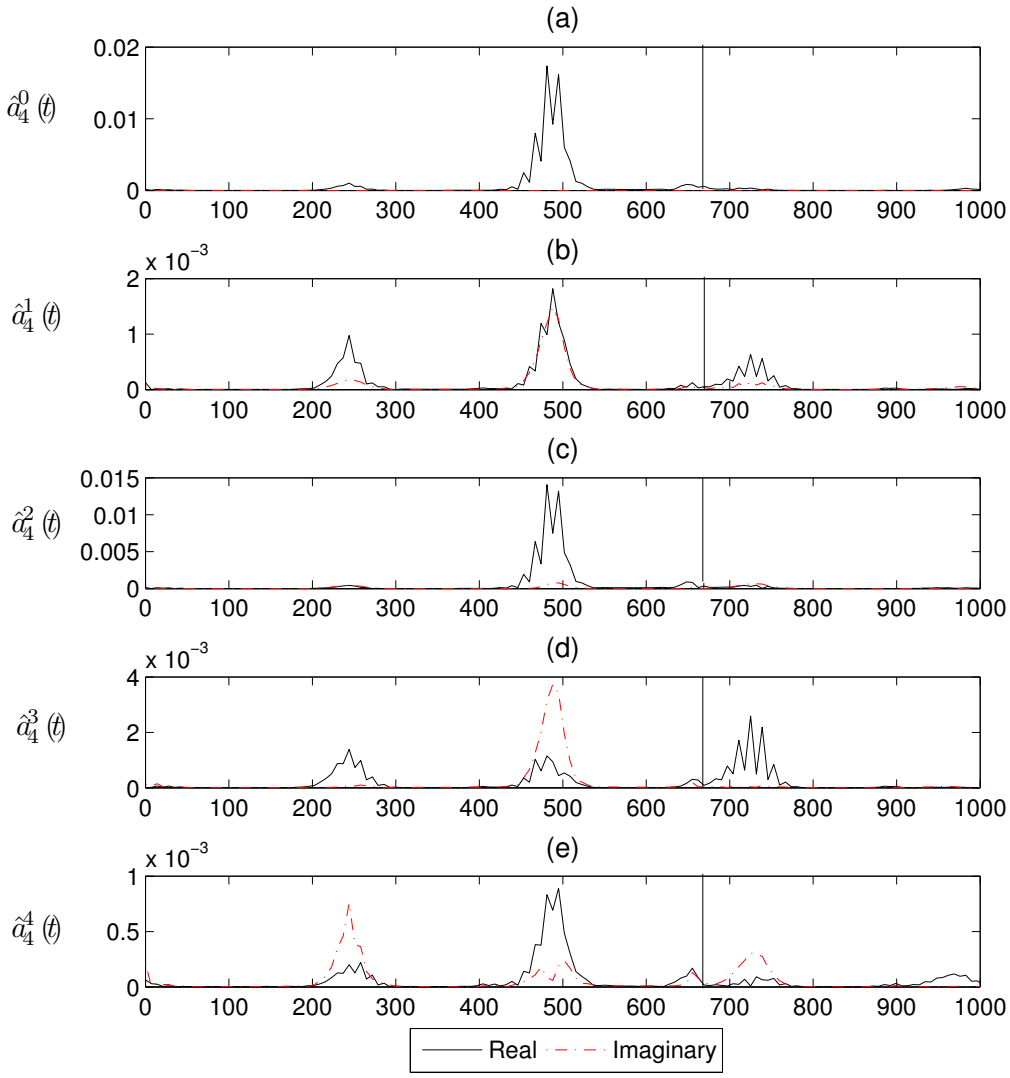

Figure 5.53: Spectral decomposition of harmonics oscillations, $\epsilon\hat{a}_0^0 = 0.1R_0, \epsilon\hat{a}_2^1 = 0.1R_0$, 1442 nodes, $\delta t = 0.025$, $R_0^* = 7.18\mu m$, horizontal axes in kHz.

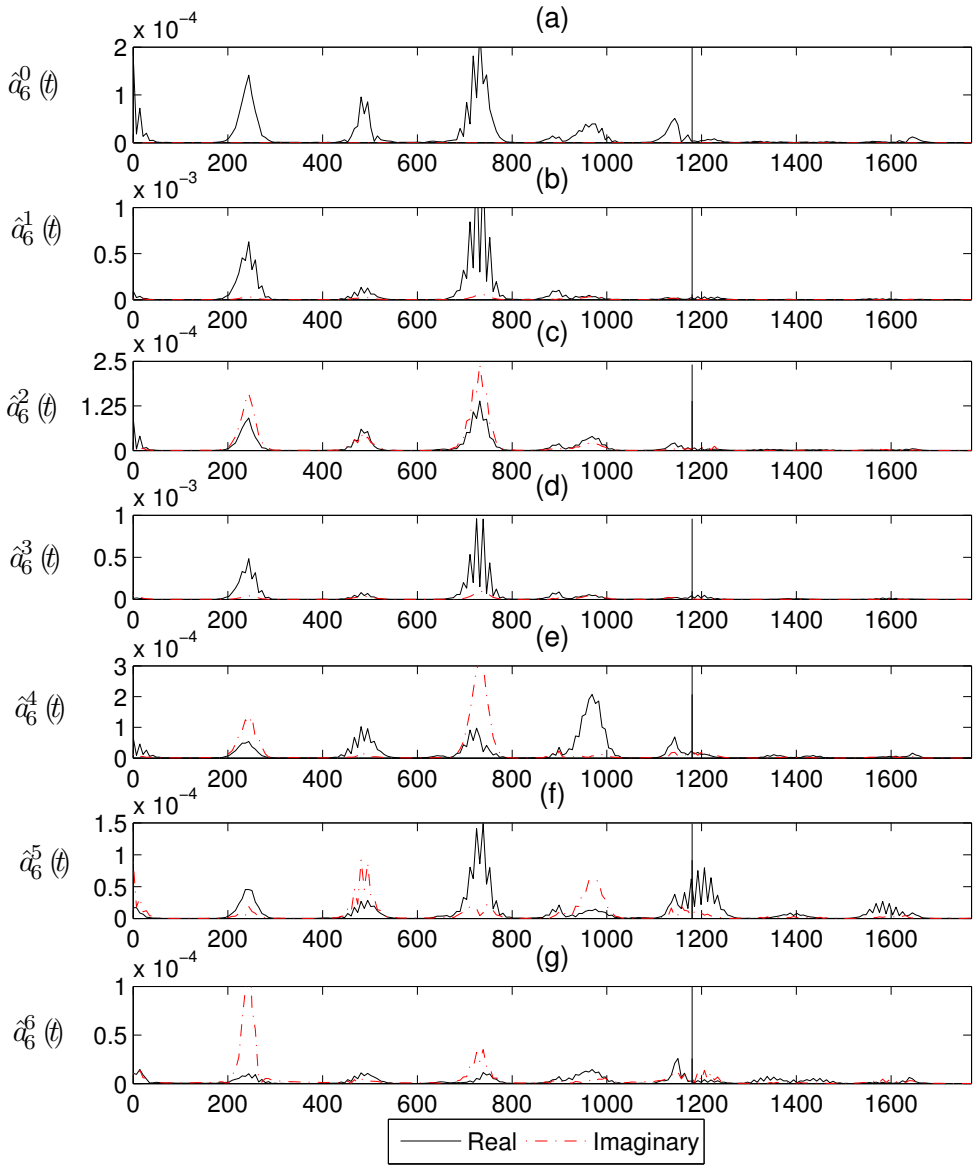

Figure 5.54: Spectral decomposition of harmonics oscillations, $\epsilon\hat{a}_0^0 = 0.1R_0, \epsilon\hat{a}_2^1 = 0.1R_0$, 1442 nodes, $\delta t = 0.025$, $R_0^* = 7.18\mu m$, horizontal axes in kHz.

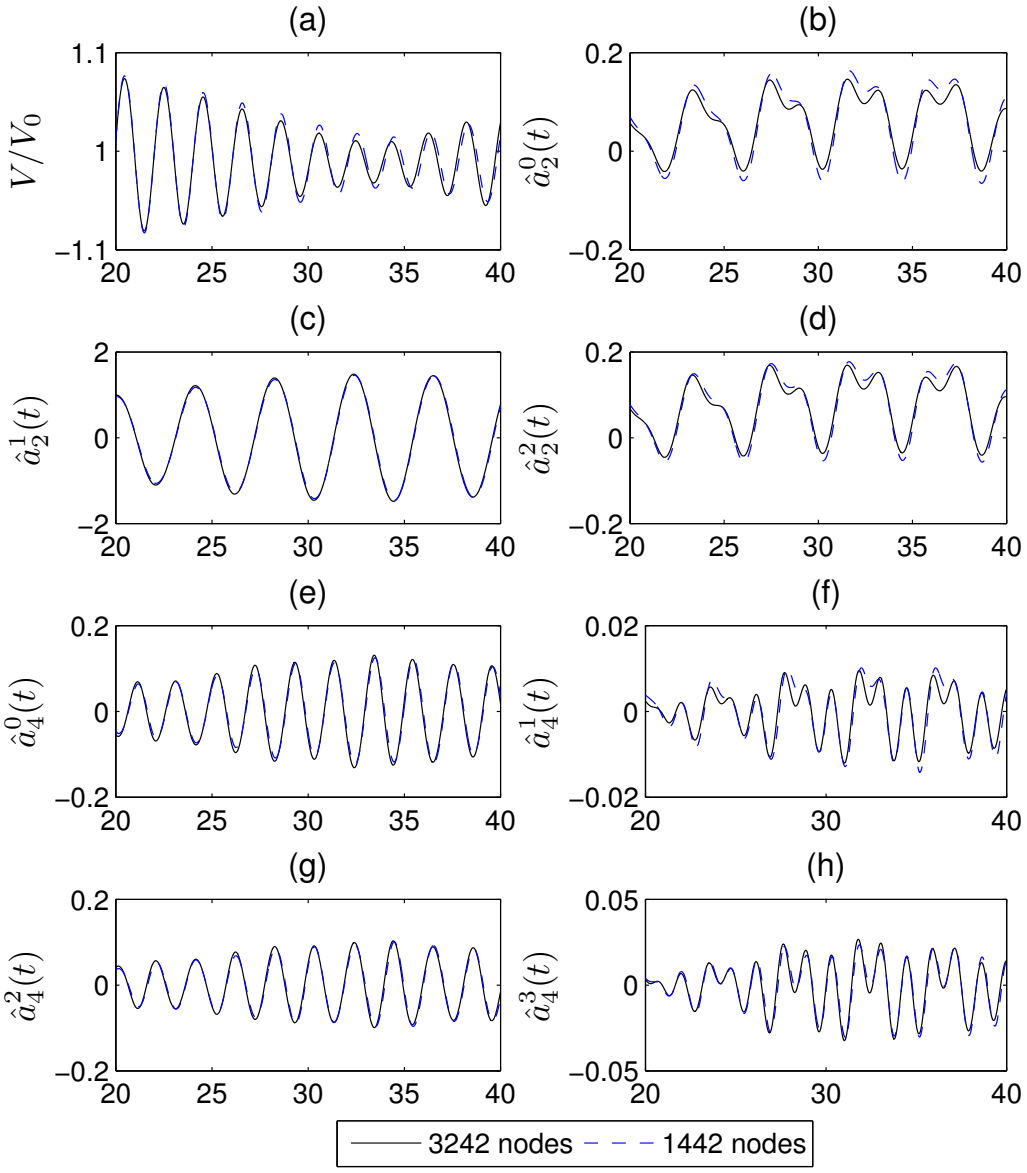

Figure 5.55: Harmonics oscillations, $\epsilon\hat{a}_0^0 = 0.1R_0, \epsilon\hat{a}_2^1 = 0.1R_0$, $\delta t = 0.025$, $R_0^* = 7.18\mu m$, horizontal axes in μs, comparison between 1442 and 3242 nodes.

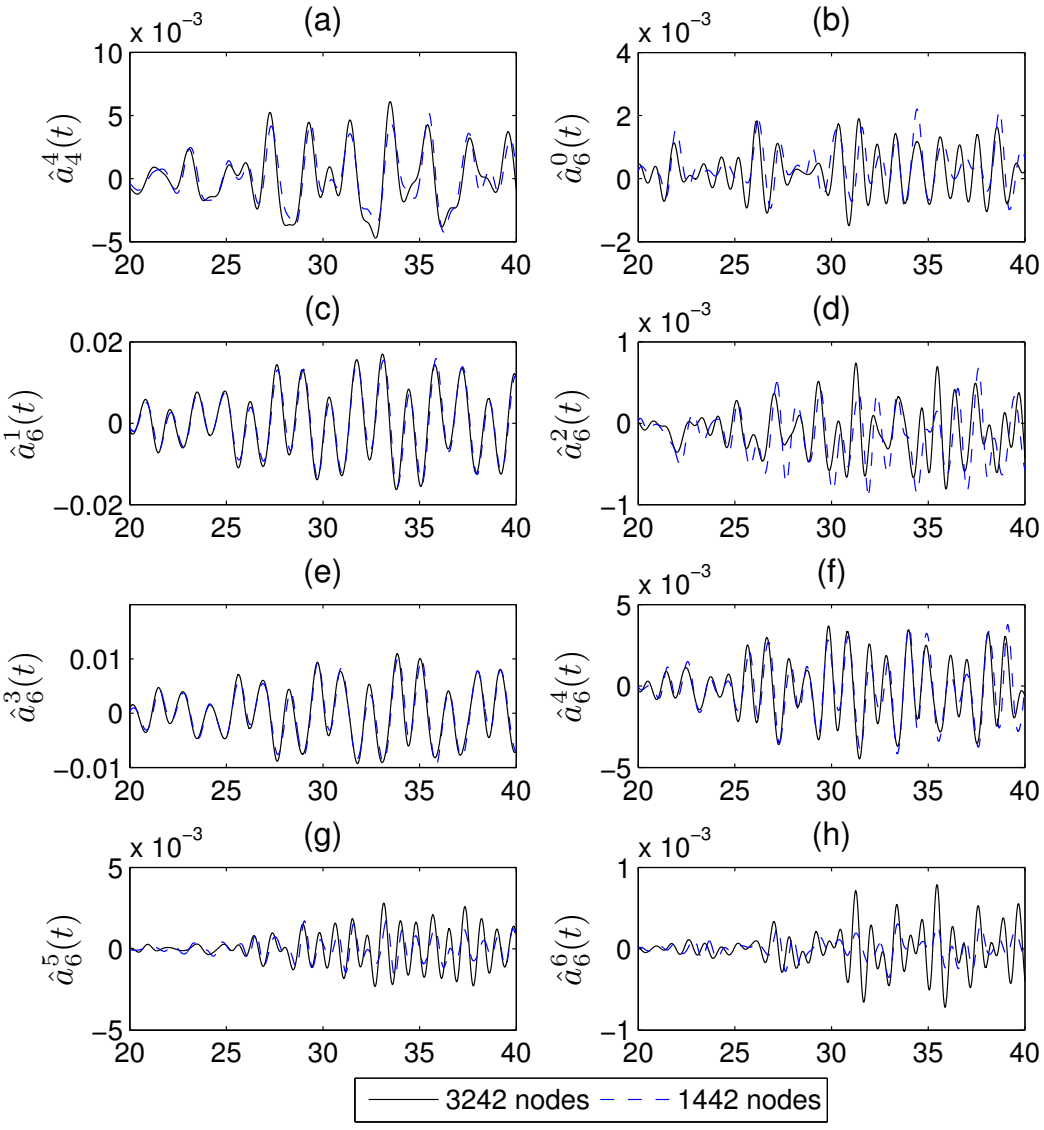

Figure 5.56: Harmonics oscillations, $\epsilon\hat{a}_0^0 = 0.1R_0, \epsilon\hat{a}_2^1 = 0.1R_0$, $\delta t = 0.025$, $R_0^* = 7.18\mu m$, horizontal axes in μs, comparison between 1442 and 3242 nodes.

Next, we apply an axisymmetric distortion of $\epsilon\hat{a}_2^0 = 0.1R_0$ in addition to the previous distortion of $\epsilon\hat{a}_2^1 = 0.1R_0$ to a bubble of the same $R_0^* = 7.18\mu m$ and simulate the oscillations using 1442 and 3242 nodes, resulting in the oscillations seen in Figures 5.57 to 5.59.

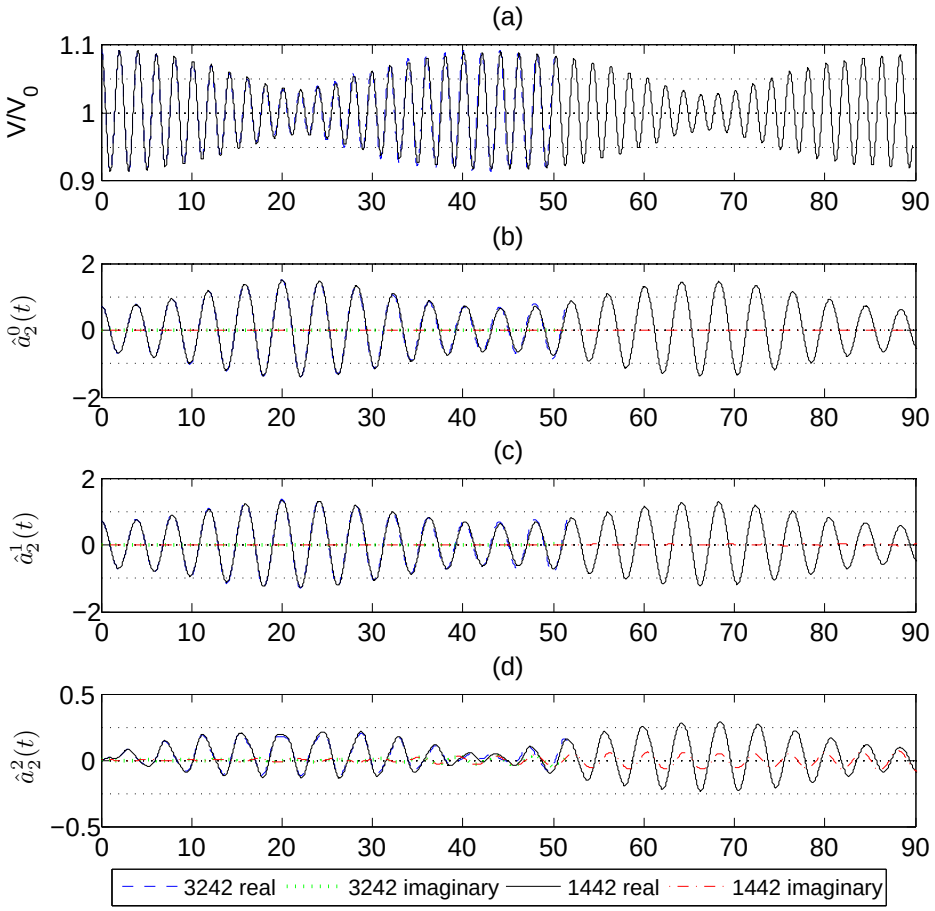

Figure 5.57: Harmonics oscillations, $\epsilon\hat{a}_0^0 = 0.1R_0, \epsilon\hat{a}_2^0 = \epsilon\hat{a}_2^1 = 0.1R_0$, $\delta t = 0.025$, $R_0 = 7.18\mu m$, horizontal axes in μs.

Due to the computational cost when using the finer mesh, the simulation using 3242 nodes is only carried out up until $50\mu s$ and used for comparison. The results using 1442 nodes appear close enough to make sound judgements concerning coefficients up to $\hat{a}_6^4$. The energy exchange is clearly considerably quicker than for the single mode $\epsilon\hat{a}_2^1 = 0.1R_0$ due to the larger combined

deformation and one period of energy exchange happens over approximately $45\mu s$ rather than $70\mu s$.

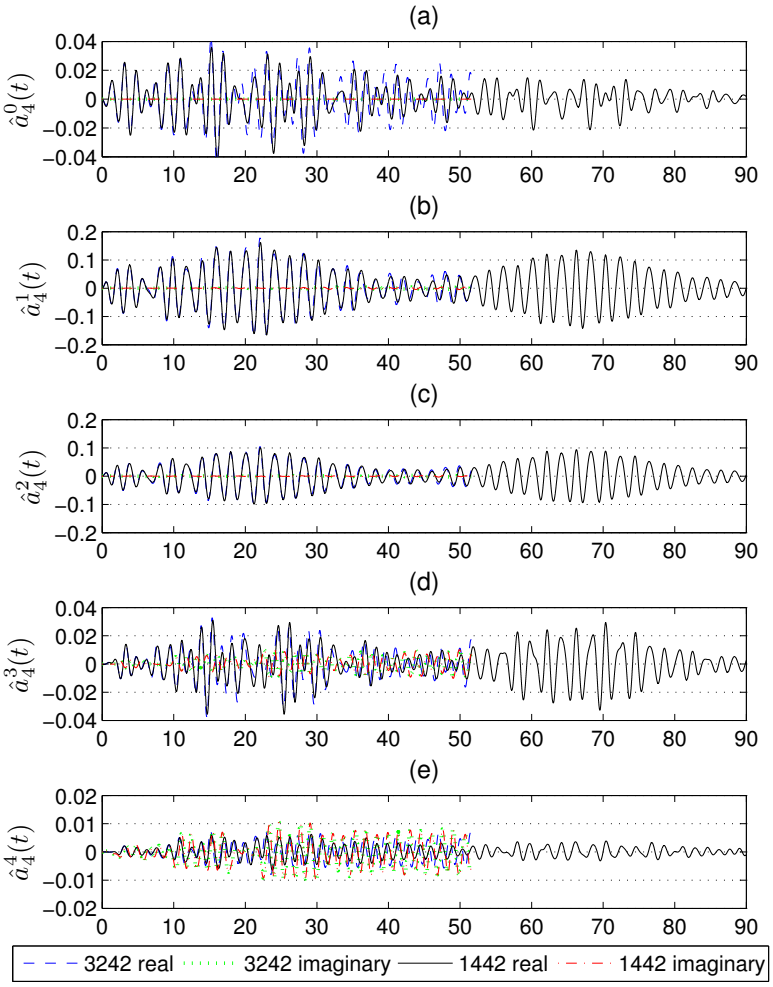

Figure 5.58: Harmonics oscillations, $\epsilon\hat{a}_0^0 = 0.1R_0, \epsilon\hat{a}_2^0 = \epsilon\hat{a}_2^1 = 0.1R_0$, $\delta t = 0.025$, $R_0 = 7.18\mu m$, horizontal axes in μs.

The change in amplitudes vary considerably between modes. The amplitudes of some coefficients, such as $\hat{a}_4^1$, $\hat{a}_6^0$ and $\hat{a}_6^2$ grow by an order of magnitude, while $\hat{a}_4$ drop by an order of magnitude. While a distortion of the axisymmetric Y_2^0 mode does not excite the non-axisymmetric modes on its own, it seems it may combine with the non-axisymmetric Y_2^1 mode to excite them. Also, despite the considerable impact a distortion to either the

$\hat{a}_2^0$ or the $\hat{a}_2^1$ coefficients may have on the a_4^0 coefficient, they seem to cancel each other out when combined.

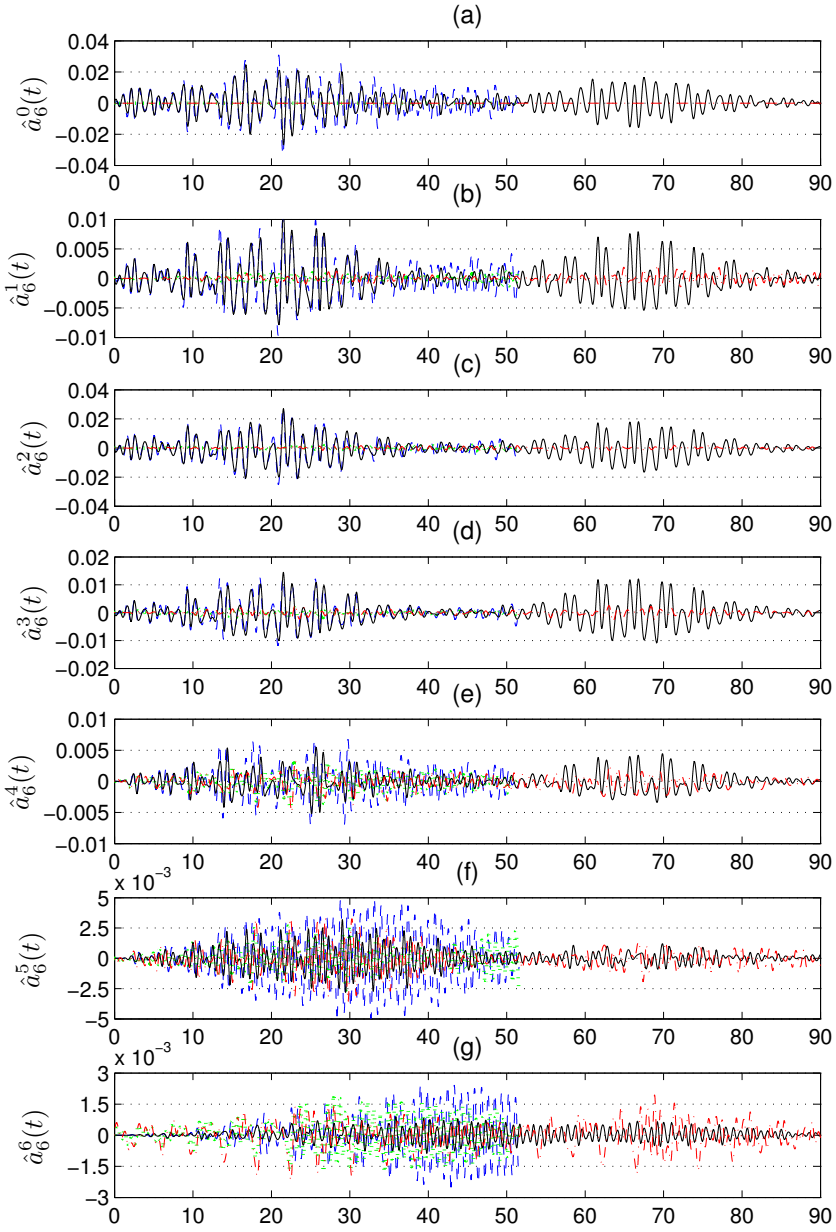

Figure 5.59: Harmonics oscillations, $\epsilon\hat{a}_0^0 = 0.1R_0, \epsilon\hat{a}_2^0 = \epsilon\hat{a}_2^1 = 0.1R_0$, $\delta t = 0.025$, $R_0 = 7.18\mu m$, horizontal axes in μs.

The reason for the two distortions leading to smaller amplitudes for cer-

tain modes may be analogous to two standing waves of opposite phase cancelling each other out. To test this out we multiply the initial distortion $\epsilon\hat{a}_2^1$ by -1 and perform a simulation using the same parameters as before using 1442 nodes, with harmonics oscillations shown in Figures 5.60 and 5.61. The change to $\hat{a}_2^1$ has no noticable effect on the volume mode oscillations and causes only a slight phase change for the imaginary component of $\hat{a}_2^2$.

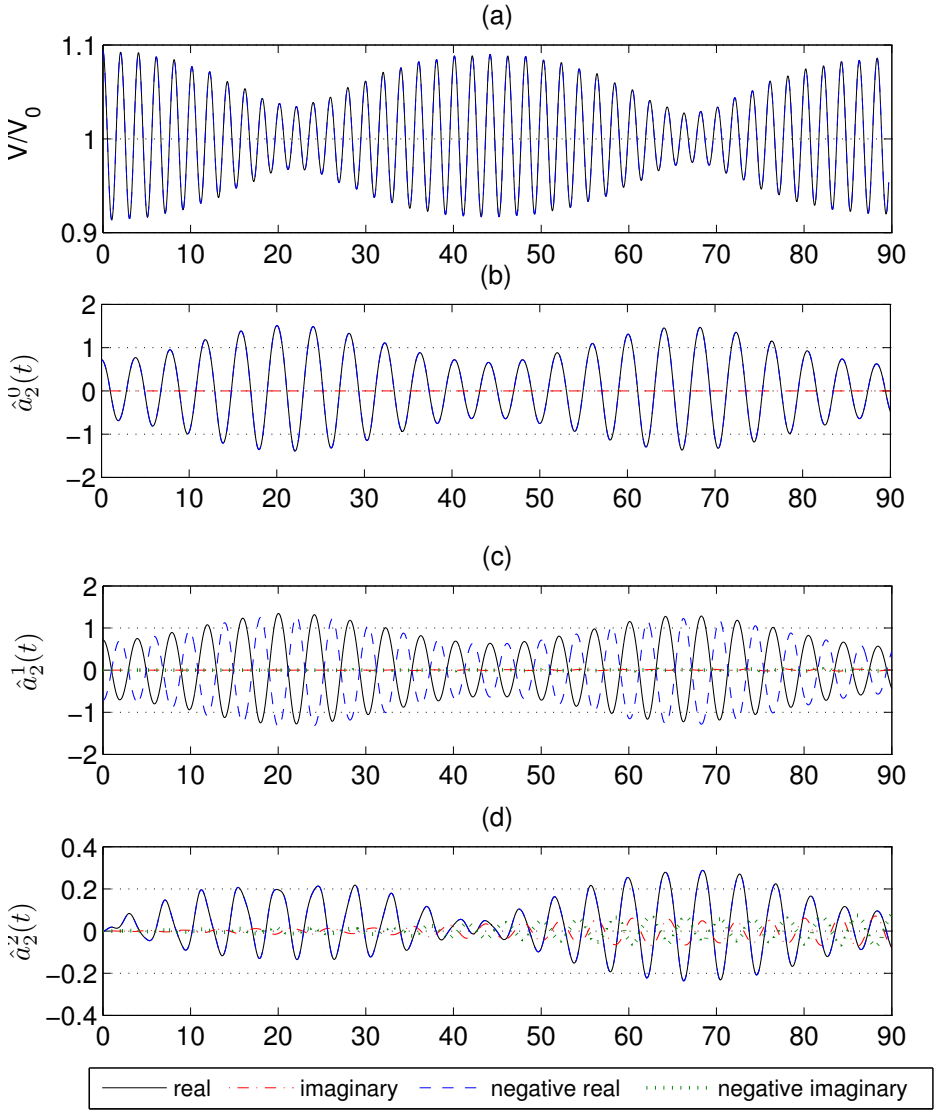

Figure 5.60: Harmonics oscillations, $\epsilon\hat{a}_0^0 = 0.1R_0, \epsilon\hat{a}_2^0 = -\epsilon\hat{a}_2^1 = 0.1R_0$, 1442 nodes, $\delta t = 0.025$, $R_0 = 7.18\mu m$, horizontal axes in μs.

For the modes $l > 2$ it seems the real component oscillations are either exactly the same or exactly opposite sign with only the imaginary components being affected differently.

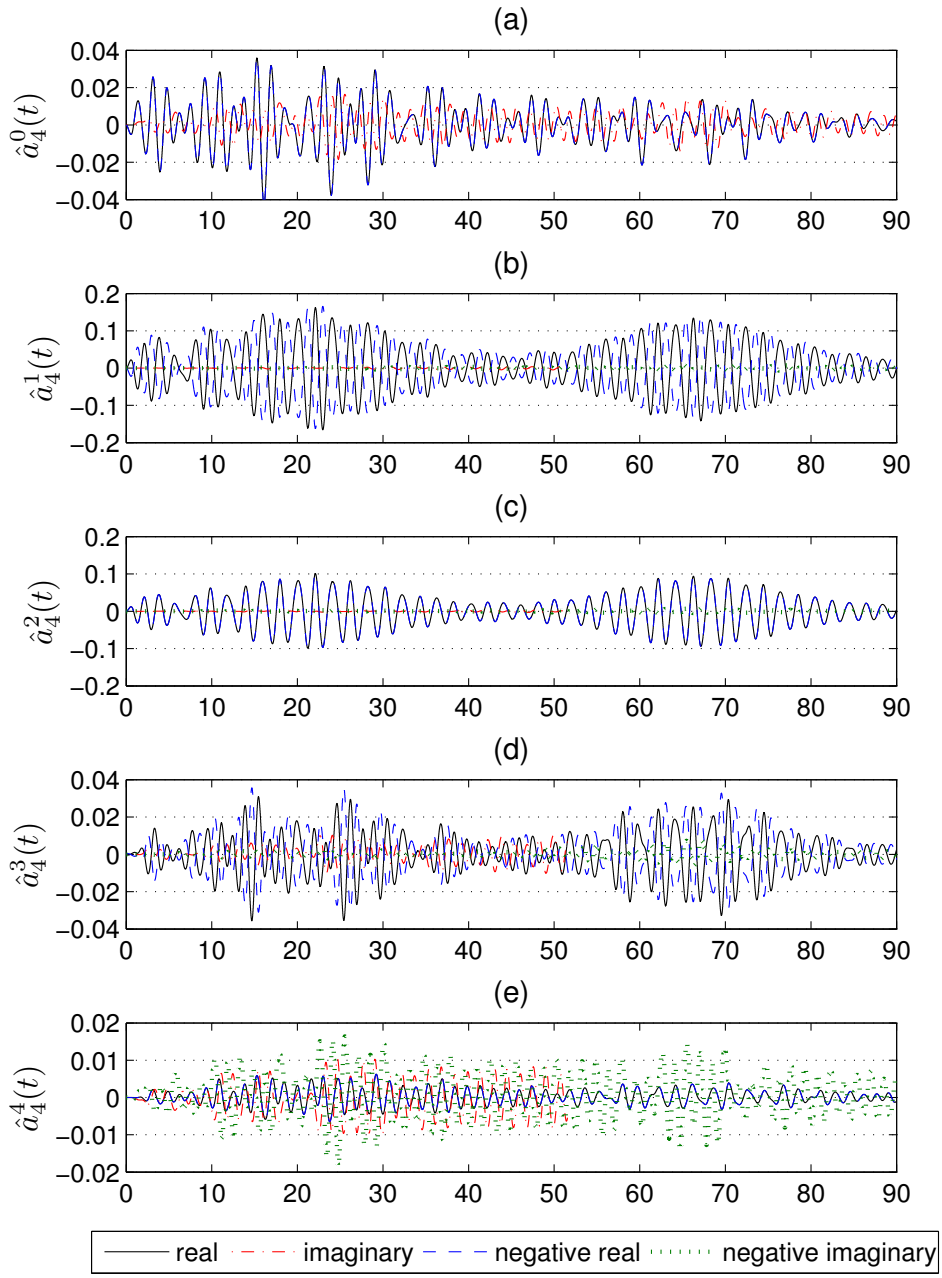

Figure 5.61: Harmonics oscillations, $\epsilon\hat{a}_0^0 = 0.1R_0, \epsilon\hat{a}_2^0 = -\epsilon\hat{a}_2^1 = 0.1R_0$, 1442 nodes, $\delta t = 0.025$, $R_0 = 7.18\mu m$, horizontal axes in μs.

After seeing resonant interaction between the Y_2^m modes and the volume mode, we move on to higher order mode distortions. First, we consider a bubble of radius $R_0^* = 40\mu m$ given an initial deformation of $\epsilon R = 0.1R_0$ and $\epsilon\hat{a}_4^1 = 0.05R_0$. The initial radius is far away from $R_R^4 \approx 61.0\mu m$ and there should thus be no energy exchange between the two distorted modes. Figure

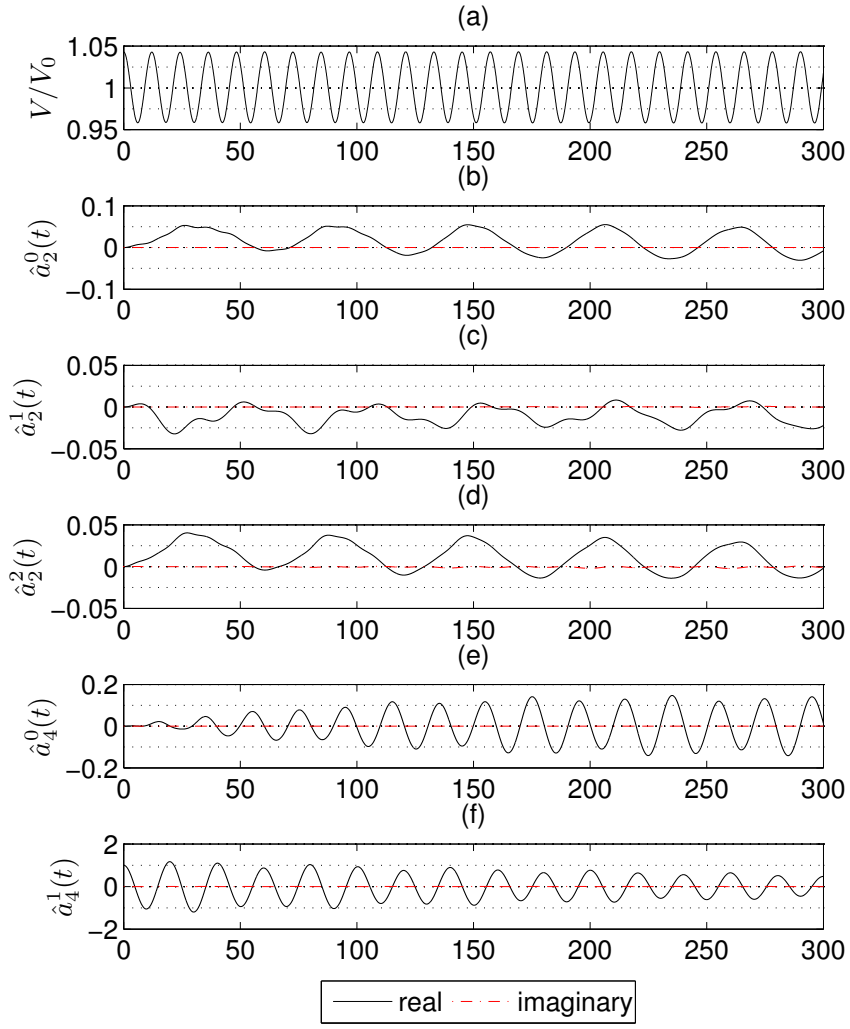

Figure 5.62: Harmonics oscillations, $\epsilon\hat{a}_0^0 = 0.1R_0, \epsilon\hat{a}_4^1 = 0.025R_0$, 1442 nodes, quadratic elements, $\delta t = 0.01$, $R_0 = 40\mu m$, horizontal axes in μs.

5.62 shows that the volume oscillates in an expected sinusoidal fashion. The amplitudes of the $\hat{a}_4^1$ coefficient is, however, clearly diminishing towards the

end of the simulation. While this could be due to smoothing, it seems more likely to be due to energy exchange with the other $l = 4$ modes, as Figure 5.62 and 5.63 show growth in the amplitudes for these modes. As the simulation was carried out with only 1442 surface nodes, we refrain from presenting oscillations of modes beyond Y_6^2.

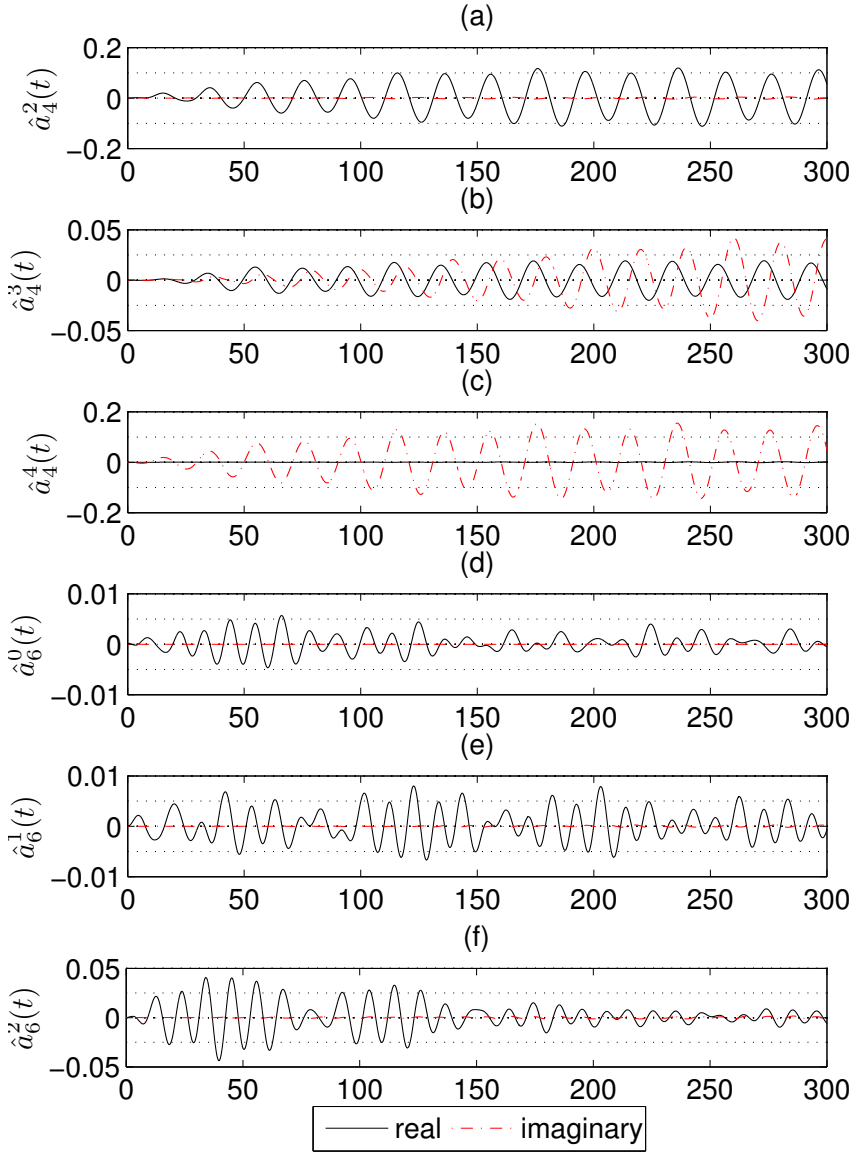

Figure 5.63: Harmonics oscillations, $\epsilon\hat{a}_0^0 = 0.1R_0, \epsilon\hat{a}_4^1 = 0.025R_0$, 1442 nodes, quadratic elements, $\delta t = 0.01$, $R_0 = 40\mu m$, horizontal axes in μs.

If we increase the initial radius to $R_0^* = 61\mu m$, we should expect to see resonant energy exchange and this is indeed seen in Figures 5.64 to 5.67. Interestingly the amplitude growth for the Y_4^1 mode seems to cause strong growth in the $\hat{a}_2^0$ and $\hat{a}_2^2$ coefficients.

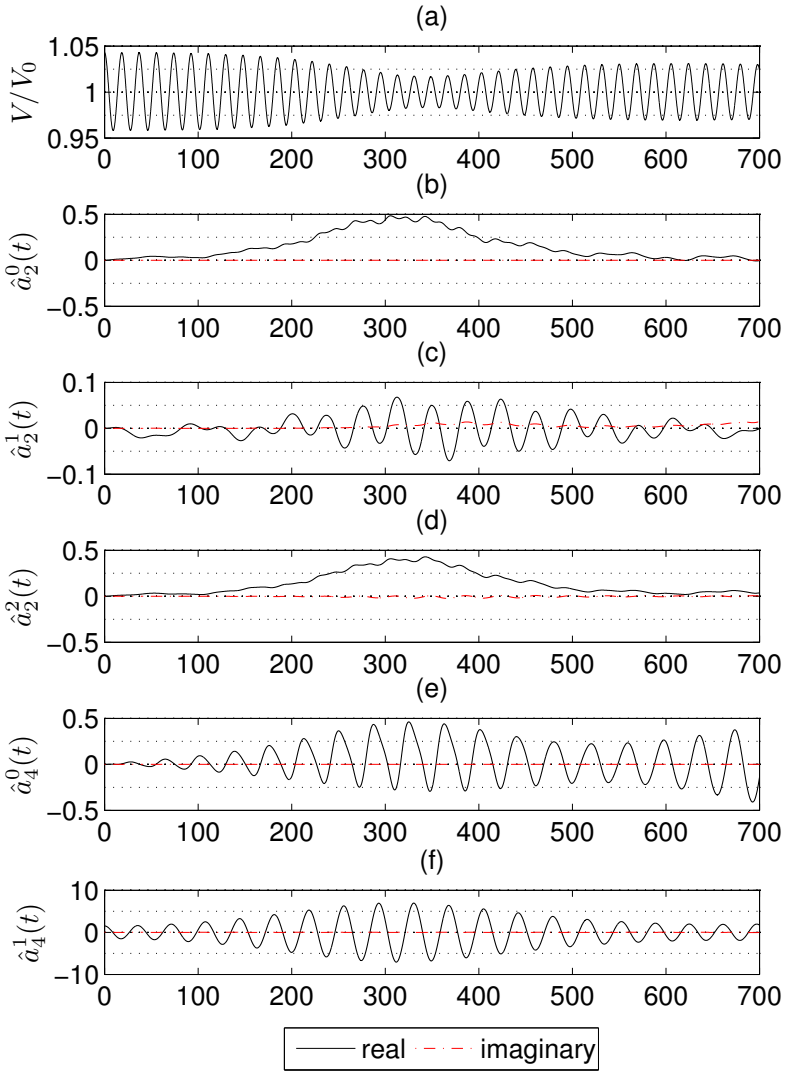

Figure 5.64: Harmonics oscillations, $\epsilon\hat{a}_0^0 = 0.1R_0, \epsilon\hat{a}_4^1 = 0.025R_0$, 3242 nodes, quadratic elements, $\delta t = 0.01$, $R_0 = 61\mu m$, horizontal axes in μs.

As in previous simulations (for example Figure 5.50) other modes get excited by the resonant oscillation in the Y_4^1 mode and thus exhibit similar growth in amplitudes at a smaller scale. For some modes, including Y_4^0, Y_4^2

and Y_6^4, this excitation appears delayed and the real $\hat{a}_6^4$ coefficient reaches maximum amplitude as the amplitudes of the $\hat{a}_4^1$ coefficients are starting to diminish.

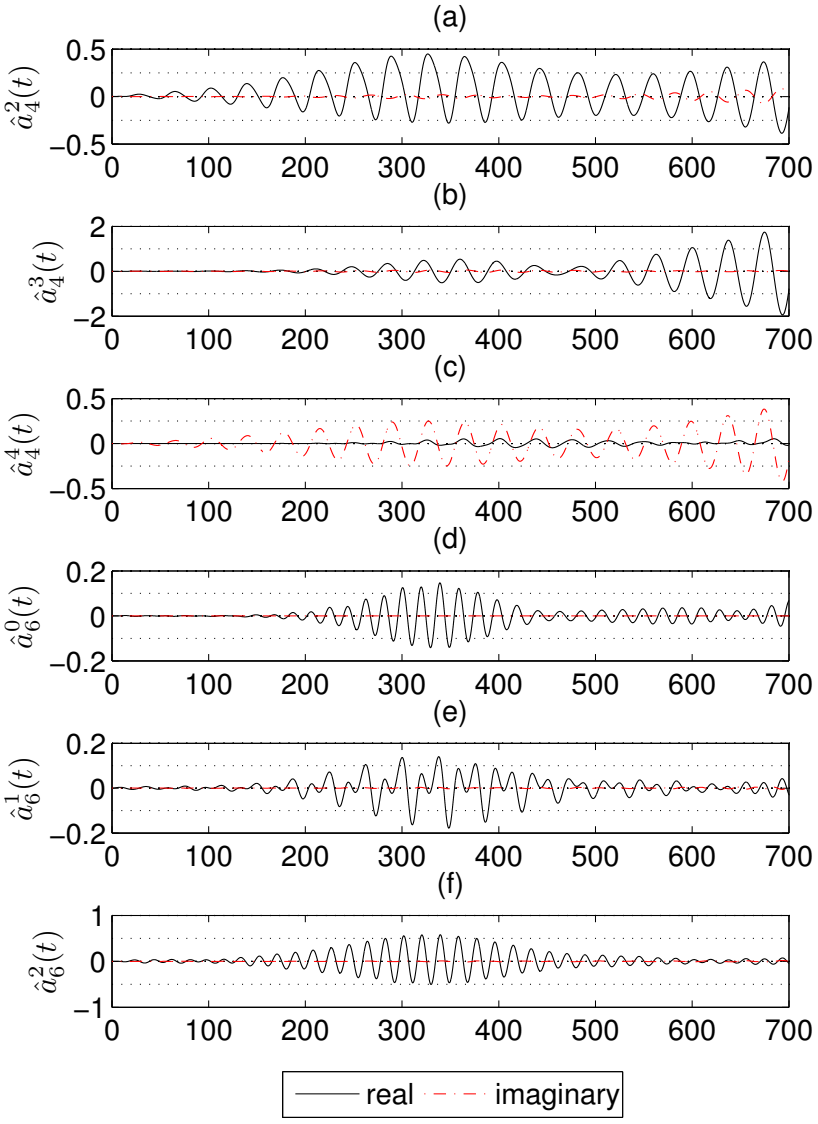

Figure 5.65: Harmonics oscillations, $\epsilon\hat{a}_0^0 = 0.05R_0, \epsilon\hat{a}_4^1 = 0.05R_0$, 3242 nodes, quadratic elements, $\delta t = 0.01$, $R_0 = 61\mu m$, horizontal axes in μs.

Apart from Y_4^m modes, the real coefficient of the Y_8^0 mode reaches the highest amplitudes, and as can be seen in Figure 5.68 it is dominated by the influence by the Y_4^1 mode so that the frequency of oscillation is exactly twice

that of its influence. This means that the real component of $\hat{a}_8^0$ reaches its maximum when the real component of $\hat{a}_4^1$ is zero. Because of this, the bubble shape at $t = 302.9\mu s$ seen in Figure 5.69 shows a clear influence of the Y_8^0 mode if compared with Figure 5.20 (g).

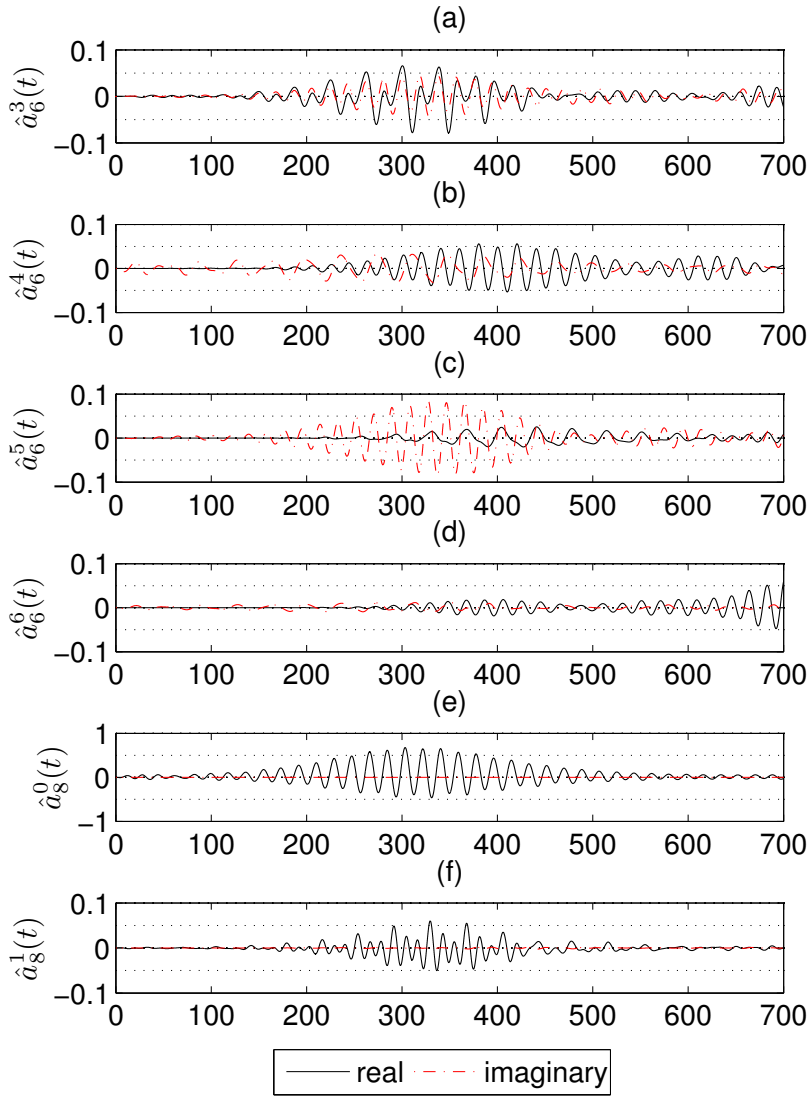

Figure 5.66: Harmonics oscillations, $\epsilon\hat{a}_0^0 = 0.05R_0, \epsilon\hat{a}_4^1 = 0.025R_0$, 3242 nodes, $\delta t = 0.01$, $R_0 = 61\mu m$, horizontal axes in μs.

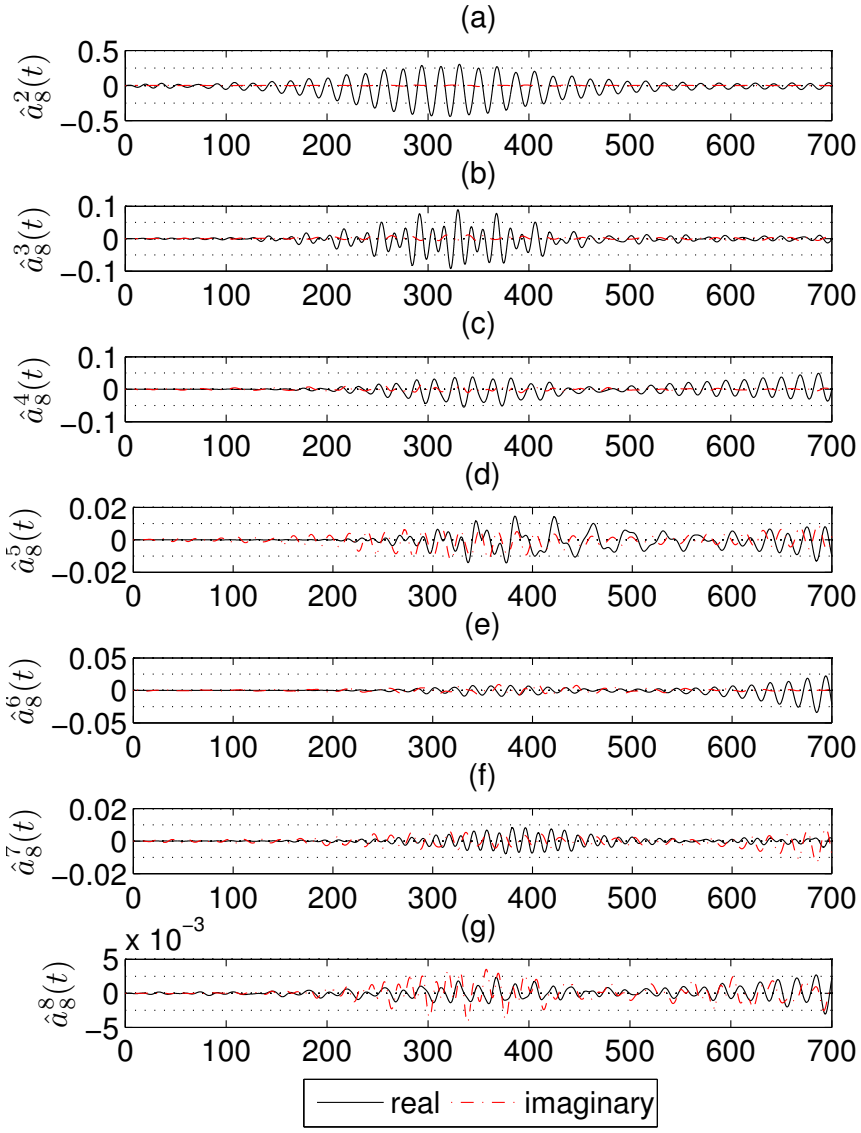

Figure 5.67: Harmonics oscillations, $\epsilon\hat{a}_0^0 = 0.05R_0, \epsilon\hat{a}_4^1 = 0.025R_0$, 3242 nodes, $\delta t = 0.01$, $R_0 = 61\mu m$, horizontal axes in μs.

Again the bubble shapes look increasingly distorted as energy leaks from the volume mode into the resonant mode and the bubble shapes at $t = 293.7\mu s$ and $t = 311.6\mu s$ are clearly heavily influenced by the Y_4^1 mode.

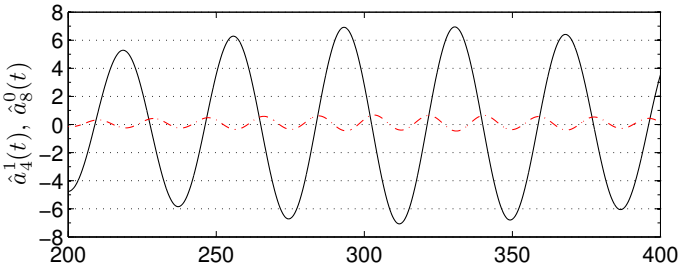

Figure 5.68: Mode $\hat{a}_4^1$ and $\hat{a}_8^0$ between $t = 200\mu s$ and $t = 400\mu s$.

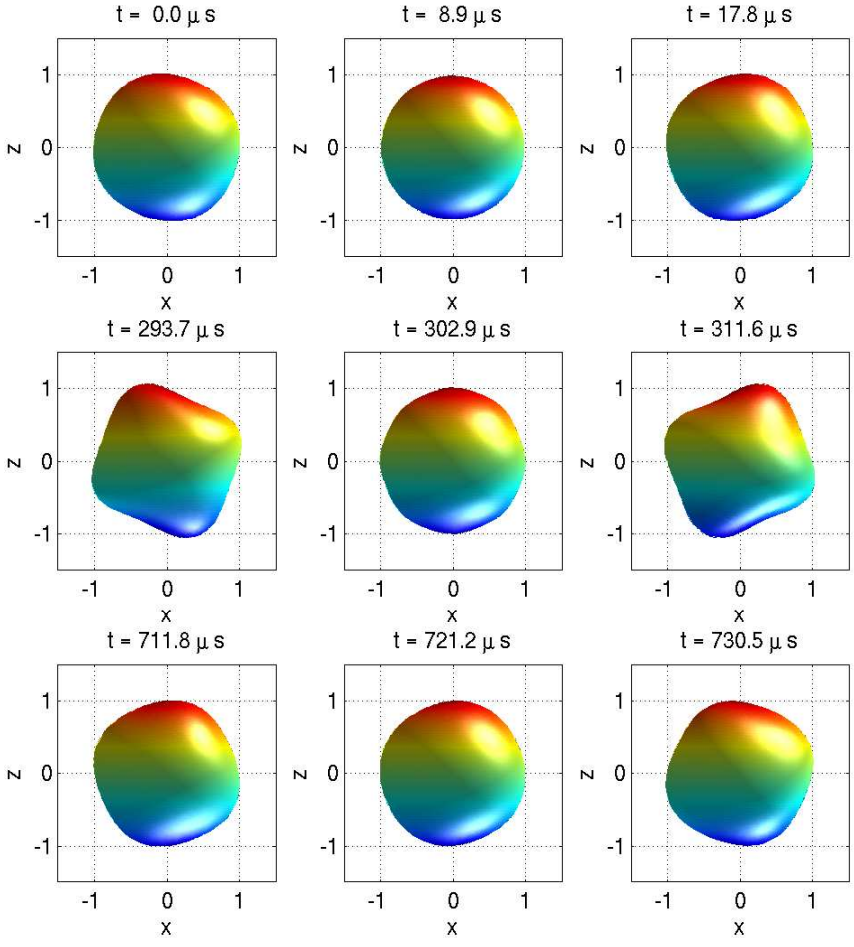

Figure 5.69: Bubble shape at specific times during simulation

5.3.3 Initial Potential Distortions

The previous bubble simulations in this Chapter has involved an initial distortion of the bubble body. Consider instead a spherical bubble which is subjected to the following intial distortion of the surface potential [3]

$$\Phi^* = -\epsilon\alpha_l^m \sqrt{\frac{\tau^* R_0^*}{\rho^*} \frac{(l-1)(l+2)}{l+1}} Y_l^m(\theta, \varphi), \tag{5.16}$$

where α_l^m is the real part of the Fourier-Legendre coefficient $\hat{a}_l^m$ applied to potential. When the substitutions in (5.2) are applied, this becomes

$$\Phi = -\epsilon\alpha_l^m \sqrt{\tau \frac{(l-1)(l+2)}{l+1}} Y_l^m(\theta, \varphi). \tag{5.17}$$

Pozrikidis applied the *generalized vortex method* to various bubble problems near 2 : 1 resonance between the volume and the second order shape modes [3]. For consistency we keep the parameters defined in (5.1), which are slightly different, albeit comparable, to the ones used by Pozrikidis, although for comparison we use Pozrikidis' definition of *reduced time*, $t' = t\sqrt{\frac{\tau}{\rho R_0^3}}$.

Figure 5.70 shows the volume and $\hat{a}_2^0(t)$ for a bubble given an initial distortion of $\epsilon\hat{\alpha}_2^0 = 0.15$. In [3], spectral truncation had to be applied after every time step with $l_{\max} \leq 8$ to allow the scheme to progress beyond one period of volume oscillation. In contrast, the IBEM completes the simulation up to $t' = 30$, *completely without smoothing*, using over 3 times as many triangles.

Similarly, Figures 5.71 and 5.72 shows a bubble given an initial non-axisymmetric distortion of $\epsilon\hat{\alpha}_2^1 = 0.25$, as well as a sudden increase in the ambient pressure by $0.1P_{B0}$ under the same conditions as before. The quadratic IBEM now has to have smoothing applied every time step to complete the simulation, although an l_{max} as high as 14 is sufficient for stable operation.

Figure 5.73 shows the amplitudes of the fourth order coefficients, something which wasn't included in Pozrikidis' work. We can see that the axisymmetric Y_4^0 mode and the non-axisymmetric Y_4^2 mode are excited considerably

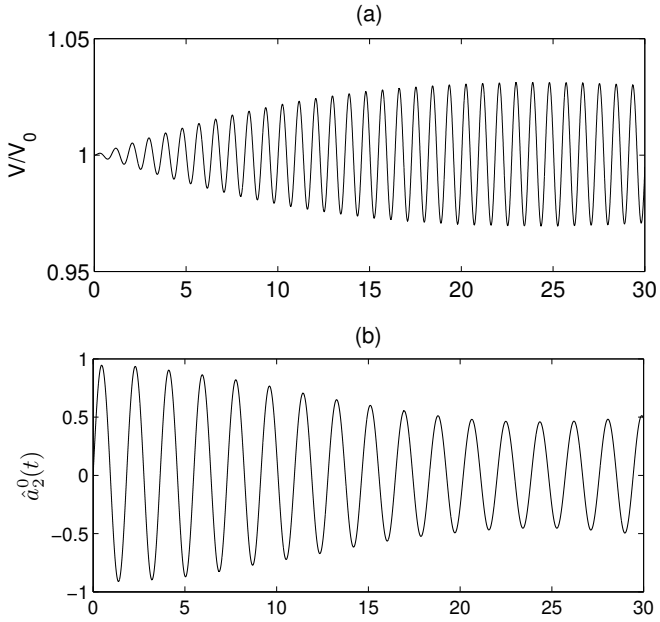

Figure 5.70: Volume and $\hat{a}_2^0(t)$ for $\epsilon\hat{a}_2^0 = 0.15$, 3242 nodes, quadratic elements, $\delta t = 0.01$, $R_0 = 7.18\mu m$, horizontal axes in *reduced time* [3].

from this non-axisymmetric distortion. In particular, the high amplitude of $\hat{a}_4^0$ suggests that the mode should be prominent in the bubble shape at approximately $t' = 10$, something which can seen in Figure 5.74. This again suggests that higher order modes can not be discounted as an influence on the shape when lower order modes are excited by an external force.

According to Pozrikidis, the generalized vortex method yields one order of magnitude better accuracy than comparable boundary element methods for near spherical bubble oscillations, meaning more elements will have to be used with the quadratic IBEM to yield comparable results [3]. It should, however, be clear that the quadratic IBEM is considerably more reliable for higher amplitude shape oscillations, and with the use of parallel computers it should be possible to retain a high degree of accuracy for bubble simulations. This limits the advantages of the generalised vortex method to an area of bubble simulation, where there are several alternatives based on small perturbation techniques [1, 7, 10].

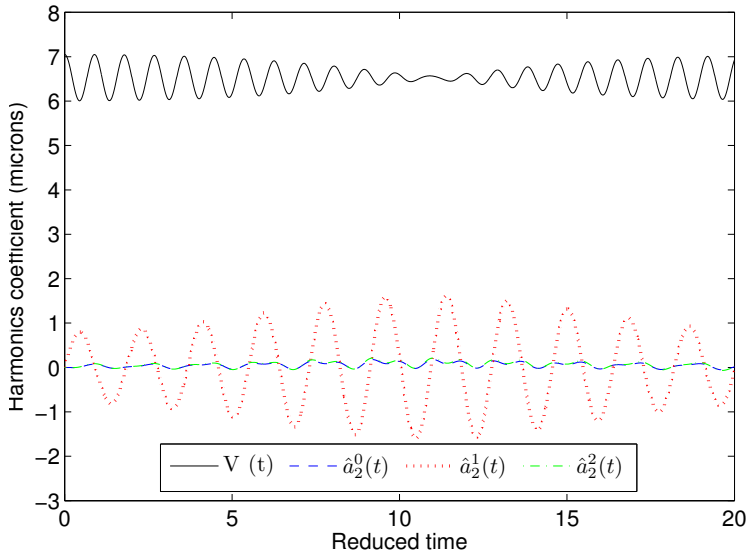

Figure 5.71: Amplitudes for $\epsilon\hat{\alpha}_2^1 = 0.25$ and pressure distortion of $0.1P_{B0}$, 1442 nodes, $\delta t = 0.025$, $R_0 = 7.18\mu m$, horizontal axes in *reduced time*.

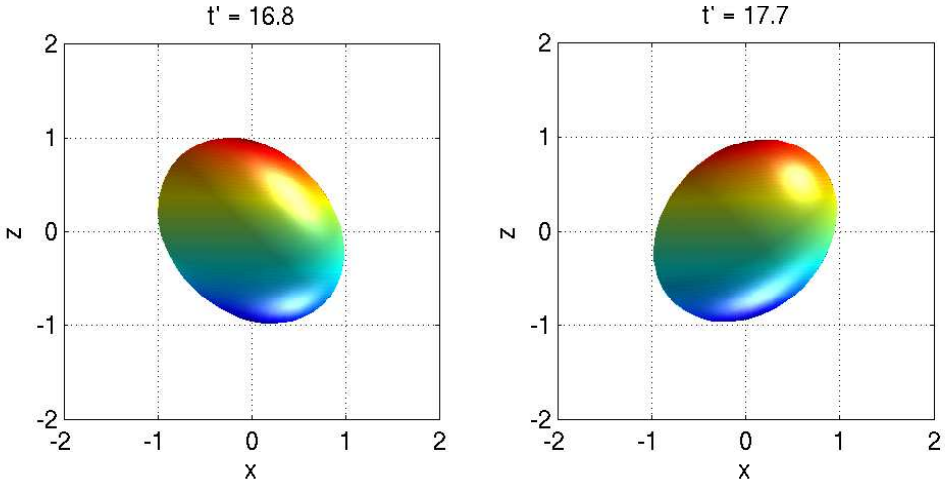

Figure 5.72: Snapshots of bubble for initial potential deformation $\epsilon\hat{\alpha}_2^1 = 0.25$ and pressure distortion of $0.1P_{B0}$

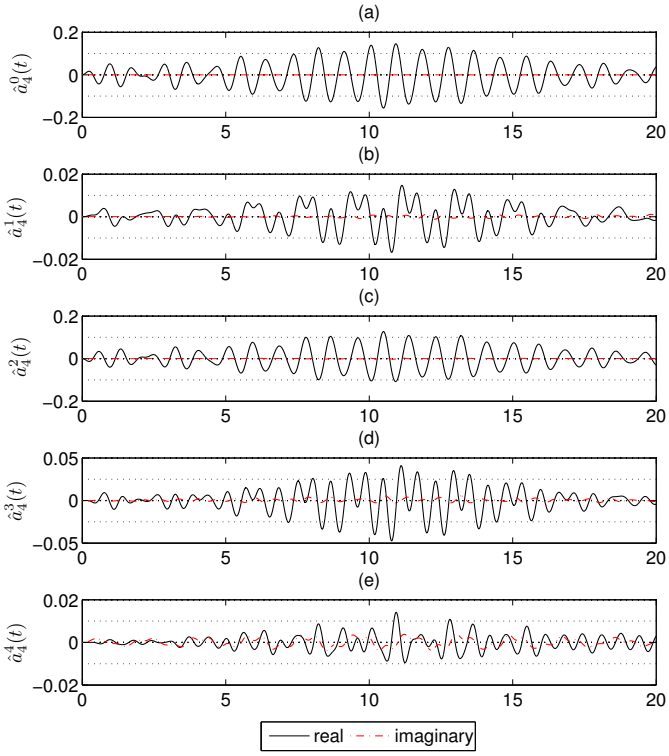

Figure 5.73: Amplitudes for $\epsilon\hat{\alpha}_2^1 = 0.25$ and pressure distortion of $0.1P_{B0}$, 1442 nodes, $\delta t = 0.025$, $R_0 = 7.18\mu m$, horizontal axes in *reduced time*.

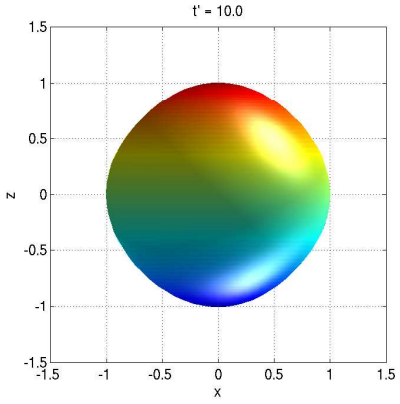

Figure 5.74: Snapshot of bubble for initial potential deformation $\epsilon\hat{\alpha}_2^1 = 0.25$ and pressure distortion of $0.1P_{B0}$

5.4 Uniform Acoustic Fields

While all the shape oscillations demonstrated so far have been due to a non-spherical distortion or forcing of the bubble, it is also possible to excite shape oscillation through purely radial volume oscillation as long as the amplitudes of the volume oscillations are large enough [5, 7]. Consider an acoustic field where the acoustic wavelength is much larger than the radius of the bubble, so that the far-field pressure p can be replaced with

$$p^* = p_0^* + p_A^* \sin(2\pi\omega^* t^*), \tag{5.18}$$

or after applying (5.2) and $\omega = \sqrt{\frac{\rho^*(R_0^*)^2}{p_0^*}}$ we get the non-dimensional form,

$$p = p_0 + p_A \sin(2\pi\omega t), \tag{5.19}$$

where p_0 is the ambient pressure, p_A is the forcing amplitude and ω is the frequency of the acoustic field. When the amplitudes of the acoustic forcing are small, the bubble will oscillate in a purely spherical fashion. When the amplitudes increase, however, the spherical shape becomes unstable, leading to an onset of shape oscillations.

For *isotropic* (uniform) forcing, where the bubble's mean shape is spherical, and the amplitudes of the volume oscillations are small, the spherical shape will be stable as long as the radial oscillation amplitude f (non-dimensionalised by bubble radius) satisfies [11]

$$f < \frac{2\sqrt{[2(2l+1)(l+2)D]^2 + (\omega' - 2F_l')^2}}{(4l-1)F_l'}, \tag{5.20}$$

where

$$F_l' = 2\pi\sqrt{\frac{\rho R_0^3}{\tau}} F_l \,, \omega' = 2\pi\sqrt{\frac{\rho R_0^3}{\tau}}\omega^*, \tag{5.21}$$

where ω is the frequency of the volume oscillation. D is a damping parameter, which in [11] was the Ohnesorge number

$$D = D_\mu = \frac{\mu}{\sqrt{\rho\tau R_0}} \tag{5.22}$$

Care has to be taken if this is used as a prediction about real bubble physics as other damping effects such as acoustic radiation and thermal dissipation may be important [12, 13]. For example, the damping term D may be modified to include acoustic radiation [13]

$$D = D_\mu + D_{ar}\,,\ D_{ar} = \frac{\omega'}{4c}\sqrt{\frac{\tau}{\rho R_0}}, \tag{5.23}$$

where c is the speed of sound in the liquid. Acoustic radiation increases with the frequency of the volume oscillation while the viscous damping does not. Thus the acoustic radiation is expected to dominate the viscous damping at large frequencies [13]. This can be seen in Figure 5.75, which shows

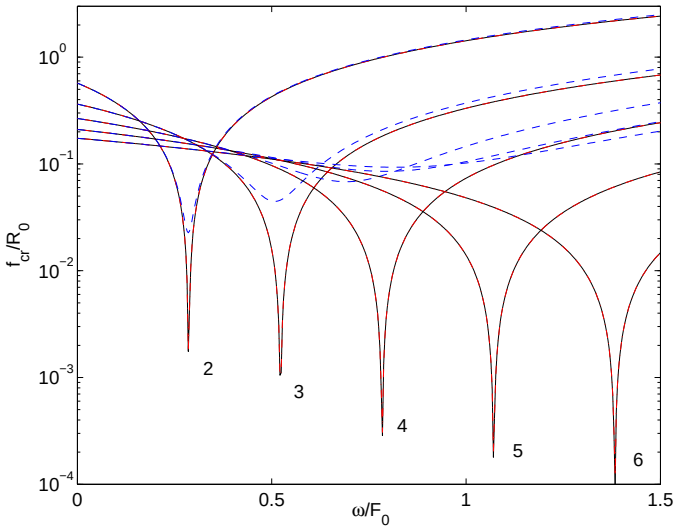

Figure 5.75: Stability of radial oscillation, $R_0 = 0.1$ mm

the stability threshold f_{cr} of a bubble of radius $R_0^* = 0.1$ mm, using the parameters from (5.1) as well as $\mu = 8.9 \times 10^{-4}$ Pa s and $c = 1500$ m/s, with solid lines denoting no damping, dash dotted lines refers to viscous damping only and dashed lines includes both viscous damping and acoustic radiation. For these parameters the natural natural frequencies of the shape modes are $F_2 \approx 4699$ Hz, $F_3 \approx 8579$ Hz, $F_4 \approx 12869$ Hz, $F_5 \approx 17582Hz$ and $F_6 \approx 22699$ Hz, leading to unstable regions around $2F_l$. At these frequencies

viscous damping seems to have no discernable effect on the stability of the spherical oscillation, while acoustic radiation is dominant. Also it seems only the shape oscillations for $l \leq 4$ should destabilise the spherical shape for amplitudes smaller than $\approx 0.1R_0$.

For comparison Figure 5.76 shows the same stability thresholds for a bubble of radius $R_0 = 0.1$ m. Here the natural frequencies for $l \leq 6$ are all of order 10^{-1} Hz. For these low frequencies, the viscous damping should have considerable effect on the spherical stability for $l > 4$, although all modes up to at least $l = 6$ have the potential to destabilise the spherical shape.

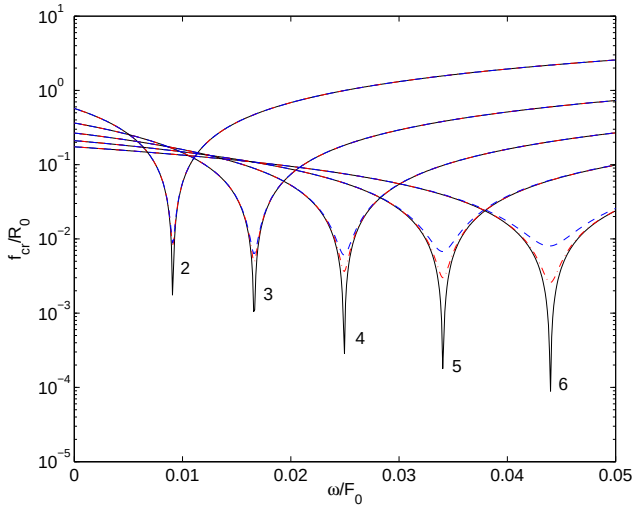

Figure 5.76: Stability of radial oscillation, $R_0 = 0.1$ m

We focus on modelling a bubble of radius $R_0 = 0.1$ mm around the unstable region for the second order modes, where the effects of acoustic radiation seem smallest. This may give the simulations some physical relevance, although the intent is mainly to show that the quadratic IBEM performs as expected given its physical assumptions.

We consider forcing frequencies of $\approx$ 10000 Hz so that the period of oscillation is of order 10^{-4} seconds. Given $c = 1500$ m/s, the wave is expected to travel a distance of order 10^{-1} m per period of oscillation. Since this is

considerably larger than the radius of the bubble, the assumption of a uniform pressure over the bubble surface is valid.

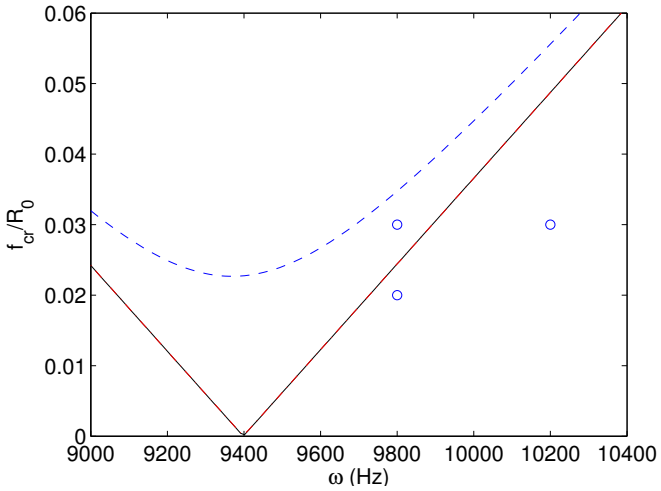

Figure 5.77: Stability of radial oscillation, $R_0^* = 0.1$ mm, close up

Figure 5.77 is a close up of the stability thresholds for three bubble simulations. The two first simulations use the same forcing frequency of 9800 Hz, with $P_a = 0.02R_0$ and $P_a = 0.03R_0$, putting them on separate sides of the stability threshold. The last simulation uses $\omega = 10200$ Hz and $P_a = 0.03R_0$. The bubble is initially given a small perturbation of $Re(\hat{a}_2^i) = 1.0 \times 10^{-6} \times R_0$ for $i = 0, 1, 2$. All simulations are performed with 1442 nodes and $\delta t = 0.025$ with spectrum truncation applied every time step with $l_{\max} = 12$

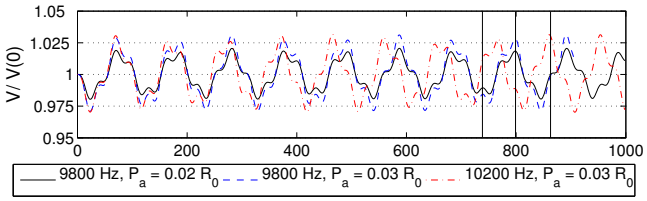

Figure 5.78: Volume oscillations, horizontal axes in μs

Figure 5.78 shows the bubble volume, non-dimensionalised by initial volume, for the three simulations. The vertical lines show the times where

the bubble shapes in Figure 5.80 have been taken. It can be seen that the difference in p_a leads to very pronounced differences in bubble shape and Figures 5.79 shows that the amplitudes of the even mode shape oscillations for $\omega = 9800$ Hz and $p_a = 0.03R_0$ rises considerably after $t = 500\mu s$, leading to the clearly non-axisymmetrically deformed bubble seen in Figure 5.80. The shape amplitudes for the two other simulation stay bounded below 1.0×10^{-6} and can thus not be seen on this scale.

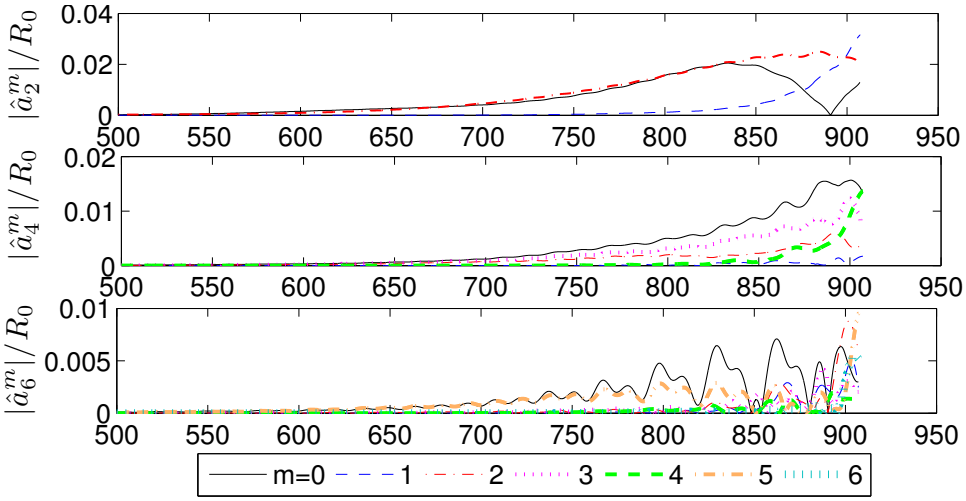

Figure 5.79: Amplitudes, $\omega = 9800$ Hz, $p_a = 0.03R_0$, horizontal axes in μs

The onset of shape oscillations through the enforcing of uniform acoustic fields is an interesting problem, for which axisymmetric bubble models may not be well suited. The reason for this is that the natural frequencies of the shape modes Y_l^m are independent of m and so any forcing frequency ω_l in resonance with the natural frequency of Y_l^0 should also cause the excitation of $Y_l^{m\neq 0}$. The quadratic IBEM, with its completely three dimensional bubble model, seems capable of exploring the instability of spherical oscillation in uniform acoustic fields, with some reservations due to the physical assumptions in the ideal fluid flow model.

As in previous bubble simulations shown, the oscillations of the second order shape modes also leads to oscillations of higher order shape modes,

although in this case only even modes are excited. If, on the other hand, the forcing frequencies are chosen so that odd shape modes are excited, the bubble centroid may move away from origin during the simulation, in a phenomenon often referred to as *bubble dancing*. This is a phenomenon which it may be interesting to explore for future work. It may also be interesting to perform parameter sweeps to explore the limits of current theory with regards to spherical stability.

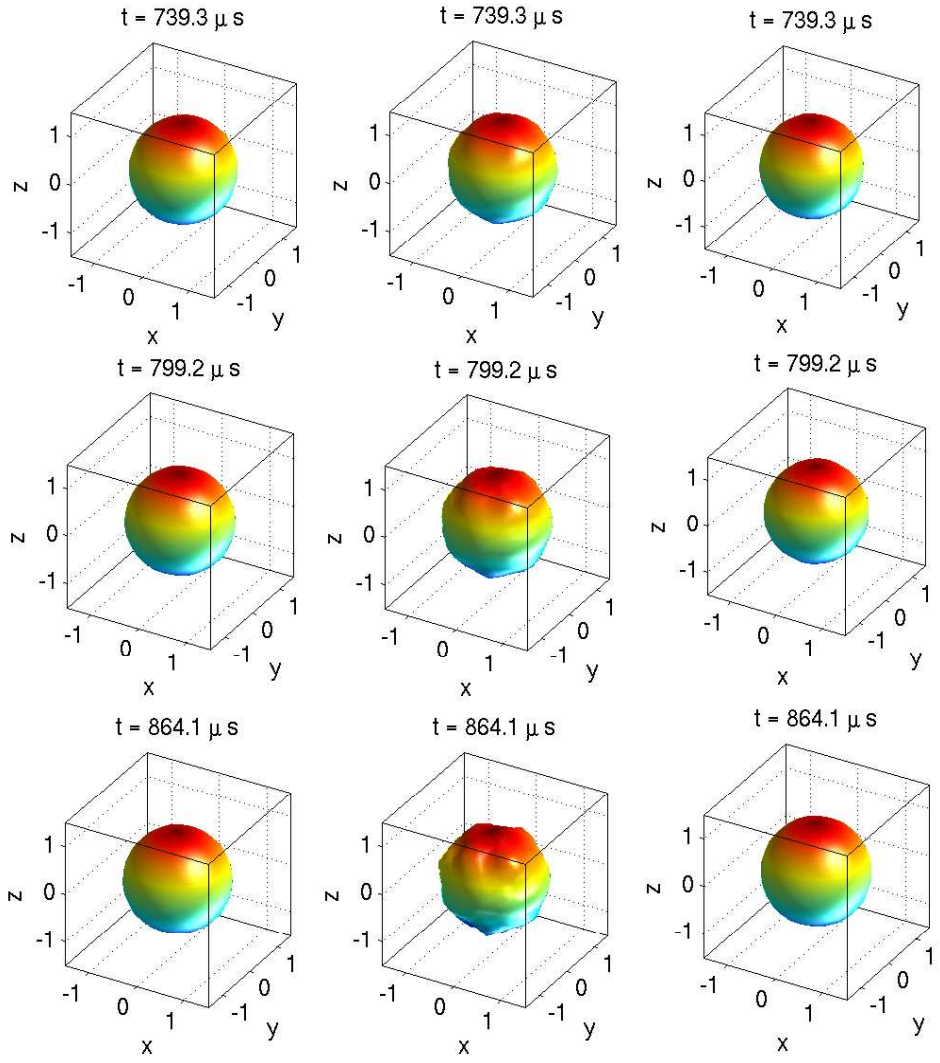

Figure 5.80: Bubble shape. Left $\omega = 9800$ Hz and $P_a = 0.02R_0$, middle $\omega = 9800$ Hz and $P_a = 0.03R_0$ and right $\omega = 10200$ Hz and $P_a = 0.03R_0$

5.5 Large Amplitude Spherical Oscillations

In the previous section we discussed how large amplitude spherical oscillations tend to be unstable, resulting in the onset of shape oscillations. This complicates the numerical simulations as any inaccuracies in the method may be greatly emphasised during the bubble oscillations. As discussed in Section 3.5, no polyhedron sub-division meshes can be completely uniform. When approximating a sphere, the icosahedron based sub-division mesh used in the current IBEM simulations has an initial distortion to the Y_6^m modes of order 10^{-5} for a quadratic mesh of 362 nodes and 10^{-7} for 5762 nodes. This distortion is likely to be amplified during large amplitude bubble oscillations, leading to a highly distorted bubble which could cause the simulation to break down early. Smoothing may be applied, although in the case of spectrum truncation, the truncation level will have to be set to truncate the initially distorted Y_6^m modes, something which may lead to a significant loss of physical effects arising in the simulation.

Consider a bubble of radius $R_0 = 40\mu m$ at equilibrium using the same parameters as in (5.1). The pressure inside the bubble is then dropped by $\Delta P = 0.8$ times the outside pressure, resulting in the bubble radius oscillating between R_0 and approximately $0.4R_0$ with a minimum volume of less than 6.5% of the original volume. Figure 5.81 shows that the simulation using 362 surface nodes breaks down after only a couple of oscillation cycles when smoothing every time step with a truncation parameter of $l_{\max} = 8$. Reducing $l_{\max}$ to 6 has very limited effect on the simulation and as predicted the simulation only becomes robust once $l_{\max}$ is set to 5 so that the oscillations in the Y_6 mode are contained.

Figure 5.82 depicts the same simulation using 1442 nodes. When applying spectral truncation with $l_{\max} = 5$ the simulation breaks down after approximately two oscillation cycles. Lowering $l_{\max}$ further or applying a

smaller time step does not seem to change this.

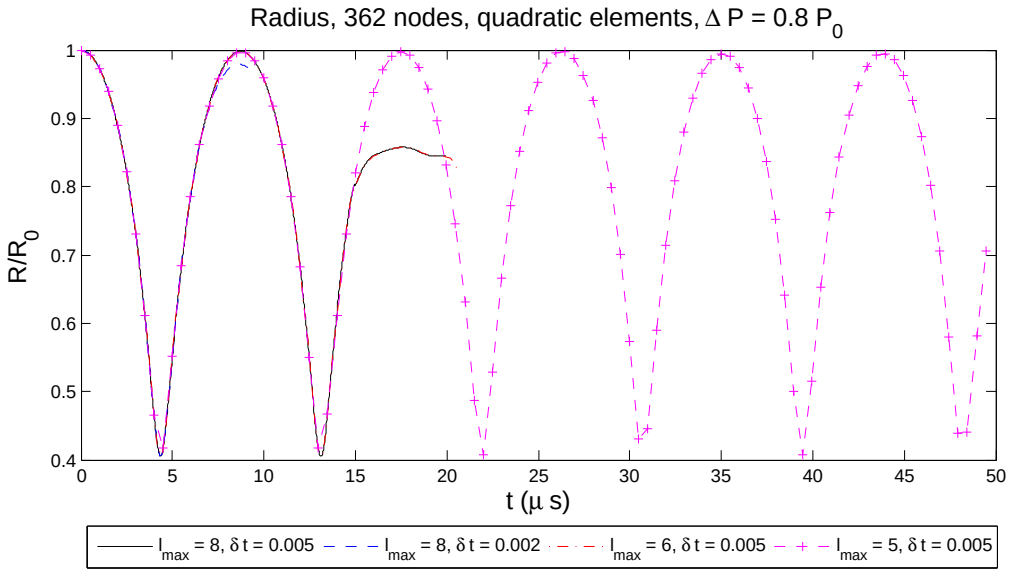

Figure 5.81: Spherical Oscillation, large pressure difference, 362 nodes

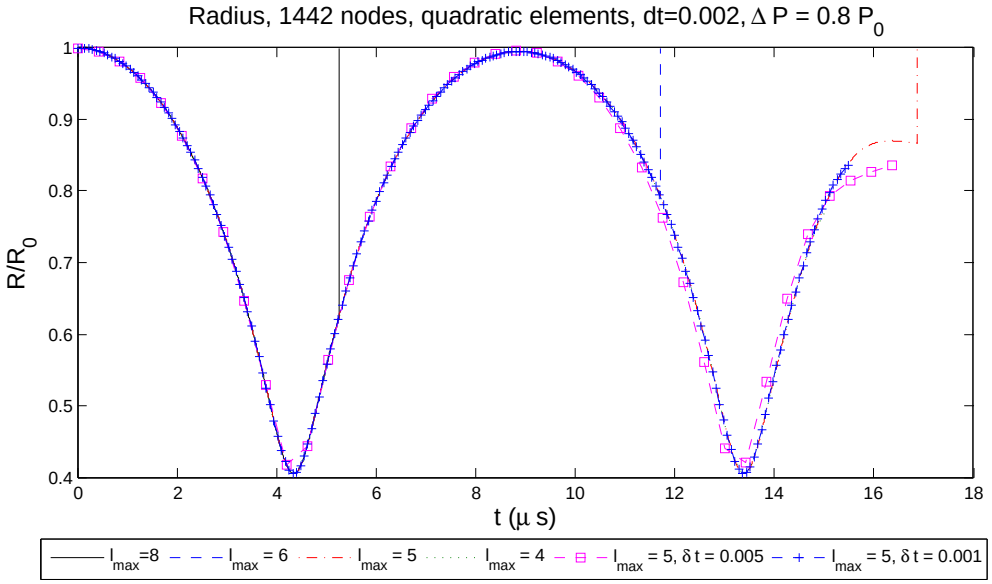

Figure 5.82: Spherical Oscillation, large pressure difference, 1442 nodes

Note that the the lack of previous work on large amplitude bubble oscillations using 3D methods, especially taking into account the effects of surface tension, makes it particularly important to compare with experimental results before any conclusions are drawn on the validity of these results. These strong amplitude oscillation results are thus mainly included to explore the robustness of the IBEM.

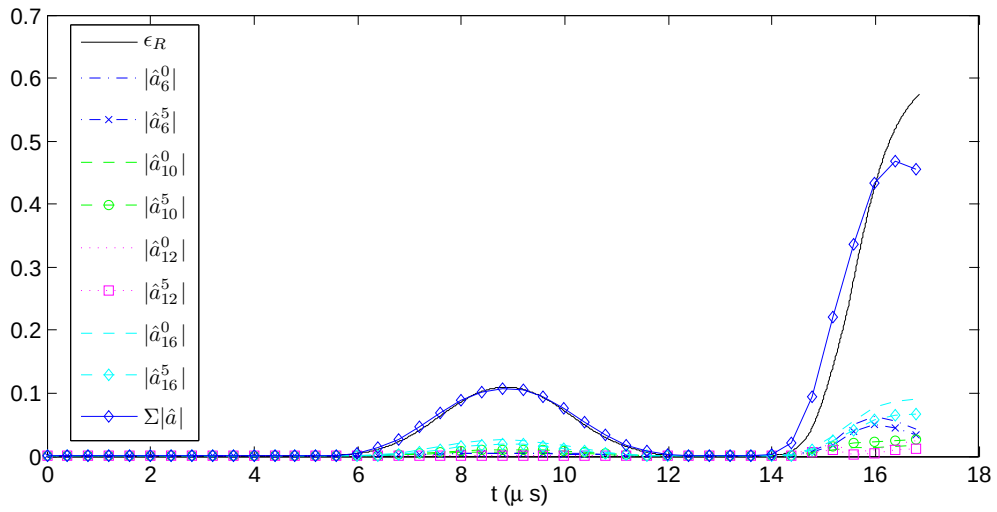

Figure 5.83: Spherical Oscillation, major shape mode distortions, 1442 nodes

In this context, there are many possible reasons for the breakdown of the simulations. Given that only potential is truncated, surface effects of order $l \geq 6$ may still arise on the surface through the simulation and this can be seen in Figure 5.83. Here, the amplitudes of all shape modes showing distortions higher than 10^{-4} are depicted, revealing a considerable growth in these modes during the simulation. The shape mode oscillations are compared with $\epsilon_R = (R_{\max} - R_{\min})/R_0$, where $R_{\max}$ and $R_{\min}$ are the maximum and minimum radius as measured from each nodal point on the surface. Also it can be seen that the sum of the amplitudes of the selected modes, $\Sigma|\hat{a}|$, is of the same order as ϵR. Notably, in addition to a select number of axisymmetric ($m = 0$) modes, the major oscillations occur in the $m = 5$ modes, all of which have five

local maxima along the azimuthal contour lines. It is thus likely that these oscillations arise from the icosahedron based mesh, which is created from an icosahedron with nodes forming pentagons in two horisontal planes. Further evidence for this can be seen in Figures 5.84 and 5.85 showing the deformed shapes of the mesh before breakdown. With the finer mesh it can be seen that the local maxima closely matches the nodal points of an icosahedron.

Since physical effects has been shown to occur in the harmonics modes $l > 6$ it may be necessary to smooth the surface positions themselves in addition to the surface potential in order to prolong the simulation. Also it may be beneficial to introduce variable time stepping used in work such as [14]. This may allow a smaller time step to be used for the parts of the simulation exhibiting particularly violent motion, such as around minimum volume. However, given the strong amplitudes of the radial oscillations, spherical instability is to be expected. Since no real bubble will be perfectly spherical, physical bubble deformation and break up may occur under these conditions. The current IBEM is not equipped to handle bubbles breaking up into smaller units and consequently any sufficiently large deformation will lead to a breakdown of the simulation.

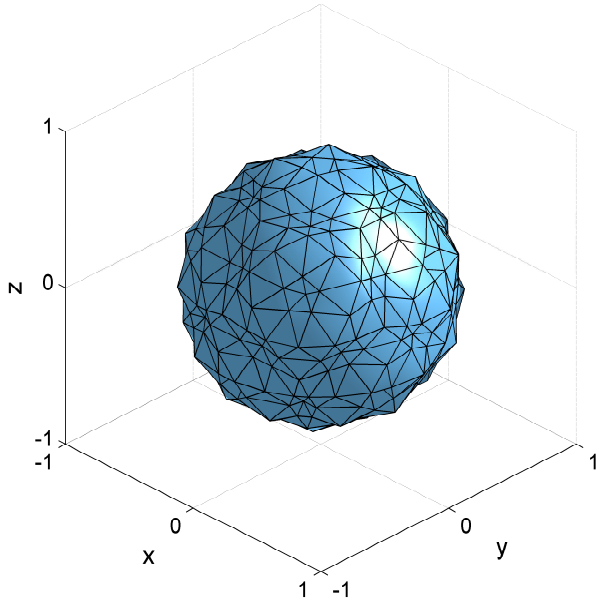

Figure 5.84: Deformed body, 362 nodes, $l_{\max} = 6$, $\delta t = 0.005$, $t = 14.8\mu s$

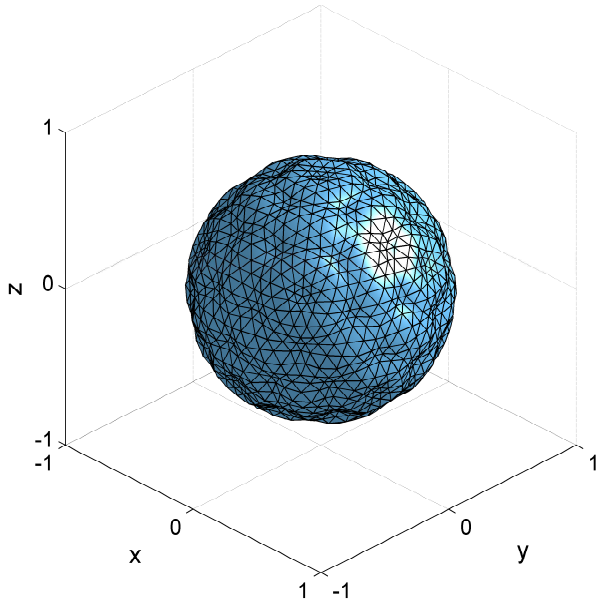

Figure 5.85: Deformed body, 1442 nodes, $l_{\max} = 5$, $\delta t = 0.002$, $t = 14.8\mu s$

Bibliography

[1] S.J. Shaw. Translation and oscillation of a bubble under axisymmetric deformation. *Physics of Fluids*, 18(7):072104, 2006.

[2] E.W. Weisstein. Spherical harmonic. MathWorld–A Wolfram web resource. http://mathworld.wolfram.com/SphericalHarmonic.html.

[3] C. Pozrikidis. Numerical simulation of three-dimensional bubble oscillations by a generalized vortex method. *Theoretical and Computational Fluid Dynamics*, 16:151–169, 2002.

[4] E.W. Weisstein. Legendre polynomial. MathWorld - A Wolfram web resource. http://mathworld.wolfram.com/LegendrePolynomial.html.

[5] Z.C. Feng and L.G. Leal. Nonlinear bubble dynamics. *Annual Review of Fluid Mechanics*, 29:201–243, 1997.

[6] H. Lamb. *Hydrodynamics, Dover Edition 1945*. Cambridge University Press, US, 1932.

[7] N.K. McDougald and L.G. Leal. Numerical study of the oscillations of a non-spherical bubble in an inviscid, incompressible liquid. Part I: free oscillations from non-equilibrium initial conditions. *International Journal of Multiphase Flow*, 25:887–919, 1999.

[8] M. Frigo and S.G. Johnson. FFTW: An adaptive software architecture for the FFT. *Proceedings of the International Conference on Acoustics, Speech and Signal Processing*, 3:1381–1384, 1998.

[9] M.S. Longuet-Higgins. Monopole emissions of sound by asymmetric bubble oscillations. Part 1. Normal modes. *Journal of Fluid Mechanics*, 201:525–541, 1989.

[10] N.K. McDougald and L.G. Leal. Numerical study of the oscillations of a non-spherical bubble in an inviscid, incompressible liquid. Part II: the response to an impulsive decrease in pressure. *International Journal of Multiphase Flow*, 25:921–941, 1999.

[11] Z.C. Feng and L.G. Leal. Bifurcation and chaos in shape and volume oscillations of a periodically driven bubble with two-to-one internal resonance. *Journal of Fluid Mechanics*, 266:209–242, 1994.

[12] M.S. Longuet-Higgins. Resonance in nonlinear bubble oscillations. *Journal of Fluid Mechanics*, 224:531–549, 1991.

[13] N.A. Gumerov. Effect of acoustic radiation on the stability of spherical bubble oscillations. *Physics of Fluids*, 10(7):1767–1768, 1998.

[14] C. Wang and B.C Khoo. An indirect boundary element method for three-dimensional explosion bubbles. *Journal of Computational Physics*, 194:451–480, 2004.

Chapter 6

Conclusions and Future Work

6.1 Numerical Method

In the long term future, as understanding and computational power increases, it is likely that many boundary element simulations will be superseded by methods capable of modelling more physical effects, such as compressibility and full viscous effects. For the short term, however, the simplicity and speed of the boundary element method allow for a very high level of mesh refinement concentrated on the bubble surface. This makes the method particularly attractive for studying subtle effects on the bubble surface. In order to better approximate real physics for certain situations, weak viscous effects may also be included in the boundary element methods through a boundary layer formulation [1]; if viscous effects are ignored it is possible to derive boundary integral formulations for compressible flow [1]. Both of these subjects are, however, outside the scope of this Thesis.

The BEM is a well known numerical method, which has been extensively deployed for bubble problems since the 1970s in axisymmetric form, and more recently in fully three dimensional form. The BEM has also been used extensively in other research areas including elastics and electromagnetic problems. The Indirect BEM presented in this Thesis is an evolution of the

previous BEM formulations, in particular that of Wang & Khoo [2] for bubble problems incorporating some developments used in other BEM work.

The method is node-centric and uses the same interpolation functions to interpolate both the shape and the potential and velocity influences on the surface, something which arguably makes the method more elegant than some previous methods which were based on retrofitting polynomial patches to a linear surface mesh for the purpose of velocity interpolation [3, 4]. Indeed the method itself can be generalised, as discussed in Section 3.3, from linear and quadratic elements to cubic elements and beyond, through relatively simple substitution of elements. However, as has been demonstrated, extending the IBEM beyond quadratic elements may require the application of a weighted mesh regularisation technique capable of keeping the nodes at optimum position throughout the simulation. The introduction of quadratic elements, however, does not seem to yield any negative side effects for the bubble simulation problems demonstrated in this Thesis, and the quadratic elements allow for much higher accuracy in evaluating the spherical harmonics coefficients, which are used to study the oscillations of bubble shape and volume in detail. It should be noted that a similar quadratic IBEM has been developed by other authors in parallel with this work [5], and deployed for simulating large explosion bubbles, also demonstrating the effectiveness of a quadratic IBEM. Note that a method based on simple polynomial patches, depending only on nodal positions, will not offer derivative continuity. However, methods that do, such as NURBS based methods [6] require surface information which may not be available at each time step when simulating a deformable surface.

Previous bubble simulations using BEM have mostly been performed on regular desktop computers with a single processor. Since assembly of the solution matrix scales like $O(N^2)$ for N surface nodes, the increase in computational cost when refining the mesh is substantial. Also since the matrix

assembly is embarrassingly parallel, it makes sense to invest some effort in making the method capable of running on modern computer clusters. The IBEM used in this Thesis, as described in Section 3.7, has been parallelised with MPI and ScaLaPACK. The parallel implementation is not particularly memory efficient, with the full geometric information of the bubble being copied to the memory of every processing node, and there are far more efficient linear solvers available than the $O(\frac{2}{3}N^3)$ complexity LU-decomposition deployed through ScaLaPACK, yet the method scales almost linearly with the number of processors, as can be seen in Section 4.4, and the current implementation has been demonstrated using 2880 quadratic elements (5762 nodes) which, to the best of our knowledge, is higher than the resolution used in previous three dimensional bubble simulations using boundary element methods. In comparison, Pozrikidis [7] deployed 500 elements, while recent work by Zhang *et al* deployed 320 elements for the deformable bubble surface and 1680 elements for a rigid cylinder.

6.2 Summary of Results

The current IBEM was first, in Sections 4.3 and 4.4, demonstrated to give good accuracy for a set of initial tests with a known analytical solution, including that of flow past a sphere and the problem of a constant potential over the surface of the body. In particular the quadratic IBEM showed good accuracy and expected quadratic convergence towards the analytical solution, offering nearly three orders of magnitude better results for 5762 surface nodes than the linear IBEM. The two cubic methods demonstrated, was not nearly as efficient and they were consequently only included in some bubble simulation tests for comparison.

As for bubble simulations, the IBEM was, in Section 5.1, initially tested on a simple spherical oscillation problem with a known solution from the

Rayleigh-Plesset analysis. The IBEM was shown to perform with accuracy and stability, provided suitable integration orders were used. The IBEM was then demonstrated, in Section 5.2 to converge to results using Shaw's perturbation approach for a range of small axisymmetric initial distortions of shape. Some divergence was seen in the fourth axisymmetric mode when the second and third order axisymmetric modes were distorted, despite very good agreement for some higher order modes. Whether this difference is due to inaccuracies in the IBEM or whether some interactions can not be fully captured by Shaw's approach may need some study in the future.

While the quadratic IBEM proved to be stable for small amplitude oscillations, some smoothing was necessary to allow for reliable simulation of large amplitude oscillations. We applied Pozrikidis' spectrum truncation method which, as was demonstrated in Section 5.3, allowed the quadratic IBEM to simulate large amplitude oscillations for well over 30 periods of volume oscillation without any sign of break down. This may, of course, have the side effect of smoothing out physical effects. Such a degredation was mitigated by setting the truncation limit so only modes of order 13 and above were truncated, modes for which numerical error is expected to dominate at the mesh sizes used in this Thesis.

In Section 5.3.1, we simulated the interaction between the volume mode and second axisymmetric mode for several initial bubble radii. We showed that near the 2:1 resonant condition, there is a continuous energy exchange between the volume mode and the resonant shape mode, confirming the predictions by Feng and Leal [8] as well as McDougald and Leal [9]. It was also shown that higher order even modes were also excited with the maximum amplitudes following those of the second order mode.

When the bubble was far away from the resonant conditions, no energy exchange between the volume mode and the shape modes were seen. However some apparent periodic resonant energy exchange between the second and

fourth axisymmetric shape modes was observed, leading to visually prominent fourth mode distortion to the bubble shape, suggesting that resonant energy exchange may happen between shape modes as well as between shape and volume. These simulations also suggested that, despite the initial distortions being axisymmetric, this axisymmetric shape may be "unstable" in the sense that an infinitesimal perturbation to a non-axisymmetric shape mode may lead to resonant growth into finite non-axisymmetric oscillations. Moving on to non-axisymmetric initial distortions, we demonstrated, in Section 5.3.2, the resonant interaction between the non-axisymmetric mode Y_2^1 and the volume mode. It could be observed that an initial non-axisymmetric distortion of even order would excite other modes of the same degree as well as all other even order shape modes. It was shown that slight changes of frequency among the shape mode oscillations may lead some modes to shift in and out of phase with the resonant mode oscillations, with amplitudes either rising or falling sharply. When two modes of the same order were distorted, it was shown that these could either combine to increased amplitudes, or cancel each other out, depending on the phase of the oscillations.

The final initial distortions of shape presented were distortions to the non-axisymmetric fourth order mode Y_4^1 at resonant and non-resonant conditions. For non-resonant conditions no energy exchange was seen between the volume mode and the shape modes, however considerable loss of energy in the perturbed mode was observed to the benefit of the other fourth order modes. Also, the fourth mode oscillations led to non-sinusoidal oscillations of the second order modes. At resonant conditions the excitation of the second order modes was far more prominent, with the Y_2^0 and Y_2^2 modes showing a strong positive growth with an oscillation period similar to the period of energy exchange between the volume and the Y_4^1 mode. Higher modes were also excited, with some of them seeing a delayed energy exchange which may suggest that these modes were excited indirectly.

We also performed two bubble simulations with surface potential distortions, in Section 5.3.3, one axisymmetric and one non-axisymmetric. These were compared with results by Pozrikidis' [7] using the generalised vortex method, confirming Pozrikdis' admission that the boundary element method is more reliable for large amplitude shape oscillations. In particular, the axisymmetric simulation was completed without smoothing using the quadratic IBEM.

We presented, in Section 5.4, three cases of a bubble trapped in a uniform acoustic field, forcing the bubble to oscillate spherically, between a minimum and maximum volume. However, if the frequency of the forcing field is close to the natural frequency of a shape mode, the spherical bubble oscillation may become unstable if a certain critical oscillation amplitude is exceeded. This may lead to the onset of shape oscillations, which was observed for the bubble simulation in this *unstable region*, confirming previous work on the stability of spherical oscillations (see Feng and Leal [1] for an overview).

Finally we demonstrated that when smoothing is performed, the quadratic IBEM could be used to simulate strong amplitude spherical oscillations subject to the effects of surface tension for a long period of time with a coarse mesh of 362 nodes and for a short period of two oscillation cycles for a finer mesh with 1442 nodes. The early breakdown when using the finer mesh could be attributed to build up of numerical errors which can be greatly emphasised due to spherical instability. Improvements such as variable time step sizes and smoothing of surface positions in addition to potential smoothing were discussed as possible means of prolonging the simulations.

6.3 Future Work and Final Words

While the method has been demonstrated to yield good accuracy for a range of bubble problems, there are several improvements, which are outside the

scope of this Thesis, but may be readily applied to the IBEM in future work. All bubble simulations in this Thesis have used fixed time steps for easier comparison between meshes and for better demonstrating the stability of the method. Instead the step size may be chosen to be variable (see for instance [10, 11]), which should yield a considerable performance improvement. A performance boost should also be had by employing an iterative solver such as the Bi-CG solver used by Wang & Khoo [2]. There are also potential improvements to both performance and accuracy by removing evaluation of singular integrals altogether from the IBEM [12].

As for curvature approximation on triangular meshes, most work on this topic has been in the area of Computer Graphics, where the meshes are generally linear and visual accuracy is typically sufficient. The time may thus be right for separate studies on curvature approximation for higher order triangular meshes, which may benefit many other areas of science than the understanding of bubble dynamics.

In addition to these possible improvements to the solution method, there are several applications of the method which would be interesting for future work. One of these areas is comparisons with experimental research such as Holt *et al* [13], Trinh *et al* [14] and Ohsaka and Trinh [15] so as to build more confidence in future explorations of volume and shape oscillations using boundary element methods.

Most results presented could have been obtained accurately by extending the analysis of Shaw *et al* [16] to non-axisymmetric modes. This process is cumbersome, however, and would also be limited to smaller amplitude oscillations. It may thus be interesting to use the IBEM both for validation of any such undertaking and for further exploring the limits of the small amplitude theory.

We would also like to further explore the behaviour of a bubble in both uniform and non-uniform acoustic fields. For larger amplitude oscillations,

the body of work using numerical method is still limited, especially for non-axisymmetric oscillations, an area which is still largely unexplored. In particular the areas of $1:1$ resonance in non-uniform acoustic fields may be interesting to explore using a fully three dimensional method.

Finally, since the IBEM used in this Thesis has been derived from methods developed to study the collapse of bubbles near solid boundaries, it may be time to explore the interactions between shape and volume oscillations in combination with nearby solid objects.

The interaction between shape and volume oscillations is clearly a complex topic, which has previously mostly been explored using small perturbation techniques and spectral methods. Numerical simulation using boundary integral and boundary element methods is a fairly new addition to this topic and can be used as a way of predicting bubble behaviour for amplitudes beyond the realm of small amplitude theory, and also as a tool to confirm or correct predications made using the other methods.

Building upon previous boundary element formulations used in the related fields of bubble collapse near a solid boundary and the oscillation of large explosion bubbles, we have arrived at a method capable of simulating the rapid volume and shape oscillations of fully three dimensional bubbles subject to the effects of surface tension.

The method has been demonstrated for a range of bubble problems, although many other features of bubble dynamics remain to be explored and validated by experimental data.

Bibliography

[1] Z.C. Feng and L.G. Leal. Nonlinear bubble dynamics. *Annual Review of Fluid Mechanics*, 29:201–243, 1997.

[2] C. Wang and B.C Khoo. An indirect boundary element method for three-dimensional explosion bubbles. *Journal of Computational Physics*, 194:451–480, 2004.

[3] G.L. Chahine and T.O. Perdue. Simulation of the three-dimensional behaviour of an unsteady large bubble near a structure. In *3rd International Colloquim On Bubbles and Drops*, volume 197, pages 188–199, Silver Spring, Maryland, USA, Sept 1988. AIP Conference Proceedings.

[4] Y.L. Zhang, K.S. Yeo, B.C. Khoo, and W.K. Chong. Three-dimensional computation of bubbles near a free surface. *Journal of Computational Physics*, 146:105–123, 1999.

[5] A.M. Zhang, X.L. Yao, and X.B. Yu. The dynamics of three-dimensional underwater explosion bubble. *Journal of Sound and Vibration*, 311:1196–1212, 2008.

[6] J. Kouh and J. Suen. A 3d potential-based and desingularized high order panel method. *Ocean Engineering*, 28:1499–1516, 2001.

[7] C. Pozrikidis. Numerical simulation of three-dimensional bubble oscillations by a generalized vortex method. *Theoretical and Computational Fluid Dynamics*, 16:151–169, 2002.

[8] Z.C. Feng and L.G. Leal. On energy transfer in resonant bubble oscillations. *Physics of Fluids A.*, 5(4):826–836, 1993.

[9] N.K. McDougald and L.G. Leal. Numerical study of the oscillations of a non-spherical bubble in an inviscid, incompressible liquid. Part I: free oscillations from non-equilibrium initial conditions. *International Journal of Multiphase Flow*, 25:887–919, 1999.

[10] J.R. Blake and D.C. Gibson. Cavitation bubbles near boundaries. *Annual Review of Fluid Mechanics*, 19:99, 1987.

[11] Y.L. Zhang, K.S. Yeo, B.C. Khoo, and C. Wang. 3d jet impact and toroidal bubbles. *Journal of Computational Physics*, 166:336–360, 2001.

[12] Y.J. Liu. On the simple solution method and non-singular nature of the BIE/BEM-review and some new results. *Engineering Analysis with Boundary Elements*, 24:789–795, 2000.

[13] R.G. Holt, J. Holzfuss, A. Judt, A. Philip, and S. Horsburgh. Forced nonlinear oscillations of single air bubbles in water: experimental results. In *Frontiers of Nonlinear Acoustics. 12th ISNA*, page 497, 1990.

[14] E.H. Trinh, D.B. Thiessen, and R.G. Holt. Driven and freely decaying nonlinear shape oscillations of drops and bubbles immersed in a liquid: experimental results. *Journal of Fluid Mechanics*, 364:253–272, 1998.

[15] K. Ohsaka and E.H. Trinh. Experimental coupling of oscillating gas or vapor bubbles in water: an experimental study. *Physics of Fluids*, 12(2):283–288, 2000.

[16] S.J. Shaw. Translation and oscillation of a bubble under axisymmetric deformation. *Physics of Fluids*, 18(7):072104, 2006.